THREE DIMENSIONAL SEISMIC KINEMATIC INVERSION WITH APPLICATION TO RECONSTRUCTION OF THE VELOCITY STRUCTURE OF RABAUL VOLCANO

by

Chao-ying Bai

B.Sc., M.Sc. (China)

Department of Physics

The School of Chemistry and Physics

The University of Adelaide University

SA 5005, Adelaide

Submitted in partial fulfillment of the requirements

for the degree of Doctor of Philosophy

July 2004

Contents

Abstract

The fundamental strategy in designing an efficient 3-D seismic tomographic inversion technique is to minimize the computational work without sacrificing accuracy. To some extent, one can say that the main task in 3-D seismic tomography is not the algorithm itself, but its practical computational realization. Therefore, notwithstanding the theoretical development of new methodologies in the thesis, much effort has been concentrated on how to make the algorithms (or methods) applicable and tractable in real 3-D cases.

A cell node modification was introduced by adding secondary nodes to reduce the total number of nodes and cells without losing accuracy in the 'irregular' shortest path ray tracing procedure, and for relative ease of incorporation in the inversion procedure without a prohibitively large number of velocity unknowns. An automatic model adaptation process was devised to save both the memory space requirement on the computer and to decrease the program run time. A relative arrival time tomographic procedure was developed to overcome the drawbacks of having a database contaminated with systematic timing errors and to maximize the data coverage. A multiple earthquake hypocenter location process with simple calculation of the analytic Jacobian matrix was implemented to deal with a large travel time database in the 3-D case. A multi-step travel time tomographic procedure was developed to make a large 3-D model computable on a standard personal computer and also to fully use all the available earthquake data (for example, regional events, local earthquakes and explosions) to reveal deep structure for a local velocity model. Other contributions include the joint inversion for determining both the velocity model and the source hypocenters in the absence of well determined source parameters, and an automatic onset time picking algorithm using a combined (energy and autoregressive coefficient) method to pick both first P and S arrival times simultaneously. All the above works

were undertaken to make the tomographic procedure fast and realizable for 3-D real problems.

As an application of newly developed inversion techniques, the velocity field under Rabaul volcano was recovered down to a depth of 20 km. Two low velocity zones (with ~ 10% velocity contrast) are present in the shallow crust. An overturned velocity structure exists in the medium depth region, suggesting SW-NE compression. A deep low velocity zone (possibly with ~10% partially melt status) is linked to the top shallow magma reservoir by a pipe-like low velocity channel, inferring the possibility of existence of deep magma storage.

Statement

This work contains no material that has been accepted for the award of any degree or diploma in any university or college and, to the best of my knowledge and belief, contains no material previously published or written by another person, except where due reference has been made in the text.

I give consent to this copy of my thesis, when deposited in the University Library, or the School of Chemistry and Physics, being available for loan and photocopying in the case where it is cited as a reference.

Bai Chao-ying

July 1, 2004

Acknowledgments

This PhD thesis would have been impossible without the support and encouragement of my supervisor, Professor Stewart Greenhalgh, who gave me helpful suggestions to my research project, and spent a lot of time in correcting the text and modifying the English language presentation so as to reach its present state.

In particular, I would like to thank Dr. Bing Zhou, who gave me the 2-D ray tracing code and some useful discussions. Dr. Doug Finlayson (former staff member of AGSO) supplied the RELACS dataset and some useful information from his studies on Rabaul volcano. Mr. Arcidiaco Armando (RSES, ANU) helped me to quickly grasp the onset time picking code he developed (7sudview.c).

I greatly appreciate the help accorded to me by staff in the Dept. of Geology and Geophysics (where I spent three and one half years) and also in the Dept. of Physics during the progress of this research.

This research work was supported by an IPRS Scholarships (from Jul., 2000 to Jan., 2004) at the University of Adelaide.

Finally, I wish to thank my family, both my wife and my son, for their help and moral support.

Chapter 1: Introduction

1.1 Motivation

The Rabaul region of Papua New Guinea is an area of major volcanic and seismological interest. The last major eruption of Rabaul volcano was in 1994. Several refraction seismic investigations have been carried out in the region to elicit information on crustal structure. The deduced 1-D velocity model has been used for determining the hypocentres of local earthquakes. A much more refined 3-D velocity model is needed to improve the accuracy of earthquake locations. To this end, the RELACS experiment was undertaken in 1997/98, involving the deployment of portable seismic instruments both on land and on the sea floor around the volcano. Explosions, local earthquakes, regional earthquakes as well as teleseisms were recorded over an extended period, with the objective of tomographically imaging the caldera structure and mapping the crustal architecture. The data from this experiment provided the motivation for the present study.

Seismic tomography has been applied on a variety of scales, from near-surface velocity structure and attenuation estimation (e.g. Matthew and Brzostowski, 1992) to deep mantle dynamic structure determination of the Earth's interior (Van der Hilst et al, 1997; Kennett et al, 1998). Some specific uses have been to lithospheric studies (Aki et al., 1977; Mc Queen and Lambeck, 1996; Graeber et al, 2002); petroleum exploration (Justice et al, 1991), mineral deposit evaluation (e.g. Cao and Greengalgh, 1995), and civil engineering investigations (e.g. Witten et al, 1992). Very few papers have dealt with volcano structure determination (Thurber, 1987; Laigle and Hirm, 1999; Dawson et al, 1999; Haslinger et al, 2001; Finalyson et al, 2003).

1.2 Seismic Tomography and Inversion

The main idea of kinematic seismic inversion (traveltime tomography) is to image the interior of an inaccessible body (target) by using raypaths and traveltime information

obtained from sources and receivers along its boundaries. Well-known and routine examples of image reconstruction are in medical examination (CT or computerized tomography) where the interior of the human body is made visible by X-rays without physical intrusion. Similarly, in the earth sciences, it is possible to use seismic waves to determine and distinguish the velocity structure without taking a dense array of drill core samples.

In traditional travel time tomography, one first guesses the velocity field (à *priori* information) and then performs an actual physical experiment within the medium to obtain observational data. The velocity field can be modeled to find the theoretical raypaths and traveltimes according to Fermat's principle or the eikonal equation. This process is called forward modelling. The calculated traveltimes (theoretical times) are compared to those observed from the seismograms and the differences between the theoretical and observed data are used to estimate a change to the model along the travel paths so as to decrease the residual errors of the traveltimes. The new updated model is re-simulated by another synthetic experiment, iterating the above sequence until the residual error is sufficiently small, or until no further improvement (in the least squares error sense) can be achieved. Finally, the updated velocity model (last velocity model) is taken to be a good approximation to the velocity structure of the study area.

Seismic tomography provides the exciting prospect of systematic and knowledge-based exploration, much superior to and more efficient than blind search. The significant attention it has hence received is reflected in the vast amount of literature over the last three decades. For example, seismic ray tomographic techniques have been developed for various kinds of seismic surveys for different purposes, such as VSP, surface or cross-hole, and successfully applied to reconstructing the 2-D and 3-D wavespeed structure of the subsurface from a few metres depth down to several kilometers using the active source data; and from the crustal structure to mantle structure of the Earth using natural earthquake sources. However, many applications and researchers have shown that seismic ray tomography does not yield resolution as good as seismic diffraction tomography or waveform inversion (e.g., Williamson, 1991; Pratt and Goulty, 1991), especially in the spatial resolution and in distinguishing the velocity discontinuity.

Diffraction tomography also has a weak assumption (weak energy scattering assumption), and hence has its limitation in applications, due to ignoring second-order effects of plane-wave scattering, such as multiples. To overcome above drawbacks, there have been increased interesting in incorporating more complex model (Gen et al, 1993 and 1994), or ray-based diffraction tomographic techniques (Gelius, 1995a, b and c). These are the techniques of 'generalized diffraction tomography'.

Full-waveform inversion offers a more complete solution of the wavefield than does diffraction or ray tomography (e.g., Pratt and Worthington, 1988; Tarantola, 1984). Both the time-domain (see for example, Sambridge et al, 1991) and frequency-domain (see for example, Pratt, 1999) approaches of full-waveform inversion make it possible to produce a high-resolution image of the wavespeed structure. However, due to the consideration of computational efficiency, much emphasis has been addressed on frequency-domain approach.

A brief review on the main steps in seismic tomography will now be given under the following heading, (1) data collection and picking error estimation; (2) model division or cell discretisation of the velocity field; (3) ray tracing and traveltime calculation; (4) inversion algorithm; (5) error estimation and results of analysis.

1.2.1 Data collection and error estimation

The collection and processing of observational data is an important first step in seismic tomography. Squires et al (1992) investigated the effects of statics on velocity tomography, and found that traveltime errors of 2 percent can cause tomographic velocity errors of up to 7 percent. Gruber (1998) also analyzed the influence of data errors on the final imaging results. He concluded that the velocity contrast could be masked by relatively moderate data errors. In this situation the inversion image could not give the true velocity distribution in target areas having a relatively small velocity contrast. To some extent one can say that a good dataset can lead to the true velocity estimation. Traveltime errors are most likely introduced by source parameter uncertainty (for example, origin time uncertainty) in the event location and data processing, random noise at the observation site, especially when the S/N ratio is low or the later arrivals are buried in the strong coda of the early arrivals.

Phase onset time picking becomes acute when dealing with a large number of data. Earle and Shearer (1994) used an energy method to deal with the records from the Global Digital Seismic Network (GDSN) and compared the automated onset time picking with analyst time picks previously reported to NEIC. Tong and Kennett (1996) also used the energy technique to identify and pick the later phases of broadband seismograms. Vidale (1986) exploited polarization analysis applied to complex traces to recognize Rayleigh and Love waves, whereas Aster et al (1990) used a polarization filter to highlight the direction of linear ground motion so as to produce a linearity-enhanced seismogram. Wagner and Owens (1996) proposed the use of the principal eigenvalue in the frequency domain as a detector. Takanami and Kitagawa (1988, 1993) used an auto-regressive technique to pick secondary arrivals in a regional seismic network, while Leonard and Kennett (1999) extended auto-regressive methods to three-component analysis of broadband records. Withers at al (1998) have systematically compared several trigger algorithms currently used for onset time picking and give details of comparisons in the time and frequency domains, and also for particle motion and adaptive processing. Bai and Kennett (2000; 2001) developed a novel synthetic algorithm for onset time picking. They combined the energy technique, auto-regressive representation and instantaneous frequency analysis to form a robust onset time picking algorithm directly applied to unfiltered records without rotation, and used polarization attributes to separate S waves from P waves.

Based on the above discussion, it is necessary to estimate the data errors before proceeding with tomographic inversion. Otherwise, there is no guarantee of obtaining a reasonable velocity estimation. In some cases one can obtain a velocity image, but it may lose physical meaning. In such situations, one must find another way to get a realistic velocity image. For example, data pre-processing and data pre-selection (Tinti and Ugolini, 1990) can be used to improve the inverse problem solution. The double-trace tomography algorithm (Dobroka, 1992) can be used to neglect the origin time contribution; while relative travel time tomography (in chapter 5) eliminates the source parameter uncertainty, and overcomes systematic arrival time errors.

The selection of a suitable dataset is also an important factor in obtaining a realistic image. One must have enough rays to illuminate the target field and data coverage

around the target must also be sufficient to image it. To get full ray angular coverage, different depths of earthquakes and also different epicentral distances of events from different azimuths must be employed.

In exploration, Chiu and Stewart (1987) combined well logs, vertical seismic profiles and surface seismic data to determine three-dimensional velocity structure. McCaughey and Singh (1997) presented a method that recovers velocity and interface geometry simultaneously by combining normal-incidence and wide-angle traveltime data via a tomographic method. Bai and Greenhalgh (2004) put forward a new approach: a multi-step travel time algorithm-combining regional events with local earthquakes to improve the data coverage and explore deep seismic raypaths so as to image local deep velocity structure.

The most suitable technique for onset time picking in the future will be to develop a robust automatic trigger algorithm in real time analysis or an on-line facility for simultaneously picking at least two main arrivals.

1.2.2 Model division and cell discretisation of the velocity field

One must first divide the study area into a 3-D grid of velocity values using some à *priori* information on the geology of the target area, so as to simplify the model and make it suitable for numerical modelling. The 3-D grid may be regular (rectangular, triangular), irregular, or dynamic in that it may change. It is often assumed that the velocity in each small cell is constant or obeys a linear relationship along a fixed direction, but more complex approximations to the real world involve using irregular grids. Sambridge et al (1995) used Delaunay and Tetrahedra natural neighbour cells to interpolate an irregular data set to reconstruct the velocity field. This is a very useful idea in the case where one has an irregular distribution of observation stations on a global or regional scale. Vladimir and George (1997) also used irregular cells to develop a two-point ray tracing technique in 3-D transversely isotropic, heterogeneous media. The advantage of this method is that it yields traveltimes as an explicit function of the model parameters.

Michelini (1995) exploited an adaptive-grid formalism that allows for simultaneous inversion of velocity and modification of the position of the grid points. The method therefore seeks the optimal grid configuration to define the model. This can help in

experimental design in choosing the best points for observation stations. Vesnaver (1996) also used an irregular grid in seismic tomography and developed a new ray-tracing algorithm, which was able to simulate transmitted, reflected, refracted and diffracted waves. Bohm and Vesnaver (1999) systematically analyzed the effect of grid division on inversion results and concluded that the possible non-uniqueness and inaccuracy of seismic inversion solutions may be the result of an inadequate division of the model space with respect to the acquisition geometry and the velocity field sought. They overcame this problem by modifying the grid of the inversion system according to the velocity distribution obtained at an intermediate step.

An alternative method to approximate the non-linear nature of the study target is to use a regular basic cell (for example, a cubic cell in the 3-D case) with specified secondary nodes. This enables the definition of a tri-linear (or non-linear) velocity distribution across the cell (Bai and Greenhalgh, 2004).

The most suitable grid in the future will be an irregular one that better represents the real target geometry, along with a non-linear velocity function across the cell to approximate the velocity field of the target.

1.2.3 Ray tracing and traveltime calculation

Seismic ray tracing has been tackled by a number of authors (Julian & Gubbins 1977; Um & Thurber 1987; Sambridge & Kennett 1990). As part of the inversion process one must incorporate a ray-tracing algorithm to calculate raypaths and traveltimes at the various iterations. There are many algorithms for ray tracing and traveltime estimation so that it is not easy to decide which one is superior. No detailed comparison among the different methodologies has been given in the literature. There are basically three approaches for two-point ray tracing: the shooting method, the bending method and the method of characteristics (Sun 1993).

In the shooting method, ray tracing is accomplished as an iterative initial value problem. In moving from the source to the receiver, the shooting process is guided by Snell's law or the ray equation. The shooting angle at the source point is iteratively adjusted until a ray intersects the targeted receiver. Shooting methods can be very efficient if a large set of rays is traced for closely spaced receivers. The drawback of the

shooting method is that the target points are frequently not well-behaved functions of the shooting angle, making some rays impossible to trace.

In the bending method, ray tracing is handled as an iterative boundary-value problem. To trace a ray, a proposed ray path connecting a source and receiver is iteratively refined. In many bending algorithms, the path is refined by discretizing some form of ray equation or by minimizing the traveltime with respect to the node positions along the path. Such an algorithm often leads to a set of equations with the node positions as the unknowns. Bending methods are advantageous over shooting methods when the receiver positions are ill-behaved functions of the shooting angle. The disadvantages are that it is computationally expensive to prepare and simultaneously solve these linear systems of equations, and sometimes the solution gets trapped in a local (as opposed to global) minimum.

In the method of characteristics, the traveltime fields or wavefronts are first constructed by solving the eikonal equation (for example, Coultrip, 1993). The stationary paths having minimum traveltimes constitute the raypaths. Alternatively, rays can also be traced by following the wavefront normal from the receiver to the source. The method of characteristics can be efficient if rays for a large set of receivers and sources are required.

A popular method in recent year is the wavefront construction (WC) method (Vinje et al., 1993), which enables one to recover later as well as first arrivals.

Among so many methods two approaches have turned out to be promising in the sense of computational efficiency and solution accuracy in first arrival calculation. One is graph theory (GT) or the shortest-path method, and the other is the finite difference method (FDM).

(1) Network method using graph theory

The shortest-path method in seismic ray tracing (Nakanishi and Yamaguchi, 1986; Saito, 1989; Moser 1991; Klimes and Kvasnicka, 1994; and many revisions thereafter) offers advantages in computational efficiency, accuracy, robustness and global results. The global result means that the algorithm constructs the shortest paths from one source point to all other points of the seismic network simultaneously. The shortest-path method is robust, because it always gives the first arrival time of the wave energy,

regardless of the complexity of the velocity medium, and even when classical ray theory breaks down, such as in shadow zones. By increasing the ray angular coverage and density of nodes of connections between them, the shortest paths can be brought arbitrarily close to the global minimum travel time paths between sources and receivers. There are no problems with ray path convergence or with being trapped in local minima. Meanwhile, the shortest-path method calculates not only the travel times, but also keeps track of the ray paths. This is important information for use in an inversion procedure that requires the ray path information to form the Jacobian matrix, or in other seismological applications, where ray paths are required or need to be updated (such as in seismic event location). Much work has been done to improve both the algorithm itself and reduce the program run time. For example, based on graph theory, Cao and Greenhalgh (1993) proposed a new minimum traveltime tree algorithm to calculate seismic first-break time fields and raypath distributions. They used a dynamic directed graph (digraph) to keep track of nodes requiring updating, which is claimed to require fewer edges than other approaches. Fischer and Lees (1994) presented a technique to improve the efficiency of shortest path ray tracing. The improvements included a perturbation of rays at interfaces according to Snell's law, using fewer nodes. Klimes and Kvasnika (1994) developed a 3-D network-based ray tracing method (INTERVAL), which finds first breaks with the help of an improved heap algorithm. They gave an analysis on computation time that they found to be at least five times faster than the method of Moser (1991). Bai at al (2004) revised the 'irregular' approach of the shortest-path method in 3-D ray tracing with two new features. Its advantages over the 'regular' approach of the shortest-path method are its ability to handle high contrast velocity models due to the tri-linear velocity function applied to calculate the velocity value on the secondary nodes, less memory requirement and less CPU time, and the capability to calculate a relatively large 3-D model without losing accuracy, provided enough secondary nodes are employed to maintain a good angular coverage.

(2) Solution of the Eikonal equation by the finite difference method

Vidale (1988) and many revisions thereafter (for example, Van Trier and Symes, 1991; Qin, and Luo, 1992; Cao and Greenhalgh, 1994) suggested a ray tracing method based

on solving the eikonal equation using a finite difference approach and then extended it to the three dimensional situation (Vidale, 1990). Based on the finite difference approach of Van Trier and Symes (1991), William and Schneider (1995) extended the upwind finite difference method to 3-D cases to estimate traveltimes and raypaths, and gave an example of application of this technique to 3-D prestack Kirchhoff depth migration.

In the future the most promising algorithm in ray tracing and traveltime calculation will combine two factors: *(1) The algorithm will not only calculate the first arrival, but also deal with the later arrivals (such as head waves, reflections, refractions, diffractions, or multiple arrivals, at the same time); (2) the efficiency of the computation will be dramatically improved, which is an important issue in forward modeling.*

1.2.4 Inversion algorithms

Inversion algorithms fall into two main categories: Traveltime tomography and waveform inversion. Traveltime tomography includes first arrival (P or S waves) traveltime inversion, because it only uses picked arrival times to compare to the data obtained from forward modeling to form the misfit function (objective function), no matter which arrival time is used. Waveform inversion (including reflection, refraction and diffraction tomography) is normally called wave-equation tomography, because it requires the theoretical solution of the wave equation in either the time-domain or the frequency-domain. It uses the observed full waveform to match the waveform amplitudes and phases obtained from forward modeling. It is best implemented in the frequency-domain for reasons of computational efficiency. To minimize the misfit or objective function there are three basic approaches: a linear solver, a linearized solver or a non-linear solver. For linear and linearized inverse problems there are many well-established methods such as Least Squares Criterion (LSC), Conjugate Gradient (CG), Algebraic Reconstruction Technique (ART), Backpropagation, Simultaneous Iterative Reconstruction Technique (SIRT), and Singular Value Decomposition (SVD).

To assure convergence and to regularize the problem, a smoothing or filtering technique is always incorporated to form a combined method. For less severe non-linear inverse problems, the simple way is to linearize it on a local scale and

transform the large-scale non-linear problem into a local linearized problem. For highly non-linear inverse problems the usual approach is to use ray perturbation theory, a Monte Carlo approach, or more efficient global optimization techniques, such as Simulated Annealing or a Genetic Algorithm.

For reasons of computational efficiency, travel-time tomography and full waveform inversion in a strict non-linear sense are seldom pursued in the 3-D case. There are only a few papers that deal with real 3-D seismic tomography (i.e., Zelt, 1994; Colombo et al, 1997; Gochioco, 2000). In order to overcome the drawbacks of a single method of seismic tomography, there are a few genuine combined approaches that have turned out to be useful and practical. Pratt and Goulty (1991) put forward an algorithm to combine wave-equation images with traveltime tomography to form high-resolution images. In this method they first estimated the velocity field using traveltime tomography, and then used the velocity estimates from traveltime tomography as a reference model for wave-equation imaging. They overcame the imaging result uncertainties of full waveform inversion where there is a relatively large deviation of the à *priori* model from the true model. Luo and Schuster (1991) also proposed a wave-equation traveltime inverse algorithm (WT) to overcome the high-frequency assumption of traveltime tomography and the high non-linearity of the misfit function with respect to velocity perturbations in full waveform inversion. They also demonstrated that in the high-frequency limit, WT inversion reduces to ray-based traveltime tomography and is approximately equivalent to full-waveform inversion when the starting velocity model is close to the actual model. These novel ideas can be easily extended to the 3-D case.

To further overcome the drawbacks of traveltime tomography, it has proven useful to combine later arrivals and amplitude information to form a joint inversion algorithm. For example, Su and Dziewonski (1997) first used a joint seismic tomographic approach of bulk sound and shear wavespeed to reconstruct the upper mantle structure with different P and S arrival datasets. Kennett et al (1998) also used joint seismic tomography of bulk sound and shear wave speed, but with the same P and S wave datasets, to reconstruct the mantle structure on a global scale. These papers were the first to separate the influence of compressibility and shear modulus variations. Vinji et al (1993) used wavefront construction to simultaneously calculate the traveltime and

amplitude. The basic idea of this wavefront construction (WC) is to use ray tracing to estimate a new WF from the old WF. Vasco et al (1996) also simultaneously used traveltime and amplitude inversion to reconstruct the velocity field and the attenuation distribution.

Much work on waveform inversion has been performed for 2-D and 2.5-D cases, especially in the frequency domain. Song and Williamson (1995) proposed a full-waveform inversion algorithm in the frequency domain, which used a 2.5-D finite-difference forward modeling method. Zhou and Greenhalgh (1998) put forward another approach: a full waveform inversion algorithm in the frequency domain, which used a 2.5-D finite-element forward modeling method. Bunks at al (1995) used the multi-grid method in waveform inversion in order to avoid trapping by local minima. The implementation of this multi-scale technique required three steps. The first is an operator that restricts the original problem to large scales; the second is an operator that performs relaxation on each scale; the third is an operator that injects the solution available from a large scale into the problem setting at a shorter scale. An important direction for future research for this study must include a thorough study of different types of multi-grid schemes, and how automatic, adaptive methods can be obtained for determining the optimum scale decomposition and the number of relaxation iterations per scale.

Another promising field in seismic tomography is reflection, refraction and diffraction tomography. Zhang and Toksoz (1998) proposed a new non-linear refraction algorithm in travel-time tomography and applied this method to image the shallow velocity structure. Lailly and Sinoquet (1996) used a smooth model in reflection tomography to compare with blocky models, and applied it to estimate geological structure. Wang and Braile (1996) proposed a new approach to simultaneous inversion of reflection and refraction seismic data using a stochastic method. In this field the depth migration technique (prestack or poststack) is always used jointly to obtain a relatively accurate solution.

Future inversion schemes will chiefly concentrate on novel approaches to overcome problems with *non-linearity, computational efficiency, sensitivity, convergence, accuracy, resolving power, and solution non-uniqueness.*

1.2.5 Error estimation and results of analysis

Unlike medical tomography where the human body is accessible in any direction by ray paths, seismic tomography experiments are in most cases restricted in a fixed direction or plane such as in boreholes, between two orthogonal lines (i.e., walkaway VSP), two parallel lines or a local network of recording stations on Earth's surface. These restrictions may result in solution non-uniqueness, which means that two or more different solutions satisfy the same set of data. Another major problem is non-linearity that certainly reflects the true velocity structure of the study area, but usually the non-linear problem has been simply linearized for reasons of theoretical development and computational efficiency, as discussed above. This imposes limitations on solution accuracy, where an image result is invariably obtained, but it may not be meaningful. Therefore error estimation and results of analysis (uncertainty and resolution) are important integral parts of seismic tomography. There are a large number of different inverse schemes available; it is necessary to understand their limitations and the validity of their applications. Because of the non-linearity and high-dimensionality of the inverse problem, these objectives are more difficult to achieve than the development of a new inverse scheme. However, the typical routine for error estimation and results of analysis is to compare the results obtained to the results that have an analytic solution (in the case of synthetic or numerical experiment), or were extracted by well-known inverse schemes in the same field.

The main areas of future research in 3-D seismic tomography will be concerned with: *(1) the choice of velocity model for forward modelling, including an efficient algorithm for raypath estimation and traveltime calculation; (2) the data collection and data coverage; (3) the development of a novel inverse approach to tackle the non-linearity, computational efficiency, convergence, sensitivity, accuracy and solution non-uniqueness; (4) the development of a result analyzer and comparator to evaluate the merits of the inverse scheme; (5) the use of later arrivals, amplitude information, or other geophysical data to improve data density, and image reliability.*

1.2.6 Problems in seismic tomography

(1) Configuration restrictions

The placement of sources and receivers imposes restrictions on the ray distribution and view angles at which the target can be illuminated. Such configuration restrictions may result in some regions being not amenable to imaging.

(2) Number of parameters

In seismic tomography (especially in travel-time inversion) there are only a few parameter restrictions in the misfit function (or in the waveform correlation function). In this situation, one always faces more equations than unknown parameters. Too few parameter restrictions are more likely to lead to solution non- uniqueness.

(3) Computation restriction and theoretical simplifications

The natural world is non-linear in most cases. Thus the non-linear aspect certainly reflects the true velocity structure of the study area, but one usually simplifies the non-linear problem as a linearized one for reasons of theoretical development and computational tractability. This is especially true in 1-D and 2-D inversions, where the effects of the second or third dimension are neglected. This imposes limitations on solution accuracy.

(4) Limitation of the inversion algorithm itself

Another problem is the limitation of the inversion algorithm itself. For example, travel-time tomography with restricted information (just first P or S arrival time information) fails to distinguish the discontinuity in the velocity field, while waveform inversion requires a much more accurate first guess model, which is impossible in most cases (especially for initial investigations). These limitations restrict the applications of seismic tomography.

(5) Unobtainable data quality in most cases

For conventional traveltime tomography, small onset time errors and a good picking function are required. This is even more important for later arrival picking, where one cannot tolerate a large picking error, especially when dealing with small contrasts in the velocity field. For waveform inversion, one cannot synthesize the theoretical seismogram if there is a lack in detail about the velocity model. For a satisfactory picking function, one seeks an algorithm that can pick at least two arrivals

simultaneously (say first P and first S arrival). In many situations, especially large datasets, manual picking is intolerable. A large picking error (in travel-time tomography) or a large deviation from the true velocity model (in waveform inversion) leads to imaging results that are unreliable.

1.3 Seismicity of Rabaul Volcano Region and Related Investigations

Earthquakes can be categorized into two main types: tectonic and volcanic. The former relates to structural deformation and movement, which mostly takes place along plate boundaries or pre-existing faults. The latter is related to volcano generation and development. Whether earthquakes lead to volcanic eruptions or whether volcanic activity triggers nearby earthquakes is still an open question. This hot topic has attracted much attention in the international geophysical literature. The evidence is clear however that before and after volcanic eruptions there is associated seismic activity.

Rabaul Volcano lies on the active Circum-Pacific earthquake belt. This belt accounts for most the world's earthquake energy release and also hosts most of the world's volcanos – the so-called "Pacific Rim of Fire". Figure 1.1 shows the locations of Rabaul volcano and other active volcanoes of the Bismarck Volcanic Arc, eastern Papua New Guinea and the corresponding earthquake locations in the same region. The seismicity in this region is mainly distributed along the volcanic arc.

Rabaul volcano is located on the island of New Britain in Papua New Guinea. Its caldera is one of the major volcanoes of the New Britain Island. Rabaul volcano and associated seismicity provide a good example of the correlation between volcanic eruptions and earthquake activity. Figure 1.2 is a histogram of the Rabaul Volcano caldera-related earthquakes from 1968 to 1998. The seismic ring before the volcanic eruption of 1994 is shown in left panel of Figure 1.3 (This seismic pattern was observed as early as 1970's). The relatively random distribution of epicenters after the 1994 Rabaul volcano eruption is shown in right panel of Figure 1.3.

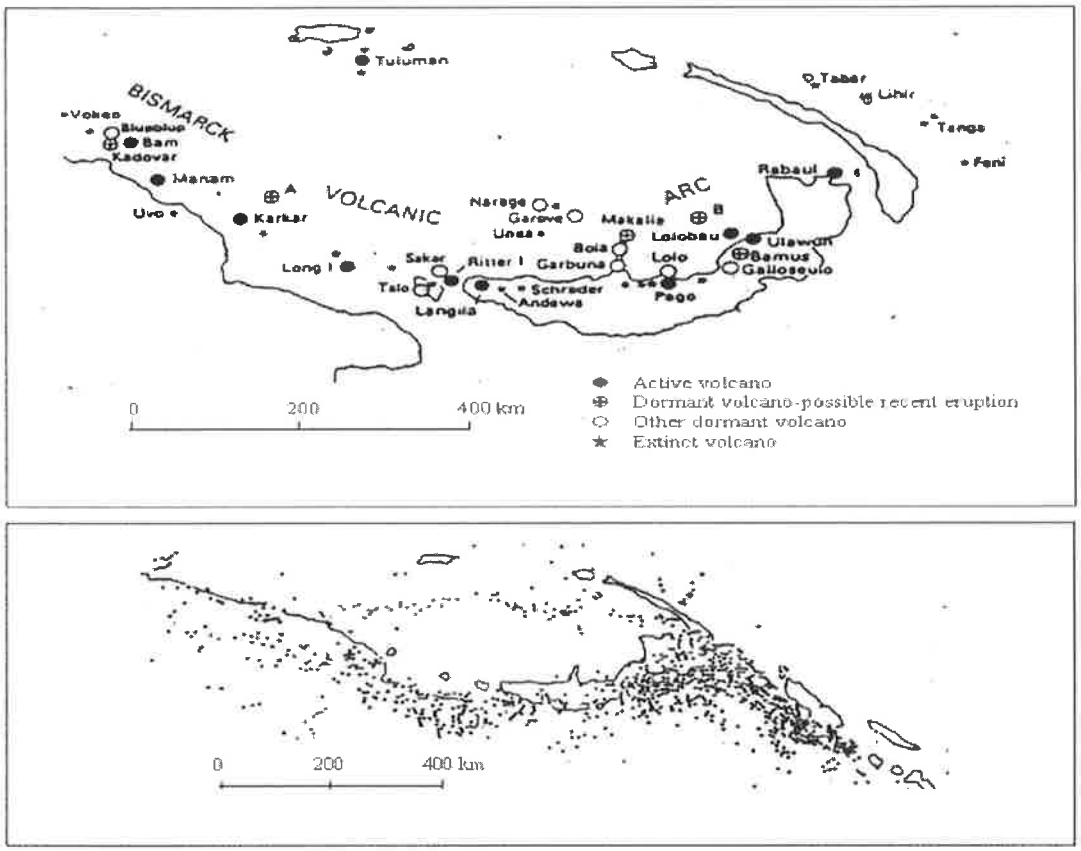

Fig.1.1 The location of Rabaul volcano and the active volcanoes of the Bismarck Volcanic Arc (upper panel), eastern Papua New Guinea, and corresponding earthquake locations (bottom panel), from Finlayson et al, 2001

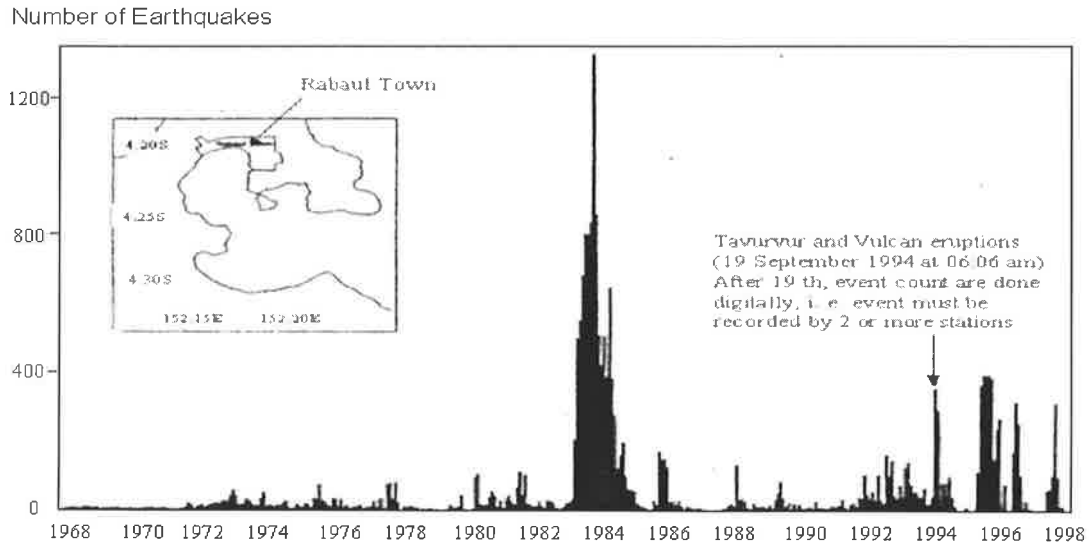

Fig.1.2 Histogram of Rabaul volcano-related earthquakes for period from 1968 to 1998 (Itikarai, unpublished)

From Figure 1.2, it can be seen that a large number of earthquakes occurred during 1983 to 1985, which was followed by a quiescent interval, and then actively increased a little before the 1994 eruption. The significance is that two medium sized earthquakes

($M_L = 5.1$ and $M_L = 4.1$) occurred immediately before (24 hours ahead) the eruption, causing much damage and disruption in Rabaul township and the surrounding area. Three seismic swarms occurred after the eruption, until 1998.

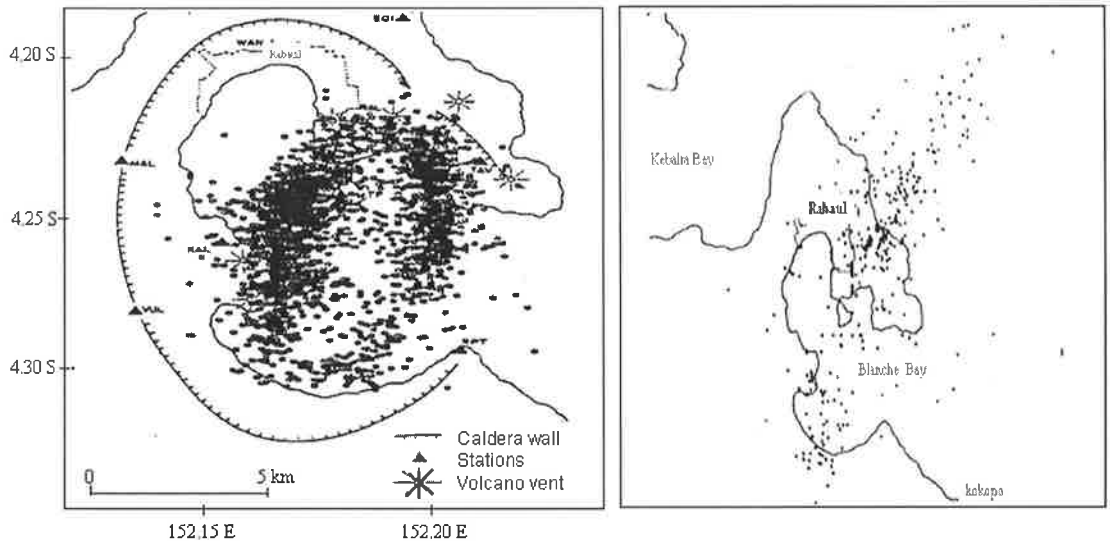

Fig.1.3 Volcano-related earthquake distribution before and after 1994 Rabaul volcano eruption (Left panel: Seismic ring from 1983 to 1985; Right panel: Random distribution from 1995 to1998; from Finlayson et al., 2001)

One may ask the questions: Did the two earthquakes lead to the volcanic eruption? Why did the seismic ring disappear after the eruption? Does the nearby seismic activity tell us anything about an impending eruption? How can the public be warned? To help answer these questions, one needs to analyze the relationship between earthquakes and volcanic activity. These require improvements in the accuracy of hypocentres of volcano-related earthquakes, which in turn requires a valid 3-D velocity model for the Rabaul region.

The controlled source seismic experiments conducted around Rabaul in 1967 and 1969, and reported by Finlayson et al (1972) and Finlayson and Cull (1973), are reviewed in chapter 2. From these studies two basic velocity models were derived for the region:

(1) A 1-D velocity model for the P wavespeed down to depth of 40 km, deduced by Wiechert-Herglotz inversion of explosion travel time data; and (2) Two roughly layered 2-D velocity models for P wavespeed down to a depth of 40 km, determined by

time term analysis of refraction data. One profile is for the Bismarck Sea to Solomon Sea, the other for the Bismarck Sea to the Pacific Ocean.

The RELACS experiment of 1997/98 (see chapter 2) has been analyzed in a preliminary sense (Gudmunsson et al, 1999; Finlayson et al, 2003) to yield more detailed information on the velocity structure over a much more restricted region and to shallower depth. Two wide-angle reflection/refraction profiles from marine shots, running from the Baining Mountains to St Georges Channel, and from Towakundum to Tokua Airport (Finlayson et al., 2001), were interpreted by iterative ray tracing to produce 2-D velocity models extending to 10 km crustal depths. Seismic data from both explosions and local earthquakes, recorded on an areal distributions of up to 76 stations (both land and marine) around Rabaul, were tomographically analyzed to produce a rough 3-D velocity model extending also to the depths of 10 km.

The 1967/1969 refraction profiles were aimed at delineating tectonic boundaries and deducing Moho topography on a relatively large scale, while the RELACS experiment was designed to map velocity structure on a small scale around Rabaul volcano. The primary purpose of this recent experiment has not been fully met. There are several unanswered questions that remain:

(a) What is the deep 3-D velocity structure under the Rabaul region, which is important to explain the volcanism (say at least 20 km depth)?

(b) What is the S-wave velocity model (1-D, 2-D and even 3-D) around the Rabaul region, which is more critical to explain the shear modulus?

(c) How can the volcanic earthquakes be located more precisely; this needs a deeper 3-D velocity model for mid-depth events around the Rabaul region (these mid-depth earthquakes may be much more linked with generation and development of volcanic structure)?

1.4 Thesis Objectives and Research Achievements

This doctoral dissertation was undertaken to answer the above questions. The main objective was to make full use of the RELACS dataset to reconstruct the 3-D velocity structure around Rabaul volcano. To achieve this objective, it was necessary to make

improvements, refinements and further developments to 3-D ray tracing, event time picking and tomographic inversion. Specifically, new techniques were devised to accommodate timing errors, to incorporate regional earthquakes, to recomputed regional event hypocentres prior to tomography, and to make the whole process accurate and efficient.

A summary of the main research achievements is given below:

1.4.1 Data collection and onset time picking

It was necessary to develop an automatic onset time picking algorithm to determine at least two arrival times (say first P and first S arrival) simultaneously for both single- and three-component records of local and regional events from the RELACS database. This adds both P and especially S arrival time picks to the database of the original RELACS project (see Finlayson et al, 2001), in readiness for P and S-wave travel time tomography. In chapter 9, some revised picking functions are presented (such as the energy function, an auto-regressive technique, and a combination technique), and several algorithms are compared. Finally, a combined picking technique was used to simultaneously deduce both first P and S-arrival times as much as possible for local events (including explosions), and especially near-regional earthquakes.

1.4.2 Ray tracing in 3-D arbitrary media

In chapter 3, a new 3-D ray-tracing program based on the 'irregular' shortest path approach of the graph theory was devised, with modified cell node definition and a tri-linear velocity function across each cell. It was set up for arbitrary media and requires less memory storage and is much faster than the 'regular' approach. It is used to calculate travel times and associated raypaths, for subsequent inversion. The maximum error bound was obtained within a homogeneous media, which may be considered as an upper error bound in the whole model for real problems.

The 'irregular' approach in this study has been compared with the 'regular' approach both in theoretical consideration, and in two specific velocity models that were previously used by the 'regular' approach. The numerical tests indicate that the new approach is able to obtain a high accuracy of traveltimes and related raypaths for a high contrast velocity model involving a relatively large cell size, but with sufficient

secondary nodes. In the sense of computational efficiency and the accuracy of the computed travel times, the 'irregular' approach is more applicable than the 'regular' approach in real 3-D problems.

To achieve the computer memory reduction and improved run time, an automatic function was incorporated into the ray-tracing program to automatically select a relatively small (variable) model according to each source to seismic network deployment. This results in nearly 50% reduction in the memory requirement and a corresponding decrease in the program execution time. It is thus of practical usage in 3-D seismic forward modeling.

1.4.3 Non-linear travel time inversion

In chapter 4 an efficient and accurate procedure for non-linear travel time inversion was developed so as to incorporate it with the forward modelling to form a fast and reliable algorithm for 3-D traveltime tomography. The inverse solver is based on a damped, minimum norm, least-squares approach (DMNLS), incorporating constraints. Instead of taking segments of ray paths as the elements of the Jacobian matrix, the time derivative to changes in velocity as elements of an analytical Jacobian matrix are calculated according to specified velocity and travel-time equations. A 2-D alpha-trimmed means filter is applied in the final image to avoid sharp velocity changes. Finally, several numerical tests were performed to analyze the efficiency, accuracy and sensitivity of the inversion procedure. The results indicate that the program works well in high contrast velocity media (say, more than 20% velocity contrast), and also under tolerable levels of noise (less than 10% relative error both in travel time and model perturbation).

1.4.4 Event hypocentral determination in 3-D arbitrary media

In order to reduce the location errors of events and provide a good quality of travel time dataset, a new earthquake hypocentral location program was developed for 3-D arbitrary media to relocate local and near-regional events around the Rabaul volcano before starting the RELACS data inversion. In chapter 7, the details of the robust and accurate event hypocenter location program were presented for 3-D arbitrary media. It uses a modified shortest-path algorithm as the ray tracer and DMNLS-1 as the inversion

solver. In order to avoid the instability of elements of the Jacobian matrix, a simple, but robust method of analytic Jacobian matrix calculation was followed. The time derivatives with respect to source position changes in three directions were achieved through six search directions to explore the octant space. To test the accuracy of the location program in arbitrary 3-D media, several synthetic tests and a real example in relocating explosions were conducted. They showed the remarkable ability to locate events, even in depth, when the starting source hypocenters are in appreciable error.

1.4.5 Relative arrival time tomography

Chapter 5 is concerned with an alternative to travel time tomography, especially important where there are systematic timing errors, source location uncertainty, and limited data coverage. It uses relative times, referred either to the minimum time, or the mean time. The two approaches are analyzed and compared against each other as well as against absolute travel time tomography. Several numerical tests on synthetic models indicate the success of relative arrival time tomography. An investigation is made into accuracy and sensitivity to noise for both the systematical and random errors in travel time data.

1.4.6 Joint seismic tomography

To develop a program of 3-D joint travel time (or arrival time) inversion for updating both the velocity model and the source positions, a combination approach that ties together the new 3-D earthquake location and 3-D travel time tomography procedures was devised in chapter 8. In order to test the efficiency and accuracy of the procedure, three numerical tests were simulated to analyze and examine the above issues. The results show that a good velocity image and improved source location can be obtained only if there is a rough estimate of the velocity model and the source locations. Otherwise, there is no reason to proceed. As expected, there is a trade-off between the quality of the velocity model and the precision of the source hypocenters.

1.4.7 Multi-step travel time tomography

Given the need to reconstruct local but deep 3-D velocity structure, chapter 6 presents a multi-step travel time tomography algorithm. Regional sources are included, along with local sources (explosions, earthquakes) to maximize the data coverage and to illuminate deep parts of the structure. The regional events have rays that arrive at

steeper angles from below the local model volume. Without the additional sources, it would be difficult to image beyond shallow depth. The local velocity model, on a fine grid scale, is embedded within the regional velocity model (large scale). Rays are traced in 3-D through the regional model to find the intersection points (and corresponding travel times) from the regional sources. These intersection points on the local model volume constitute new "secondary sources". Tomography then proceeds on the local model using both primary plus secondary sources around the local volume. Results indicate that this is a feasible way to proceed, because it saves on computer requirements and yields an accurate 3-D velocity distribution.

1.4.8 Application to reconstruction of the Rabaul volcano structure

The newly developed techniques are applied to real data analysis in chapter 10 to reconstruct the 3-D velocity structure of Rabaul volcano. A 1-D velocity model both for P- and S-waves was first obtained by the Weichert-Herglotz inversion method. Then using this 1-D velocity model to relocate the regional events to reduce the initial location errors (due to the large-aperture (global) seismic array used) before the final 3-D travel time tomography was undertaken. Finally the 2-D velocity model across Rabaul, and also the 3-D velocity model under the Rabaul region were recovered down to a depth of 20 km. This is a more complex and detailed structure than obtained from previous studies. The deduced velocity models and the Rabaul volcano structure are briefly discussed.

In summary, all the above works were undertaken to make the tomographic procedure fast and realizable for 3-D real problems. For these purposes, the associated programs all link in such a way that the input and output files have a simple and easy to handle format. There are also intermediate outputs, which can be easily checked as the program runs or as new input data is available. In this way, the tomographic inversion procedure can be done consecutively without interrupting and disturbing the final results of the whole process.

Chapter 2: The Seismic Experiments and Preliminary Results for the Rabaul Region

2.1 Introduction

In this chapter I review and summarize the main finding of the 1967 and 1969 seismic refraction surveys and the 1997-1998 RELACS project (acronym for Rabaul Earthquake Location and Caldera Structure). To some extent, this dissertation is a continuation and supplementation of the RELACS project, and so it is important to understand how the experiment was conducted, how the data were acquired and what was initially achieved.

2.2 Previous Seismic Refraction Profiles

Two phases of geophysical investigation were carried out in the New Britain-New Ireland region in 1967 and 1969 (Brooks, 1971; Finlayson, 1972). They involved refraction profiles and gravity surveys, as well as marine sparker reflection profiling and magnetic profiling in surrounding waters. The work was done by the Bureau of Mineral Resources, Australia (now named Geoscience, Australia), and was aimed at studying the crustal structure of the region, specifically to define major boundaries of the complicated tectonic plates. Geological mapping was also carried out in the region. The Hawaii Institute of Geophysics conducted companion marine geophysical investigations, which have also contributed to the knowledge of crustal structure in the New Britain and New Ireland areas.

The primary purpose of the refraction surveys was to determine depth to the Moho, map variations in its topography, and to delineate major boundaries in the upper crust.

The 1967 survey entailed 26 seismic stations and 46 shots, mainly concentrated on a small region around Rabaul volcano. The 1969 survey was distributed over a much

wider area of New Britain-New Ireland so as to gain regional data coverage. It entailed 47 stations and 54 shots (Finlayson et al, 1973).

From these seismic refraction surveys, a 1-D velocity model was obtained for the Rabaul region, down to depths of 40 km, by Wiechert Herglotz inversion of the travel time vs distance graph (Finlayson et al., 2001); two 2-D roughly layered velocity models for P wavespeed down to a depth of 40 km, determined by time term analysis of refraction data. One profile is for the Bismarck Sea to Solomon Sea, the other for the Bismarck Sea to the Pacific Ocean (see Figure 2.1 for details).

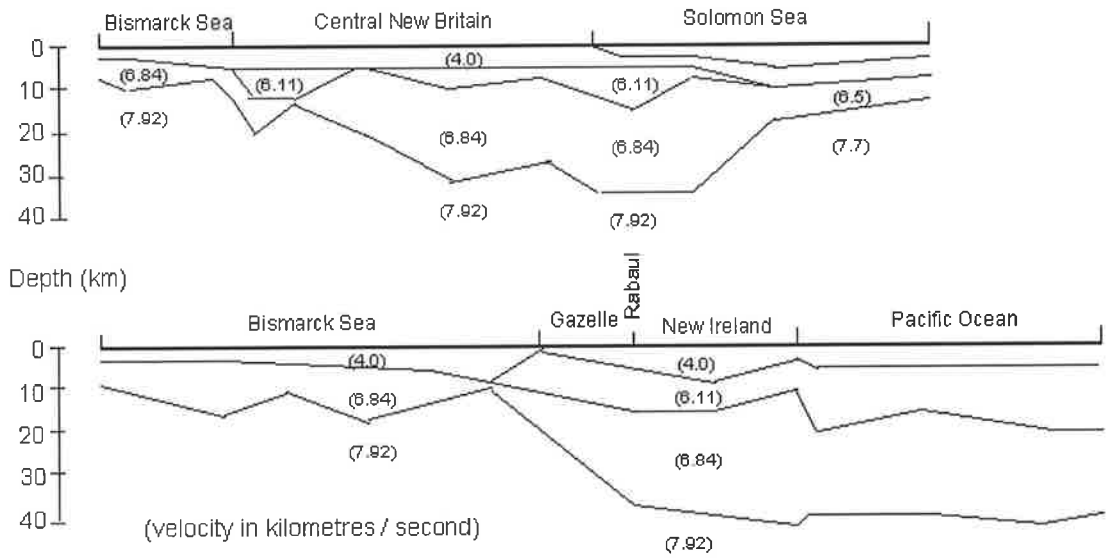

Fig.2.1 Representative crustal cross-sections from time-term analysis in the New Britain-New Ireland region (from Fig. 9 of Finlayson and Cull, 1973)

2.3 RELACS Experiment

The seismic velocity model routinely used at RVO (Rabaul Volcanological Observatory) is a one-dimensional plane-layered model, based mostly on the P-wave velocity results of Finlayson and Cull (1973a, b), with later modifications (Almond and McKee, 1982). The FASTHYPO method (Herrman, 1979) is used to determine the earthquake locations from the travel-time database of the Rabaul seismic network. But studies have shown that changing the velocity model results in both lateral and vertical shifts in the hypocentral distributions (for example, Stewart, unpublished RVO

technical note, 1994). That is, the location process is model-dependent. Clearly, there is a need to develop an improved method of determining earthquake hypocenters based on a valid 3-D velocity model for the Rabaul caldera. This would improve the credibility of the RVO interpretations of the earthquake focal patterns in the uppermost 15 km of the crust, and within a radius of 25 km from the caldera. Such improvement would yield a better image of the possible magma source regions at depths down to about 20 km.

The 19 September 1994 eruption of the Rabaul volcano drew much attention to the limitations in the capacity of the existing volcano monitoring system at RVO to provide timely warnings of eruptions. It was clear that an improved volcano monitoring system and seismic analysis capability at Rabaul and other locations throughout PNG was needed. The RELACS project was undertaken to address this need. Specifically, the plan was to improve the capability to successfully monitor volcano activity, and to develop a better understanding of the relationship between earthquakes and volcanic eruptions. A 3-D velocity model was deemed to be an important first step at improving the accuracy of hypocenter location, and visualizing the subsurface.

RELACS was a collaborative project involving the former Australian Geological Survey Organization (AGSO-but now renamed as Geoscience Australia or GA), the Research School of Earth Sciences, Australian National University (RSES, ANU), the Laboratory for Ocean Bottom Seismology, Hokkaido University, Japan (LOBS, HU), the Dept. of Geology and Geophysics, University of Wisconsin, USA (DGG, UW) and Rabaul Volcanological Observatory (RVO, PNG). The project was funded by AUSAID and JICA, the foreign aid organizations of Australia and Japan, respectively.

2.3.1 Purpose of RELACS

The project had three important goals (Finlayson et al., 2001):

(1) To provide an improved 3-D model of the seismic-wave velocity structure in the Rabaul volcano area to depths of at least 15 km in order to improve the accuracy with which the locations of volcano-related earthquakes can be determined.

(2) To improve knowledge of magma storage and the possible magma generation region.

(3) To improve the capability of RVO staff to analyze, interpret and display earthquake data from the Rabaul earthquake database for public planning and decision-making purposes using a volcano-hazard mapping and information system (VMIS).

2.3.2 Design of field investigations

(1) Three wide-angle seismic profiles

A wide-angle seismic profiling technique using marine shot sources was designed to determine the velocity variations in the uppermost 10 km of the volcano caldera. This method has the precise timing and positioning of sources, which helps to reconstruct a 3-D shallow velocity model in details. Figure 2.2 shows the location of three wide-angle seismic profiles used in the Rabaul region during the RELACS project. The data acquisition was conducted over five-month period (from 5 November 1997 to 12 January, 1998).

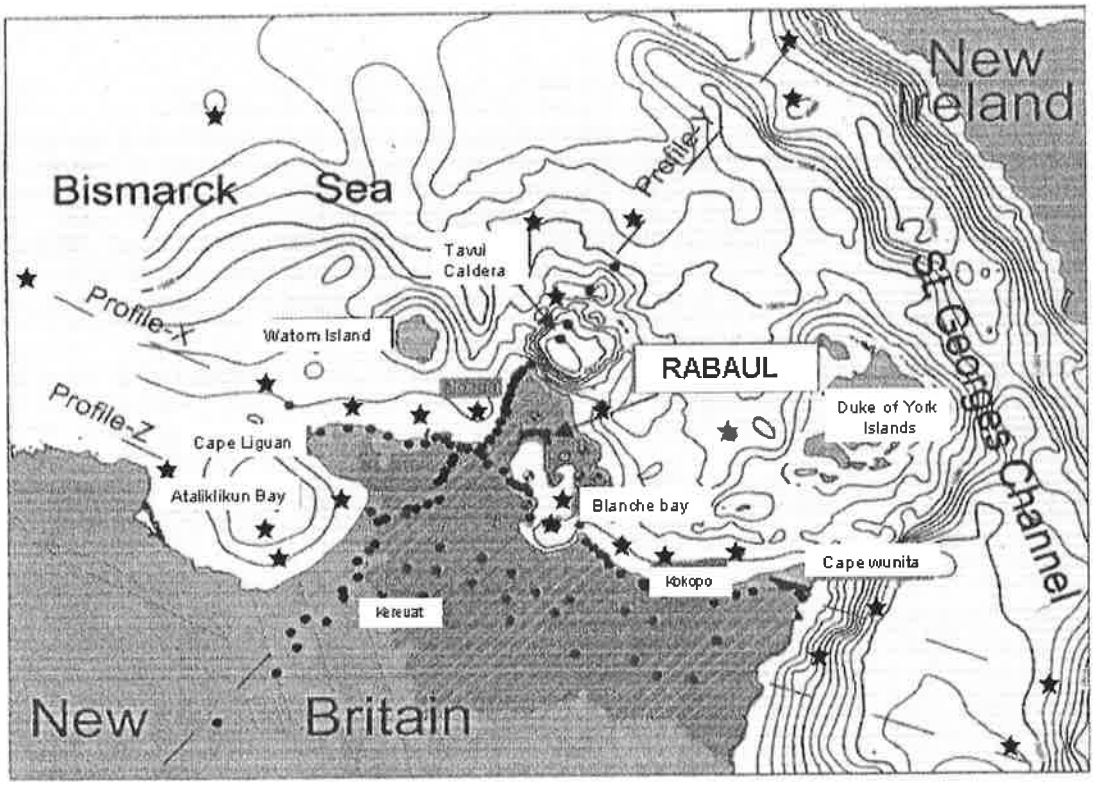

Fig.2.2 Location of three wide-angle seismic profiles used in Rabaul region during RELACS project (Star: Explosions; Circle: Onshore recorders, from Finlayson et al., 2001)

(2) Temporary seismic network deployment

A seismic network comprising a maximum of 75 recorders (single as well as three-component recorders) at 5 km spacing across the target region was deployed for a

5-month period in three stages (Stage 1: 21 August to 3 November, 1997; Stage 2: 4 to 17 November, 1997; Stage 3: 18 November, 1997 to 12 January, 1998). This was mainly for recording the local earthquakes, regional events in the New Britain--New Ireland region, but also teleseismic events from the Pacific-SE Asian-Indian Ocean--Southern Ocean regions. Figure 2.3 shows the location of all temporary and permanent RVO seismic stations and marine shots in the Rabaul region during the RELACS project (for more detailed information, see Finlayson et al., 2001).

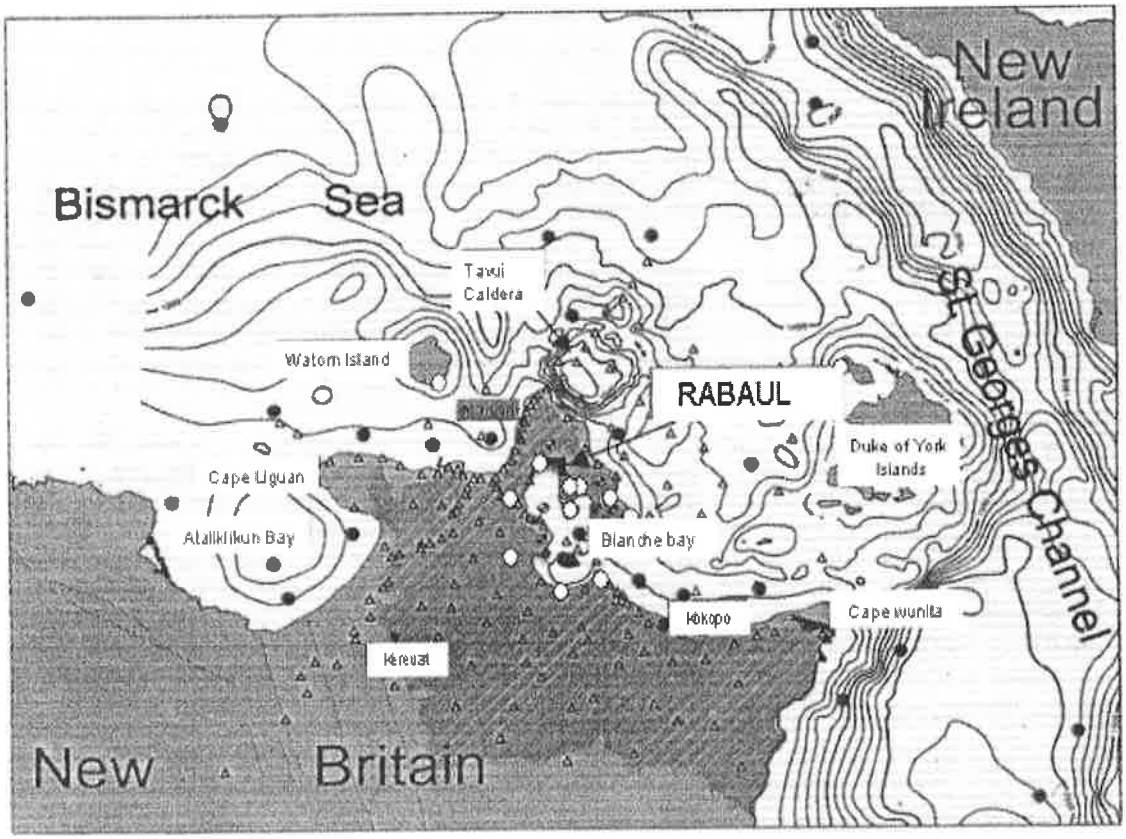

Fig.2.3 Location of all temporary (triangles) and permanent RVO (White circles) stations and marine shots (black circles) during RELACS project (1997-1998)

2.3.3 Data acquisition and preliminary processing

Among the recorders were 30 single component solid-state seismic instruments (built at ANU) provided by AGSO. They used a sampling rate of 50 samples/sec and provide 80 Mbyte data storage. Another 25 identical single component solid-state recorders were from RSES, ANU, which were adapted to three-component recording during seismic profiling with shots at sea. RVO provided 13 recorders (including 6

three-component recorders) with 1 Hz short-period seismometers. They form the stations of the permanent network. A total of eleven three-component analogue and eleven three-component digital recorders were supplied by University of Hokkaido, Japan. They used 3.5 Hz geophones as the sensor and the digital recorders having a sample rate between 64-256 samples/sec. Seven three-component portable seismographs with 1Hz HS-10 geophones and recording at a sample rate of 100 samples/sec were provided by the University of Wisconsin, USA. Another 2 Refraction Technology (RefTek) broadband seismic recorders with RefTek 72A digital acquisition and CMG-3T 3-component seismometers were supplied by RSES, ANU. It is worth pointing out that these recorders were not all simultaneously in operation during the 5-month period. The RELACS database has an average 40 records per event. This number was decreased in stage 3 to about 10 records per event at the end of the period.

The data described in the following sections were mostly obtained on the ANU digital recorders. These recorders use solid-state PC cards (flashcards) as the data mass storage device in each instrument (two per recorder). During service visits to the seismic sites these flashcards were exchanged so as to maintain continuous recording. Data were then downloaded to larger storage devices at a central processing office based at the Rabaul Volcanological Observatory. The data processing included three main stages:

(1) Data conversion from ANUF field data to SUDS format

The first data processing step undertaken by RELACS staff consisted of developing an automated event detection routine that was then used to construct lists of seismic events from the RELACS experiment. Cross comparison of the timing of these events at all the recording stations then served the purpose of eliminating various noise events.

Approximately 2300 events were detected automatically. About 850 events were recorded by more than 50 % of all recording stations in operation at a given time. These 850 events form the basis of a seismic event list for which data were archived. Additional events were chosen at strategic locations and azimuths from NEIC (The National Earthquake Information Centre) and USGS (US Geological Survey) seismic

bulletins where the earthquake magnitude indicated that the event might be detected by the seismic array around the Rabaul region during the observation period of the RELACS project.

Usually two minutes of data were extracted for each station and event pair using the program 'codfatsg.c' developed by RSES staff at ANU. This was increased to three minutes and even more for distant events (the greater the distance to the earthquake, the greater the time separation of P waves and S waves, thus the need for a longer record). The solid-state recorder stored the data in ANUF (ANU format); it later was converted to SUDS (Seismic Unified Data System) format. All other data from OBS and RVO were transferred to ANU in SUDS format. Finally, there were in total 977 events in the RELACS database.

(2) Manual seismic phase (event) time picking

In order to manually pick arrival times with seismograms displayed on screen, a program 'viewsud.c', based on 'pitsa' (IASPEI program for arrival-time picking) was developed at RSES, ANU. It operates entirely from the keyboard and produces a separate output file for each event 'vpick.xxx', where 'xxx' is the event number.

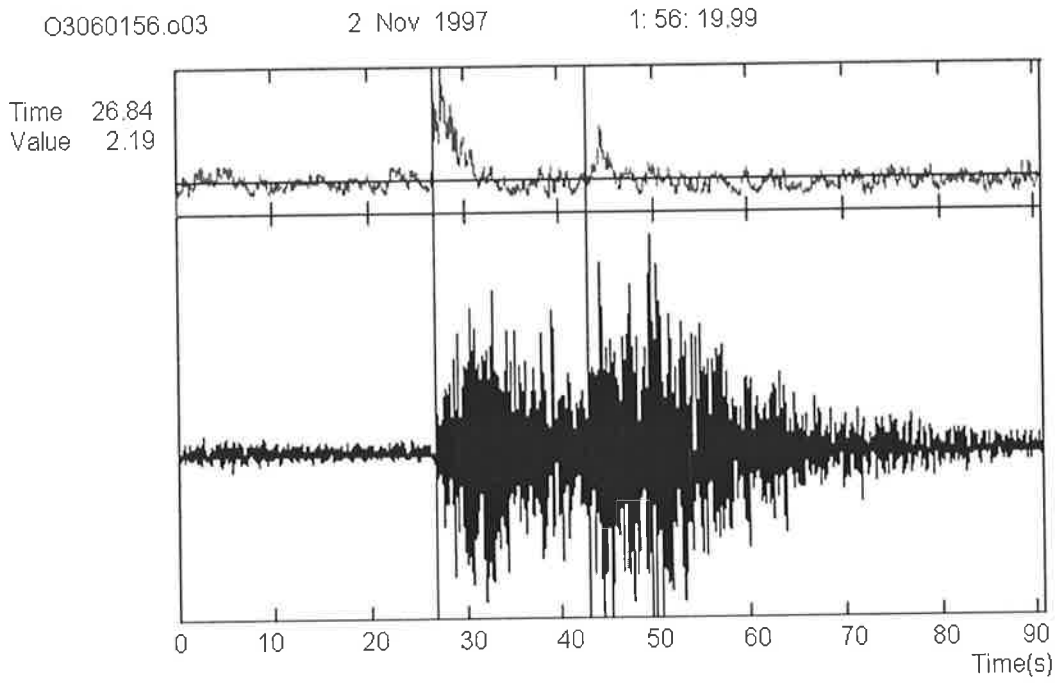

Fig.2.4 An example of manual pick by '7viewsud.c'—energy-picking function incorporated by author (upper panel) and original trace (lower panel)

To assist in the picking of events for which the S/N ratio was relatively low, two procedures were adopted. For events which had a weak signal, but still recognizable on many stations, and for which a location was given, the program 'viewsud' was used to scan and determine a station that possessed a high quality signal. The arrival time at this station would then be used, together with the location of the event, to predict an arrival time at every other station (program 'distance.for' was developed for this purpose). However, traces would only be picked for which there was an unambiguous onset. There were in total 145 events (including 30 explosions), which were manually picked. Figure 2.4 gives an example of arrival time picking by this modified version of '7viewsud.c'.

In Figure 2.4, the first capital letter 'O' in 'O3060156.o03' represents ocean bottom seismograph and o03 is its related station code. The 3 numbers immediately following after 'O' (in this case is 306) is the Julian day, the remaining 4 numbers are the seismic trace starting time (in hours and minutes). The time 26.84s is the picked time. This gives the arrival time (that is 01h:56m:46.83s) when added to the starting time (01h:56m:19.99s). The value '2.19' indicates the value of the energy function (see chapter 9) when the pick is made. Table 2.1 is an example of the output file 'vpick.xxx'.

(3) Automatic seismic phase (event) time picking

The remainder of the archive is not of direct use for the primary purpose of the RELACS project. The 802 events that were not manually picked comprise mainly tectonic events related to subduction processes at the New Britain Trench and crustal deformation in the area around the triple junction between the Solomon, Bismarck and Pacific plates. These events were clearly detected by the RELACS array, but not by other seismic networks, and have thus not been independently located. In order to make these data more accessible, an automated picking procedure ('autopick.c') was developed by RSES staff at ANU. The 'autopick' program performs well with respect to the picking of the first P-wave phase. The output file is 'apick.xxx', where 'xxx' is again the event number. A program 'histogm.for' was written to give a quick overview of the reliability of 'apick' files on screen with station code. Stations with large

deviations from a modal distribution were deleted by 'delstn.c'. The 'apick' file has the same format as 'vpick' file so that it was easy to use both picking results.

Table 2.1 One example for VPICK file

STN	ID	TY	Y	M	D	H	MI	SEC	QUAL	E/I	UNL	UNR	TC	CH	Dist
K67	74	P	1997	9	2	4	51	46.18	9.69	E	-0.04	0	0	1	123.07
K67	74	P	1997	9	2	4	51	46.76	22.56	I	-0.04	0	0	1	123.07
N68	74	P	1997	9	2	4	51	45.8	26.77	E	-0.04	0	0	1	118.25
N68	74	P	1997	9	2	4	51	46.76	13.21	E	-0.06	0.06	0	1	118.25
S66	74	P	1997	9	2	4	51	46.66	24.69	E	-0.06	0.02	0	1	126.29
S66	74	P	1997	9	2	4	51	48.04	0.68	I	-0.04	0.02	0	1	126.29
S66	74	P	1997	9	2	4	51	48.78	0.68	E	-0.04	0.04	0	1	126.29
B69	74	P	1997	9	2	4	51	45.8	19.8	E	-0.06	0.06	0	1	116.12
B69	74	P	1997	9	2	4	51	49.66	0.83	I	-0.02	0.04	0	1	116.12
G08	74	P	1997	9	2	4	51	47.82	22.84	I	0	0	0	1	130.69
G08	74	P	1997	9	2	4	51	51.88	1.76	I	-0.04	0	0	1	130.69
H40	74	P	1997	9	2	4	51	45.6	17.37	I	0	0	0	1	110.15
I10	74	P	1997	9	2	4	51	47.14	29.31	E	0	0	0	1	125.77
I10	74	P	1997	9	2	4	51	48.74	1.04	I	0	0	0	1	125.77
I10	74	P	1997	9	2	4	51	49.2	0.99	I	-0.02	0.02	0	1	125.77
K07	74	P	1997	9	2	4	51	47.98	38.92	I	-0.02	0	0	1	134.79
K07	74	P	1997	9	2	4	51	49.1	0.62	E	-0.02	0.04	0	1	134.79
K07	74	P	1997	9	2	4	51	49.52	0.56	E	-0.02	0.04	0	1	134.79
R11	74	P	1997	9	2	4	51	46.66	6.27	E	-0.14	0.16	0	1	122.08
R11	74	P	1997	9	2	4	51	47.58	4.5	I	0	0	0	1	122.08
R11	74	P	1997	9	2	4	51	48.3	1.75	I	0	0	0	1	122.08

Explanation for Table 2.1:

The fields are station code (STN), event number (ID), phase type (TY), arrival time (TIME—six fields: Y/M/D/H/MI/SEC), signal quality (QUAL), phase onset (E/I—emergent/impulsive), pick uncertainty in seconds (two fields-UNL and UNR), time correction applied (TC), Channel (CH), distance of event in kilometer (Dist).

2.3.4 RELACS database

A final archive of data was made at RSES on tape ('exabyte' tapes in both PC and UNIX format) and at AGSO on CD ROM. During the 3 stages over the 5-month period, the final listed events in the RELACS database number 977, including 30 explosions, 187 local earthquakes, 89 regional events and 97 teleseisms. The remaining 574 are unknown events. By unknown events I mean that they had not been picked and located

in the NEIC and USGS bulletins. Table 2.2 displays the first 15 events in the event list, for illustrative purposes.

Table 2.2 First 15 events in the RELACS database, as an example.

1	2	3	4	5	6	7 8	9	10	11	12	13	14	15
1	1997	237	11	51	30	10.833	10	99.9990	999.9990	999.9	9.9	-9.9000	-999.9
2	1997	237	15	28	10	00.750	9	99.9990	999.9990	999.9	9.9	-9.9000	-999.9
3	1997	237	18	05	40	00.750	9	99.9990	999.9990	999.9	9.9	-9.9000	-999.9
4	1997	237	18	23	20	00.750	9	99.9990	999.9990	999.9	9.9	-9.9000	-999.9
5	1997	237	23	48	10	10.917	11	99.9990	999.9990	999.9	9.9	-9.9000	-999.9
6	1997	238	03	43	20	10.857	12	99.9990	999.9990	999.9	9.9	-9.9000	-999.9
7	1997	238	04	15	30	10.533	8	99.9990	999.9990	999.9	9.9	-9.9000	-999.9
8	1997	238	15	27	50	10.999	17	99.9990	999.9990	999.9	9.9	-9.9000	-999.9
9	1997	238	18	40	20	00.941	16	99.9990	999.9990	999.9	9.9	-9.9000	-999.9
10	1997	238	18	44	30	00.824	14	99.9990	999.9990	999.9	9.9	-9.9000	-999.9
11	1997	238	19	07	00	00.824	14	99.9990	999.9990	999.9	9.9	-9.9000	-999.9
12	1997	238	20	16	50	10.824	14	99.9990	999.9990	999.9	9.9	-9.9000	-999.9
13	1997	239	03	42	36	01.000	0	-4.6160	153.9190	100.0	3.9	1.7000	103.7
14	1997	239	06	30	50	10.391	9	99.9990	999.9990	999.9	9.9	-9.9000	-999.9
15	1997	239	11	43	30	10.999	23	99.9990	999.9990	999.9	9.9	-9.9000	-999.9

Explanation for Table 2.2:

(1) Event number, (2) year, (3) Julian day, (4) Hours, (5) Minutes, (6) Seconds; (7) two-column field before decimal point: First column: '1' or '0'; 1=recorded by an RVO station, 0=not recorded by an RVO station. Second column: event type; 0=unknown, 1=local event, 2=regional event, 3=teleseism, 9=explosion. (8) Three digits after decimal point: percentage of recorders that registered the event, (9) Number of stations recording the event; 0=all stations recorded event. (10) Latitude; 99.9990 corresponds with location unknown. (11) Longitude; 99.9990 corresponds with location unknown. (12) Depth; 999.9 corresponds with depth unknown. (13) Magnitude; 9.9 corresponds with magnitude unknown. (14) Epicentral distance (degrees); -9.9000 corresponds with location unknown. (15) Back Azimuth; -999.9 corresponds with location unknown.

The data was primarily analyzed and stored as sub-directories on the CD in suds-format with Capital letter E, followed by 7 numbers {for example, [E2991826], 'E' represents event, the immediate following three numbers '299' give Julian day, the remaining 4 numbers '1826' indicates the record start time (in hour and minute).

Figure 2.5a (left panel) shows the distribution of located local and near-regional events (including explosions) around the Rabaul region.

Of the 403 known events, ANU/AGSO staff manually picked arrival times for a total of 145 events. They were stored in file 'vpick.xxx', where 'xxx' represents event number (for example: 'vpick.074'). Among the picked events, there were 30 explosions, 78 local events, 22 regional events and 15 teleseismic events. There were 11,860 arrival times in the RELACS database. Of these, more than 90 % are P-wave phases and the rest are S-wave phases. Figure 2.5b (right panel) shows the epicentral distribution of the picked local and near-regional events (including explosions) around Rabaul volcano.

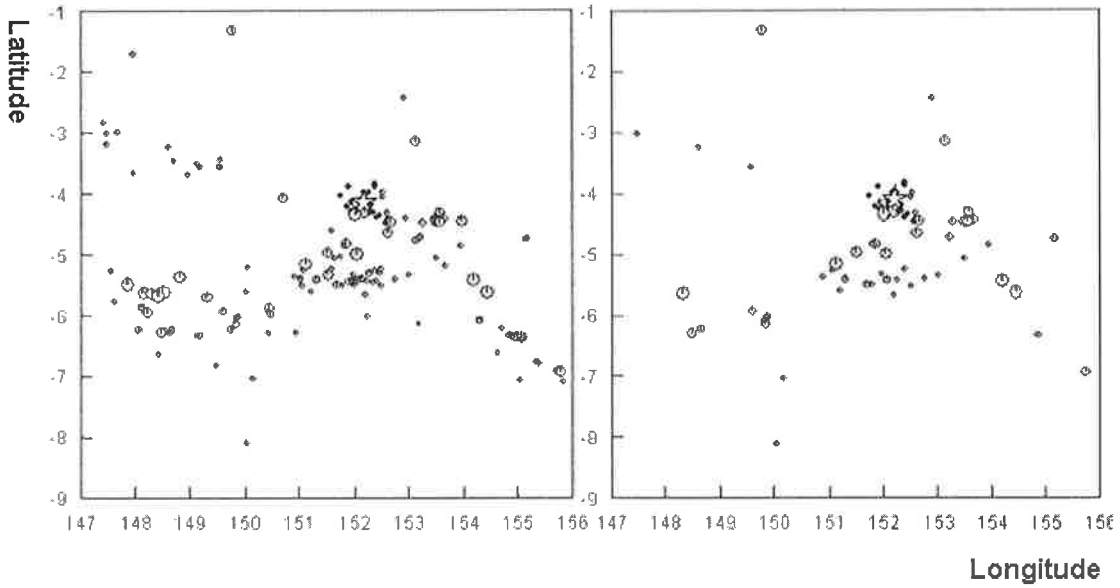

Figure 2.5 The distribution of total known events (left panel) and total picked events by RELACS project (right panel) around Rabaul volcano (white star); the circular size represents different focal depths of local and regional events (from 0 to 200 km)

2.4 Primary Results from RELACS

Finlayson et al (2003) used wide-angle reflection and refraction profile data (explosion data) and obtained two 2-D velocity models for P-wavespeed across Rabaul region down to depth 10 km. One section is across the Rabaul caldera complex; the other is from the Tavui caldera to the northwest of Rabaul. They found a low velocity zone under Rabaul caldera complex between 3 and 6 km depth, and suggested it to be the volcano magma chamber. Gudmunsson et al (1999) used local earthquakes plus

explosions (including explosions from 1967-1969 seismic refraction survey) to obtain the 3-D velocity structure for P-wavespeed around Rabaul Region down to 10 km depth.

Figure 2.6 shows a slice through the 3-D model of the velocity perturbation at 4 km depth (upper panel) and one Rabaul cross section along the line A to B (bottom panel). The low-velocity anomaly (magma chamber) under Rabaul central caldera is clearly visible (top panel in Fig.2.6). A similar clear low-velocity anomaly was found to lie at 3-6 km depth directly beneath the Blanche Bay caldera (bottom panel in Fig.2.6), the youngest and seismically active collapse structure of the volcanic complex. This low-velocity zone is about 5 km across and has at its margins a ring of volcanic vents that have been active after the formation of the collapse structure.

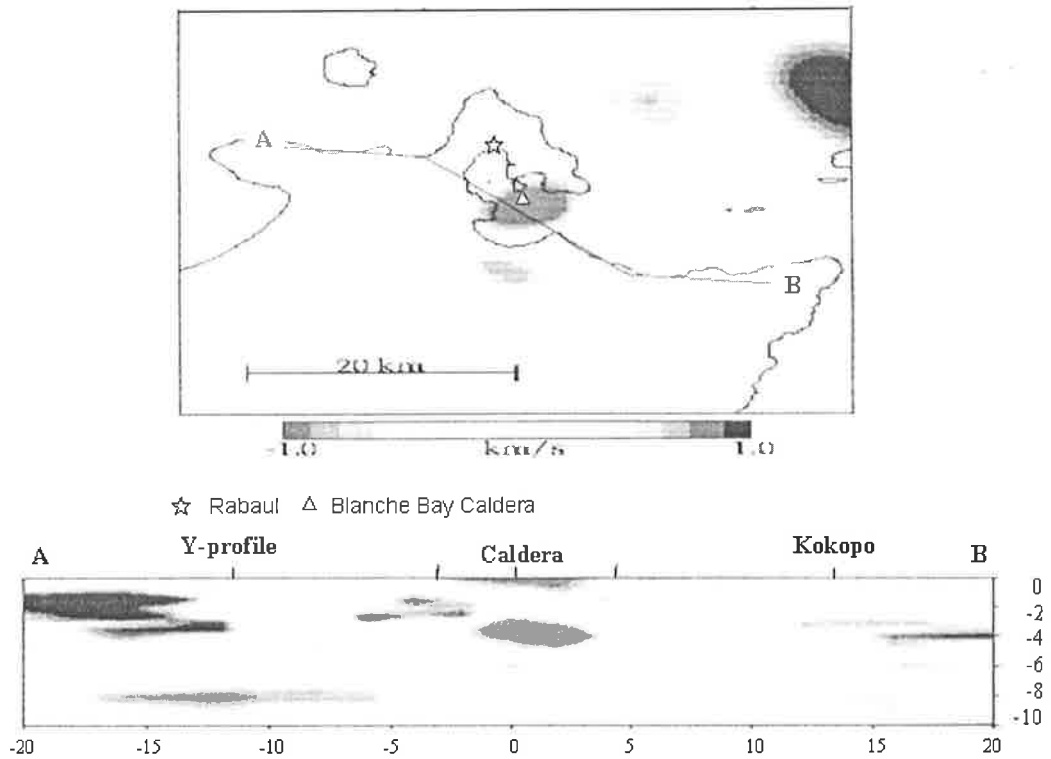

Fig. 2.6 Images (velocity perturbation) from the 3-D model of the velocity structure in the Rabaul region (Top: 4 km depth slice; Bottom: cross section along the profile A-B)

The data cannot resolve the velocity within this low-velocity zone clearly, but do constrain it to lie in the range from 3.0 to 4.5 km/s. This represents a major anomaly compared with background velocities of 5.5-6.0 km/s in the adjacent crust at the same

depths. This anomaly lies beneath the seismicity of the Rabaul volcano and is interpreted to be a shallow magma reservoir. The surface velocities above the magma reservoir, within the caldera structure, are found to be very low, between 1.5 and 2.0 km/s (Gudmundsson and Miller, RSES report, ANU, 1999).

In summary, the main results from the RELACS project so far are (Finlyson et al., 2003):

- a 30-35 km^3 volume of low-velocity material at 3-6 km depth was found beneath the central Rabaul caldera;
- the high-velocity rock unit around the rim of the caldera is interpreted to indicate large volumes of mafic intrusive rock at shallow (< 4 km) depth;
- Tavui caldera (a spectacular bathymetric feature) does not have a prominent low-velocity zone at depth and is therefore regarded as inactive.

2.5 Unsolved Problems from the RELACS Project

The RELACS project only gave 2-D and 3-D velocity models for P-wavespeed in the uppermost 10 km depth around Rabaul region. To the best of my knowledge no P wave results were available for greater depths. Moreover, no S wave velocity model has been obtained prior to beginning my PhD project. The unsolved problems can be summarized as follows:

(1) To correct and adjust the systematic timing errors which occurred on some stations, and time delays (or advances) that affected certain recorders. The challenge is to find another way to perform ray tomography (for example, relative arrival time tomography) so as to improve the data coverage (or ray angular coverage) and get a better image;

(2) To find an efficient method to pick both P- and especially S-arrival times, so as to yield as many arrival times as possible;

(3) To recover 1-D, 2-D and even 3-D velocity distributions for the S-wavespeed;

(4) To combine regional and local seismic data to obtain deep velocity structure under the Rabaul region (say to at least 20 km depth).

This research project was developed to solve most of the above existing and unsolved problems, and to maximally exploit the RELACS data to fulfill the original project goals.

In summary, the velocity distribution around Rabaul obtained from the RELACS project is not enough to build up a new 3-D velocity model under Rabaul region down to depth at least 20 km and to further relocate the volcanic earthquakes accurately. It is essential to combine near-regional events with local earthquakes to increase the data coverage and to image the deep velocity structure. To achieve these objectives, it is first necessary to develop the analysis tools for modeling seismic waves in a 3-D earth, measuring traveltimes and raypaths, and also devising suitable velocity reconstruction (inversion) algorithms.

Chapter 3: Three-Dimensional Ray Tracing in Arbitrary Media

3.1 Introduction

As reviewed in chapter 1, there are many approaches to ray tracing. Among them, two approaches have turned out to be promising in the sense of computational efficiency and solution accuracy in first arrival calculation. One is graph theory (GT) or the shortest-path method, and the other is the finite difference method (FD). Vidale (1988) suggested a ray tracing method based on solving the eikonal equation using a finite difference method (FD) and later extended it to three-dimensional situations (Vidale, 1990). Thereafter, many authors have developed and revised the FD eikonal equation solver. For example, Cao and Greenhalgh (1994) presented a method incorporating wavefront tracing. A convolutional differentiator method was proposed by Zhou et al (1993) as a superior alternative to high order finite differencing. Zhou and Greenhalgh (1998) gave a finite element method for synthetic seismogram computations. The shortest-path method in seismic ray tracing (Nakanishi and Yamaguchi, 1986; Saito, 1989 and 1990; Moser, 1989 and 1991; and many revisions thereafter, for example, Klimeš and Kvasnička (1994); Gruber and Greenhalgh (1998), offers advantages in computational efficiency, accuracy, robustness and global results.

Basically, there are two algorithms in the shortest path (network) method: the original extended version (i.e., 2-D case, Moser, 1991; 3-D case, Klimeš and Kvasnička, 1994), or 'regular' approach. In the 'regular' approach, the ray angular coverage (which affects the accuracy of the computed travel time) is improved by decreasing the cell size, and then increasing the level (n_{FS}) of the forward star, which refers to the geometric arrangement of network connections. The quantity n_{FS} is a positive integer, which is the half-length of the edge of the smallest cube containing the forward star, expressed in grid intervals. The intention is to increase the number of cells around the source in one-step calculation (hereafter referred to as one INTERVAL run). It is 'regular',

because the cell size and the node density are the same everywhere crossing the model. The 'regular' approach is able to obtain a high accuracy of the computed travel times, but with a relatively slow run speed. The run time is still quite long even when dramatic improvements in computational efficiency were made (say, at least five times faster than that of Moser's algorithm, 1991), such as by modifying Dijkstra's (1959) algorithm as demonstrated by Klimeš and Kvasnička (1994). They showed on an example using the improved Dijkstra algorithm, that the consumed CPU time on a PC/AT-486/33 MHz is still roughly 3 hours if the model has up to 500,000 nodes. Following the rough linear relationship between the CPU time and the number of total nodes (for details see Fig.1 of Klimeš and Kvasnička, 1994), it will take at least 6 hours to calculate a typical model with up to one million nodes. Such speed is unacceptable in most cases, especially for tomographic purposes where multiple sources and multiple (iterative) ray tracing must be carried out. For this reason, the 'regular' approach is seldom used to perform the ray tracing for seismic inversion, even though the accuracy of the computed travel times can reach a high level.

The other approach, named the 'irregular' approach, seeks to improve the ray angular coverage (and hence to improve the accuracy of computed travel time) by maintaining a relatively large cell size, and then supplies sufficient secondary nodes along the cell boundaries. This was demonstrated for the 2-D case by Fischer and Lees (1994) and further analyzed by Gruber and Greenhalgh (1998). Here the secondary nodes will be inserted on the cell surfaces in the 3-D case (see later). In such a model presentation, the node density is non-uniform across the model.

3.2 Model Division and Cell Size Definition

The problems faced with 3-D ray tracing when applying the GT or FD methods are the large computer memory requirement, and the efficiency of computation. For a 2-D case, these problems are seldom considered. One can select a small cell size to grid the velocity model, or alternatively, select a relatively large cell size with sufficient secondary nodes applied on the cell boundary (see for example, Fischer and Lees, 1994;

Gruber & Greenhalgh 1998) without losing accuracy in the computed travel times. For a 3-D problem (for example, Vidale 1990; Klimeš and Kvasnička, 1994), the velocity model is divided into cubic cells with only primary nodes on each corner of the cell. This discretisation of a large 3-D velocity model with a small cell size, results in a large number of nodes, making computations intractable in the absence of a supercomputer. It is especially difficult to incorporate such an approach into an inversion algorithm and to solve real problems. Note that the accuracy improvement of the computed travel times depends not only on the cell size, but also on the ray angular coverage (Fischer & Lees 1994; Gruber & Greenhalgh 1998). Thus, there is the possibility to try another approach (not to reduce the cell size, but to decrease the node density through secondary nodes) to fully develop the ray angular coverage, and hence improve the accuracy of computed travel times.

3.2.1 Cell node definition

In the Cartesian coordinate system, a simple cubic cell is selected here for explanation (see Figure 3.1). The eight corner nodes are called **primary nodes** (where the velocity model may be sampled at these nodes) and the other nodes on the six surfaces of the cell are called **secondary nodes** {Note that there are no secondary nodes in Vidale's (1990) and Moser's (1991) definition}. The secondary nodes are inserted uniformly along the six surfaces of the cell. For simplicity, in Figure 3.1, there are only three secondary nodes added to each direction of the cell. Inside the cell there is no node at all, but sources and receivers can be located inside the cell. With such a cell node presentation, the same node density as in Moser's method (1991) can be maintained when the rays travel along the cell surface planes (see Figure 3.2a for an explanation). It reduces to the simple case of Gruber and Greenhalgh (1998) when the rays travel along other planes, rather

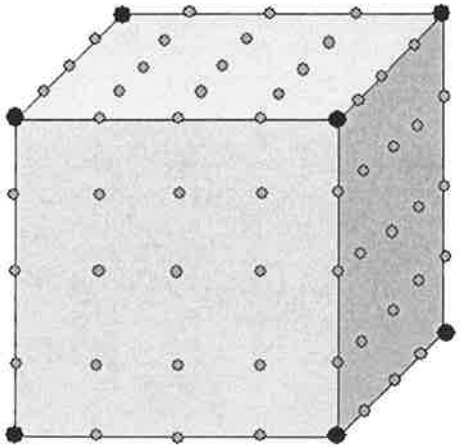

Figure 3.1 The explanation of one cell with primary (black) and secondary (grey) nodes

than the cell surface planes (see Figure 3.2b for an explanation).

If the model has dimensions L_x, L_y and L_z, and the cell sizes are C_x, C_y and C_z in the X, Y and Z directions, respectively, then for this model there are:

(1) Total number of cells:

$$N_{TC} = (\frac{L_x}{C_x}) \times (\frac{L_y}{C_y}) \times (\frac{L_z}{C_z}) \tag{3.1}$$

If $L = L_x = L_y = L_z$ and $C = C_x = C_y = C_z$

then $N_{TC} = (\frac{L}{C})^3$ (3.2)

Here L and C represent the scale of the model and the cell, respectively. From formula (3.2), it can be seen that the total number of cells is proportional to the third power of the ratio of model length to cell length.

(2) Total number of primary nodes:

$$N_{TP} = (\frac{L_x}{C_x} + 1) \times (\frac{L_y}{C_y} + 1) \times (\frac{L_z}{C_z} + 1) \tag{3.3}$$

If $L = L_x = L_y = L_z$ and $C = C_x = C_y = C_z$

then $N_{TP} = (\frac{L}{C} + 1)^3 \cong (\frac{L}{C})^3$, when $\frac{L}{C} \rangle\rangle 1$ (3.4)

From formulae (3.2) and (3.4), the number of primary nodes is roughly equal to the total number of cells.

(3) Total number of nodes:

If $N_x = \frac{L_x}{C_x} + 1, N_y = \frac{L_y}{C_y} + 1, N_z = \frac{L_z}{C_z} + 1,$

then the total number of nodes is:

$$\begin{aligned} N_{TN} &= N_z \times (N_x + (N_x - 1) \times M_x) \times (N_y + (N_y - 1) \times M_y) \\ &+ N_x \times (N_y + (N_y - 1) \times M_y) \times (N_z - 1) \times M_z \\ &+ N_y \times (N_x - 1) \times M_x \times (N_z - 1) \times M_z \end{aligned} \tag{3.5}$$

If $N = N_x = N_y = N_z$ and $M = M_x = M_y = M_z$

$$\text{then } N_{TN} \approx 3 \times M^2 \times N^3 = 3 \times M^2 \times \left(\frac{L}{C}\right)^3 = 3 \times M^2 \times N_{TC} \qquad (3.6)$$

Here M is the number of secondary nodes added in each direction of the cell. From formulae (3.2), (3.4) and (3.6), the total number of nodes is proportional to the square of the number of secondary nodes added in each direction of the cell, and is roughly $3 \times M^2$ times larger than the total number of cells (or the number of total primary nodes). This means that the total number of nodes is only proportional to a power of two, rather than to a power of three when increasing the node density.

(4) Ray angular coverage

The ray angular coverage is highly dependent on the number of secondary nodes. For example, the maximum ray angle between consecutive rays when the ray travels in the cell surface planes (see Figure 3.2a) is the same as:

$$\max imum\ (\theta) = arctg\ \left(\frac{\frac{C}{M+1}}{\frac{C}{2}}\right) = arctg\ \left(\frac{2}{M+1}\right) \qquad (3.7)$$

where M is the number of secondary nodes added in each direction (M is related to the level of the 'forward star' in the 'regular' approach, see section 3.4.2). Note that near the model boundary the maximum ray angle is 45° (see sub cell in Figure 3.2a, where the ray must travel from one node to its opposite diagonal node in a sub cell, due to the boundary restriction). Such a situation is equivalent to the maximum ray angle in the cell surface planes when only one secondary node is used in the model representation (see formula 3.7, M=1 case).

The maximum ray angle between consecutive rays when the ray crosses the cell is slightly different from the maximum ray angle in the cell planes. For simplicity in the following discussion, the ray angular coverage is constrained to the same plane. Basically there are two kinds of maximum ray angle. It depends on which kind of node position that the ray leaves, i.e., the primary node or secondary node. For the ray emanating from a primary node, there are only three planes (opposite to the primary node) that the ray can reach. In such cases the maximum ray angle is simple (see Figure

3.2b) and given by:

$$\max imum(\theta_c) = arctg(\frac{1}{M+1}) \tag{3.8}$$

But for a ray emanating from a secondary node, it is slightly more complex, and depends on the secondary node position away from the cell boundaries. In such situations, there are at least four planes (or five planes, if the secondary node is not on the cell boundaries) the ray can reach, except for its own plane. The extreme case (maximum ray angle) occurs when the ray takes off from one secondary node (the nearest secondary node away from the cell boundaries), and reaches the adjacent planes. The maximum ray angle depends on distance from the cell boundaries. The further the distance from the cell boundaries, the smaller the ray angle. For example, the maximum ray angle is $arctg(\frac{1}{1}) = 45°$ when the rays depart from the nearest secondary nodes away from the cell boundaries and reach the adjacent planes (see θ_1 in Figure 3.2b), no matter how many secondary nodes are used. In similar manner to the above, the maximum ray angle is $arctg(\frac{1}{2})$ when the rays take off from the second nearest secondary nodes away from the cell boundaries and reaches the adjacent plane (see θ_2 in Figure 3.2b). Following the above reasoning, the maximum ray angle (θ_F) for rays leaving the secondary nodes and reaching the adjacent planes can be expressed by equation (3.9), which shows that the maximum angle decreases with increasing F (see θ_F in Figure 3.2b; from symmetry considerations, only nodes on one-side away from the cell centre need to be considered):

$$\max imum(\theta_F) = arctg(\frac{1}{F}), \quad F = \begin{cases} \frac{M}{2}, M = even \\ \frac{M+1}{2}, M = odd \end{cases} \tag{3.9}$$

Here F is the number of secondary nodes from the cell boundaries.

From formulae (3.7) and (3.9), it is easy to see that the maximum ray angle (θ_F) is the same as the maximum ray angle $\{arctg(\frac{2}{M+1})\}$ in the plane when the rays emanate from the farthest node and reach the adjacent planes, only if the number of secondary

nodes added in each direction is odd. For other situations, the maximum ray angle is larger than the maximum ray angle in the plane. This means that in a 3-D model representation, one cannot expect as good ray angular coverage as for the 2-D case. This will be discussed further in the following section. However, in general one can say that the ray angular coverage is related to the number of secondary nodes in each direction of the cell. Thus, formulae 3.7 to 3.9 are the good estimates for the ray angular coverage in the 3-D case. Note that there exist some certain geometric errors, or restrictions, such as the 45° maximum ray angle near the cell boundaries (the poorest ray angular coverage in the cell), regardless of how many secondary nodes are used in model specification, which results in a relatively large travel time error compared to other directions.

The maximum ray angle is the upper bound, which can be used to represent the ray angular coverage. Thus the only way to develop the ray angular coverage, and hence improve the accuracy of the computed travel times is to increase the number of secondary nodes in each direction of the cell. The greater the number of secondary nodes, the higher the ray angular coverage, and therefore the higher the accuracy of the computed travel times.

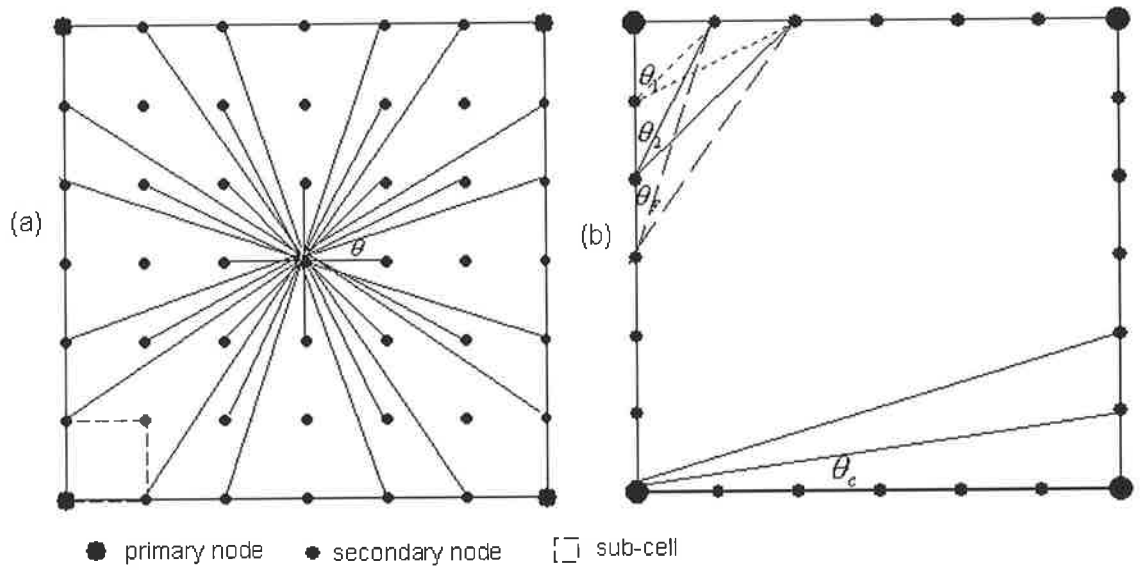

Fig. 3.2 The maximum ray angle (θ) in the plane (diagram a) and crossing the cell (diagram b) {In figure 3.2a, $n_{FS} = 3$ in the 'regular' approach for 2-D case, see Moser (1991)}

(5) The maximum distance between two neighbouring nodes

The shortest path of a seismic trajectory is the summation over a series of consecutive segments along the ray paths connected between nodes. There are basically two factors that control the accuracy of the computed travel time: (1) the ray angular coverage, which guarantees the ray can find a proper direction to go as discussed above, and (2) the distance between two node connections, which results in a large timing error with long connection if the ray follows the wrong direction (in such conditions, the longer the distance, the larger the timing error). In like manner to the previous discussion on ray angular coverage, it is necessary to analyze the maximum distance between neighbouring nodes, which is an upper bound on the node distance. The maximum distance between two neighbouring nodes in the cell surface plane is:

$$D_{\max} = \sqrt{2} \times (\frac{C}{M+1}) \tag{3.10}$$

where the ray travels from one node to its opposite diagonal node on the sub-cell (see Figure 3.2a). The maximum distance between two neighbouring nodes when the ray crosses the cell is:

$$D_{\max} = \sqrt{3} \times C \tag{3.11}$$

In this case the ray crosses the cell from one primary node to the opposite diagonal primary node of the cell. From formulae (3.10) and (3.11), it can be seen that the maximum distance between two neighbouring nodes is different when the ray travels in the plane or crosses the cell, but both are proportional to the cell size C.

From formulae (3.2) to (3.11), the advantages of the revised 'irregular' approach of the shortest path method can be seen: (1) it allows the growth of the total number of nodes in proportion to a power of two (see formula 3.6), rather than a power of three (c.f. Moser's case), resulting from simple shrinking of the node density (secondary nodes are supplied); (2) it has the same ray angular coverage as in the 2-D case (see Fig.3.2a), and comparable ray angular coverage in the 3-D case (see later in section 3.4.2); (3) it dramatically decreases the total number of cells (roughly equal to total number of primary nodes) by a factor $3 \times M^2$ (see formula 3.6), which generally results in fewer velocity unknowns in the inversion process (if the velocity values are simply sampled

only at the primary nodes). These estimates are very helpful for model design and in determining the unknown parameters in subsequent matrix inversion for tomographic purposes. For example, in order to improve the ray angular coverage, which is an important factor to reduce the computed travel time errors in the 2-D case (see, Fischer and Lees, 1994; Gruber and Greenhalgh, 1998), and to be demonstrated later for the 3-D case, the best way is to add more secondary nodes without dramatically increasing the total number of nodes.

Note that it is possible to have a prismatic cell size with different lengths in the different directions, and it is also possible to have a different number of secondary nodes added in each direction of the cell with either a uniform or non-uniform spacing interval. For example, in order to improve ray angular coverage in the Z direction, more secondary nodes can be inserted in the Z direction than in the other two directions. The selection of cell type and the number of secondary nodes (added in each direction) are made according to the model and the problem to be solved.

3.2.2 Velocity distribution across the cell

A velocity function is needed to calculate velocity values at the secondary node positions, or at source and receiver positions if they are not located on the primary node positions, because the velocity model is sampled only at the primary nodes (i.e., eight corner nodes of the cell). One simple assumption is to have uniform velocity across the cell, but this simplification is not suitable for high contrast velocity media. To overcome this disadvantage and to trace rays in arbitrary media, the velocity distribution across the cell can be taken as a tri-linear function:

$$V_c = \sum_{k=1}^{8} R_k BV(k) \tag{3.12}$$

where $BV(1), BV(2), \ldots\ldots, BV(8)$ are the sampled velocities on the eight primary nodes of the cell, and $R_1, R_2, \ldots\ldots, R_8$ represent Lagrangian interpolation function, which take the following form:

$$R_1 = (1.0 - x) \times (1.0 - y) \times (1.0 - z), \quad R_2 = x \times (1.0 - y) \times (1.0 - z)$$

$$R_3 = (1.0-x)\times y\times(1.0-z), \qquad R_4 = x\times y\times(1.0-z)$$

$$R_5 = (1.0-x)\times(1.0-y)\times z, \qquad R_6 = x\times(1.0-y)\times z$$

$$R_7 = (1.0-x)\times y\times z, \qquad R_8 = x\times y\times z \tag{3.13}$$

In the above definition of the velocity distribution, the minimum primary node of the cell is selected as the reference point, (x, y, z) is the normalized coordinate (related to the reference point) of one node on or inside the cell, to be calculated and assigned a new velocity value, as a tri-linear combination of the sampled velocities of the eight primary nodes. It is known that inside the cell the velocity distribution takes the form of a tri-linear function, but on the six surfaces of the cell, the velocity distribution is reduced to the 2-D case and takes the form of a bi-linear function. For example, the velocity distribution in the cell surface planes takes the form.

$$V_c = \sum_{k=1}^{4} R_k \times BV(k) \tag{3.14}$$

where $BV(1),.....,BV(4)$ are the sampled velocity values on the four primary nodes, respectively, and the Lagrangian interpolation function values $R_1,.....,R_4$ take the following form:

$$\begin{aligned} R_1 &= (1.0-x)\times(1.0-y) \\ R_2 &= x\times(1.0-y) \\ R_3 &= (1.0-x)\times y \\ R_4 &= x\times y \end{aligned} \tag{3.15}$$

The above definition of the velocity distribution across the cell allows me to handle arbitrary media with only a slightly increased effort in the computations to trace any ray path, irrespective of where the sources and receivers are located.

3.3 3-D Ray Tracing in Arbitrary Media

Based on the 2-D ray-tracing program of Zhou at al, (1992), I have developed a 3-D 'irregular' approach style of shortest-path ray tracing algorithm with some advanced modifications mentioned above. Saito (1989 and 1990), and Moser (1989 and 1991)

discussed the 'regular' approach of the shortest path method in detail, so there is no need to repeat the treatment here. But the present approach is advantageous over the 'regular' approach, because it allows for arbitrary source and receiver locations (that is, it is very easy to introduce a specified surface or boundary within the model to trace the reflected or later arrivals) without extra computation, whereas the 'regular' approach requires extra computations when the source and receiver are not on a node location (which is limited in practice). Meanwhile, in order to get the velocity values at the secondary nodes, an extra subroutine is required. In my experience this process only adds a small computational overhead to the whole process.

3.4 Error Estimation and Accuracy Analysis

Gruber and Greenhalgh (1998) analyzed the accuracy of first-break times obtained by the 'irregular' approach in the 2-D case. They concluded that only by increasing the number of secondary nodes and thereby decreasing the angular error was it possible to improve the accuracy of the computed travel times. Reducing the cell size only improves the approximation of the velocity field. Here I perform further tests in the 3-D case with the new formulations. To test the accuracy of the ray-tracing program and to give the error estimates of the computed travel times, it is necessary to estimate the maximum error bound for the 'irregular' approach in the 3-D case.

3.4.1 The upper error bound and algorithm accuracy

Following a simple, but meaningful explanation for the 2-D case (Gruber and Greenhalgh, 1998), it is possible to estimate the maximum error bound for 3-D situations. In the 2-D case, the maximum relative error bound with the 'irregular' approach is defined as (Gruber and Greenhalgh, 1998, equation 10):

$$\delta_{\max}(2D_{irr-est}) = \sqrt{2(1+n^2 - n\sqrt{1+n^2})} - 1 , \qquad n = M + 1 \tag{3.16}$$

where n is the number of nodes per cell boundary, and M is the number of secondary nodes added in each cell boundary.

As discussed above, for a given network, there exists a direction of the exact ray with the worst relative geometric error. The approximated ray path is the summation over a

sequence of short, straight-line segments, which have different angles from the source position. Among these straight-line segments, the larger the angular deviation from the true path and the longer the segment, the larger the resulting timing error will be. This is more likely in a homogeneous medium, whereas in a heterogeneous medium, at least a portion of the ray probably finds a better direction than the worst direction. Thus I will concentrate on the homogeneous medium situation. The estimated error will be the upper bound for the heterogeneous medium case. Both theory and numerical tests in a uniform velocity field (see Figure 3.6) indicate that the maximum error occurs in the θ_c area (see Figure 3.2b) where the ray takes off from a primary (or secondary) node and reaches the opposite cell planes (both a maximum ray angle and a larger distance of node connections are involved). This θ_c area is a small triangular area in the 2-D case (see Figure 3.6a), and a conical volume in the 3-D case. It is true that one obtains a relatively larger angle, up to $\frac{\pi}{4}$ (see θ_1 in Figure 3.2b), for rays taking off from the nearest secondary node away from cell boundary and reaching the adjacent cell planes (see formula 3.9). However, the path lengths are respectively shorter, and the continued path may travel via the longer segment (node connection), which again is included in the above discussion. Supported by these observations, it is reasonable to estimate the maximum error in this θ_c area, which may be the upper error bound for the whole model. Thus for a uniform velocity field (for simplicity, I set V=1.0 km/s everywhere), the relative travel time error is calculated as:

$$\delta = \frac{T_{irr} - T_{exact}}{T_{exact}}, \text{ for } T_{exact} \neq 0 \tag{3.17}$$

where T_{irr} is the approximated travel time obtained by the 'irregular' approach. IRR stand for 'irregular' approach of the shortest path method in this study, and T_{exact} is the analytical travel time (distance divided by velocity, the latter being unity). As shown in Figure 3.3, the exact travel time from source to receiver is:

$$T_{exact} = \sqrt{r_x^2 + r_y^2 + r_z^2} = \sqrt{r_z^2 + 2} \tag{3.18}$$

A possible approximated travel time from source to receiver is:

$$T_{irr} = \sqrt{n^2 + 2} + r_z - n, \qquad n = M + 1 \tag{3.19}$$

Note that there are other possible ray paths from source to receiver, but all possible ray paths yield the same travel times. Thus, the maximum relative error is obtained as:

$$\delta_{relative} = \frac{\sqrt{n^2 + 2} + r_z - n}{\sqrt{2 + r_z^2}} - 1 \tag{3.20}$$

To determine the maximum relative error, I set the zero derivative condition:

$$\frac{d}{dr_z}(\delta_{relative}) = \frac{d}{dr_z}\left(\frac{\sqrt{n^2 + 2} + r_z - n}{\sqrt{2 + r_z^2}} - 1\right) = 0 \tag{3.21}$$

from which I find:

$$r_z = 2(\sqrt{n^2 + 2} - n)^{-1} \tag{3.22}$$

Replacing r_z in equation (3.20) with formula (3.22) gives the maximum relative error for any given n in the 3-D case:

$$\delta_{\max}(3D_{irr-est}) = \sqrt{2 + n^2 - n\sqrt{2 + n^2}} - 1, \qquad n = M + 1 \tag{3.23}$$

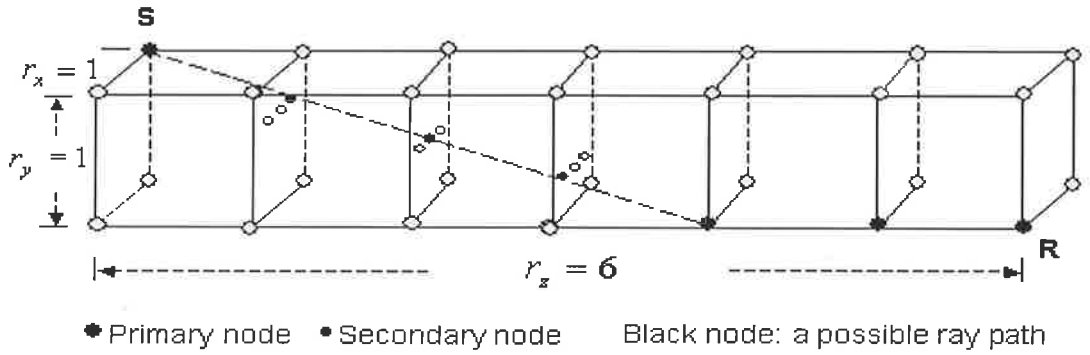

Figure 3.3 Difference between exact and approximated raypath in θ_c area. Note that the given approximated raypath is not unique, but all possible raypaths have the same traveltimes

For further comparison, I rewrite the maximum relative error estimated in the 'regular' approach, related to only the geometric error. It is defined through the level (n_{FS}) of the forward star. In a cubic cell model representation, it takes the following form {see Klimeš and Kvasnička, 1994, formulae (19) and (50)}:

$$\delta_{\max}(3D_{reg-est}) \approx \frac{1}{4 \times n_{FS}^2} \tag{3.24}$$

From formulae (3.23) and (3.24), there is an approximated equal relationship ($n \approx n_{FS}$) between the 'regular' and the 'irregular' approach when comparing the same level of the estimate maximum error in the computed travel times. Thus, Figure 3.4 shows the relationship between the number of nodes per cell boundary and the upper error bound estimated by the 'irregular' approach for both the 2-D case ($2D_{irr-est}$, see formula 3.16), and the 3-D case ($3D_{irr-est}$, see formula 3.23); the relationship between the level of the forward star and the upper error bound estimated by the 'regular' approach for the 3-D case ($3D_{reg-est}$, see formula 3.24). For further comparison, the actual maximum relative errors ($3D_{irr-syn}$) are also displayed in Figure 3.4. The actual maximum error, obtained from section 3.4.3 by the 'irregular' approach, is slightly smaller than the estimated maximum error, which lends supports to the above upper error bound analysis. Interestingly, on average, the estimated maximum error with the 'irregular' approach in the 3-D case is 2 times larger than that for the 2-D case, but for small n (say, $n \leq 5$), the estimated maximum error is roughly 1.65 times larger than for the 2-D case (see $2.0 \times 2D_{irr-est}$ curve in diagram for comparison). The estimate maximum error with the 'regular' approach is larger than that of the estimate

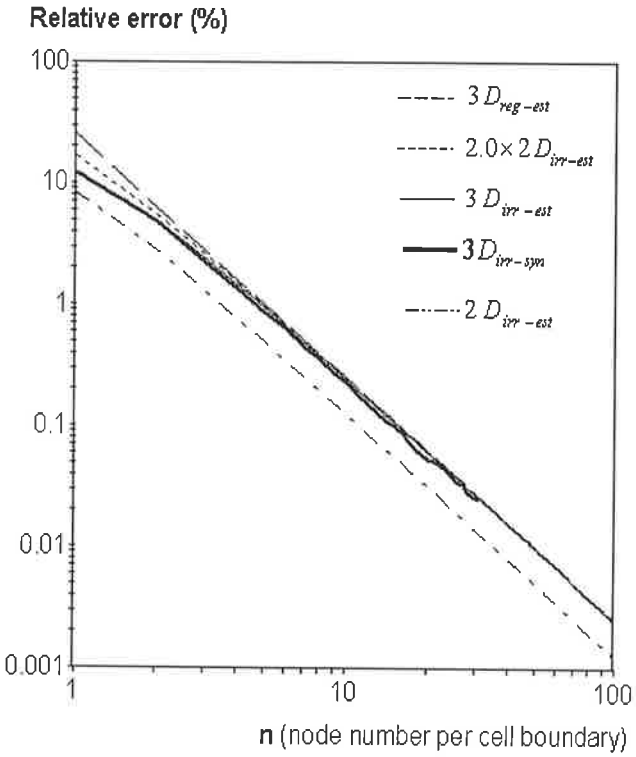

Fig.3.4 Relationship between the maximum error bound against the node number per cell boundary, or against the level of the forward star

maximum error with the 'irregular' approach when replacing n_{FS} with n (that is, $n = n_{FS}$ relationship is applied). This is especially true with $n = n_{FS} \leq 5$. It is now possible to estimate the minimum number of secondary nodes (or minimum level of the forward star n_{FS}) to obtain a specified accuracy in real problems. For example, to improve the accuracy of computed travel times from 1.0 % to 0.1 % with the 'irregular' approach, one needs to increase the node number per cell boundary (n) from 5 to 16 (that is, to increase the number of secondary nodes from 4 to 15) to guarantee the required accuracy. For a similar accuracy improvement with the 'regular' approach, the level of the forward star (n_{FS}) should be also increased from 5 to 16.

3.4.2 Computational efficiency

The 'regular' and the 'irregular' approaches both use a flood-fill algorithm to evolve the wavefield. The basic idea of the flood-fill approach (i.e., Coultrip, 1993; Qin and Schuster, 1993) is to propagate a wavefront outward from the source, keeping track of the shortest raypaths and related traveltimes, while continually eliminating slow raypaths. This should reduce the computational complexity from $O(n^2)$ to $O(n \ln_2 n)$ in the 2-D case, and from $O(n^3)$ to $O(n^2 \ln_3 n)$ in the 3-D case when switching from the 'regular' to the 'irregular' approach. Here n is the number of nodes per cell boundary.

The computational efficiency in the shortest-path algorithm is not only dependent on the computational complexity mentioned above, but is also related to the number of edges (node connections) used in one INTERVAL run. In the 'irregular' approach, for a given node (assumed source) position in the wavefront, the connection between nodes is only related to the immediate neighbouring nodes. There are at most four nearest neighbouring cells in the 2-D case and eight nearest neighbouring cells in the 3-D case, around the given node, when progressing the wavefront outwards. By contrast, in the 'regular' approach, the number of nodes that connect the given node is not restricted to the immediate neighbouring cells, but a sub-set of the total number of nearby cells,

dependent on the level of the forward star (see, Fig.3.2a, where $n_{FS} = 3$ in the 2-D case). The total number of edges (node connections) in one INTERVAL run is defined as (see Klimeš and Kvasnička, 1994, section 5.1 for details):

$$m_{reg} = \frac{4}{3} \times \pi \times n_{FS}{}^{3} \tag{3.25}$$

It reduces to the 'irregular' approach when $n_{FS} = 1$ (Of course, $n_{FS} = 1$ and 2 are never used in practice, due to the low accuracy of the computed travel times, see formula 3.24).

In the 'irregular' approach, the total number of edges (node connections) for one INTERVAL is run cell by cell, and on average is:

$$m_{irr} = 6 \times (M+1)^2 \tag{3.26}$$

There are 6 cell surfaces per cell. For each cell surface, there are $(M+1)^2$ nodes. Therefore, the minimum ratio of computational efficiency between the 'regular' and the 'irregular' approach for the same scale of velocity model can be roughly determined as follows:

$$CPU^{T}_{ratio}(\frac{regular}{irregular}) = \frac{N^{reg}_{TN}}{N^{irr}_{TN}} \times \frac{m_{reg}}{m_{irr}} = Node_{ratio} \times \frac{m_{reg}}{m_{irr}} \tag{3.27}$$

In formula (3.27), the first term is the node ratio between the 'regular' and the 'irregular' approaches, and the second part is the ratio of the total edges (node connections) between the 'regular' and the 'irregular' approaches in one INTERVAL run.

In the 'regular' approach, the longest edge in the most heterogeneous region is:

$$D_{reg} = n_{FS} \times \sqrt{3} \times H \tag{3.28a}$$

Here n_{FS} is the minimum level of the forward star.

The longest edge in the 'irregular' approach is (see formula 3.11):

$$D_{irr} = \sqrt{3} \times C \tag{3.28b}$$

To keep equal accuracy in the most heterogeneous region, we should select $D_{reg} = D_{irr}$, that is, we set:

$$C = n_{FS} \times H \tag{3.29}$$

We have the following relationship between the total number of nodes in the 'regular' approach and the total number of primary nodes in the 'irregular' approach:

$$N_{TN}^{reg} \times H^3 = N_{TP}^{irr} \times C^3 \tag{3.30}$$

Substituting (3.29) into (3.30) yields:

$$N_{TN}^{reg} = N_{TP}^{irr} \times n_{FS}^{\ 3} \tag{3.31}$$

Replacing N_{TP}^{irr} with formula (3.6), we obtain the total node ratio between the 'regular' and the 'irregular' approaches as below:

$$Node_{ratio}(\frac{regular}{irregular}) = \frac{N_{TN}^{reg}}{N_{TN}^{irr}} = \frac{n_{FS}^{\ 3}}{3 \times (M+1)^2} \tag{3.32}$$

Applying the relationship $n_{FS} = n = M + 1$, we obtain the total node ratio:

$$Node_{ratio}(\frac{regular}{irregular}) = \frac{M+1}{3} \tag{3.33}$$

Finally we obtain the computational ratio between the 'regular' and the 'irregular' approaches by replacing formula (3.27) with formulae (3.25), (3.26) and (3.33). The result is (here $n_{FS} = n = M + 1$ is applied):

$$CPU_{ratio}^{T}(\frac{regular}{irregular}) = \frac{2 \times \pi}{27} \times \frac{n_{FS}^{\ 3}}{(M+1)} = \frac{2 \times \pi}{27} \times n_{FS}^{\ 2} \approx \frac{2}{9} \times n_{FS}^{\ 2} \tag{3.34}$$

From the above discussion (formulae 3.23, 3.24 and 3.34), we can now compare the computational efficiency between the 'irregular' and 'regular' approaches with the specific accuracy requirement. For example, in order to improve the accuracy of the computed travel times from 1% to 0.1% as discussed previously, one needs n_{FS} or n both to be increased from 5 to 16 in the 'regular' or the 'irregular' approach. Therefore, to maintain 1% accuracy, the 'regular' approach will take at least 5 times more CPU time than the 'irregular' approach. Furthermore, to improve the accuracy in the computed travel times to the higher level 0.1%, the 'regular' approach will take at least 50 times more CPU time than the 'irregular' approach. This ratio of computational

efficiency will dramatically increase with a higher accuracy requirement (see formula 3.34).

With the optimum selection of the level of the forward star, the total number of edges (node connections) in one INTERVAL run in the 'regular' approach may be reduced by a factor of $\frac{n_{FS}}{4}$ (see Klimeš & Kvasnička, 1994, section 5.1). That is:

$$m_{reg} = \frac{16}{3} \times \pi \times n_{FS}^{\ 2} \tag{3.35}$$

But still up to one order of magnitude increase in CPU time will occur when switching from the 'irregular' to the 'regular' approach to guarantee a similar high accuracy of the computed travel times. Replacing the total number of edges in the Moser-Saito forward star (formula 3.24) with the total number of edges in the optimal selection of the forward star (formula 3.35), we obtain a relative measure of computational efficiency:

$$CPU^{T}_{ratio}(\frac{regular}{irregular}) = \frac{8 \times \pi}{27} \times n_{FS} \approx n_{FS} \tag{3.36}$$

With an 'irregular' approach implemented on a PC/AT-Pentium 4/2.8 GHz, it takes less than 9 minutes to calculate a model with 1 million nodes. A full plot of CPU time vs. number of total nodes is given in Figure 6. The speed can be further increased if the generalized model is separated from the ray tracing. In our experience, this will reduce the run time in the ray tracing process by nearly a factor of two (see Bai, 2004).

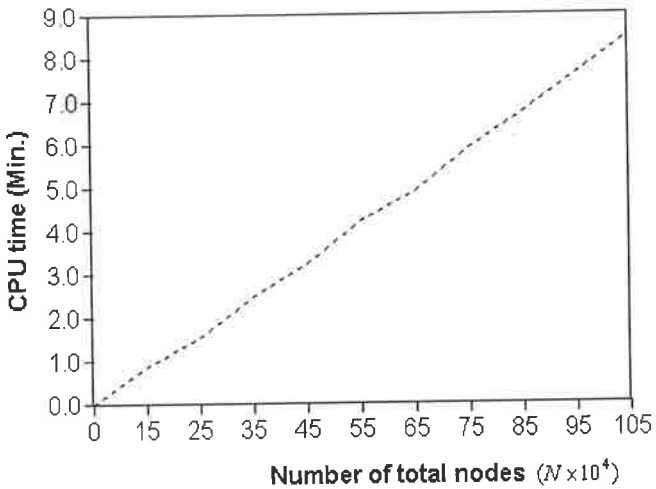

Figure 3.6 CPU time vs. the total number of nodes

This concludes the theoretical comparison between the 'regular' and 'irregular' approaches. In the following sections, some numerical tests based on specific velocity models will be undertaken to further compare the accuracy

between the 'regular' and 'irregular' approaches.

3.4.3 Uniform velocity model

To examine the location of actual relative errors in a uniform velocity field, a simple uniform velocity model (V=1.0 km/sec) having dimensions (100 km× 100 km× 100 km) was selected and the source position was set at (0.0, 0.0, 0.0). The cell size is 10 km. By varying the number of secondary nodes from 0 to 30, the corresponding maximum relative travel time errors (measured against the exact analytic solutions) were obtained within the model. The results are drawn (as curve $3D_{irr-syn}$) on Figure 3.4 for comparison with the upper error bound discussed previously. Next, I set the number of secondary nodes equal to 15, and computed travel times at various depths with a 201×201 node representation. Figure 3.6 shows the relative errors (referred to the exact straight-ray travel times) at four different depths (Z=0, 20, 40 and 60 km).

In general, the travel time errors in the 2-D case (Z=0 km) are smaller than in the 3-D case (other depths). However, the maximum relative error is located in the θ_c area, regardless of the 2-D or 3-D situation. Such error distributions lead me to use the maximum error bound (formula 3.23) for the whole model.

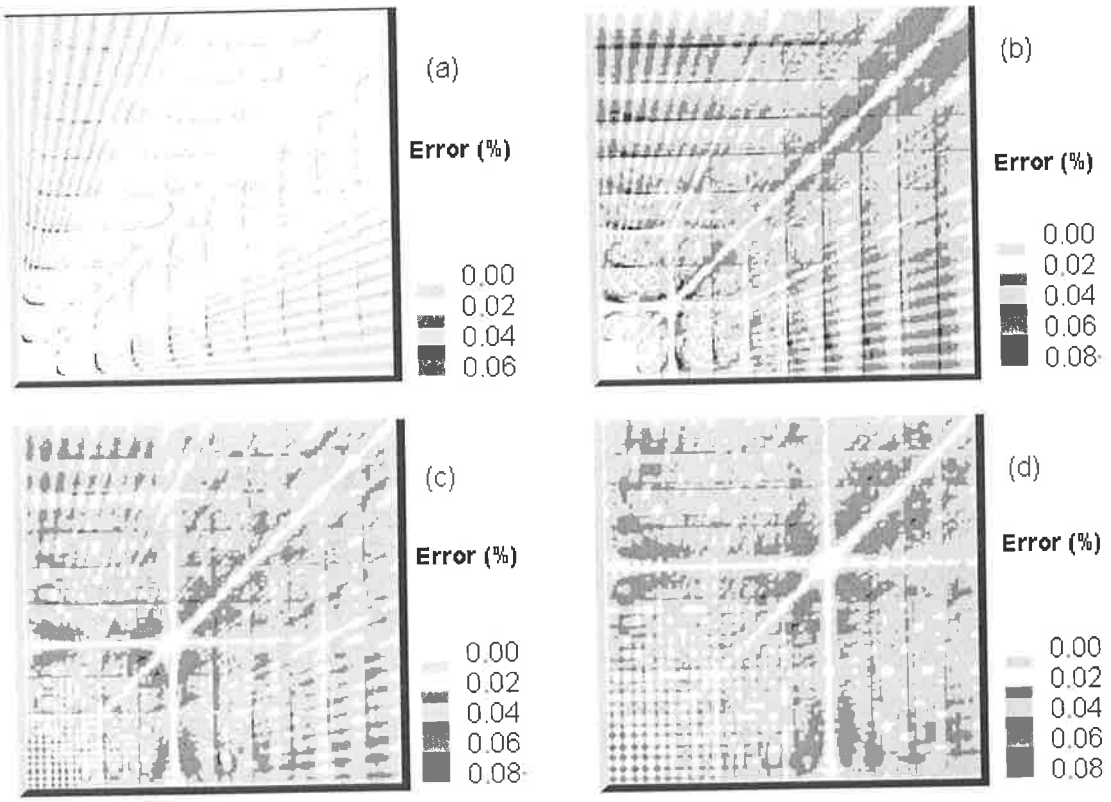

Fig.3.6 The relative travel time errors at the four different Z planes for a uniform velocity field (a) Z=0 km; (b) Z=20 km; (c) Z=40 km; (d) Z=60 km

3.4.4 Model with a 1-D linear increase of velocity with depth

A constant-velocity gradient model was next selected for comparison. The velocity ratio between the top and bottom surfaces of the model is 1:3, which is quite a high gradient. The source is set at the left-hand top corner of a vertical square in which the 'irregular' algorithm has been performed. Note that this model was used by several authors to analyze the accuracy of computed travel times, for example, Podvin and Lecomte (1991, Fig. 13c), Klimeš and Kvasnička (1994, Fig. 5). In the analysis by Klimeš and Kvasnička (1994), 201×201 nodes (200×200 cells) were used to cover the 2-D model. For comparison, in this study, 20×20 cells (21×21 primary nodes) and 39,960 secondary nodes (9 secondary nodes in each direction of the cell) are used to cover the 2-D model so that the total number of nodes is the same in both cases. The velocity model is simply sampled at the primary nodes, which are double-linked to the secondary nodes so as to obtain velocity values at the secondary node positions (see formula 3.14 for details). The basic pattern of the relative error distribution (Figure 3.7 in this study) is the same as Figure 5 of Klimeš and Kvasnička (1994). Meanwhile, the maximum relative error has the same level for both cases. The estimated maximum error in this 2-D case ($n=10$) is 0.124 % (see formula 3.16).

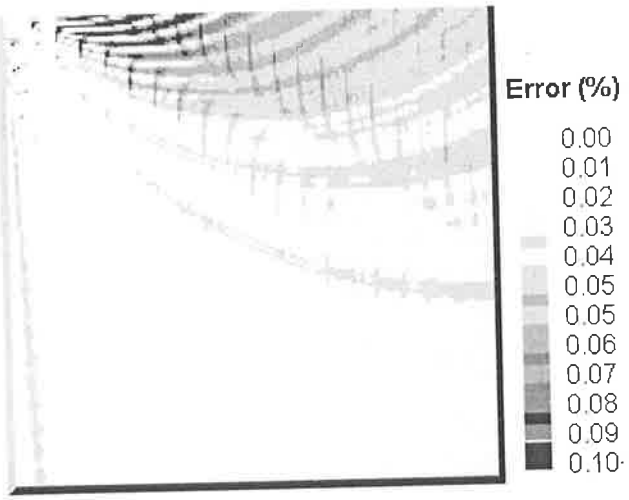

Fig.3.7 The relative error distribution in a 1-D model
Velocity ratio is 1:3 between top and bottom

3.4.5 Model with velocity changes in all three directions

It is necessary to analyze the accuracy of the computed travel times in a more complex velocity field, and to compare with other known algorithms. For this reason, the model given as Figure 6 of Klimeš and Kvasnička (1994), and reproduced here as Figure 3.8, is selected as the basic model, because they also used a revision of the shortest path method, but with the 'regular' approach. The model size in the horizontal

plane is 40 km×40 km. The velocity distribution in a box of horizontal dimensions is smooth. The velocity at the top surface of the model is 3 km/s everywhere. The velocity at the model bottom (20 km depth) oscillates between 5 km/s and 6 km/s, with a minimal and maximal 10 km interval apart (see Figure 3.8 for details). Along each vertical line, the velocity varies linearly by up to a factor of 2. The source is situated at the geometric center of the model bottom, and 66 receivers are placed on the model surface, forming a somewhat irregular seismic network. Klimeš and Kvasnička (1994) used the Complete Ray Tracing program package by Červený et al (1988) to obtain the travel times as the reference values (T_{ref}), and then compared their results (T_{net}) with the reference values. They used a grid of 101 ×101 ×51 nodes (100 ×100 ×50 cells) to calculate the travel times from source to each receiver.

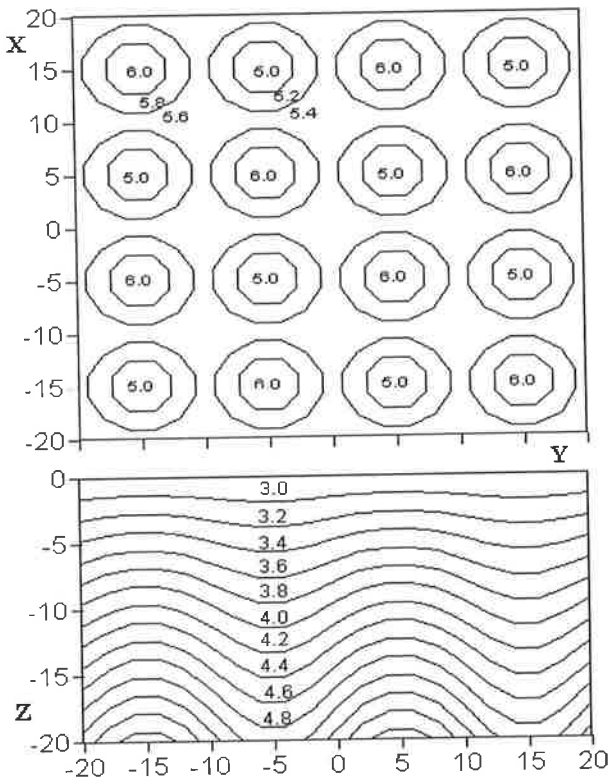

Fig.3.8 Model with velocity changes in three directions
(a) Velocity isolines along the model bottom
(b) Velocity isolines in the vertical section (X=6 km)

Following their approach, I now compare with the travel times (T_{irr}) obtained from our 'irregular' approach. In the model representation, a 2 km ×2 km × 2 km cubic cell is used. The number of secondary nodes added in each direction of the cell is set at 5, so that the minimum node distance at the cell surface planes is the same as above (0.4 km). In such a model, there are in total only 20 ×20×10 cells (21×21 ×11 primary nodes) and 393,101 nodes in total. The velocity model is again simply sampled at the primary nodes, which are tri-linked to the secondary nodes so that it is possible to obtain the velocity values at all other positions within the model. Table 3.1 lists the three-sets of

computed travel times (reference, regular, irregular) for all 66 receivers. Generally, the travel times (T_{net}) obtained by Klimeš and Kvasnička (1994) are all slightly larger than the reference travel times (T_{ref}). But the travel times (T_{irr}) obtained from our 'irregular' method oscillate around the reference travel times with a maximum relative error of ± 0.6 %, taking the reference travel times to be exact. Increasing the number of secondary nodes (added in each direction of the cell) to 19, does not eliminate this oscillatory behavior around the 'true' reference times. A partial reason for the above problem is with the coarse node sampling (2 km in the 'irregular' approach in this study), which may result in the velocity field not coinciding exactly with the fine node sampling (0.4 km in the 'regular' approach of Klimeš and Kvasnička, 1994). Nevertheless, even with fewer cells and nodes, the accuracy of the computed travel times obtained from this study is high and comparable to the travel times obtained by Klimeš and Kvasnička (1994). Figure 3.9 shows the related raypaths, which are generally smooth curves.

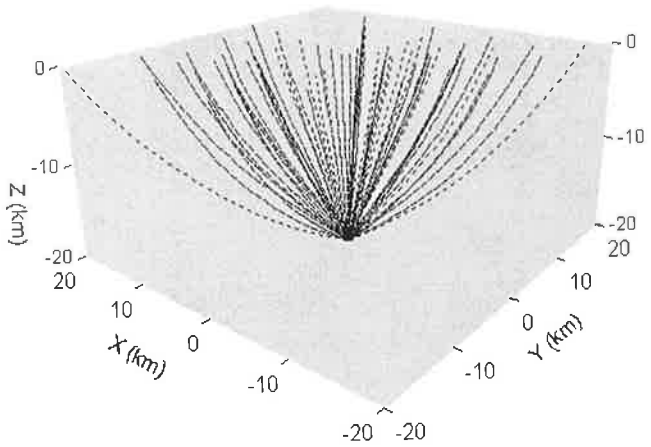

Fig.3.9 Related raypaths in 3-D variable model (Fig. 3.8)

Table 3.1 The comparison among the three different approaches for traveltime calculation based on model (Fig.3.8). T_{ref} : reference traveltimes obtained by the Complete Ray Tracing program; T_{net} : travel times obtained with the 'regular' approach (see Table 1 of Klimeš and Kvasnička, 1994); T_{irr} : traveltimes obtained with the 'irregular' approach in this study; T_{r-n} : the time difference between the T_{ref} and T_{net} ; T_{r-i} : the time difference between the T_{ref} and T_{irr} .

$X(km)$	$Y(km)$	T_{ref} (s)	T_{net} (s)	T_{irr} (s)	T_{r-n} (s)	T_{r-i} (s)
19.522	6.062	6.872	6.881	6.886	0.009	0.014
11.029	17.229	6.741	6.748	6.769	0.007	0.028
-17.633	18.451	7.911	7.919	7.885	0.008	-0.026
13.999	4.646	5.918	5.926	5.941	0.008	0.023
7.736	13.166	5.937	5.944	5.967	0.007	0.030
0.488	16.838	6.268	6.277	6.282	0.009	0.014
-7.884	15.544	6.393	6.404	6.401	0.011	0.008
-13.600	14.330	6.886	6.892	6.860	0.007	-0.026
-16.177	11.393	6.818	6.824	6.828	0.006	0.010
-10.814	-19.827	7.134	7.142	7.155	0.008	0.021
19.418	-19.802	8.317	8.324	8.283	0.006	-0.034
9.234	3.312	5.279	5.289	5.310	0.010	0.031
4.717	9.274	5.315	5.323	5.346	0.008	0.031
-1.026	12.339	5.672	5.683	5.690	0.011	0.018
-6.752	12.096	5.962	5.969	5.961	0.006	-0.001
-10.678	11.049	6.227	6.232	6.200	0.005	-0.027
-12.946	8.326	6.175	6.183	6.176	0.007	0.001
-15.475	1.776	6.083	6.093	6.099	0.010	0.016
-15.448	-5.966	6.193	6.002	6.215	0.007	0.022
-7.883	-15.401	6.275	6.281	6.301	0.006	0.026
-0.334	-18.502	6.520	6.528	6.531	0.008	0.011
9.271	-16.69	6.645	6.654	6.655	0.009	0.010
-15.158	-15.522	7.220	7.229	7.180	0.009	-0.040
17.777	-11.970	7.064	7.071	7.070	0.007	0.006
5.616	2.243	4.988	4.996	5.015	0.008	0.027
2.575	6.128	5.019	5.028	5.051	0.009	0.032
-1.524	8.683	5.310	5.315	5.314	0.005	0.004
-5.543	9.201	5.613	5.616	5.607	0.003	-0.006
-8.433	8.468	5.793	5.795	5.764	0.002	-0.029
-10.237	6.226	5.756	5.762	5.747	0.006	-0.009
-11.458	1.667	5.593	5.598	5.602	0.005	0.009
-10.327	-4.418	5.420	5.427	5.449	0.007	0.029
-4.948	-11.065	5.524	5.529	5.552	0.005	0.028
1.341	-13.750	5.852	5.863	5.868	0.011	0.016
7.735	-13.002	6.128	6.135	6.129	0.007	0.001
11.818	-11.860	6.420	6.422	6.395	0.002	-0.025
14.184	-8.603	6.318	6.326	6.326	0.008	0.008
17.202	-0.826	6.315	6.325	6.335	0.010	0.020
2.895	1.319	4.882	4.892	4.903	0.010	0.021
1.203	3.588	4.902	4.915	4.923	0.013	0.021
-1.305	5.453	5.054	5.063	5.061	0.009	0.007
-3.994	6.297	5.264	5.269	5.257	0.005	-0.007
-6.163	5.977	5.400	5.403	5.385	0.003	-0.015
-7.487	4.353	5.381	5.388	5.377	0.007	-0.004
-7.842	1.226	5.224	5.232	5.230	0.008	0.006
-6.411	-3.054	5.041	5.051	5.070	0.010	0.029
-2.709	-7.485	5.116	5.124	5.143	0.008	0.027
1.957	-9.936	5.448	5.455	5.448	0.007	0.000
6.381	-10.071	5.754	5.760	5.742	0.006	-0.012
9.379	-9.117	5.932	5.937	5.905	0.005	-0.027
11.292	-6.439	5.865	5.871	5.858	0.006	-0.007
12.809	-1.088	5.730	5.741	5.743	0.011	0.013
0.701	0.370	4.851	4.858	4.861	0.007	0.010
0.333	1.273	4.856	4.866	4.871	0.010	0.015
-0.654	2.324	4.890	4.902	4.906	0.012	0.016
-2.044	3.095	4.960	4.971	4.964	0.011	0.004
-3.431	3.204	5.029	5.034	5.014	0.005	-0.015
-4.379	2.413	5.041	5.050	5.045	0.009	0.004
-4.527	0.643	4.977	4.988	4.990	0.011	0.013
-3.541	-1.909	4.900	4.912	4.925	0.012	0.025
-1.293	-4.644	4.943	4.952	4.959	0.009	0.016
1.778	-6.632	5.156	5.165	5.163	0.009	0.007
4.846	-7.278	5.401	5.408	5.393	0.007	-0.008
7.138	-6.692	5.536	5.541	5.513	0.005	-0.023
8.525	-4.670	5.489	5.496	5.482	0.007	-0.007
8.957	-0.930	5.310	5.317	5.323	0.007	0.013

3.4.6 The minimum travel-time contours

To further test the accuracy of the computed travel times and to give a visual representation of the wavefronts in the ray tracing process, two velocity models were selected and the minimum travel time contours (wavefronts) were calculated for both media.

(1) The minimum traveltime contours for a 1-D linear velocity model

The 1-D linear velocity distribution model ($V = 4.0 + 0.05 \times Z$ km/s) is first selected. The cubic model scale is 100 km. Other parameters for the model are: cell size (10 km), and number of secondary nodes (19). The source position is still set at the origin (0.0, 0.0, 0.0). Figure 3.10 shows the minimum travel time contours for both the analytical and the numerical solutions on several X-Y planes. It is hard to discern the differences in Figure 3.10 between the analytical and the numerical solutions. The curves are essentially superimposed. In this example, the actual maximum relative error of the travel times is 0.05 % (the estimated maximum relative error is 0.06 %, according to formula 3.23).

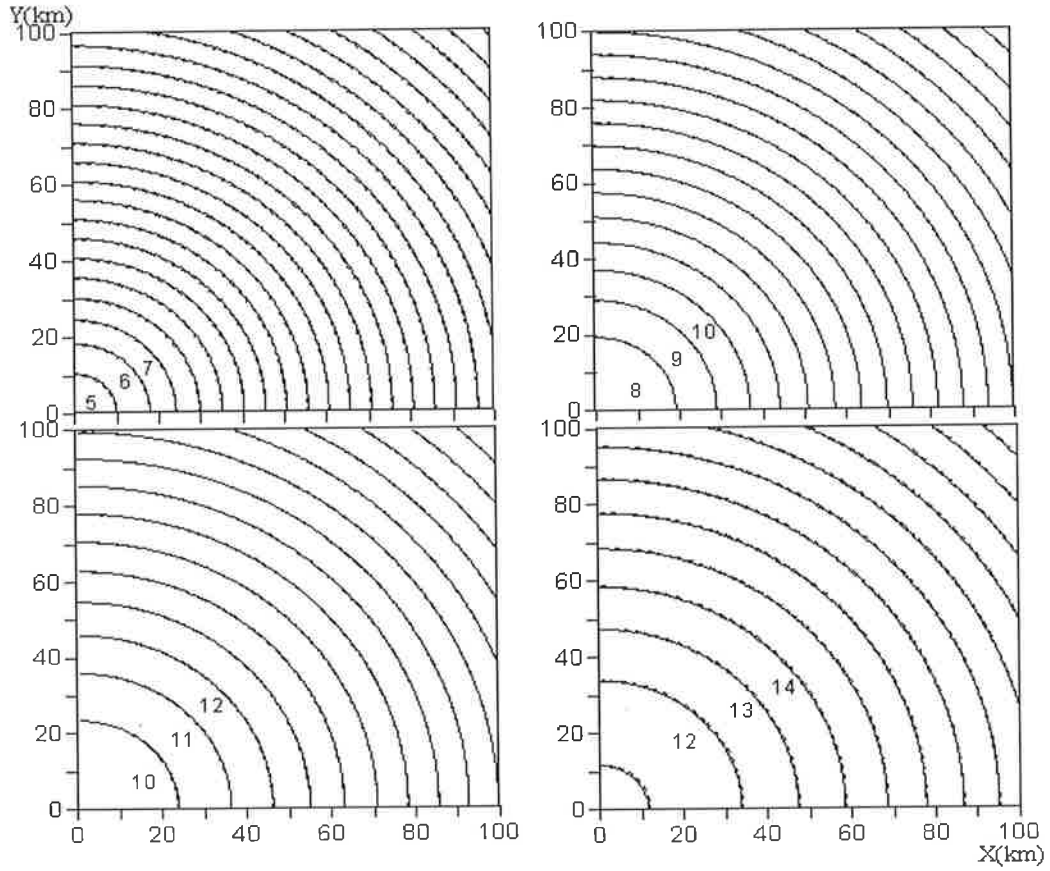

Fig.3.10 The comparison of the minimum travel time contours between analytic (continuous line) and numerical results (dashed line) on the different Z planes {from top left to bottom right are Z=20, 40, 60 and 80 km. The time interval (in seconds) is indicated on the figure}

(2) The minimum travel-time contours for a high contrast medium

The model used in the following example is a uniform background velocity model (V=4.0 km/s) with two cuboid velocity anomalies embedded in the model: one is a low velocity anomaly (V=3.0 km/s, having a velocity contrast against the background of -25%); the other is a high velocity anomaly (V=5.0 km/s, having a velocity contrast against the background of +25%). Again, the source is set at position (0.0, 0.0, 0.0), the cell size is 10 km, and the number of secondary nodes is 10 in all three directions.

Figure 3.11 shows the minimum travel time contours (wavefronts) on several X-Y planes at different depths. The low velocity anomaly extends for both X and Y between 20 km and 40 km, and over Z from 0 to 100 km; the high velocity anomalous cube extends over X and Y between 60 km and 80 km, and over Z from 0 to 100 km.

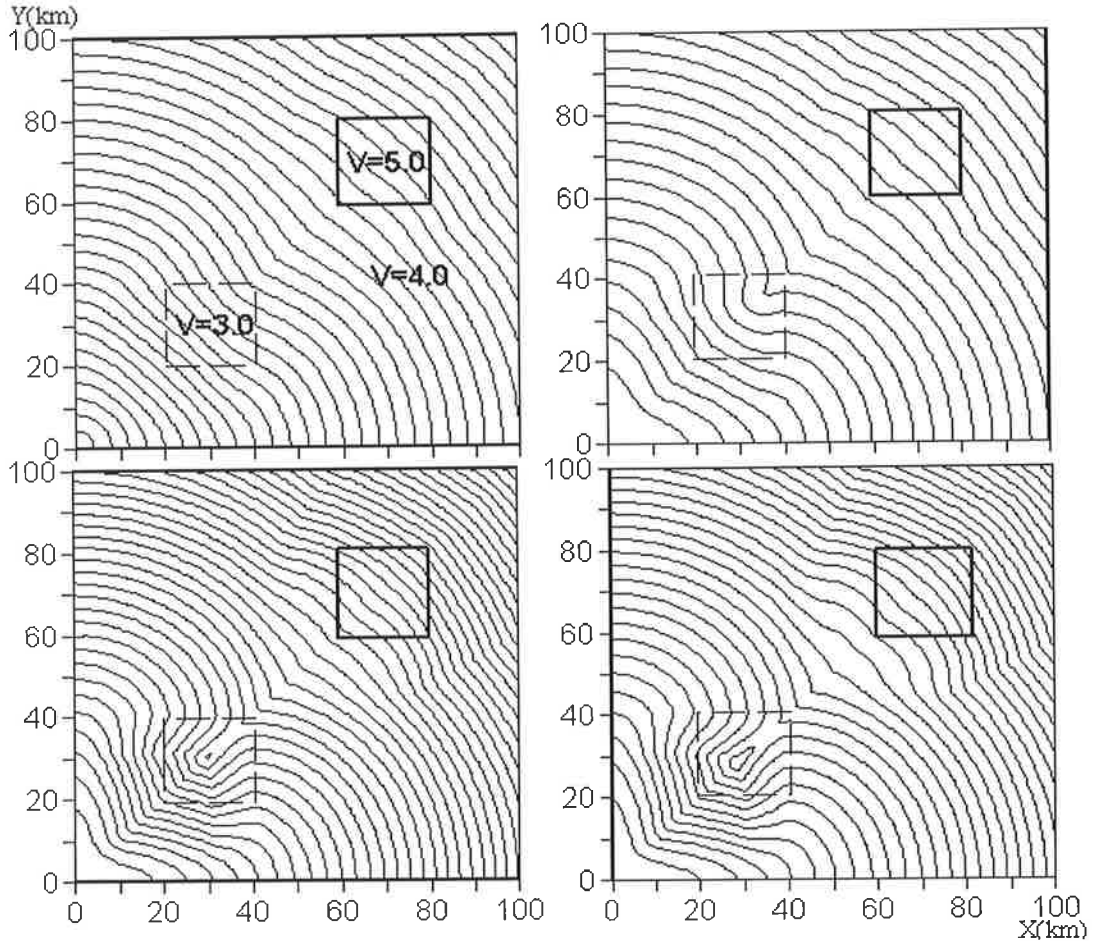

Figure 3.11 The minimum travel time contours on different Z planes (from top left to bottom right are Z=0, 40, 80 and 100 km, respectively, the corresponding time intervals are 1.0, 1.0, 0.5 and 0.5 s; Continuous line square: high velocity zone; Dashed line square: low velocity zone)

From Figure 3.11 it can be seen that the contours (wavefronts) are distorted by the two

high contrast velocity anomalies. In the low velocity block and its nearby region, the wavefront is set back or delayed. But in the high velocity block and its nearby region, the wavefront is advanced. As a result of the velocity contrast, an opposite curving wavefront is created in the low velocity region. On the other hand, an advanced wavefront is produced in the high velocity region; the less the distance from the high velocity anomaly, the more advanced the wavefront. This influence is not restricted to the low or high velocity zones, but affects the wavefields nearby.

Due to the geometric symmetry of the model, the minimum travel time contours on the Y-Z plane are the same as for the X-Z plane. So Figure 3.12 shows only the minimum travel time contours on several X-Z planes. On planes Y=20 and 40 km, the uniform velocity field is distorted by the square-shaped low velocity anomaly, where the ray is refracted at the velocity discontinuity. On the planes Y=60 and 80 km, the uniform velocity field is again distorted by the square-shaped high velocity anomaly, where the rays are refracted and cross the high velocity anomalous region. Far from the velocity discontinuity, the wavefront tends to approximate the pattern for a uniform velocity field.

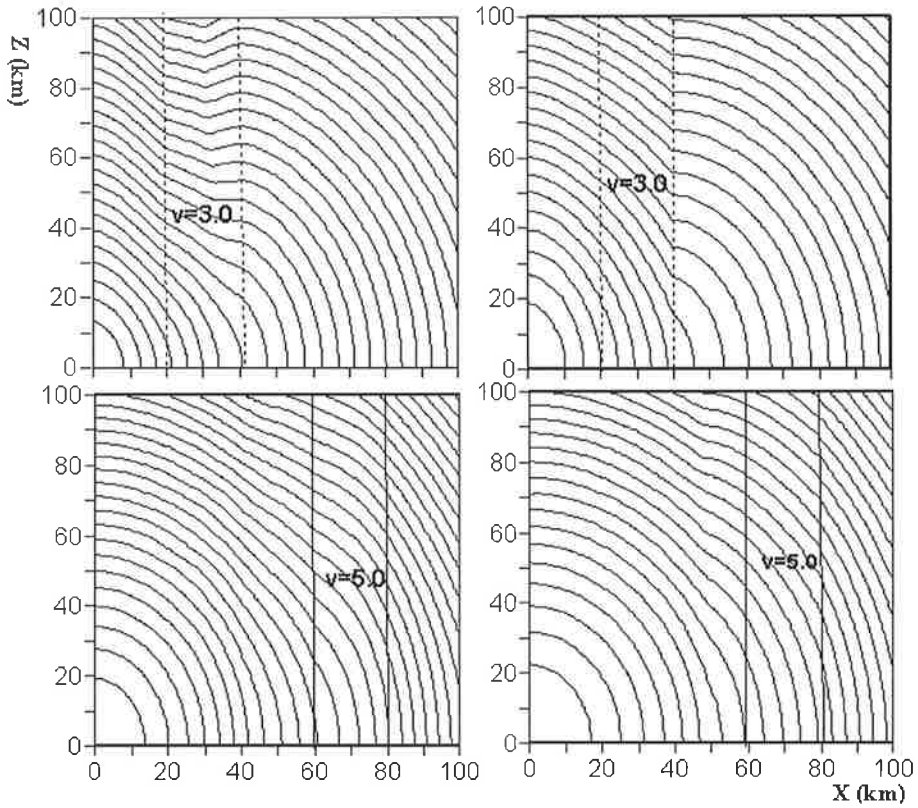

Fig.3.12 The minimum travel time contours on different Y planes (from top left to bottom right are Y=20, 40, 60 and 80 km, respectively; the corresponding time intervals are 1.0, 1.0, 0.75 and 0.75 second)

3.5 Automatic Model Adaptation in Ray Tracing

One of the problems in 3-D seismic ray tracing is the computational efficiency. Theoretically, one can select any kind of model and assign complicated parameters, but in practical applications, there are some restrictions that must be dealt with when using a personal computer. They include the running speed of the program, and the required memory space. For the shortest-path method, the required memory space varies from one model to another. In the 'regular' approach, there are at least 6 large one-dimensional arrays of length equal to the total number of nodes (in the 'irregular' approach, there are only 5 such large one-dimensional arrays). The usage of these 6 one-dimensional arrays is as follows: Three are to keep track of the X, Y, and Z coordinates of the nodes; one is to store the sampled velocity value at each primary node; another is to update the computed travel times at each node, and the final one is an indicator. Commonly the total number of nodes is in excess of 1 million in the 3-D case, so these six (or five) large one-dimensional arrays consume much memory space on the computer.

In order to overcome this disadvantage, one must find another way to reduce the length of the one-dimensional array. The ray-tracing program in most approaches is designed in such a way that it loops source by source in a fixed velocity model, i.e. one calculates travel times and raypaths from one source to all receivers, and then from the second source to all receivers, and so on. This means that the process can be separated into N steps (N is the total number of sources) for a variable size model. In a general 3-D model for travel time tomography, the receivers are restricted to a small region (say the central top region on the model), but the events are randomly distributed within the model. For this deployment of receivers and location of the sources, one can select a variable size (a relatively small) model according to each source location to seismic network deployment, if the restricted boundary of the ray paths can be predicted. For example, the maximum depth that a ray reaches can be estimated according to the specific velocity distribution and the epicentral distances between the source and the seismic stations. In the horizontal plane, it is very easy to find the restricted boundary of

the small model according to the geometry of the specified source and seismic array, if backscatter and diffraction of the seismic energy is neglected. In my experience, this automatic model adaptation process can save at least half the memory space (which is an important improvement, and hence shorten the program run time when dealing with a large 3-D model), if a large number of sources are included. To realize this process, two extra steps are required in the computation: One subroutine is to select each new (small) model according to a certain rule, that is the velocity distribution and the geometry of the source and seismic array; the other subroutine is to update the velocity input corresponding to different models, which must be consistent with the original input velocity model (large model). Considerable benefits are obtained from such an adaptation.

3.6 Bent Raypaths in Explosion and Refraction Seismic Surveys

The advantage of the specified 'irregular' approach of the shortest-path algorithm is that it not only calculates travel times according to the source and receiver pairs, but also yields the corresponding raypaths simultaneously. As the cubic velocity function is tri-linked to the secondary nodes, the trajectory of the raypaths that sums over consecutive segments along the grid, tends to be close to the bent ray, if the ray angular coverage is good, and there is little deviation from the true paths. To explain this feature, an example of ray paths in 3-D seismic explosion survey is presented.

Figure 3.13 shows the simulation of ray paths in a 3-D explosion survey. The model parameters are: model length (X=100 km, Y=100 km, and Z=30 km); cell size (5 km). The number of secondary nodes in each direction of cell is 10. For simplicity, I only select 9

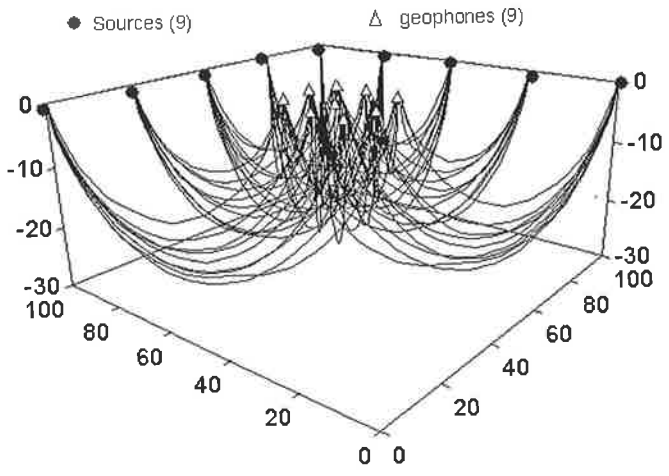

Fig.3.13 3-D ray paths in seismic explosion survey

sources along the model top boundary and 9 receivers along the top central region of the model. The bending of ray paths is clear in Figure 3.13. From this test, it is possible to properly arrange the shooting positions near Earth's surface around the target and obtain the 3-D velocity model under the seismic network.

To demonstrate that this approach is also able to trace the reflected or refracted arrivals with some specific constraints, Figure 3.14 shows another simulation of ray paths in a 3-D refraction survey. The model parameters are: model length (100 km, 100 km, 20 km), cell size 5 km in all three directions, the number of secondary nodes is 10 in all three directions, a 1-D linear increase of velocity with depth model ($V = 2.0 + 0.2 \times Z$ km/s) was used, incorporating a velocity discontinuity (refractor) with (V=8.0 km/s) at Z=15 km. Six sources are placed along one line and 35 receivers along five parallel receiver lines (which are perpendicular to the source line). The raypaths are shown for this refraction experiment. This is another test, which indicates the possibility of obtaining 3-D velocity images beneath the seismic network by properly arranging sources and receivers, using refracted arrivals.

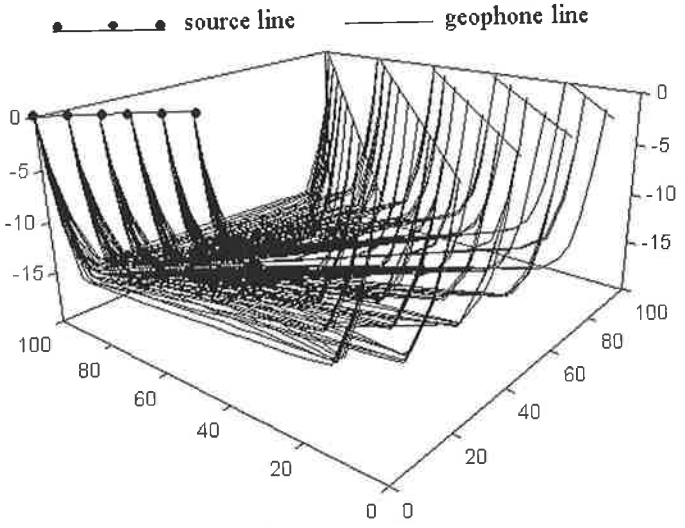

Fig.3.14 3-D ray paths in seismic refraction survey

3.7 Conclusions

The 'irregular' approach to the shortest-path method of calculating the first-arrival traveltimes has been presented with two basic innovations. That is, secondary nodes are introduced on the cell surfaces, and the interpolated velocity function is tri-linked to the secondary node positions. The maximum relative error bound is formulated, which may be considered as an upper error bound for the whole model in real problems. Synthetic

tests in a homogeneous 3-D medium strongly support the above procedure of establishing the maximum error bound, which in general is two times larger than that for the 2-D case. The accuracy of the computed travel times is analyzed theoretically, and compared with the results obtained by the 'regular' approach (Klimeš & Kvasnička, 1994) in two basic velocity models, previously investigated by other authors. Comparing with the 'regular' approach of the shortest path method, the advantages of a revised 'irregular' approach in this study can be summarized as follows:

- less computer memory requirement and less CPU time (at least one order), which indicates the capacity to handle a relatively large 3-D model;
- easy handling of high contrast velocity media, due to velocity values being tri-linearly linked to secondary node positions;
- fewer number of total cells (roughly equal to the number of primary nodes), which leads to easy incorporation with any inversion subroutines to solve real 3-D problems, if the velocity model is simply sampled at the primary nodes;
- the accuracy of the revised 'irregular' approach is comparable to the accuracy obtained from the 'regular' approach.

The technique developed with the 'irregular' approach in this study for first-arrival time calculations is equally applicable to diffracted and reflected arrivals. It is simply a case of adding times from source to node position (diffractor) to that from node position to receiver, which constitutes the later arrivals, or with some constraints (reflected surface or boundary) to trace the reflected arrivals. Therefore, the conclusions from this study concerning the accuracy of first-arrival times with the 'irregular' approach are equally applicable to reflection tomography and seismic migration, as they are to transmission tomography and seismic refraction.

Chapter 4: Non-Linear Inversion in Travel Time Tomography

4.1 Introduction

Travel time tomography is in general a non-linear inverse problem, but for purposes of model simplification and efficiency of computations, it can be reduced to a large and sparse matrix, over-determined linear equation problem after linearization (for example, McMechan et al., 1987). Unfortunately, this simplicity is not suitable in every case to fully reconstruct a satisfactory and reasonable image from the linear system of equations. The problem is that the ray paths are seriously bent in a high contrast velocity medium and the assumption of straight raypaths fails due to large deviations from the true ray paths. The higher the velocity contrast, the larger the deviation. Thus in such circumstances, one has to apply a true non-linear procedure for both ray tracing and inversion.

The non-linearity of tomographic inversion is as yet not well understood despite considerable research (e.g., Sehudanadi and Toint, 1993; Bunks et al., 1995; Reiter and Rudi, 1996; Vasco, 1997; Chunduru et al., 1997). The mostly linearized schemes that are used in practice are sensitive to noise and may create solutions that are geologically implausible. For this reason, much work has been done in adjusting or improving the various inversion strategies, typically by using filters, data pre-processing, data pre-selection, damping, or smoothing. For example, Tinti and Ugolini (1990) introduced pre-selection of seismic rays as a possible method to improve the inverse problem solution. Sambridge (1990) attempted to constrain velocity anomalies by seeking smooth models in the 3-D case. Carrion (1991) performed dual tomographic inversion by parametric optimization in the vector space of Lagrangian multipliers, yielding better results than standard algebraic and simultaneous reconstruction techniques. Zhou (1993) extended traveltime tomography with a spatial-coherency filter. Nemeth et al. (1997) introduced variable sized smoothing preconditioning in crosswell tomography as a means to speed up convergence of tomograms.

Non-linear travel time tomography can be implemented by linearization and an iterative procedure (Bregman et al, 1989), in which a constrained optimization problem incorporating à *priori* information (Tarantola and Valette, 1982) or 'hard' and 'soft' bounds for a physical solution (Carrion, 1989) must be solved. Zhou et al (1992) systematically analyzed and compared several popular inversion methods (such as SVD, ART, LSQR and CG) for the non-linear problem and developed two inversion procedures (DMNLS-1 and DMNLS-2) having solutions less sensitive to data error. The non-uniqueness of the solution is reduced by à *priori* information. DMNLS stands for the damped minimum norm, least-squares and constrained problem. It has the advantage of handling a large sparse matrix inversion with less computation time and less memory space requirements. Here, I give a brief overview of the DMNLS inversion procedure.

4.2 DMNCLS Problem

The non-linear inversion problem can be cast in the following form:

$$\min \frac{1}{2}\left[\left\|\vec{d}-A\vec{m}\right\|_{L_2}^2+\mu\left\|\vec{m}\right\|_{L_2}^2\right], \qquad \vec{a}\le\vec{m}\le\vec{b} \tag{4.1}$$

where the squared norm $\|x\|_{L_2}^2 = x^T C_d x$ is defined with the d or m subscripts standing for the positive matrix operator C to the data space (d) or model space (m) respectively; μ is a damping factor and $\vec{a}$ and $\vec{b}$ are constraint bounds on the solution for the velocity model. In the non-linear inverse problem, the operator C is often taken as the weighting matrix, or the inverse of the à *priori* covariance matrix, $\vec{d}=[\delta t_1,\delta t_2.....,\delta t_M]$ is the data vector of residuals between the observed and computed travel times; $\vec{m}=[\delta V_1,\delta V_2,.....,\delta V_N]$ is the velocity perturbation relative to the updated velocity model; and A is the Jacobian matrix with dimension (M× N), where M is the total number of ray paths and N is the total number of unknown velocity parameters. The Jacobian matrix is a large, sparse and ill-conditioned matrix (about 90% of the elements are missing).

The solution equation of problem (4.1) can be obtained (Menke, 1984) as follows:

$$\left[\mu C_m + A^T C_d A\right] Z_m \vec{m} = A^T C_d \vec{d} \tag{4.2}$$

where the truncation operator can be defined as:

$$Z_m \vec{m} = \begin{cases} m_i & a_i \le m_i \le b_i \\ a_i & m_i < a_i \\ b_i & m_i > b_i \end{cases}$$

The formula (4.2) is the generalization of linearized inversion and forms the basis for a number of inversion methods. For example:

(1) By taking $\mu = 0$ and $C_d = I$, equation (4.2) becomes the classic LSQR problem:

$$\min \frac{1}{2}\left[\left\|\vec{d} - A\vec{m}\right\|_{L_2}^2\right] \qquad \vec{a} \le \vec{m} \le \vec{b} \tag{4.3}$$

(2) By taking $C_d = C_m = I$, $Z_m = W$ and $A = GW$ where W is a banded matrix that is physically described as ray broadening, the convolutional quelling method solution proposed by Meyerholtz and Szpakowski (1989) is obtained:

$$\vec{m} = W\left[W^T G^T G W + \mu I\right]^{-1} W^T G^T \vec{d} \tag{4.4}$$

(3) By taking $C_d = I$ and $C_m = D^T D$, where D represents a first or second difference operator by which minimisation of the data residual is traded-off against obtaining a smooth solution, then the first or second regularisation method solution (Shaw and Orcutt, 1985) is obtained:

$$\vec{m} = \left[A^T A + \mu D^T D\right]^{-1} A^T \vec{d} \tag{4.5}$$

(4) By taking C_d, C_m as the inverse operators of the à *priori* covariance matrix to the data space and model space respectively, the solution of the generalised LSQR inversion problem (Tarantola and Valette, 1982; Carrion, 1989) is obtained:

$$\vec{m} = \left[A^T C_d A + \mu C_m\right]^{-1} A^T C_d \vec{d} \tag{4.6}$$

In summary, choosing different operators with different damping factors will yield different physical solutions. The best one among them is determined by the characteristics of the data and the model situation. Thus the basic task is to solve equation (4.2) using an iterative scheme.

4.3 Iterative Solution—DMNLS-1

Scales (1987) has successfully applied the classic conjugate gradient algorithm to the LSQR solution for a large, sparse matrix system, and shown that the method is fast, accurate and easily adapted to take advantage of the sparsity of the matrix. Theoretically, the CG method is also valid for the damped minimum norm, least-squares and constrained problem, since the solution exists in a physical sense and the condition number of the coefficient matrix is improved by à *priori* information (Tarantola and Valette, 1982; Carrion, 1989). Zhou et al (1992) introduced the CG method {following the Scales approach (1987), where the CG algorithm is applied to the LSQR problem} to the damped minimum norm, least-squares and constrained problem and developed two iterative procedures for solving equation (4.2); one is DMNLS-1 {by some simplifications, it reduces to the Scales approach (1987)}; the other is DMNLS-2 {it is a modification of the Carrion approach (1989), but solved with the CG method}. For more information on DMNLS-1 and DMNLS-2, see the paper by Zhou et al, (1992).

The method of DMNLS-1 can be interpreted as a certain trade-off between the perturbation length of the model space and the residual fitting of the data space; while the DMNLS-2 method seeks to find a vector orthogonal to the solution-space of the LSQR problem. Obviously DMNLS-2 has a more direct effect on reducing the non-uniqueness of the solution than DMNLS-1, but DMNLS-1 has a faster running speed than DMNLS-2. Zhou et al (1992) concluded that the nearly identical behaviour of SVD, LSQR and CG algorithms in low velocity contrast situations with noise-free data indicates that they are efficient solvers only for the LSQR problem, but they cannot offer much improvement for image quality when the data are contaminated by noise or if high velocity contrasts are embedded in the medium. In such situations, the preferable approach is to generate meaningful results and to reformulate the mathematical problem to be solved so that the ill-conditioned problem changes into a well-conditioned problem. Meanwhile, DMNLS-1 and DMNLS-2 yield a reasonable and physically meaningful solution, since the 'soft' (μ, C_m, C_d) and 'hard' (Z_m) bounds are introduced into the inversion and change the conditioning of the inverse problem.

The artifacts caused by noise and high velocity contrasts are substantially suppressed and the image quality is considerably improved, thus making the solution realistic with noisy or inconsistent travel time data.

In order to incorporate a relatively fast and accurate procedure for the non-linear inverse solver with the shortest-path ray tracer in 3-D travel time tomography, DMNLS-1 was selected as the linearized solver due to its fast running speed.

4.4 Calculation of the Analytical Jacobian Matrix

Most authors consider the segments of the raypath as the elements of the Jacobian matrix due to the assumption of constant velocity across each cell. This is strictly true only for straight ray tomography. But for bent ray paths in high contrast velocity media, one has to seek an analytic Jacobian matrix. As discussed in Chapter 3, the definition of the velocity distribution across the cell takes the form of a tri-linear function (equation 3.12).

The travel time along the j-th ray path R_j in a cell is given by the integration formula:

$$t_j = \int_{R_j} \frac{ds}{V_c(x,y,z)} \tag{4.7}$$

or

$$t_j = \sum_k \int_{R_{jk}} \frac{ds}{V_c(x,y,z)} \tag{4.8}$$

where ds is a segment of the ray trajectory in the cell, and $V_c(x,y,z)$ is the velocity distribution of the cell and k is the total number of segments in the cell. The derivative of time with respect to changes in velocity (the element of analytical Jacobian matrix) can be calculated by the following expression:

$$\frac{dt_j}{\partial V_k} = \sum_k \int_{R_{jk}} -\frac{\frac{\partial V_c}{\partial V_k}}{V_c^2(x,y,z)} ds = \sum_k \int_{R_{jk}} -\frac{BV(k)}{V_c^2(x,y,z)} ds \tag{4.9}$$

Here $\frac{\partial V_c}{\partial V_k} = \sum_k BV(k)$ are the sampled velocity values at the primary nodes of the cells.

Equation (4.9) and its integration can be calculated by a numerical algorithm. For simplicity, I calculate the derivatives as the summation over a series of averaged values between the two end points on a segment of the ray path across the cell:

$$\frac{\partial t_j}{\partial V_k} = \sum_k \int_{k_i}^{k_j} f(x,y,z)ds = \sum_k \frac{1}{2}\left[f_{k_i}(x,y,z) + f_{k_j}(x,y,z)\right] \tag{4.10}$$

$$\text{and } f_c(x,y,z) = -\sum_k \frac{BV(k)}{V_c^2(x,y,z)} \tag{4.11}$$

where k is the number of segments of the ray paths across the cell, and k_i, k_j are the two end points on the $k-th$ segment in the cell. As discussed in section 3.2.2, (x,y,z) is a normalised co-ordinate relative to the minimum primary node of the cell (reference point). With the total ray path information obtained from forward modeling, it is very easy to calculate the derivative of travel time with respect to velocity change for each cell along the ray path. Finally, the $M \times N$ elements of the analytical Jacobian matrix are obtained, where again M is the total number of ray paths and N is total number of unknown velocity parameters in the model space.

4.5 The Convergence Properties of the Inversion

I define five important quantities to analyze the accuracy and convergence properties of the inversion.

1. The convergence of the travel time residual

Here the root-mean square (RMS) of the time residuals is selected as the measurement of convergence of the travel time residuals between the observed and computed travel times for each loop of the iteration:

$$RMS\ (\delta t) = \sqrt{\frac{\sum_i^N (t_{obs_i} - t_{syn_i})^2}{M}} \tag{4.12}$$

where t_{obs} is the observed travel time and t_{syn} is the computed travel time corresponding to the current model, M and N are the total number of ray paths and total

number of unknown velocity values, respectively.

2. The convergence of the velocity model perturbation

I also use the RMS to define the convergence of the velocity model perturbation:

$$RMS\ (\delta V) = \sqrt{\frac{\sum_{i}^{N} (V_i^{(j+1)} - V_i^{j})^2}{N}} \tag{4.13}$$

where V^j and $V^{(j+1)}$ are the updated velocity values at successive iterations. The root-mean square difference of the updated velocity, averaged over the whole model, is roughly equivalent to the length of the perturbed model vector.

3. The convergence to the true model

In numerical tests another quantity can be introduced to measure the approximation of the updated model to the true model after each iteration:

$$RMS\ (\Delta V_1) = \sqrt{\frac{\sum_{i}^{N} (V_{syn}^{i} - V_{true}^{i})^2}{N}} \tag{4.14}$$

Here V_{syn} and V_{true} are the updated and true velocity values, respectively. $RMS(\Delta V_1)$ is the averaged measurement of how close the updated model approximates the true model after each iteration. It represents the accuracy of the inversion.

4 The deviation from the input velocity model

Another important quantity in evaluating the capability of the inversion is the deviation from the input or starting velocity model:

$$RMS\ (\Delta V_2) = \sqrt{\frac{\sum_{i}^{N} (V_{syn}^{i} - V_{input}^{i})^2}{N}} \tag{4.15}$$

Here V_{syn} and V_{input} are the updated and the input velocity values, respectively. $RMS(\Delta V_2)$ is the averaged deviation from the input (or starting) velocity model after each iteration. It shows absolute maximum perturbation of the updated

velocity model.

5 The ratio of current to maximum deviation from the input (starting) model

The quantity V_{ratio}, defined below, represents the relative perturbation of the updated velocity model.

$$V_{ratio} = RMS\left(\frac{\Delta V_2}{\Delta V_{\max}}\right) = \sqrt{\sum_i^N \left(\frac{V_{syn}^i - V_{input}^i}{V_{true}^i - V_{input}^i}\right)^2} \qquad (4.16)$$

Here $\Delta V_{\max}$ is the maximum deviation of the input model from the true velocity model. V_{ratio} is the fractional recovery of the velocity model if the updating process totally tackles the anomalous region.

Formulae (4.12) and (4.13) give the convergence of the matrix inversion in the mathematical sense, which only indicates the convergence feature regardless of the updated velocity model, and thus these measures cannot guarantee that the solution has physical meaning. Formula (4.14) is really needed in the inversion, but it is unavailable in practice because the true velocity model is never known for field studies. Alternatively, formula (4.15) can be evaluated for both synthetic and real problems. Theoretically, the quantity defined by formula (4.15) should have a decaying exponential form and remain stable with increasing iterations if the inversion algorithm is suitably selected. Formula (4.16) indicates what percentage of the velocity model is recovered from the inversion process. Through formulae (4.14), (4.15) and (4.16), it is possible to roughly estimate the accuracy of the inversion algorithm. A good inversion algorithm should not only have the ability to delineate the velocity anomalies both in size and location, but also should have the capacity to recover the strength (magnitude) of the velocity features. A full understanding of convergence properties is very important when undertaking numerical tests or solving real problems. One must keep in mind what is the best solution (the final one or the intermediate one) and how many iterations are needed to get a reasonable solution (it is not necessarily valid to think that the more iteration loops, the better the solution). It is desirable to obtain a reasonable

solution with physical meaning, rather than simply being a mathematical explanation. As far as I know, there have not been fully established theories in the literature to deal with the above problems. Therefore, I will discuss them according to the above five convergence features in the inversion of synthetic data (numerical tests) as a prelude to solving real problems.

4.6 Smoothing Function

In order to get a smooth image without sudden perturbations in the velocity field, sometimes it is useful to incorporate a filtering function to remove such high frequency variations (or artifacts). The filtering function can be incorporated in either of two ways: one way is to filter the updated velocity model after each iteration loop; the other is to filter the updated velocity model after the final iteration. Thus the alpha-trimmed means filter (Gersztenkorn and Scales, 1988) was introduced to fulfill this goal without destroying the sharp velocity distribution and introducing specious features. For the 3-D case, there are basically two approaches to filter the updated velocity model: with a 3-D filter or with a 2-D filter. For this purpose, I extend the 2-D filter to the 3-D case, and find that it is possible to obtain a relatively smooth updated velocity model with a 3-D filter, but with a large deviation from the background velocity of the input model due to contributions of adjacent cell velocities (from above and below) involved in the 3-D window. Therefore, the updated velocity model is filtered with a 2-D filter layer by layer. Considering the use of an analytical Jacobian matrix and hard constraints in the inversion process, it is not necessary to use a smoothing function for every iteration loop. Thus I filter the updated velocity model after the final iteration if required. A $n-point$ window of varying strength (0.0 to 0.5) was used as the filter. The quantities 0.0 and 0.5 indicate the mean-value and median-value filter, respectively. Thus the decimal number between 0.0 and 0.5 means the filter lies between the mean value filter and median value filter.

4.7 Numerical Tests and Results of Analysis

A series of models have been tested to assess the accuracy of the inversion algorithm itself, the capability of handling high contrast velocity media, the sensitivity to a

tolerable level of noise both in the travel times and the velocity model, and the ability to improve the image quality with well developed ray angular coverage (improved accuracy of the computed travel times).

4.7.1 Numerical test 1: The accuracy of the algorithm itself

In order to test the accuracy of the inversion algorithm, one numerical test (synthetic example) is carried out for a relatively high contrast velocity media. A good inversion algorithm should work well in high contrast velocity media, not only its ability to distinguish the velocity anomalies in spatial location (size and position), but also the capability to recover the anomalous strength (the true anomalous velocity value). For this purpose, the parameters of the basic model are: model length ($L_x = L_y = 100$ km and $L_z = 25$ km); cell size ($C_x = C_y = C_z = 5$ km); the number of secondary nodes in each direction is the same ($M_x = M_y = M_z = 6$). The estimated maximum relative error of the computed traveltimes in this case is less than 0.5 % (see formula 3.23). Figure 4.1 shows the velocity model that was used to obtain the theoretical travel times (as observed travel time data in the inversion process later on).

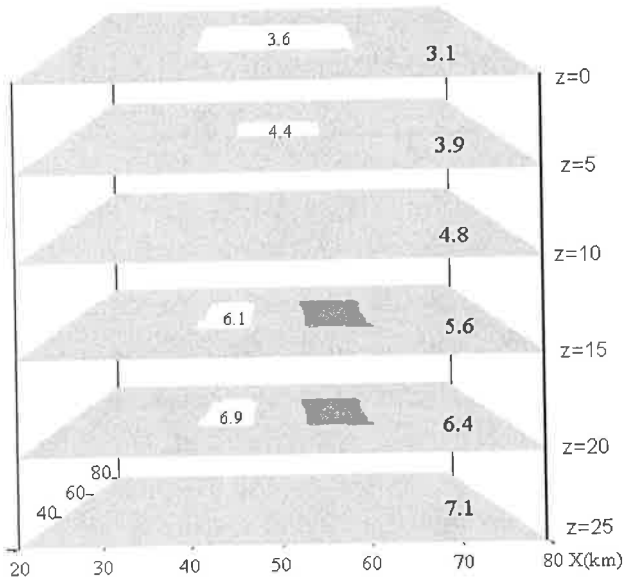

Fig.4.1 The true velocity model for numerical test 1

The background velocity distribution is a 1-D layered velocity distribution with six rectangular low and high velocity anomalies (± 0.5 km/s deviation from the background velocity) embedded in the planes Z=0, 5, 15 and 20 km; one high velocity anomaly both in the planes Z=0 km and 5 km, and two opposing velocity anomalies (high and low) both at the planes Z=15 and 20 km. The velocity contrast ranges from 8 % in the Z=20 km plane to 16 % in the Z=0 km plane.

To simulate a 3-D explosion survey and reconstruct the velocity field under the

seismic network, I put 20 sources uniformly along the top boundary of the model and 81 receivers with a 5 km equal spacing on the central top surface of the model (in total, 1620 seismic rays cross the model, and there are 2646 velocity unknowns in the inversion).

The damping factor is set at 0.01. There is a trade-off between the time residual convergence and the model perturbation when selecting the damping parameter. In our experience, based on considerable testing with different values, a soft damping factor (from 0.01 to 0.1) is suitable for the following examples.

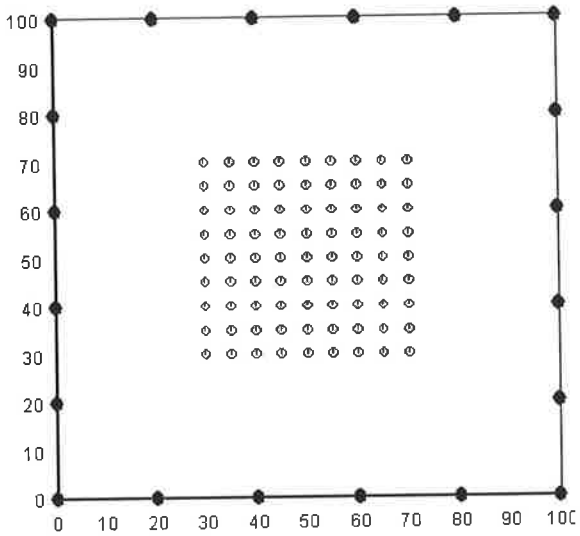

Fig.4.2 The source (black) and receiver (grey) location for numerical test 1 in plan view

The source-receiver geometry is shown in Figure 4.2. The input (starting) velocity model is the 1-D layered background velocity for the true model. In such circumstances, the travel time residuals only arise from the six velocity anomalies in the true model. In this case, I set strictly constrained bounds (with maximum value ± 1.0 km/s) as the possible deviation from the input model to the true velocity model. From these strict constraints, it is easy to analyze the updating process in the anomalous Z planes. Knowing that the velocity anomalies lie within a square region (between 40 and 60 km in both the X and Y directions), the following statistical analysis is restricted to these square regions at each anomalous Z plane so that the accuracy of the inversion algorithm can be evaluated.

Figure 4.3 shows the five kinds of convergence properties defined earlier (formulae 4.12 to 4.16). For the travel time residual and the velocity model perturbation (Figure 4.3a), they are typical decay curves with a fast convergence rate in the first few iterations and a stable trend with increasing number of iterations. After the 15-th iteration, there is not much improvement both in the travel time residual and in the

perturbation of the velocity model. It is especially interesting as to what can be observed in Figure 4.3b. All three quantities of convergence are roughly based on the anomalous velocity region (because the statistical analysis is not on the real anomalous region, but on the square region, between 40 and 60 km in both X and Y directions) in the model. From Figure 4.3b, the maximum deviation of the input model from the true model is 0.430 km/s, and the updated model closely approximates the true model (δV_1) with a discrepancy of 0.08 km/s after 20 iterations.

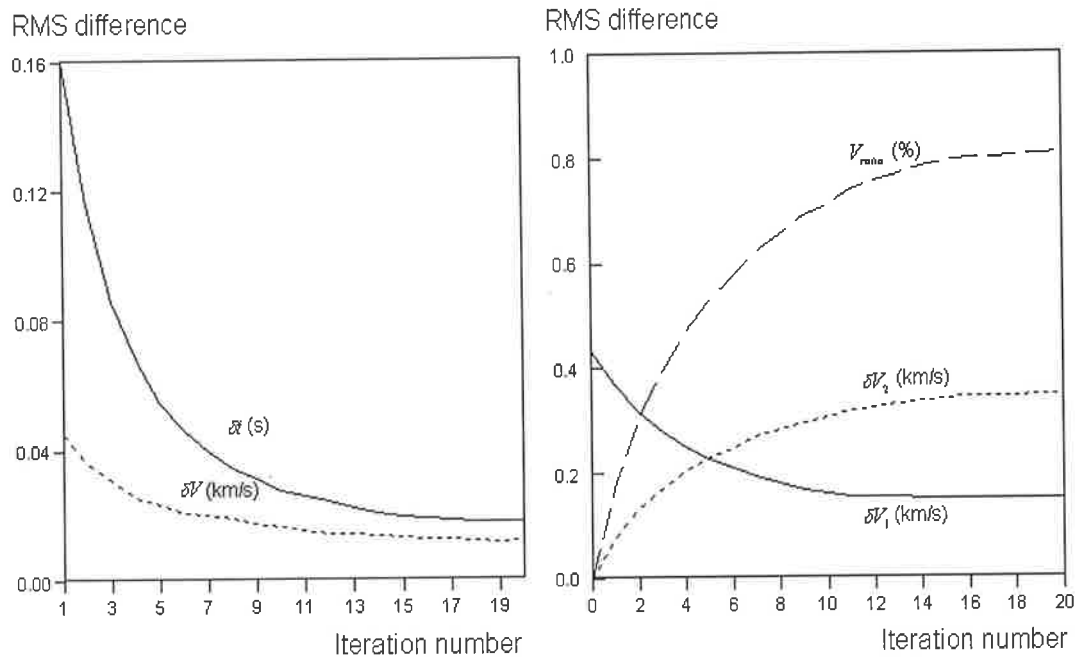

Fig.4.3 The five kinds of convergence curves (left panel: time residual and model perturbation; right panel: convergence to true model and deviation from input model) in test 1

The maximum perturbation (δV_2) of the updated velocity model (the maximum deviation from the input model) is 0.35 km/s. More importantly the relative perturbation (V_{ratio}) of the updated velocity model is more than 80.0% after 20 iterations (that is, $V_{ratio} = \frac{\delta V_2}{\delta V_1} = \frac{0.35}{0.43} \approx 81.4\%$). If all the perturbations of the updated velocity model are confined to the anomalous region, V_{ratio} is the recovery ratio of the anomalous strength. But it is known that the updating process is not only conducted on the anomalous region, but also along ray paths outside the anomalous region. Therefore, the actual recovery ratio is lower than the defined value above. Anyway, by considering

all three quantities of convergence, it is possible to roughly estimate the accuracy of the inversion algorithm.

Figure 4.4 shows the unfiltered images after 20 iterations. In the figure the unfiltered image means that the velocity value is only the difference between the final updated velocity and input velocity model; thus they are the absolute anomalous values against the input velocity model. From this numerical test, it can be concluded that the inversion algorithm has the ability to map the anomalous target in nearly the identical (true) position and of the right size even without any filter applied, but only partially recovers the anomalous strength. This means that the velocity anomaly recovered by the inversion algorithm is only a relative one (in this case), even though it is a very close to the true velocity model.

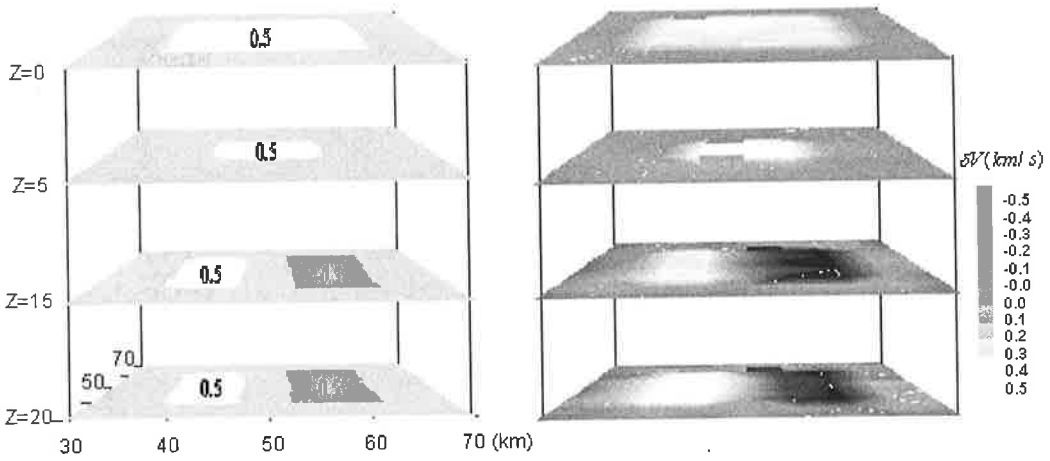

Figure 4.4 The true velocity perturbation (left) and the unfiltered image (right) from test 1 (In figure: the decimal number in the true model indicates the velocity differences against background velocity values)

4.7.2 Numerical test 2 (Ray angular test): The effectiveness of the algorithm itself

The maximum ray angle as an indicator of ray angular coverage in the cubic cell network of the model specification is {see formula 3.8):

$$\max imum(\theta_c) = arctg(\frac{1}{M+1}) \tag{4.17}$$

Here M is the number of secondary nodes added in each direction. It is the sole factor in representing ray angular coverage, and hence determining the accuracy of computed travel times. Theoretically, the image quality (both location and strength) should be improved by increasing the ray angular coverage (that is, improved accuracy of computed travel times). To evaluate the effectiveness of the inversion method, here I

perform two numerical tests to analyze the importance of ray coverage in 3-D travel time tomography. The first numerical test is developed in the following way. I obtain the 'observed travel time' by calculating the theoretical travel times on the fully developed ray angular coverage condition (increasing the number of secondary nodes in each direction to 10, the estimated maximum relative error is 0.2 % in this case, see formula 3.23). I then undertake the 3-D travel time inversion with a poor ray angular coverage condition (fewer secondary nodes, 4 in all three directions, which yields an estimated maximum relative error of up to 1.0 % in this case). Under such conditions, the travel time residual is only caused by the poor ray angular coverage (that is the inaccuracy of computed travel time, or switching the estimated maximum error from 0.2 % to 1.0 %), or by an unsuitable selection of the number of secondary nodes in the model design. In this test the basic model is the same as the numerical test 1; the only difference is that there are no velocity anomalies at all, simply a smooth increased velocity with depth.

As discussed in Chapter 3, the ray path defined by the shortest-path method is the geometrical ray. A certain pattern of travel time error exists, and even becomes worse (larger error) with poor ray angular coverage in the model representation. It can be predicted what image will be obtained in this test; it should be a symmetrical velocity 'anomalous pattern' due to the poor ray angular coverage (inaccuracy of the computed travel times).

From Figure 4.5 it can be seen that the absolute travel time residual (RMS) is less than 0.04 s (this travel time error is tolerable in most cases) even if the number of secondary nodes added in each direction is only 4.

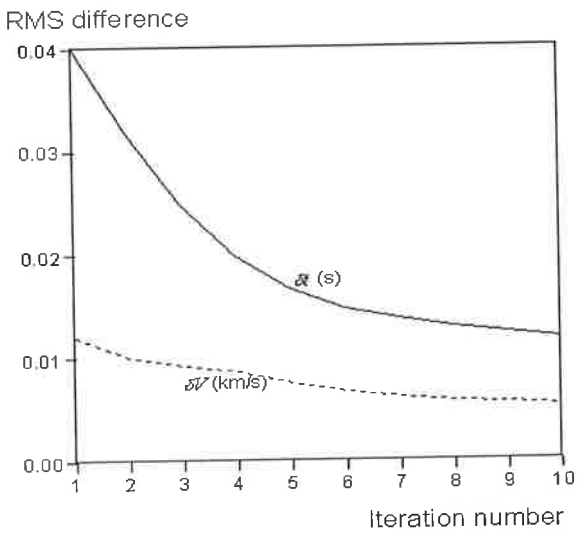

Figure 4.5 The convergence of the travel time residual and the model perturbation in test 2

Figure 4.6 shows the recovered tomogram with poor ray angular coverage. The fictitious 'velocity

anomalies' are within ±0.08 km/s and they can be neglected in most cases. The important factor is not the small anomalous scale, but the 'anomalous pattern', which has the geometrical symmetry according to the symmetrical pattern of source and receiver deployment in the model set up.

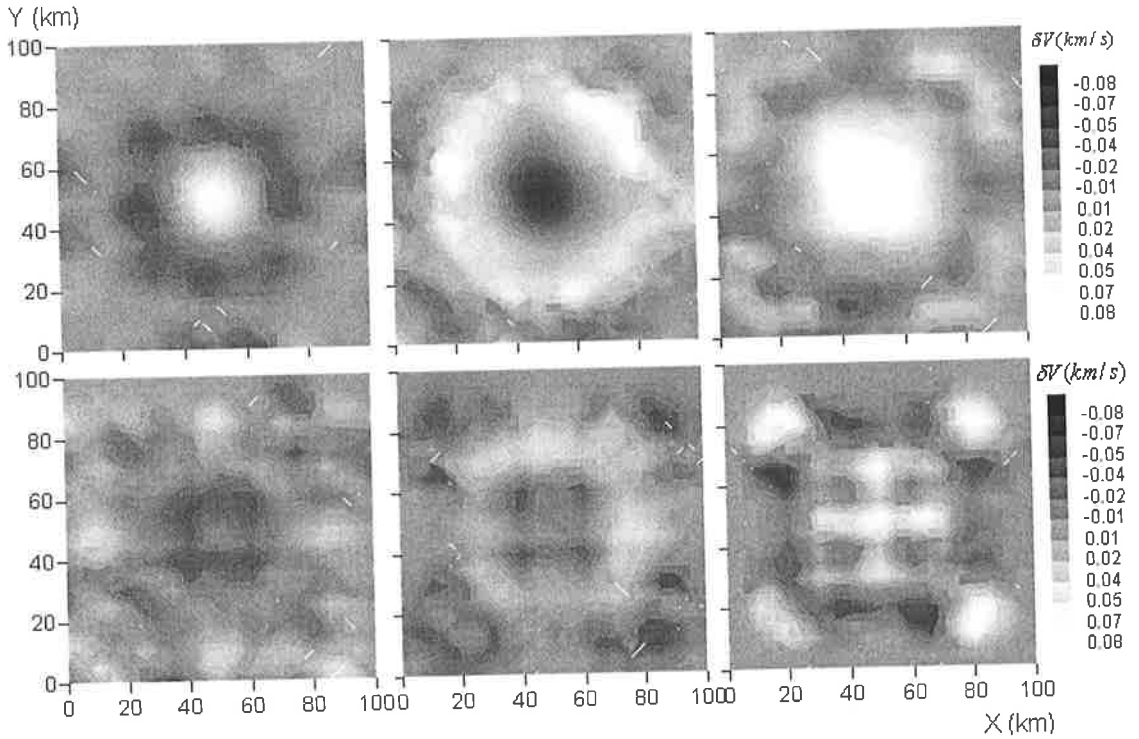

Figure 4.6 The filtered 'velocity anomalies' introduced by the poor ray angular coverage (from top left to bottom right are the planes for Z=0, 5, 10, 15, 20 and 25 km, respectively)

This example illustrates how unsuitable model division adversely affects the final image. From this test, it can be seen that ray angular coverage is an important factor in determining the accuracy and effectiveness of 3-D travel time tomography. It is worth pointing out that it is very necessary to analyze the accuracy of the computed travel times (or to use formula 3.23 to estimate the maximum relative error) on a certain model so as to meet the minimum requirement of the travel time error. Otherwise, there is no guarantee that a reasonable image will be obtained. Even worse, a false image related to the unsuitable model design is created. To further test the effectiveness of the method with increasing ray angular coverage (while keeping other model parameters unchanged), in the next test I select four different numbers of secondary nodes in each direction (M=4, 6, 8 and 10, for which the corresponding estimated maximum relative

errors are 1.0 %, 0.5 %, 0.3 % and 0.2 %, respectively) to obtain the corresponding images. The model used here is the same as the model in test 1.

Figure 4.7 shows the unfiltered images for differing amounts of ray angular coverage. The best image is the one with 10 secondary nodes added in each direction of the cell, but there is no significant difference in the image quality when the number of secondary nodes is equal to or larger than 6. Theoretically, the higher the ray angular coverage, the better the image quality. But in practical applications, there always has to be a trade-off between the accuracy and the computational efficiency. The recommendation is to find the minimum number of secondary nodes which guarantees the acceptable accuracy required.

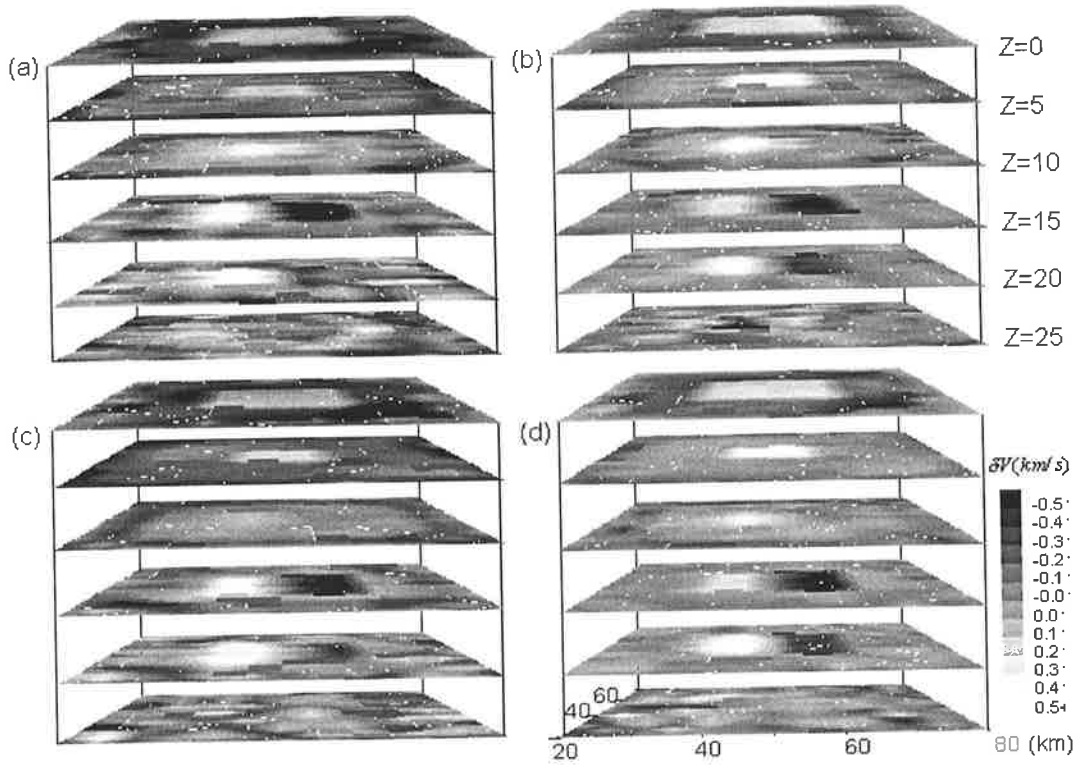

Fig. 4.7 The comparison of four travel time images with different numbers of secondary nodes involved in model representation (a: M=4; b: M=6; c: M=8 and d: M=10 secondary nodes)

To further explain the above situation, consider Figure 4.8, which shows the convergence of the travel time residual and the perturbations of the velocity model for different levels of ray angular coverage (different approximated accuracy of the computed travel times). From diagram (a), the travel time residual drops more quickly and reaches a lower level when there is good ray angular coverage (that is more secondary nodes are added in each direction of the cell), but there is not much

improvement when the number of secondary nodes exceeds 6. This means that only 8 secondary nodes are required in each direction to get good ray angular coverage in this case. From diagram (b), it can be seen that the perturbation of the velocity model maintains a relatively high level and sometimes fluctuates with poor ray angular coverage, but again there is not much difference between the results with 8 or 10 secondary nodes.

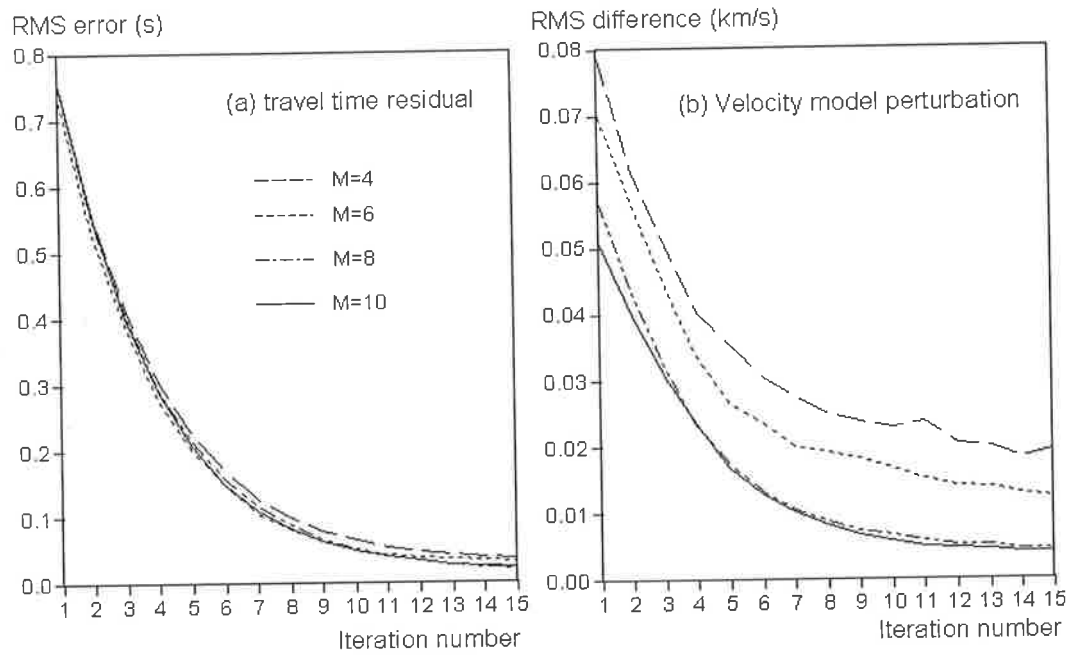

Figure 4.8 The convergence curves with different numbers of secondary nodes for ray angular coverage test

4.7.3 Numerical test 3: The capability to handle high contrast velocity media

The basic model in this test is similar as for numerical test 1, but high velocity contrast anomalies are added to test the capability of the inversion algorithm to handle such media (see Figure 4.9 for details). The velocity contrast is 22.5% on the plane Z=0, 20.5% on the plane Z=5, ± 21.5% on the plane Z=15 and ± 20.0% on the plane Z=20 km, respectively. The input model (starting velocity model) is a 1-D layered velocity model which deviates from the true background velocity by amounts -0.3, -0.3, -0.3, -0.2, -0.2 and -0.2 km/s on the planes Z=0, 5, 10, 15, 20 and 25 km, respectively). Being aware of the maximum absolute anomalous strength (velocity contrast), I set hard

constraints of $a = -2.0$ km/s and $b = +2.0$ km/s. This means that the maximum absolute model perturbation against the input velocity model is restricted within this range. Figures 4.10, 4.11, 4.12 and 4.13 give the comparisons between the true and reconstructed velocity fields at the planes Z=0, 5, 15 and 20 km respectively, with different filter parameters applied.

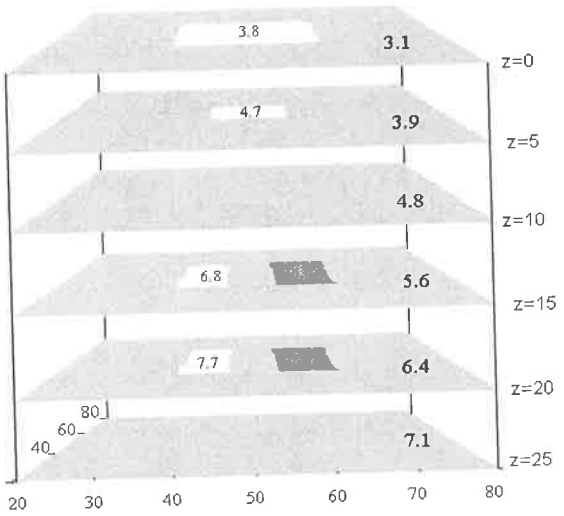

Fig. 4.9 The true velocity model for numerical test 3

The first integer in the parenthesis is the length of the filter window (in points) and the second decimal number is the weighting index (where 0.0 is to filter by the mean value; 0.5 is to filter by selecting a medium value; thus the decimal number between 0.0 and 0.5 indicates the filter lies between the mean value filter and median value filter). From the comparison, it can be seen that not only the low and high velocity anomalous regions have been separated from the background velocity (nearly identical anomalous size and location), but also the two adjacent opposite high contrast velocity anomalies at the planes Z=15 and 20 km have been resolved even without using any filters. Surprisingly, the rectangular background velocity field between the two adjacent opposite high contrast velocity anomalies is nearly unperturbed, i.e. the inversion was able to resolve a small object with length less than the cell size. Meanwhile, the reconstructed high velocity anomalous region is slightly larger than the true high velocity anomalous region, but the reconstructed low velocity anomalous region is slightly smaller than the true low velocity anomalous region, because of the effect of rays being drawn into the high velocity anomaly and being deflected away from the low velocity anomaly. It is reasonable to say, the mean value filter is able to smooth the image, but sometimes it makes the image obscure. The medium value filter has the ability to capture the main feature, but sometimes it fails to smooth the image. Thus, the recommendation is to use a filter with a value between the

mean and medium values.

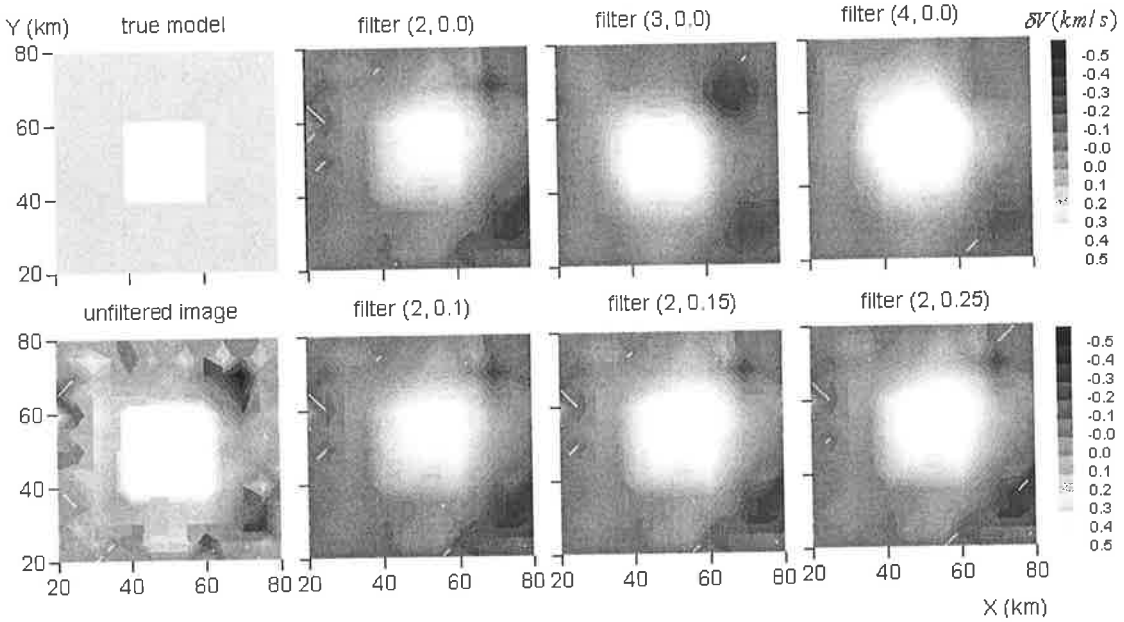

Figure 4.10 The comparison between the true model, unfiltered and filtered images with different filter parameters at the plane Z=0 km

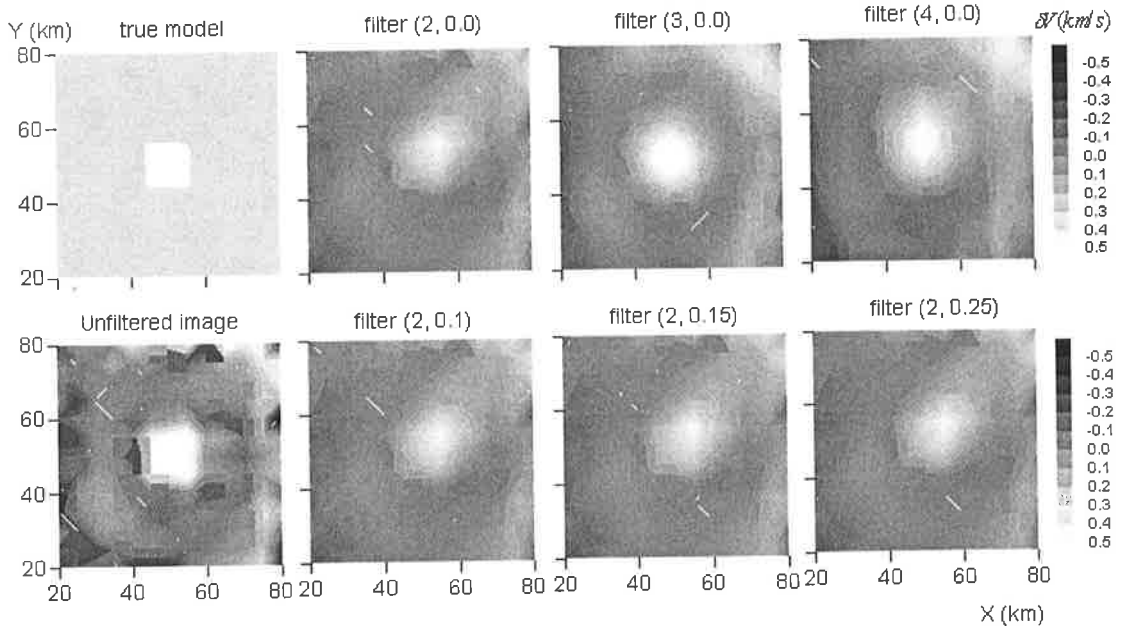

Figure 4.11 The comparison between the true model, unfiltered and filtered images with different filter parameters at the plane Z=5 km

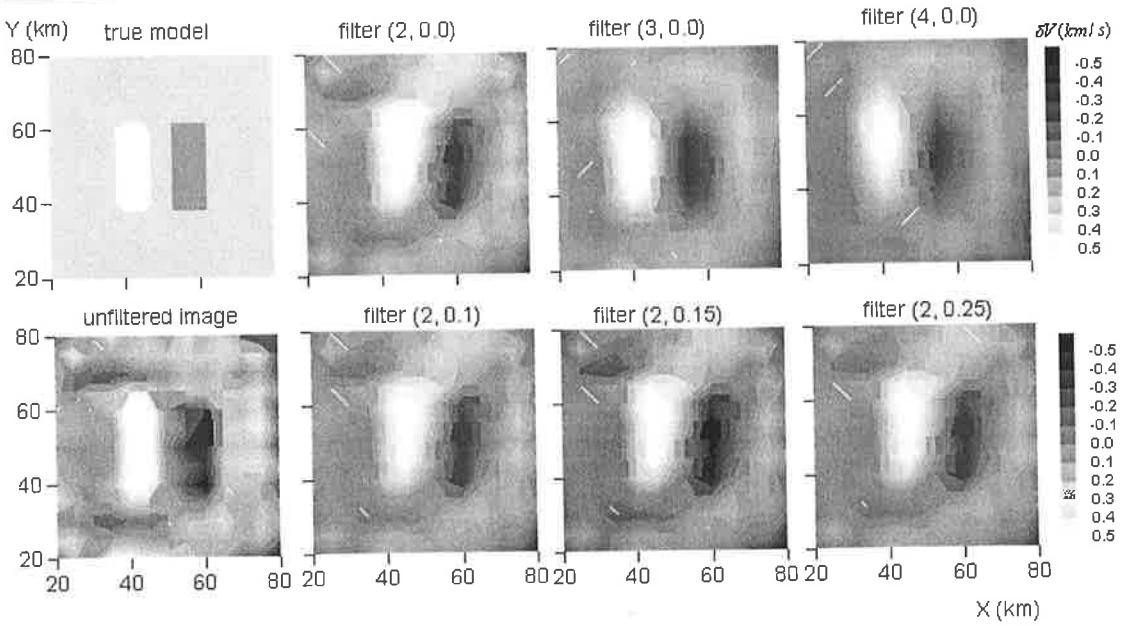

Figure 4.12 The comparison between the true model, unfiltered and filtered images with different filter parameters at the plane Z=15 km

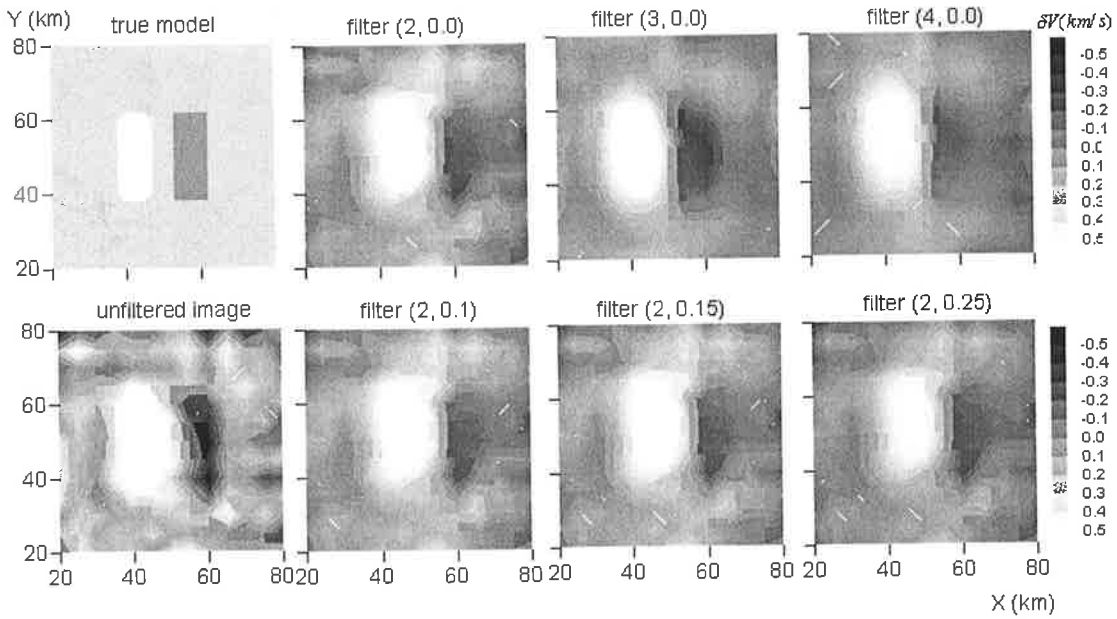

Figure 4.13 The comparison between the true model, unfiltered and filtered images with different filter parameters at the plane Z=20 km

The results of this test show that the inversion algorithm works well even on the suddenly changing high velocity contrast media, and thus has the capability to handle velocity discontinuity media (at least 20% contrast) without loss of accuracy.

4.7.4 Numerical test 4: The sensitivity to noise in travel times

In order to test the sensitivity of the inversion algorithm to noisy data, the model selected here is the same as in numerical test 2. That is, moderate velocity contrast anomalies are embedded in the model with maximum anomalous strength of

± 0.5 km/s. The starting velocity model deviates from the true background velocity model at each Z plane by amounts 0.4, 0.4, 0.2, 0.1, 0.0 and 0.0 km/s at Z=0, 5, 10, 15, 20 and 25 km, respectively. The constraint bounds on the velocity model perturbation, and the damping factor are the same as for numerical test 2. Random noise was added to the observed travel time data (theoretical travel time data were obtained from the true model). The relative error level is defined by:

$$\pm n\% = (|noise|_{\max\_Amp} (\frac{\sum_{j}^{m} (t_{ob_j} - \bar{t}_{ob})^2}{m})^{\frac{1}{2}}) \qquad (4.18)$$

Here n is the noise level. Based on the definition of formula (4.18), I add random noise with relative levels of 2.5%, 5.0% and 10.0% to the observed travel time data, respectively, and obtain the corresponding images with the same constraint bounds and damping factor. Figure 4.14 shows the corresponding images obtained with different noise levels. Good quality images can be recovered when the noise level is not so high (for example, less than or equal to 5%), and still a visible image can be obtained when the noise level reaches 10%, but some velocity anomalies are obscured.

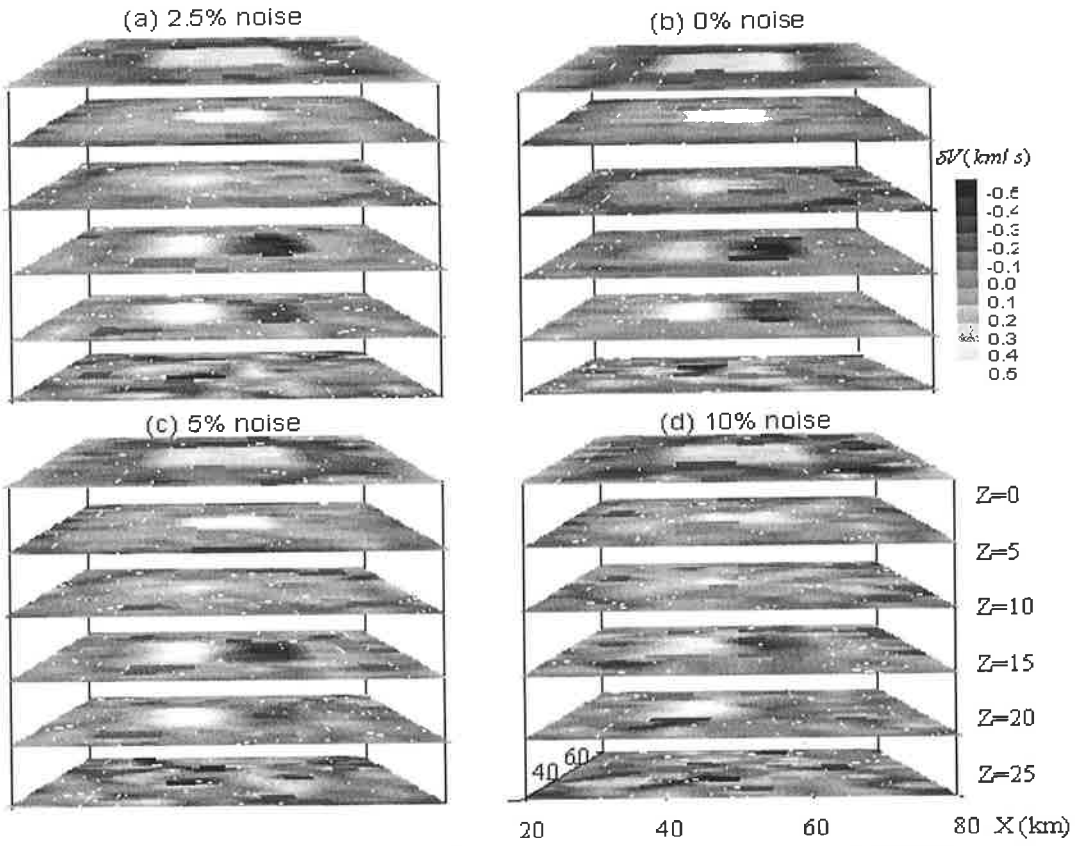

Figure 4.14 The unfiltered images with different noise levels added to travel times (Noise levels are indicated in the figure, 0% means noise-free)

Figure 4.15 is a comparison of the convergence curves with different noise levels. The stronger the noise level, the poorer is the convergence (higher level) for both the travel time residual and the perturbation of the velocity model. Meanwhile, there is not much difference among the convergence curves if the noise level is below 10.0 %, which means that this approach is not sensitive to a tolerable noise level (say the relative noise level does not exceed 10.0%). There is a practical benefit in developing an inversion procedure that is not too sensitive to a tolerable noise level.

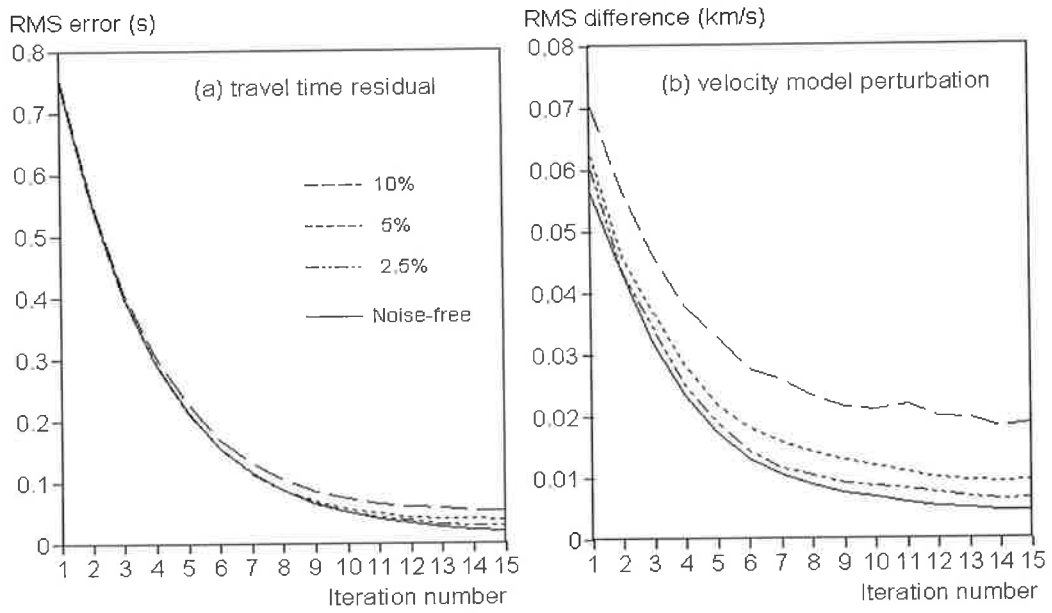

Fig.4.15 The tomographic convergence curves with different random noises in the travel times

4.7.5 Numerical test 5: The sensitivity to errors in the velocity model

It is possible that the travel time data obtained are from a corrupted or noisy velocity model, or a model with a relatively large timing error due to unsuitable selection of cell size and model parameters. In such circumstances, the travel time errors are possibly introduced by the corrupted velocity model. In order to simulate this situation, the random noise was added to the true velocity model and the theoretical travel times (treated as the observed travel times in the inversion process) were calculated. The model used here is the same as for numerical test 2; the only difference is that the random noise was added to the true velocity model rather than to the travel times. The relative random noise is introduced through following expression:

$$\pm n\% = (|noise|_{\max - Amp} (\frac{\sum_{j}^{m} (V_j - \overline{V})^2}{m})^{\frac{1}{2}}) \tag{4.19}$$

Here $\overline{V}$ is the averaged velocity at a certain Z plane, V_j is the velocity value on the $j-th$ primary node at this Z plane and m is the total number of primary nodes on this Z plane. I select three noise levels (2.5%, 5.0% and 10.0%) and obtain the corresponding images. Figure 4.16 shows the unfiltered images for the different noise levels. Again there is not much difference in the image quality if the noise strength is within a tolerable level (in this case, less than or equal to 5.0%). The image quality is distorted (some velocity anomalies are missed, others are transformed both in size and location) if the random noise strength reaches 10.0%.

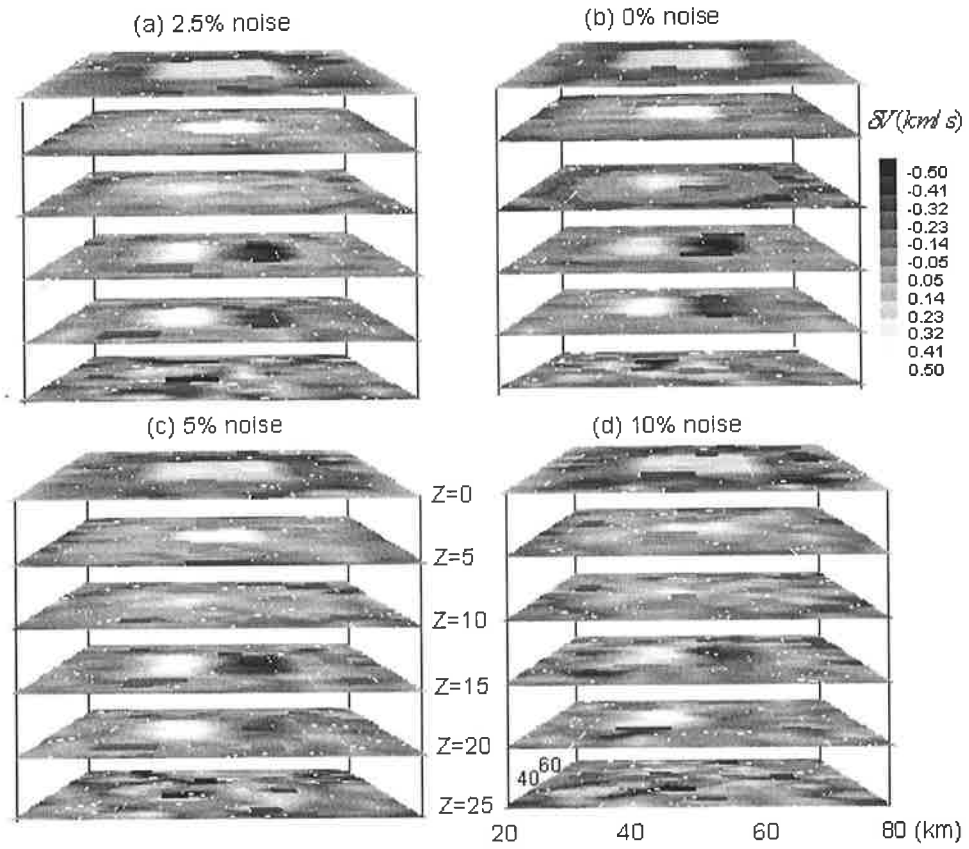

Fig.4.16 The unfiltered images with different noise levels added to the velocity model

Figure 4.17 shows the convergence curves for both the travel time residual and the perturbation of the velocity model with different noise levels added to the velocity

model. Again there is not much difference among the convergence curves for the time residual, but slightly different strengths for the perturbation of the velocity model. The stronger the noise, the larger the convergence level (plateau region) of the model perturbation, or the worse the result. The physical explanation for the same rates and levels of convergence of the time residual, but different convergence in the model perturbation with different noise levels, is that the inversion algorithm seeks different perturbed velocity models to fit the travel time residuals no matter how strong the noise that was introduced to the true velocity model. To reduce the residual of the travel time obtained from a model with a large deviation from the true model to the same level requires a relatively large perturbation length on the model space. Thus, it converges to a relatively high RMS level.

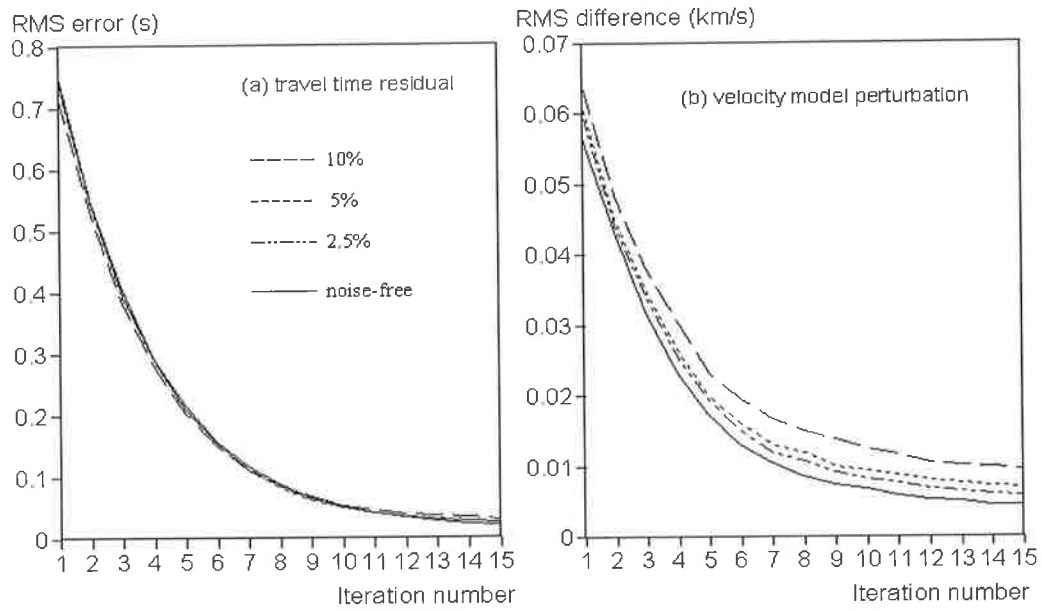

Fig.4.17 The tomographic convergence curves for different noise levels in the velocity model

As discussed above, the program works well in a high contrast velocity field, even with noisy traveltime data, or a corrupted velocity model. Now it is time to test the ability to recover the fine velocity structure in a real 3-D variable velocity model. The velocity model selected in this test is the same as that used in chapter 3 (Fig.3.8). To simulate a real 3-D explosion survey, the model size is extended to 60 km × 60 km in the horizontal plane, and truncated in depth at 16 km. The velocity distribution in a box of

these horizontal dimensions is smooth, and is 3 km/s everywhere at the top surface of the model. The velocity at the model bottom (16 km depth) oscillates between 4.7 km/s and 5.4 km/s, with 10 km being the spacing between minima and maxima (see Figure 3.8 for details). The velocity in the vertical direction increases linearly from top to bottom.

48 sources, 5 km spacing, were located along the top boundary, and 74 receivers lie on the top surface of the model, forming a somewhat irregular seismic network (the 66 receivers were previously used in section 3.4.4 of chapter 3, and another 8 receivers were added to make up the large gap between the receivers). Figure 4.18 shows the locations of the sources and receivers in this test. This is a real 3-D variable velocity model and a suitable example to test for recovery of the fine velocity structure. A cubic cell (2km ×2km ×2km) is selected to divide the whole model, and the number of secondary nodes is set at 6. The damping factor is 0.01. The model-update constraint is the physical constraint. In other word, the velocity cannot be negative, and cannot be larger than the specified maximum velocity value (in this case, the maximum velocity value is set at 10 km/s). Taking the 1-D linear background velocity of the true model as the input model, I obtained the final velocity images after 10 iterations.

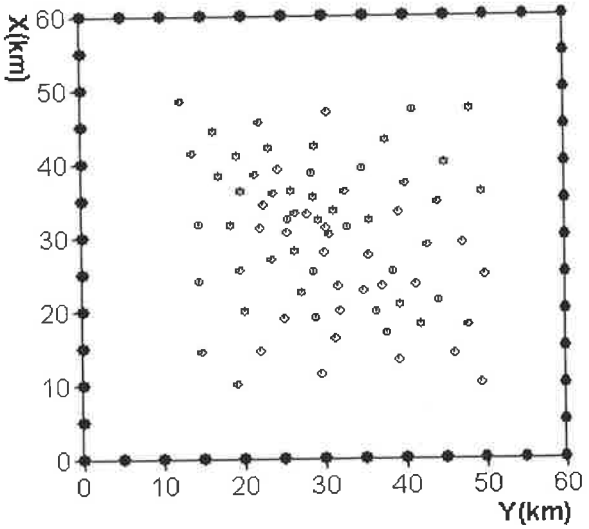

Fig.4.18 Source (black) and receiver (grey) locations in test 6

Figure 4.19 shows the comparison of two different depth slices between the true model and recovered velocity. Even without any filter applied, I obtained nearly the same anomalous patterns as in the true model. The scale of the anomalous velocity pattern increases with the depth, but a relatively small perturbation in each Z plane (similar to a checkerboard test in chapter 10, but more complex in velocity variation).

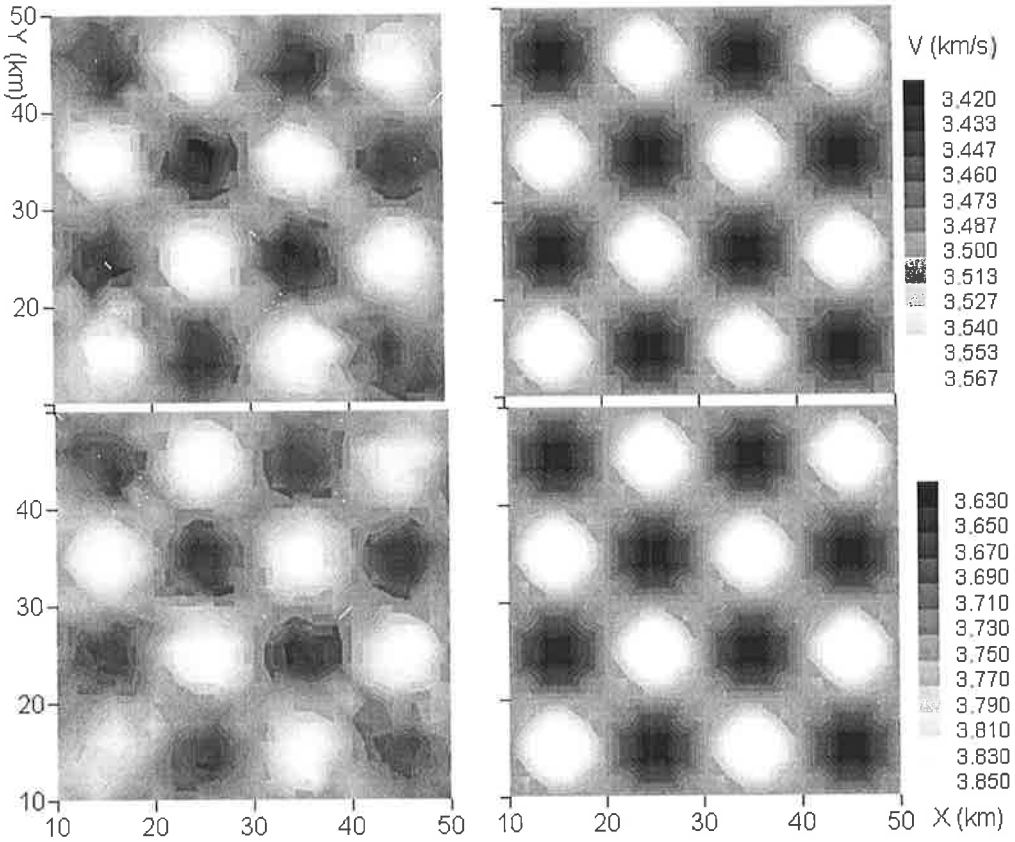

Fig.4.19 The comparison between the true model (right) and recovered velocity (left) (upper: Z=4 km depth; bottom: Z=6 km depth)

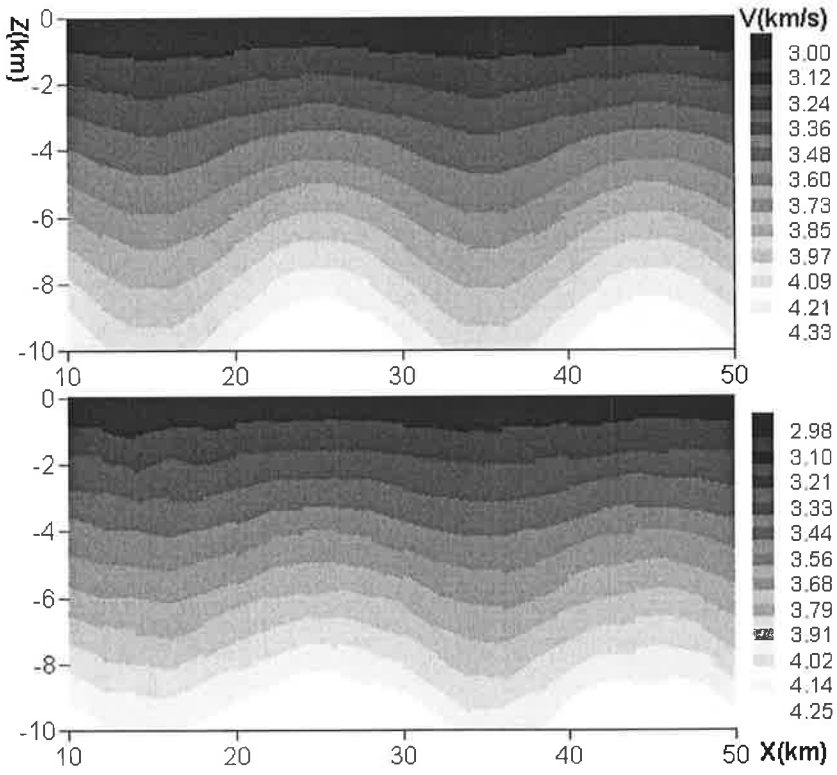

Figure 4.20 The comparison between the true model (upper) and recovered velocity (bottom) at X=24 km cross-section

Figure 4.20 displays the comparison between the true model and recovered velocities in one X-direction cross-section. Very similar velocity variation patterns were obtained along this cross-section, but the recovered strength (magnitude) is slightly smaller than that of the true model. Due to the relatively short source-receiver distance and restricted source location on the top boundary of the model, there are few rays that pass below 10 km depth. Hence I cannot recover the velocity field well below 10 km depth. To do so, would require relatively large source-receiver distance, and corresponding deep raypaths.

4.8 Conclusions

I first discussed the constrained minimum norm and least squares problem in non-linear inversion and then introduced a linearized solver: DMNLS-1 and explained how it works to solve the non-linear problem. Secondly, I defined an analytical Jacobian matrix and showed how to get the elements (derivatives of time with respect to velocity changes) of the Jacobian matrix. Finally, I performed six numerical tests to evaluate the capability, accuracy, sensitivity, and efficiency of the inversion algorithm. The capability of the algorithm means that the method can handle sudden changes in high velocity contrast media (say more than 20%) without losing accuracy and any extra computational effort. This means the inversion algorithm is a non-linear inversion solver. The accuracy of the algorithm indicates that the inversion method can recover the velocity anomalies in all three ways: location, size and strength, although the latter is not well recovered. The sensitivity of the inversion procedure shows that the method can still work well for tolerable conditions of travel time errors introduced, such as onset time picking error, background random noise or uncertainty in the velocity model estimation. This is promising for practical usage. The efficiency of the algorithm is that this approach can obtain a reasonable image with a moderate number of cells and nodes for fewer than in the "standard" method. The image quality can be improved by increasing the ray angular coverage (increasing the number of secondary nodes in each direction, and therefore improved accuracy of the computed travel times) while the number of cells remains unchanged.

The image quality cannot be guaranteed if the travel time error is high. The timing error mainly arises from the picking error (especially, if the background level of random noise is high or the later arrivals are buried in the strong coda of earlier arrivals), unsuitable model division and an incorrect timing system. I have carried out two numerical simulations to test and analyze the effect of these two former kinds of time errors. But the latter error is a systematic timing error and has no random noise feature. It must be treated in a different way. The purpose of the following Chapter is to deal with this kind of systematic timing error and to try an alternative approach (that is, relative arrival time tomography) to obtain a reasonable image without losing accuracy.

Chapter 5: 3-D Relative Arrival Time Inversion

5.1 Introduction

The collection and processing of the correct arrival times is an important factor in travel time tomography. For example, Squires et al (1992) investigated the effects of static timing errors on tomographic velocity reconstructions. Interestingly, they found that the local static error indirectly influenced ('contaminated') the result in other areas of the tomogram. Their results showed that travel time errors of 2 percent could cause tomographic velocity errors of up to 7 percent. The study by Pratt et al (1993) in an anisotropic medium found that it was impossible to completely resolve the distribution of rock properties at all scales and that it is a difficult and ill-posed problem, with a high level of ambiguity. External roughness constraints were used to make the problem better posed. Later, Squires et al (1994) applied borehole transmission tomography to real world data, Exxon's Friendswood datasets, whilst improving the accuracy of the standard algorithm by simultaneously inverting for velocity and statics. Cao and Greenhalgh (1995) presented a similar method, applied to tomographic delineation of mineral deposits. Wang and Pratt (1997) investigated the sensitivity of seismic traveltimes and amplitudes in the context of reflection tomography, while Dorren and Sneider (1997) analysed the error propagation due to linearization in non-linear delay time tomography. Gruber (1998) also discussed the influence of data error on final imaging results. He concluded that the velocity contrast might be masked by relatively large data errors. In this situation the inverted image may not give the true distribution of the velocity field in the target areas having a relatively small velocity contrast. To some extent one can say that a good dataset is a critical factor in reconstructing the true velocity features.

In many practical applications, only the arrival time information is available, and there is no exact knowledge of the velocity model (only the roughly estimated velocity field may be obtained) underneath the seismic array. The source positions are known in cross-hole experiments, or explosion surveys, but not in seismo-acoustic emission measurements, or in earthquake recordings. Without precise information on the velocity field, the estimated source origin time in the location procedure has a large time uncertainty. This means that the travel time information obtained from the location process has a time delay or advance (DC shift). In such circumstances, traditional traveltime tomography cannot be reliably applied. To overcome the source parameter uncertainty, one must eliminate or separate out the source contribution (such as source strength in waveform inversion or source origin time in ray tomography). For example, waveform inversion with unknown source and receiver functions was attempted by Frazer et al (1997) and further discussed by Frazer and Sun (1998). Dobroka et al (1992) proposed a double-trace scheme for seismic ray tomography. In double-trace ray tomography, the measurable data are the arrivaltimes relative to the reference station. Thus the source origin time can be eliminated. But this will introduce another timing uncertainty (systematic time shift) and thus destroy the relative time pattern among the receivers if the selected reference station has the incorrect arrival time (as demonstrated below).

The concept of 'relative arrival time' has been widely used in earthquake location (for example, Fremont and Malone, 1987; Got et al., 1994; Waldhauser and Ellsworth, 2000). Waldhauser and Ellsworth (2000) used the so called 'Double-difference' method (DD), which can also be used in simultaneous inversion for determining both the velocity model and the source hypocenters in a relative sense (e.g., Thurber, 1999). In the DD method, the basic assumption is that events i and j have a common ray path to receiver k, so that it is possible to directly compare the observed arrival time differences with the calculated theoretical arrival time differences between events i and j for the common receiver k. Such an assumption is a valid approximation when the distances between sources are close, or the source-receiver distance is large compared to the scale length of the seismic network. Zhao and Thurber (2003) attempted to take into

consideration a 'common ray path' (previously neglected in the DD method) to achieve absolute event location in simultaneous inversion.

Alternatively, for 'relative arrival time' tomography, there is a simple, but more physically meaningful solution, as demonstrated later. That is, relative arrival time tomography referred to the minimum arrival time or referred to the mean arrival time.

Basically, the source origin time uncertainty (or receiver function uncertainty) in a ray tomographic experiment can be ascribed to the following two kinds of arrival time errors: (1) the arrival time at a certain station has a systematic time delay (or advance) to consecutive events over a fixed period (receiver function uncertainty); (2) some events have incorrect origin times or mis-locations of the hypocenters (source parameter uncertainty), which result in another systematic arrival time delay (or advance) to all recorded stations.

For the first kind of systematic timing error, specific to a single station, one usually deletes such data if it cannot be adjusted to the correct time (due to a lack of timing accuracy of the station). For the second kind of systematic timing error, the best way to proceed is to adjust the origin time or hypocenter co-ordinates by a relocation process, but sometimes it is impossible to restore the data to the correct time due to a lack of some basic information. For example, a lack of a suitable velocity model underneath the stations precludes reliable relocation. For simplicity, one may delete such data, but this means severe loss of data coverage in many cases, because the recorded information is unobtainable again for natural earthquakes. The question arises as to what else can be done in such a situation. Is there another way to get the image without losing the data coverage? The answer lies in relative arrival time (as opposed to absolute travel time) tomography.

5.2 Relative Arrival Time Tomography

The second kind of timing error discussed above has an important property. That is, it is invariant with distance. There is a constant DC shift (time delay or advance) to the T-D curve, which means that a simple static adjustment (time added or subtracted to all records) for a certain event will adjust them to the correct arrival times. The relative

time difference between two recording stations is constant, no matter what time (arrival time or travel time) is used to calculate the time difference. This means that there is a definite distribution pattern of the time differences among the recorded stations for a certain event, which is entirely dependent on the velocity distribution underneath the seismic array and the epicentral distances from the source to the receivers, and also the relative distances among the receivers. The velocity field does not change for different events, but the relative distances and raypaths do. Thus one expects that different events will have different patterns of time differences among the stations. Therefore, it is possible to use the different patterns of time differences for various events to reconstruct the velocity field. Different velocity media will provide different patterns of time differences among the recording stations. This is the basic principle to apply for arrival time tomography. Theoretically, one can distinguish two kinds of relative arrival time tomography: one is according to the minimum arrival time; the other is according to the mean arrival time. To some extent, one can say that arrival time tomography is 'relative arrival time tomography'. This is explained below.

5.2.1 Methodology

The relative time, defined through the minimum arrival time (or mean arrival time), can be written as:

$$T_j^i(R) = T_j^i(A) - \min \sum_j^{N_i} T_j^i(A), \quad i = 1, M \tag{5.1}$$

$$\text{or} \quad T_j^i(R) = T_j^i(A) - \frac{1}{N_i} \sum_j^{N_i} T_j^i(A), \quad i = 1, M \tag{5.2}$$

where i represents the $i-th$ event, j represents the $j-th$ station, N_i is the total number of stations that recorded the $i-th$ event and M is the total number of events. $T(A)$ and $T(R)$ are the arrival time and relative time, respectively. That is, the arrival time is re-arranged to a relative time either according to the station that has the minimum arrival time, or according to the mean arrival time across the stations. For different events, the 'minimum station' (the relative time at this station is zero) or the 'mean arrival time' is different. That is to say, the relative time is unchanged if the

arrival time contains a positive or negative time shift error (or uncertainty) for a given event.

5.2.2 Analytical Jacobian matrix

The analytical Jacobian matrix has a somewhat different form in relative arrival time inversion. On the definition of relative time according to the minimum arrival time, the calculation of the elements (the derivatives of time with respect to the velocity changes) of the Jacobian matrix is not based on the original ray paths, but on the relative ray paths ($RT_i^{i'}$ or $RT_j^{j'}$), where i or j represents the i-th or j-th receiver, other than the receiver ($R_{\min}$) that has minimum arrival time. A 2-D explanation is given in Figure 5.0. Cognizant of the constant 'min-wavefront' (which has the same arrival time as the minimum receiver) for each source, but noting that different 'min-wavefronts' exist for different sources, the integration is along the relative ray path $RT_i^{i'}$ (taking the i-th receiver as an example), as shown in Figure 5.0. The relative time ($t_i^{i'}$) along the relative ray path ($RT_i^{i'}$) is given by:

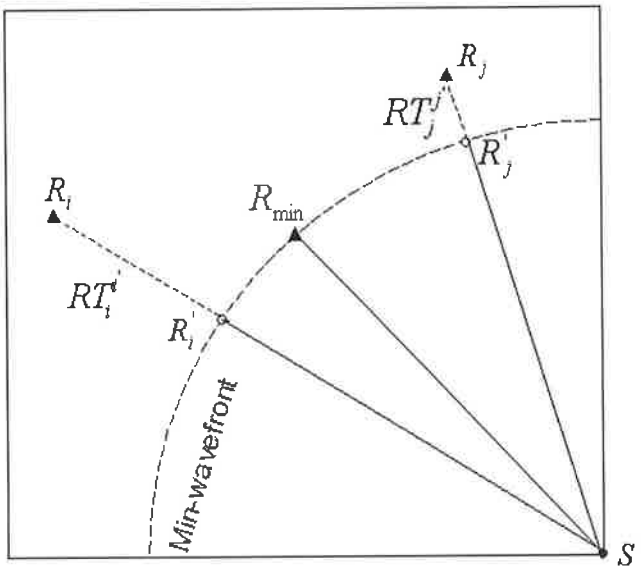

Fig. 5.0 Explanation of relative ray path in the 2-D case
S: Source; R: Receiver
$R_{\min}$: Receiver has Min-arrival time

$$t_i^{i'} = \int_{RT_i^{i'}} \frac{ds}{V(x,y,z)} = \int_{R_s^{i'}} \frac{ds}{V(x,y,z)} - \int_{R_s^{i}} \frac{ds}{V(x,y,z)} \qquad (5.3)$$

Therefore the derivative of time with respect to velocity changes along the relative ray path includes two parts:

$$\frac{dt_i^{i'}}{\partial V} = -\int_{RT_i^{i'}} \frac{\frac{\delta V}{dV}}{V^2(x,y,z)} ds = \int_{R_s^{i'}} \frac{\frac{\delta V}{dV}}{V^2(x,y,z)} ds - \int_{R_s^i} \frac{\frac{\delta V}{dV}}{V^2(x,y,z)} ds \qquad (5.4)$$

Here $RT_i^{i'}$ is the relative raypath along the i-th raypath. The R_s^i and $R_s^{i'}$ are the ray paths from the source to the i-th receiver and the 'i'-th predicted min-receiver' that has the same arrival time as the minimum arrival time receiver, respectively. With the arrival time at the minimum receiver ($R_{\min}$) in hand, one can easily determine the 'predicted min-receiver' that has the same arrival time as the minimum receiver along any raypath. It is worth pointing out that the 'min-wavefront' is not a smooth circular curve in the 2-D case, nor is it a smooth spherical surface in the 3-D case, due to the non-uniform velocity distribution.

I have already shown in Chapter 4 how to calculate the elements of the analytical Jacobian matrix. Thus it is only necessary to subtract the contribution of the time derivative with respect to changes in velocity along the 'minimum ray path' for a given source to obtain the time derivative to changes in velocity along the relative ray path.

For the definition of relative time according to the mean arrival time, the only difference from minimum-arrival time tomography is to replace the minimum index by the mean index in the previous formulation. In the analytical Jacobian matrix, instead of removing the contribution of the derivatives of time with respect to velocity changes along the 'minimum ray path', here the mean time derivative according to each source is subtracted. Due to the different mean values for different sources, I calculate the elements of the Jacobian matrix in three steps: (1) obtain the elements of the Jacobian matrix as in travel time tomography, (2) find the mean value for each source, and (3) subtract the mean value for each source and obtain the time derivative to velocity change corresponding to the mean-arrival time.

5.2.3 The comparison between travel time and minimum-arrival time inversion

To test the efficiency and accuracy of this approach, and also to compare with the results of travel time tomography, an identical model to that used in section 4.7.3 of Chapter 4 (numerical test 3) was selected. This is a model that has high velocity

contrast anomalies (more than 20% velocity contrast against the background velocity) embedded in a 1-D layered velocity function. Figure 5.1 shows the two unfiltered images obtained from travel time and arrival time tomography referred to the minimum arrival time. To make the comparison, the model parameters and starting velocity model are the same as in numerical test 3 of section 4.7.3. Even the hard bounds and the damping factor are the same as before.

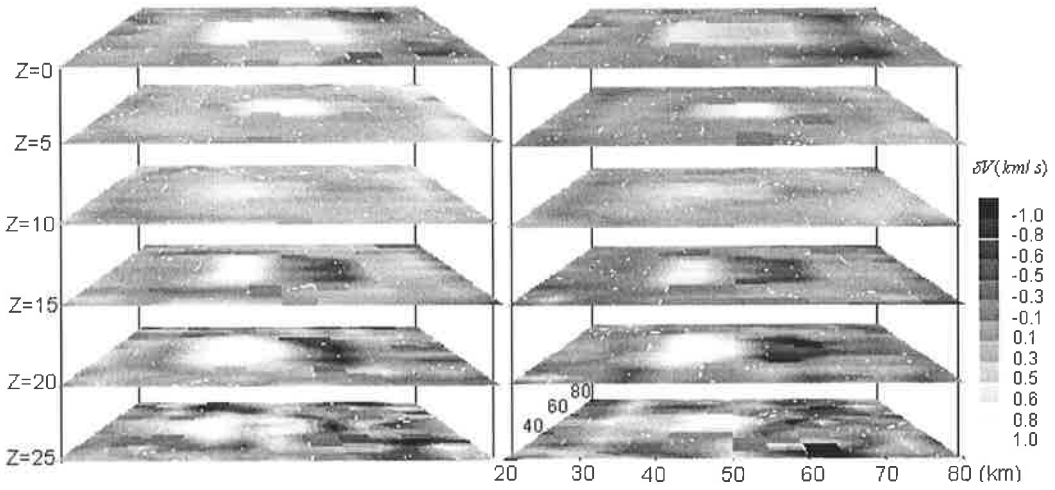

Fig.5.1 The comparison of unfiltered images between travel time (left panel) and relative arrival time (right panel) tomography in high contrast velocity media

From Figure 5.1 it can be seen that the two images are nearly identical. The anomalies are recovered in both cases and it is not possible to determine which one is the better image. This is a good example to show the effectiveness of minimum-arrival time tomography. The results indicate that minimum-arrival time tomography is comparable to travel time tomography, even for high contrast velocity media.

Figure 5.2 is a comparison between the two sets of convergence curves for the time residual and the model perturbation. The convergence level for both the time residual and the model perturbation reaches the same level for both cases, regardless of the starting point. The decay curves exhibit a similar trend with increasing iteration number in both cases and show negligible improvement after the 15-th iteration.

In real world situations, the relative time difference referred to the minimum station may have large scatter (sometimes, such datasets will affect the sensitivity of the inversion) when the geometry of the seismic network is comparable to the source-receiver distance. In such circumstances, it is possible to select the station that

has the shortest distance to the geometric center of the seismic network as the reference station (similar to the minimum station) or to use the mean arrival time as the reference (discussed later) to avoid the occurrence of such problems.

So from a theoretical perspective, one can apply minimum-arrival time tomography to real problems and obtain a satisfactory result. But in practical applications, there is another problem that must be considered. It is that the arrival time at the 'minimum station' must be the correct time. Otherwise, it will introduce another systematic timing error in the relative time database. It is worth pointing out that this kind of systematic timing error, introduced by an incorrect time at the 'minimum station', destroys the original distribution pattern of relative time differences between the recording stations so that it cannot be treated in the same way as before. In such circumstances, one must find another way to avoid this problem. That is, to use relative arrival time tomography according to the mean arrival time.

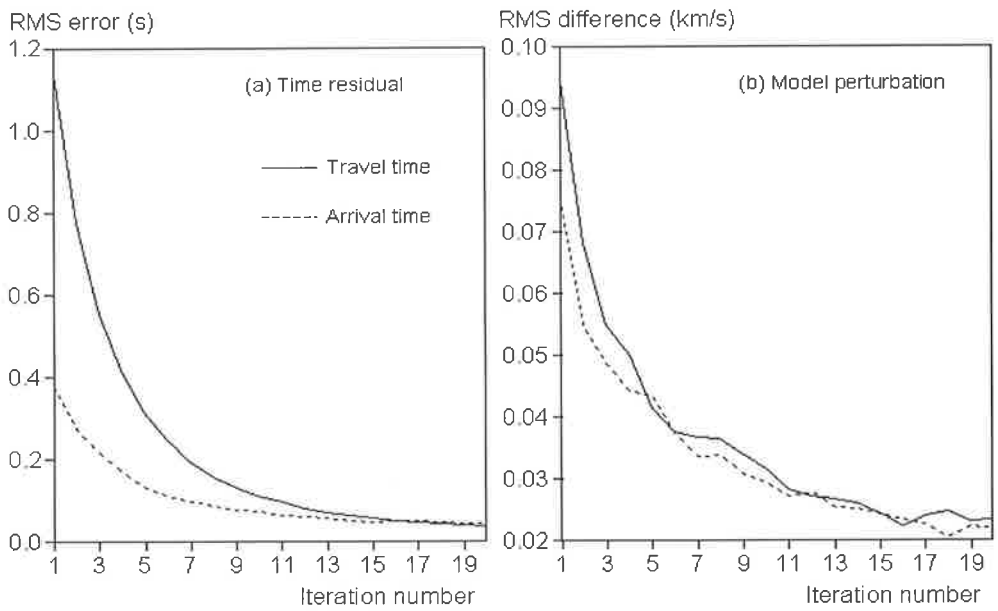

Fig. 5.2 The comparison between the convergence curves of travel time and relative arrival time tomography (referred to minimum arrival time) in high contrast velocity media

5.2.4 The comparison between travel time and mean-arrival time inversion

To overcome the problem with an incorrect arrival time at the 'minimum station' or to avoid creating large scatter in the relative time dataset, it is possible and reasonable to obtain the relative time according to the mean arrival time between stations.

To make a comparison with the image of arrival time tomography according to the minimum arrival time, the same model parameters and constraints were used as in numerical test 3 of section 4.7.3. Figure 5.3 shows the three un-filtered images obtained from travel time tomography and the two kinds of arrival time tomography-referred to the "minimum" and the "mean" arrival time. The three images are almost identical. There is no preference for one over the other.

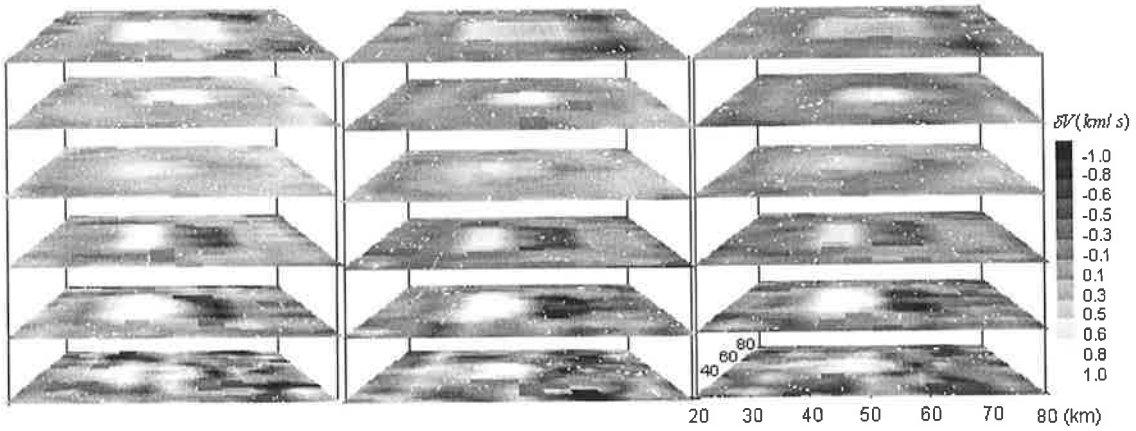

Fig.5.3 The comparison of three un-filtered images between travel time (left) and two arrival time inversions (middle: referred to minimum time; right: referred to mean time)

Figure 5.4 displays the associated convergence curves. Both the time residual and the model perturbation have the same convergence trend, regardless of the starting point, except there is a small amount of fluctuation in the model perturbation. The curves flatten to a nearly equal constant value after the 15-th iteration. These are very important results, because I started from different formulations (physical background) and obtained nearly identical images. The reason is very simple: the relative time distribution pattern among the stations is unchanged regardless of which time information (travel time or arrival time) is used. This unchanged relative time pattern among the recorded stations is dependent on the velocity structure beneath the stations.

Recall that the arrival time is the sum of the travel time and the origin time. In some circumstances (for example, when arranging arrival times according to the minimum arrival time or the mean arrival time), the influence of the origin time can be separated from the arrival time information. Therefore, the 'min-arrival time' or 'mean-arrival time' is just another expression of travel time. Theoretically, arrival time tomography should exhibit similar behavior to travel time tomography, such as insensitivity to noise,

accuracy improvement with increasing ray angular coverage, and also the capability to handle high velocity contrast media, as discussed in chapter 4. The latter has already been tested. Here I will test the sensitivity and accuracy. For reasons of space economy and applications to the real world ('mean-arrival time' is more applicable than 'min-arrival time'), in the following sections I will only analyze and discuss arrival time tomography referred to the mean value.

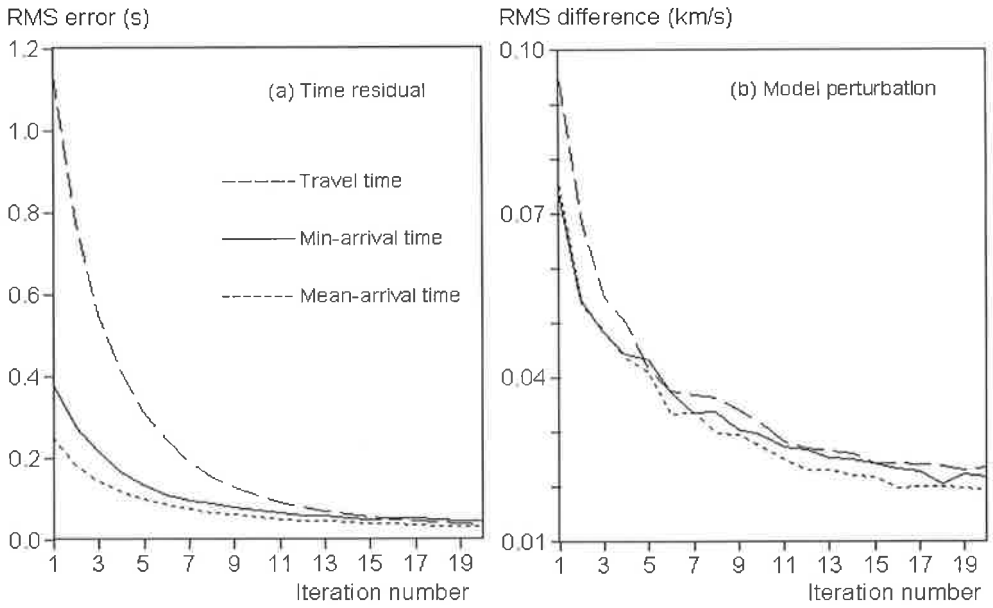

Fig.5.4 The comparison of convergence curves for the three different seismic inversions

5.3 Numerical Tests and Results of Analysis

5.3.1 The accuracy of arrival time tomography

To facilitate comparison with results of travel time tomography, exactly the same model and the same parameters (such as constraint bounds, damping factor and input velocity model) were selected as in numerical test 3 of section 4.7.3. The only difference is that in this case arrival time tomography, rather than travel time tomography, was undertaken, to recover the 3-D velocity images.

Figure 5.5 shows the un-filtered images obtained using both travel time and arrival time inversion at different Z planes (Z=0, 5, 15 and 20 km). It can be seen from the figures that nearly identical images are recovered; both yield the anomalous velocity structures quite well. Arrival time tomography (like travel time tomography) recovers the location, shape and strength of the various velocity anomalies. The recovered

anomalous strength is +0.54, +0.76, -1.14 to 0.83 and -1.08 to 1.21 km/s at the planes Z=0, 5, 15 and 20 km, respectively, which is very close to the recovered anomalous strength (+0.54, +0.82, -1.2 to +0.8 and -0.97 to +1.19 km/s at Z=0, 5, 15 and 20 km) from travel time inversion. There is no evidence to tell which results are better: travel time or arrival time tomography.

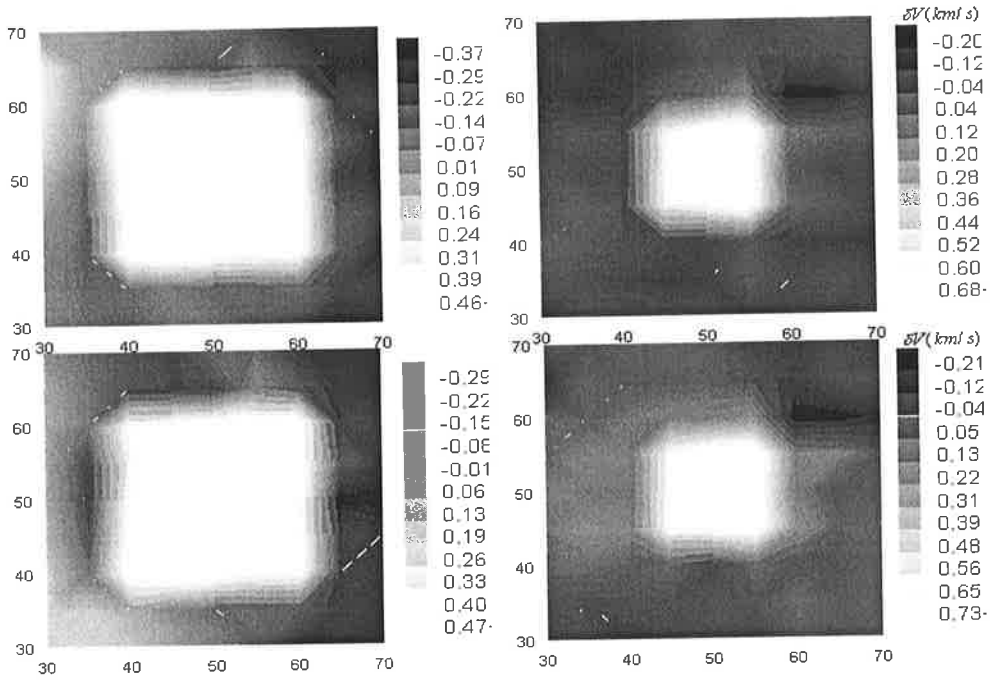

Fig.5.5a The un-filtered images between travel time (bottom) and relative arrival time inversion (top) at the planes Z=0 km (left) and Z=5 km (right)

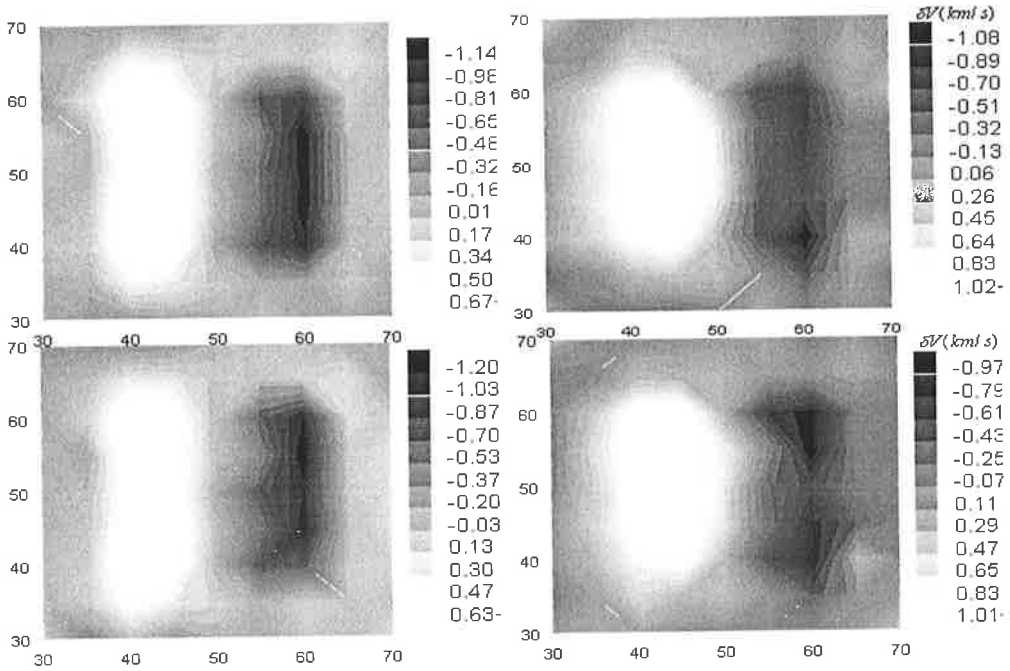

Fig.5.5b The un-filtered images between travel time (bottom) and relative arrival time inversion (top) at the planes Z=15 km (left) and Z=20 km (right)

Figure 5.6 shows the five different convergence curves (see section 4.5 for details) for travel time and arrival time inversion. Figure 5.6a shows that the perturbation of the velocity model is nearly the same in both cases. The time residual curves start at different RMS errors, but converge to a stable condition after 12 iterations. The convergence of the updated model to the true model and the deviation of the updated model from the input model have nearly the same behavior in each case (see Figure 5.6b). The velocity recovery ratio is very high (over 90% after 15 iterations) for both travel time and arrival time inversion. From these numerical results and from the theoretical analysis above, it can be concluded that arrival time tomography performs admirably, and no worse than travel time tomography in distinguishing the velocity anomalies and in almost recovering the true strength of the velocity features.

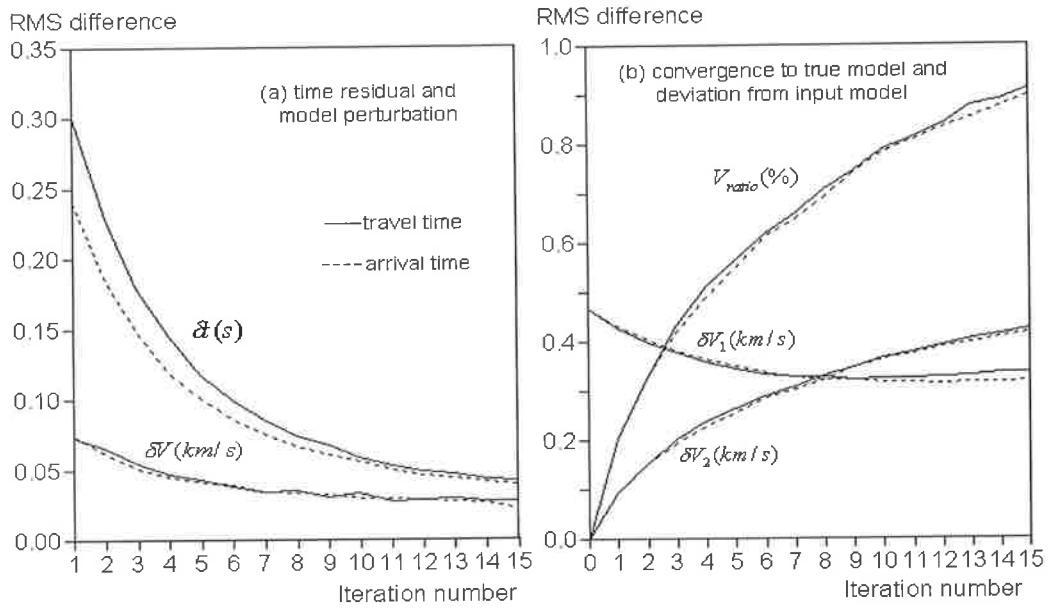

Fig.5.6 The five kinds of convergence curves between travel time and arrival time inversion

5.3.2 The sensitivity to modest random noise

Following numerical test 4 in section 4.7.4 of Chapter 4, the same model parameters and constraints were used to analyze the noise sensitivity of arrival time tomography and compare it with travel time tomography. The noise was added to travel times according to formula (4.18). Figure 5.7 shows the un-filtered images obtained by arrival time tomography for differing levels of noise (i.e., 2.5%, 5.0% and 10.0%).

Image quality is impaired when the random noise level reaches 10.0%, but the anomalies are still visible. A nearly identical image to the noise-free data was obtained when the relative noise level is around 5% or less (an image with 2.5% noise level was not displayed for space economy).

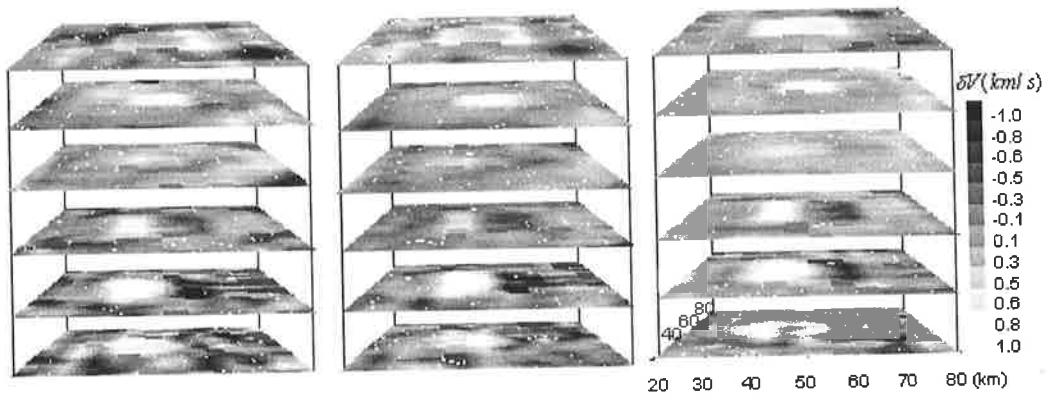

Fig.5.7 The un-filtered images of relative arrival time inversion with different levels of input noise (left panel: 10 %; middle panel: 5 %; right panel: noise-free)

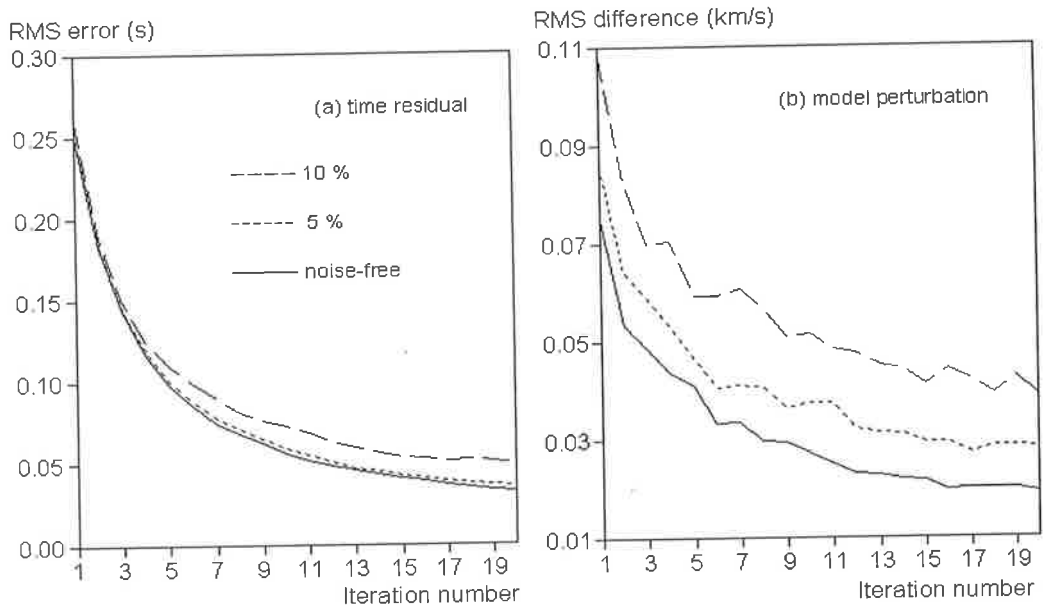

Fig.5.8 The convergence curves of relative arrival time tomography for different noise levels

Figure 5.8 is a plot of the associated convergence curves for the time residual and the model perturbation at different noise levels. The convergence of both the time residual and the model perturbation remains at relatively high levels and oscillates with increasing noise level. The numerical tests also indicate that the quality of the image can be improved with increasing ray angular coverage just as in the case of travel time

tomography in section 4.7.2 of chapter 4. Thus there is no need to further display those results.

5.3.3 The sensitivity to systematic timing error

Since the main purpose in this chapter was to overcome the systematic timing error in travel time tomography due to source parameter uncertainty (such as origin time or hypocentral coordinates) and to fully utilize available travel times, it is necessary to carry out numerical simulation tests for such errors and to assess the performance under such conditions. For this purpose, I first created a random sequence within the range ± 1.0, and then added a *relative systematic timing error* (time delay or advance) to the travel time data subset of a specified source according to this random sequence. That means I moved the origin time of each source back or forward a random time interval so that the subset travel times for a specified source are all delayed or advanced by the same amount. In the different subset travel times (for the different sources), the random time interval is different and dependent on the random sequence and the mean value among the subset travel times.

The velocity model, source and receiver deployment are the same as numerical test 3 of section 4.7.4. Again the damping factor is 0.01 and the model update constraint is ± 1.5 km/s. The relative strength of the systematic timing shift error is 10%, 20% and 50%. For the 10% timing error, the maximum time delay is 2.2944 s and the time advance is 1.2712 s; for the 20% timing error, the maximum time delay is 2.5424 s and the time advance is 4.5889 s; for the 50% timing error, the maximum time delay is 11.4722 s and the time advance is 6.3560 s. Figure 5.9 displays the filtered images with these different levels of systematic time shift errors. Nearly identical images were obtained, regardless of the error. Such features can be further tested and very similar convergence behavior is observed. Figure 5.10 shows the convergence curves with the different systematic timing errors introduced to the travel time dataset. It is hard to distinguish one curve from the other in the convergence of the time residual (left panel in Fig.5.10). The same oscillatory behavior is found in the convergence of the updated velocity model (right panel in Fig.5.10). The results are exactly as expected. That is, to use relative time data, any systematic timing error disappears.

The results of the numerical tests indicate that relative arrival time tomography is the best way to proceed when the travel times include a large source parameter uncertainty (such as origin time or hypocentral coordinate error) or there are only arrival times available. In such situations, one can forget using travel times and directly use arrival times to tomographically process the data on the condition that the arrival time dataset has a consistent time-distance relationship.

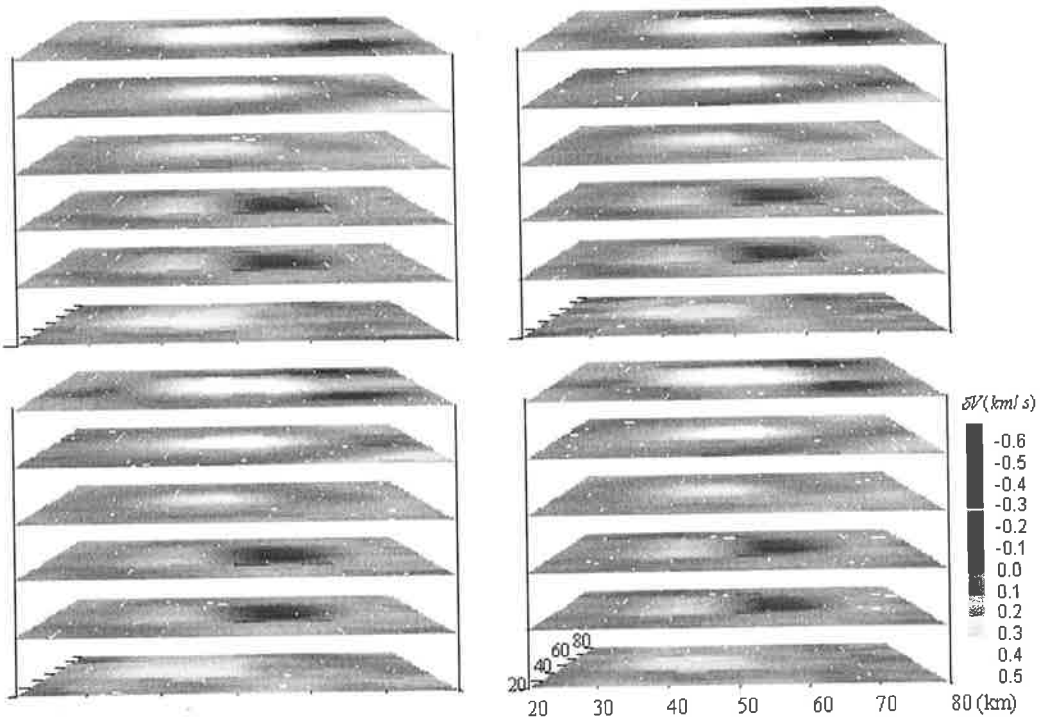

Fig.5.9 The comparison between the filtered images with different systematic time shift errors (upper left: 50%; upper right: 20%; bottom left: 10%; bottom right: error-free)

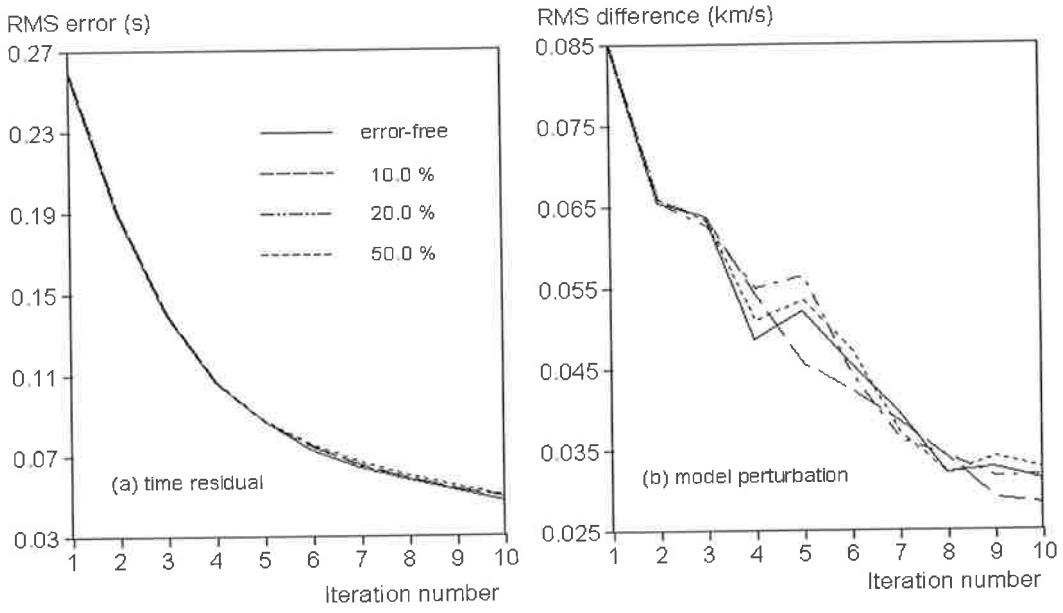

Figure 5.10 The convergence curve comparisons with different systematic timing errors (left panel: time residual; right panel: velocity model perturbation)

5.4 Conclusions

It was shown that arrival time tomography is able to obtain as good an image as travel time tomography, even for high velocity contrast media and for noisy data, such as random timing fluctuations or systematic timing errors. This is a very promising approach and has wide application to real problems, where there are often problems with only roughly estimated source parameters (including the hypocenter coordinates and the origin times) due to the lack of a suitable velocity model to locate them. In such cases, arrival time tomography is the preferred choice over travel time tomography. Theoretically, there is little difference when arrival time tomography is referred to the minimum arrival time, or the mean arrival time. But in practical situations, arrival time tomography according to the mean arrival time is preferred because it avoids the possibility of systematic timing errors introduced by incorrect times on the 'minimum arrival time station' or the creation of large scatter of the relative time dataset due to comparable geometry between the seismic network and the source-receiver distances.

I have completed the theoretical development and numerical tests for 3-D travel time or arrival time tomography. There is no difficulty, in principle, in dealing with the 3-D inversion problems, not withstanding favorable station / source coverage and acceptable levels of noise. But for real 3-D problems there is another issue; it is not the algorithm itself, but the computational demands. Sometimes, it is theoretically feasible, but computationally intractable, to perform very large-scale 3-D inversion. In practical problems, one often needs to know the fine velocity structure under a small region (such as in oil exploration, or imaging a volcanic structure, or outlining mineral deposit), but it is desirable to include as many sources as possible to guarantee the data coverage. In some cases, it is required to image deeper velocity structure (such as in the case of Rabaul volcano). In such circumstances, one has a relatively dense seismic array placed across a small region, with a wide range and large scale of source locations. This begs the question as to what should be done with such a large model. **Is there a sensible computational approach to obtain a reasonable velocity image?** I tackle this question in the following Chapter, where the procedure of seismic tomography is separated into two (or more) steps. A numerical example is given to show how to use

additional regional earthquake data to reveal the deeper, local velocity structure of the crust. This is a promising idea, because the data coverage for a local target is generally good on a large-scale (say regional scale) survey, but there have been few application of incorporating such data to reconstruct the local, deep velocity model (especially in 3-D), mainly due to the computational limitations.

Chapter 6: 3-D Synthetic Case Studies: Multi-Step Travel Time Inversion

6.1 Introduction

Faced with the difficulty of restricted source and receiver geometry for obtaining local deep velocity structure, and the limitations of first arrivals only, there has been increasing interest in making use of more available data, especially including regional events and teleseisms (for example, Lyer and Dawson, 1993; Gresilaud and Cara, 1996), or supplementing with additional sources (for example, Chiu and Stewart, 1987; McGaughey and Singh, 1997). In principle, through inclusion of regional events (or teleseisms), it is possible to obtain more information on deep velocity structure, but still on a local scale.

The problem is that one must create a large 3-D velocity model to include as many regional events as possible, with a dense cell size, comparable to the local station density (say, less than a few kilometers). With such a model, it is difficult or sometimes impossible to invert for the 3-D velocity field due to the computational demands (a supercomputer is required), or the excessive number of velocity unknowns. This in turn slows the convergence rate and even worse, may stall the convergence process. Alternatively, increasing the cell size or using a non-uniform cell size (see, for example, Michelena & Harris, 1991; Sambridge et al., 1995; Vesnaver, 1996; Lin and Roecker, 1997; Widiyantoro and Van der Hilst, 1997) will make the problem tractable, but with a loss of resolution or at the expense of introducing travel time errors as demonstrated in chapter 4 and to be further tested later in this chapter.

Meanwhile, there are two factors which need to be considered in the model design when performing 3-D travel time tomography: (1) the cell size has to be comparable to the station density; (2) the total number of cells (roughly equal to the total number of velocity unknowns in the inversion) must be comparable to the total number of ray

paths. Otherwise, the inversion problem may lose resolution (condition 1 is not satisfied) or becomes non-unique and ill-conditioned due to an excessive number of unknown parameters to be solved for in the inversion (condition 2 is not satisfied).

To overcome the first problem, one can use a non-uniform cell (for example, a tetrahedral cell) size model to maintain a relatively high resolution and to best fit the station density in the target region. That is, a fine cell size in the target model, and a coarse cell size outside the target (for example, Thurber, 1987; Sambridge and Gudmundsson, 1998). I call this a non-uniform cell model (NUCM).

To overcome the second problem, one can constrain the updated velocity process within the target volume, perhaps by using a small partial model in the whole model to reduce the large number of unknowns (for example, Roecker, 1982; Eberhart-Phillips, 1990). In this way, the velocity field is updated in the target part of the model only and the other parts of the inverted model are left unchanged. In turn, one can also constrain the velocity field (for example, the shallow part of the velocity field with the observed velocity value) within a fixed model volume and invert for the rest of the velocity field. I call this a partially inverted model (PIM).

To overcome both problems 1 and 2, one can simultaneously exploit NUCM and PIM approaches. That is, update the target region of the model with high resolution (dense distribution of nodes or cells), and leave the region outside the target with poor resolution (coarse distribution of nodes or cells) unchanged. For example, Thurber (1987) and Eberhart-Phillips (1990) devised one progressive inversion strategy for improving the versatility of the gridding by specifying grid points whose velocity values would remain fixed throughout the inversion. They begin the inversion on a large model with coarsely gridded nodes, and then the coarse-grid inversion results are used as the input model for the final inversion on a finer grid target portion of the model, keeping velocity values fixed outside the target volume.

The above approaches imply a 'multi-step' process. That is, the whole inversion procedure can be separated into two parts: (1) forward modeling in the partial model (outside the target region) in which the velocity field is unchanged; (2) inverting for the target model (embedded in the whole model) where the velocity field needs to be

updated. With this basic idea in mind, I was able to extend the application. The idea is to perform the forward modeling on a large (regional) model to obtain the crossing points where the ray paths intersect the boundaries of the small model volume (which is embedded within the large model), and to compute the related travel times from regional sources to these crossing points, and finally perform tomographic processing on the small model using local events, plus these predicted crossing points as new sources from the regional events. This is how the concept of a 'multi-step' procedure arises.

In practical applications, one wants to exploit as many events as possible to increase the data coverage and one also seeks to combine the local earthquake data with regional data to reveal the local, deep velocity structure as well as the shallow structure. There is a depth limitation when using only local sources. Thus, not only is a relatively large model needed to include as many regional events as possible to increase the data coverage and exploit deep seismic rays, but also a relatively small cell size comparable to the station density on a local scale is required. In such circumstances, it is not possible to compute such a large model to obtain the local fine deep velocity structure without major computational resources. For example, in the revised 'irregular' approach of the shortest-path method for 3-D forward modeling (chapter 3), a moderate-sized model of dimension (500 km, 500km and 100 km), and cell size (5 km, 5 km and 5 km) in the X, Y and Z directions, involving only 4 secondary nodes in each direction of the cell (the minimum distance among the nodes in this model is 1 km) will have 214,221 cells and 12,551,101 nodes. Enlarging the cell size to 10 km (the minimum distance among the nodes is increased to 2 km) and keeping the other model parameters unchanged, will still result in 28,611 cells and 1,613,051 nodes. As discussed in chapter 3, there are at least 5 large one-dimensional arrays with maximum length equal to the total number of nodes, which must be used in the calculations. They consume much computer memory, even if staged in some cases, so it is difficult to run the program. With an automatic model selection function applied (see section 3.5 of chapter 3 for details), it is possible to reduce the maximum length of the one dimensional arrays by half, but still nearly 1 million elements of the one dimensional

array will be considered. In order to overcome the above problems and to reconstruct the local, deep velocity structure from combined regional and local events; one may exploit both NUCM and PIM. But I have proposed an alternative procedure to separate the tomographic processing into two (or more, if required) steps, referred to here as 'multi-step seismic tomography'.

Obviously, multi-step tomography is advantageous over the 'NUCM+PIM' approach both in accuracy and computational efficiency. For example, in the multi-step procedure, one can select a smaller cell size to divide the large model because there is only one forward modeling run, or separate the large model into several sub-regions without dramatically increasing the computational effort to obtain travel times and ray paths to greater accuracy. To reduce the relatively large source parameter uncertainty of regional events in a local sense, one can relocate these regional events in the multi-step procedure, before the final local inversion is undertaken. Theoretically, the information that pertains to the velocity structures on a regional scale is removed after relocation, and only information on local velocity anomalies remains. But in the 'NUCM+PIM' approach, the large uncertainties of regional events can only be partially removed with the simultaneous inversion procedure (that is, to update the velocity model and source parameters simultaneously). In a simultaneous inversion procedure, both the updated velocity model and the source parameters have in a sense only a relative accuracy. There is a trade-off (see chapter 8 later) or coupling effect between the velocity model and the source parameters (Thurber, 1992). Meanwhile, in the final tomographic procedure, there are seldom considerations of both the model division and having an excessive number of unknowns (the large model reduces to a small model). An obvious disadvantage is that this approach, like the 'NUCM+PIM' approach, forces all model perturbations into the target (local, or small) model, so that any travel time errors in the forward modeling within a large model with a coarse grid spacing will be mapped as artifacts in the updated target model. This is especially true when the velocity field outside the target model is poorly estimated. In such circumstance, the best way to proceed is to obtain a relatively smooth, but realistic à *priori* model from the large

model inversion with coarse grid nodes, and then the rest of the process is the same as for the multi-step procedure.

6.2 How to Use Combined Data to Reconstruct a Local, Deep 3-D Velocity Model

With the need to determine a relatively deep, local velocity structure (such as in the case of Rabaul volcano), it is both necessary and feasible to combine the near-regional events with local natural earthquake (or explosion) information. Theoretically, one can select any model with some conditions imposed and obtain the velocity structure at any depth within the limitations of the computer. Whilst generally feasible, in most cases it is not practical due to the restrictions on source geometry, station distribution and computer power. Here only the limitation of the computer was considered. The problem is how to use regional earthquakes as supplementary information to obtain the 3-D local velocity structure within the computer memory limitation and make it applicable to real cases. In other words, how can one make a large 3-D model feasible by a consecutive inversion procedure without losing accuracy?

If one assumes that the background velocity on the regional scale is known (or can be roughly estimated), then one can separate the whole tomographic procedure (the case with a large model length and small cell size) into two (or more) consecutive processes. Thus the multi-step travel time tomographic procedure can be summarized as follows:

- Create the 3-D regional and local velocity model with à *priori* information;
- Predict the new source positions and related travel times with the 3-D regional (known) velocity model;
- Assign the new observed travel times to the new sources;
- Perform tomographic processing on the local velocity model using the combined sources;
- Stop when the RMS errors of both the time residual and the model perturbation meet the specification.

6.3 Multi-Step Travel Time Tomography-Synthetic Example

To test the efficiency and accuracy and to see how the method works, I selected a 3-D regional velocity model (large model) and a local velocity model (small model). I placed 20 regional sources on the top surface within the regional model and 20 local sources near the top boundary of the local model, and 41 receivers with a spacing of $\sqrt{2} \times 5$ km on the top central region of the local model.

Figure 6.1 shows the distribution of the sources and receivers. It also indicates the length and location of both the regional and the local model in the horizontal plane. For the regional model, the sizes of the cell and the model volume in the X, Y and Z directions are 10 km, 10 km, 10 km, and 500 km, 500 km, 60 km, respectively. The number of secondary nodes for the regional model is set at 9 in all three directions. In this model 15,000 and 4,376,061, and the minimum distance between two neighboring nodes is 1.0 km. For the local model, the sizes of the cell and model volume in the X, Y and Z directions are 5 km, 5 km, 5 km, and 100 km, 100 km, 30 km, respectively, and the number of secondary nodes is held at 6 in all three directions. In this configuration, the total numbers of cells and nodes are 2,400 and 336,483, and the minimum distance between two neighbouring nodes is 0.715 km. Figure 6.2 depicts the true regional velocity model (for clarity, only the partial model that relates to the local model was shown, other parts of the model are extensions in the X-Y plane), with which the theoretical travel times (treated as 'observed travel times' later on) are calculated. In

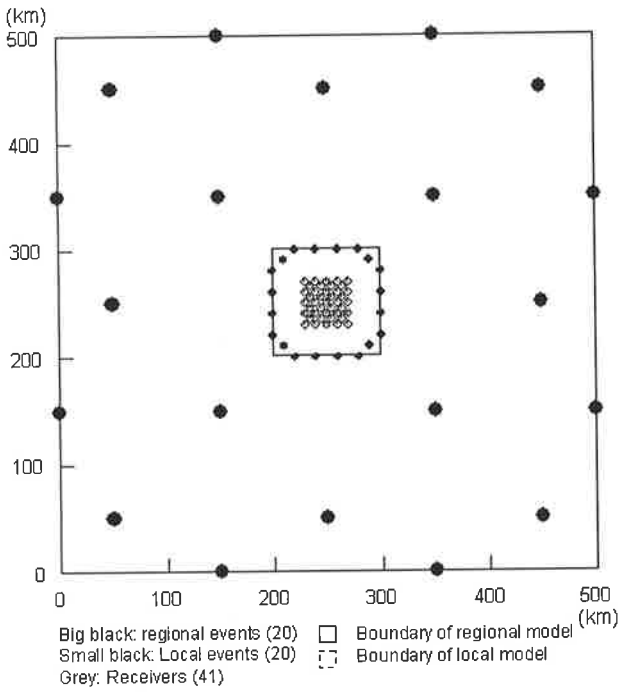

Fig.6.1 The distribution of sources and receivers for multi-step tomography in plan view

this known regional model, I inserted one velocity anomaly on the plane Z=0 (a high velocity anomaly with 25% velocity contrast against the background) and two anomalies on the plane Z=20 km (one high velocity anomaly, one low velocity anomaly, both have a 16.7% velocity contrast against the background). The background velocity is a 1-D layered velocity distribution, as shown in figure.

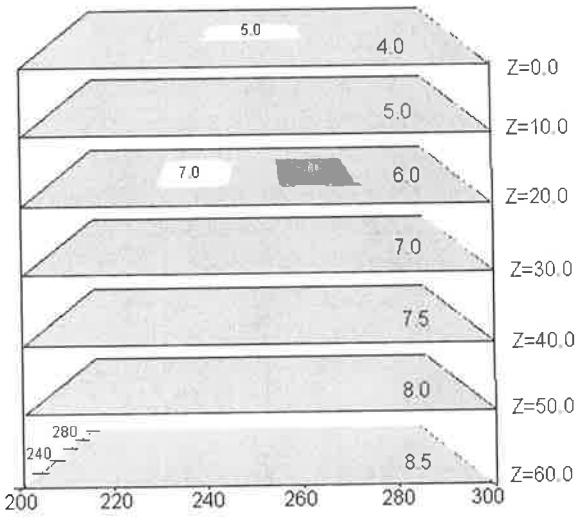

Fig.6.2 Regional model in multi-step tomography

6.3.1 Prediction of the new source positions and related travel times

With the ray tracer from the revised 'irregular' approach of the shortest-path algorithm (see chapter 3), it is possible to calculate the new source positions (the crossing points on the boundary surfaces of the small local model volume) and the related travel times from the regional sources to these new source locations. The original travel times (from regional sources to receivers) minus these new travel times (from regional sources to these new sources) will constitute the theoretical travel time dataset, which will be used as the observed travel times for the inversion on the local model. The problem is that for a given regional source there are a number of such new source positions, depending on the source and receiver pairs, because of the different ray incidence (crossing) points on the local model. In the general case, these new sources for one regional earthquake cannot be assumed to be a single point on the local model. One must be careful when predicting these new source positions because there are two types of crossing point: (1) down-going crossing point (it is possible to intersect the local model volume with an up-going ray again), and (2) up-going crossing point. Thus, the first crossing point along the ray path (from the receiver back to the source) is what is needed, regardless of the up-going or down-going crossing point.

Figure 6.3 is an example showing the positions of the new sources. It only displays five sets of new source positions; the other 16 sets have similar distribution patterns due

to the symmetry of source and receiver locations according to the model. From Figure 6.3 it can be seen that there is large scatter in the new source positions when the rays from a specified original source cross the local model volume. Most are from the bottom of the local model (source 1, 2, and 4 in Figure 6.3); others are from the lateral boundary surfaces of the local model (source 3 and 17 in Figure 6.3).

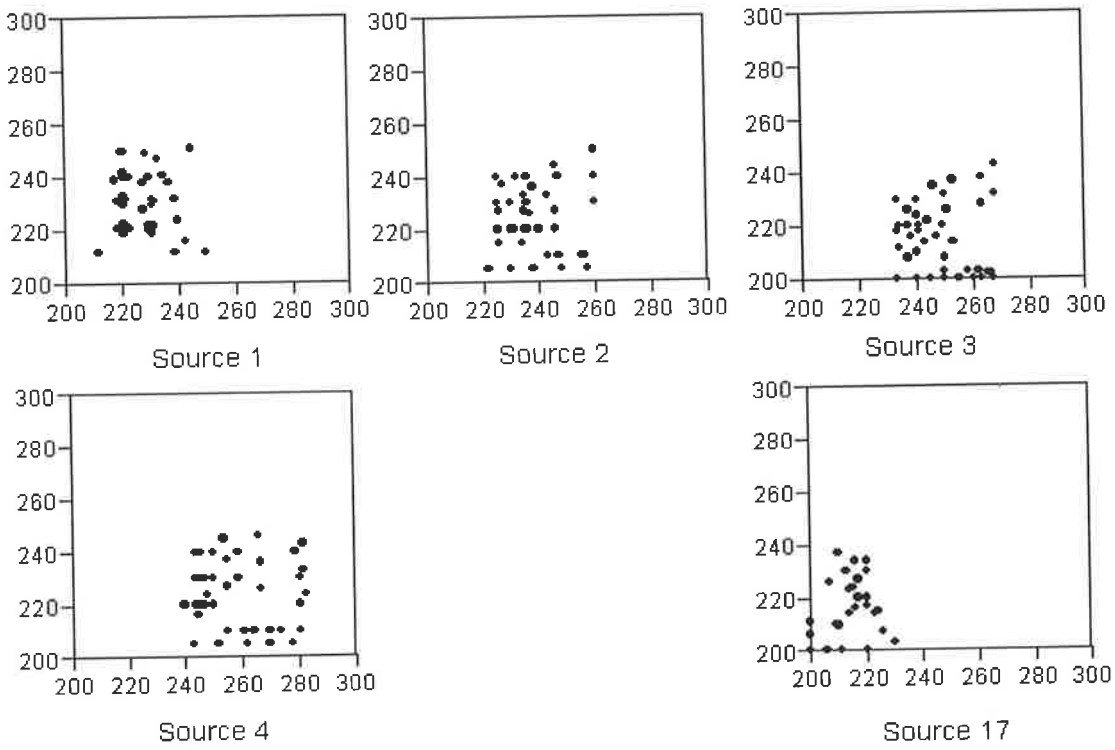

Fig.6.3 The five sets of crossing points (as new sources) on the local model, as an example
The size of the black dot indicates different depths of new sources.
The larger the dot, the deeper the source (from 26 to 30 km).

The position where each up-going ray crosses the local model is dependent on both the velocity field and the epicentral distance. For each original source, there are 41 new source positions on the local model. In this numerical test, there are in total 20×41 new source positions on the local model. In order to avoid changing the original ray paths, and to get a reasonable physical image, the best way to proceed is to use all the crossing points as the new sources for local tomography. For travel time inversion on the local model, I exploited the principle of reciprocity, by looping over the receivers. This saves computer run time with the program due to the large number of new sources generated. In the ray tracing process, it only needs the information regarding traveltimes and raypaths that related to the original source-receiver pair. With a slight

increase in computational effort, it is easy to arrange the calculated travel time data according to the original source-receiver pairs, and sort out the continued ray paths from the original sources. This is the correct data required for the subsequent inversion process. In my experience, this re-arrangement operation only slightly increases the computation time.

6.3.2 Multi-step travel time tomography using only regional data

To evaluate the contribution of regional earthquake information to the multi-step travel time tomography process, I began by using only the source information from the regional sources to reconstruct the local velocity field. In the process of travel time inversion on the local model, a slightly high 1-D layered velocity distribution was taken as the input (starting) model. The deviation from the background velocity of the true model is 0.2 km/s. The velocity values at the planes Z=5, Z=15 and Z=25 km are obtained by linear interpolation between the uppermost and basal plane velocity values from the regional model. The constraint parameters are $a = -2$ km/s, $b = -2$ km/s and $\mu = 0.01$. Figure 6.4 shows the two-step image (the image was filtered with 3-point window and mean value filter) obtained with only the new source data. The high and low velocity anomalies at the planes Z=0 km and Z=20 km are well recovered, both in location and size, but nearly the same velocity anomalies also appear on the neighbouring Z planes. Here a typical 'X-ray' picture was obtained, similar to medical examination, due to the nearly vertical ray paths from the bottom of the local model. In such circumstances, the velocity anomalies are real, but with no depth constraint. That is to say, the velocity anomalies can be moved anywhere along the vertical direction, and it makes little difference to the fit of the travel time residuals. Because the rays from the bottom of the local model are not absolutely vertical, it is still possible to resolve the anomalous patterns at Z=0 and 20 km. This is a useful example to show what can be obtained from regional data. Thus, one can figure out that most rays with nearly zero incidence angle will intersect the bottom surface of the local model volume if the regional sources are far away from the local model and the scale of seismic network is small compared to the source-receiver distance. In such circumstances, one may only

obtain an 'X-ray' type velocity image with nearly parallel seismic ray paths from the bottom 'new sources' to the top receivers.

Figure 6.5 shows the five kinds of convergence curve in this numerical test. After the 10-th iteration, there is not much improvement in the convergence trend. The results indicate that two-step travel time tomography works well, but it needs to incorporate local earthquake data to set a depth constraint and produce a reasonable velocity image.

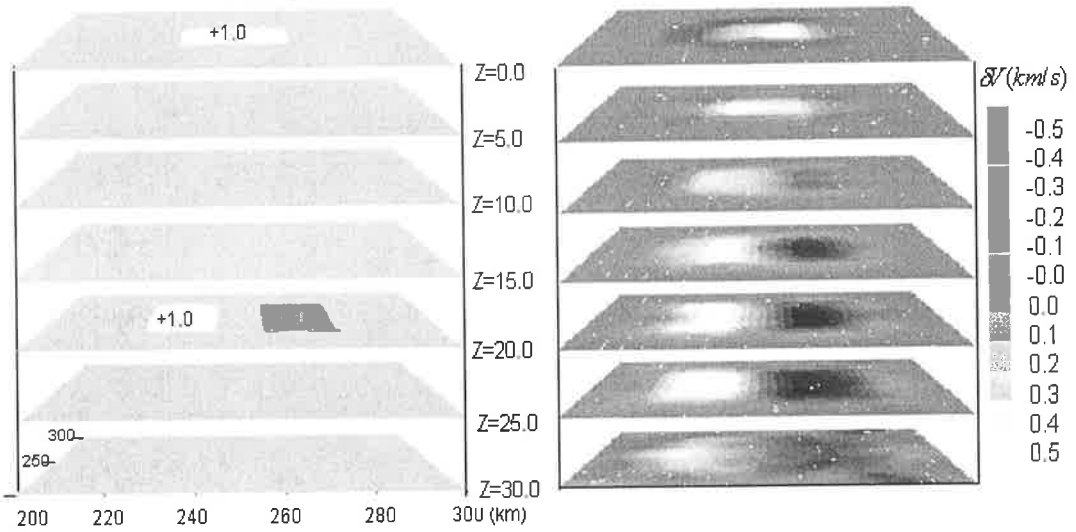

Fig. 6.4 The comparison between the true model perturbation (left panel) and the filtered images (right panel) from the only new sources

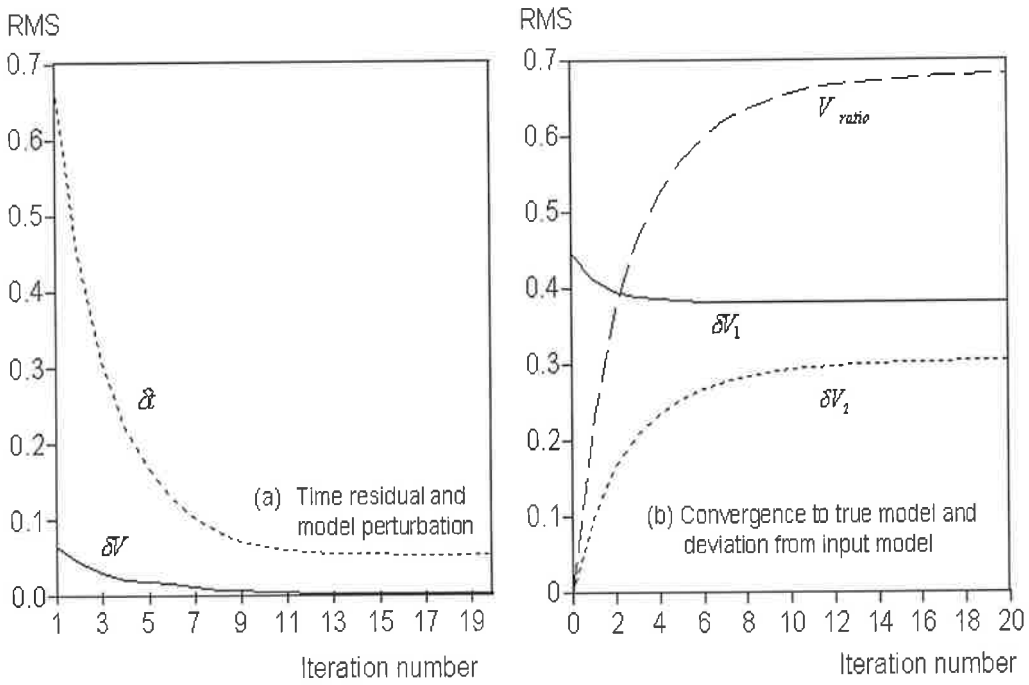

Figure 6.5 The five kinds of convergence curves in multi-step tomography using only the new sources (regional sources)

6.3.3 Multi-step travel time tomography using combined data

To make a comparison with regional data alone, in the next numerical test same velocity model and inversion parameters are used, but the local event data (see Figure 6.1 for details) are included in the multi-step tomographic process. Figure 6.6 is a comparison between the true model, and the tomographic image (same filter routine was applied as Fig.6.4) from the combined (local +regional) sources.

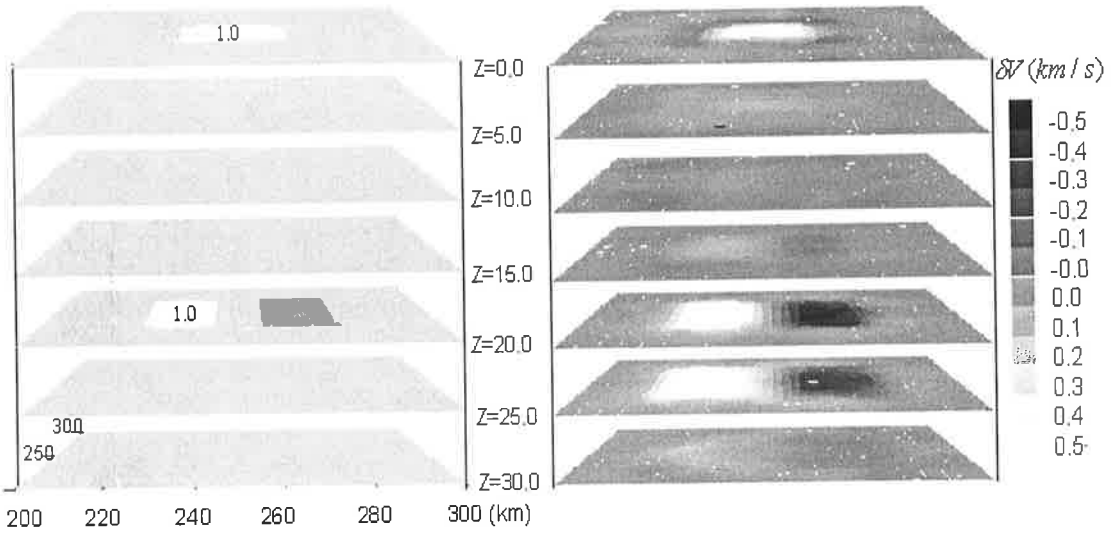

Fig.6.6 The comparison between the true model (left panel) and filtered images from the regional sources (middle panel) and the combined sources (right panel)

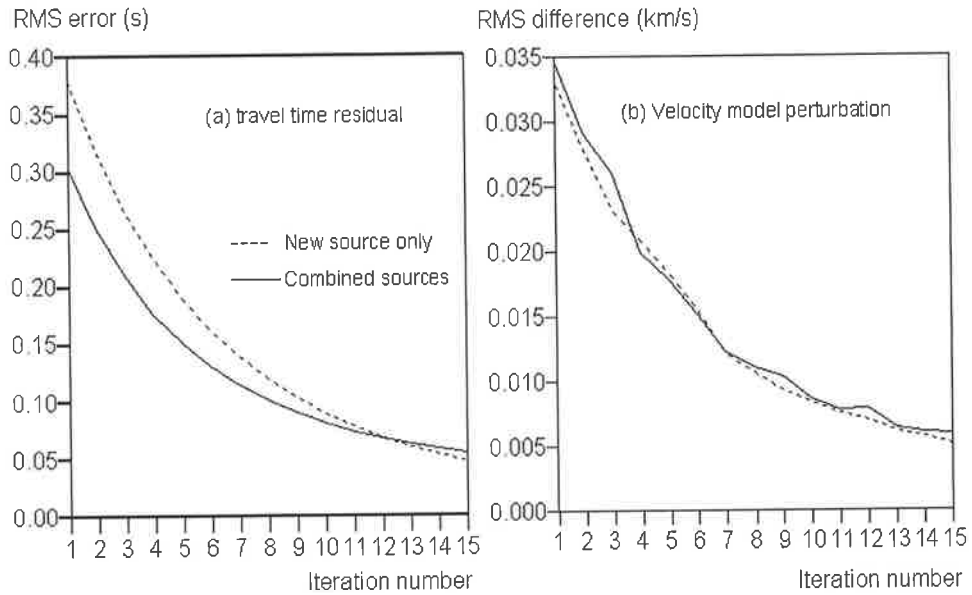

Fig.6.7 The convergence curves of multi-step tomography from new sources (dashed line) and from combined sources (continuous line)

The results show that: (1) both approaches are able to reveal the shapes of the high velocity contrast anomalies (see Fig.6.4 and 6.6); (2) with the additional local source constraints, two-step tomography is able to delineate the correct depth of the velocity anomalies (see Fig.6.6); (3) the image quality (both shape and strength of velocity anomalies) with the combined sources is much better than that using only the new sources (from regional earthquakes) alone; (4) there is still an 'X-ray'-type image in the Z=25 km plane due to the constraint limitation of local events, which I will discuss in the following section. Figure 6.7 shows the convergence curves for the time residual and the velocity model perturbation, using the new source data only, and the combined source data. The updating processes (the convergence curves for the model perturbation) are nearly the same in both cases.

6.3.4 The accuracy of multi-step tomography

In principle, it should be possible to obtain satisfactory images if the local sources are included to constrain the depth variation of the velocity field. It is worth pointing out that the ray paths are changed in the two-step process of travel time tomography, even if the node density of the local model is finer than that of the regional model. On the other hand, there may be a relatively large travel time error introduced by the coarse node density and poor ray angular coverage within the regional model. Therefore, it is essential to analyze the accuracy of the two-step tomographic procedure.

To test the accuracy, it is necessary to compare three approaches to travel time tomography: (1) travel time tomography with only local data; (2) travel time tomography with only the new source data (related to regional events); (3) travel time tomography with combined local and regional data. The latter two images were already obtained (Figures 6.4 and 6.6). Here it is only need to invert for velocity field with local data using the above same model parameters and filter routine. For easy comparison, the velocity images (from regional data alone, and from combined data) obtained previously were redisplayed here. Figure 6.8 shows the filtered images from these three kinds of inversion using the same synthetic examples as before. For travel time tomography with only local events, the ray paths seldom pass through depths greater than 20.0 km. Therefore, the velocity anomalies in the Z=20 km plane are only partially

recovered in both shape and strength. For travel time tomography with only the regional source data, the velocity anomalies are reconstructed well in shape and increased strength, but with the effect of 'X-ray'-type images at neighbouring planes due to the nearly zero incidence angle for rays passing from the new sources on the bottom of the local model volume to the top plane containing the surface receivers. For travel time tomography with combined source data, both shape and strength of the velocity anomalies are well recovered, except for the Z=25 km plane due to the lack of constraint from local data. This is a useful example to show why I advocate the two-step tomography approach and also to illustrate how it works.

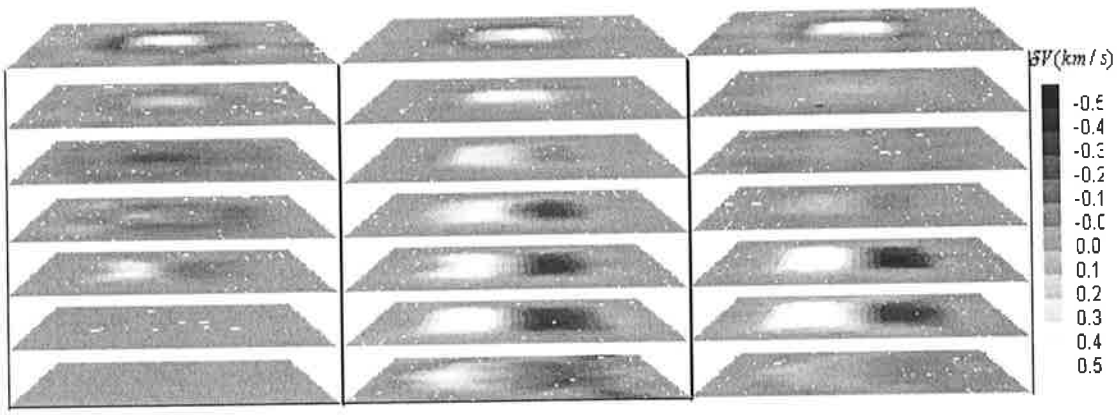

Figure 6.8 The comparison between the filtered images from local sources (left panel), regional sources (middle panel) and combined sources (right panel). The scale is the same as Fig. 6

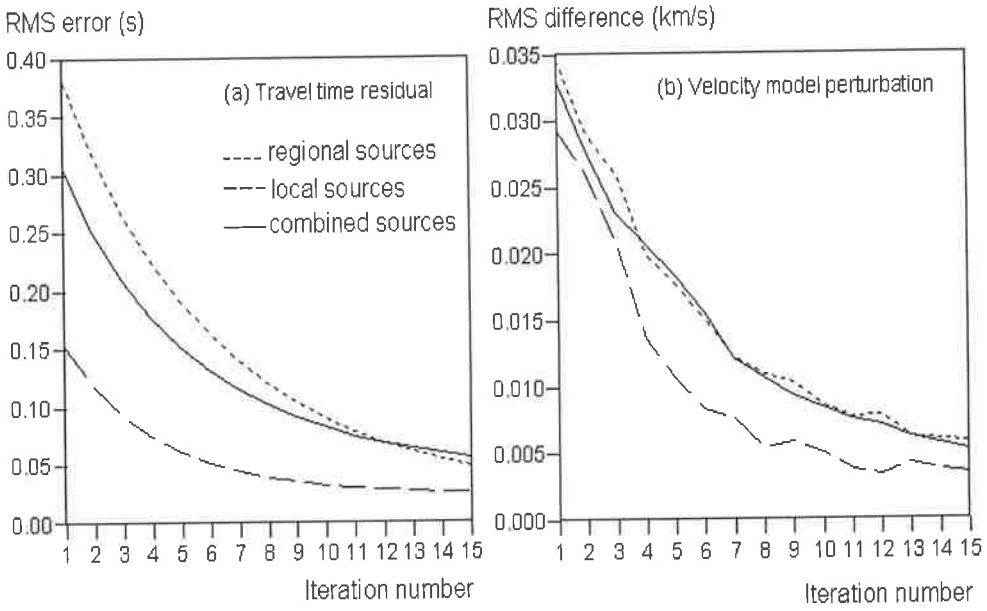

Fig.6.9 The comparison of convergence curves among the three tomographic inversions with different datasets

As discussed previously, a good inversion algorithm should recover the velocity anomalies in location, size and strength, subject to adequate ray illumination. Figure 6.8 clearly shows that the multi-step tomographic process with combined sources can do a much better job than tomography with only one kind of source. Figure 6.9 compares the convergence curves among the three travel time tomographic approaches.

6.4 Tomography with Non-Uniform Gridded Cells

It is possible to grid the velocity model with a non-uniform cell size. As a comparison in this case, I used the regional model with a non-uniform gridded cell size and obtained the local updated velocity model. The cell length is selected in such a way that it is relatively small on the local scale and relatively large on the regional scale. Figure 6.10 shows (in plan view) the gridded regional model with a non-uniform cell size. In the Z direction the location of each cell boundary is at 0, 10, 20, 30, 40 and 60 km, respectively. Thus I have the minimum cell size in the local model (10 km, 10 km and 10 km) and the maximum cell size in the regional model (20 km, 20 km and 20 km). The other cell sizes lie between the minimum and maximum values.

The input velocity model is still a 1-D layered velocity distribution with (-0.1, 0.1, 0.1, 0.1, 0.1 and -0.1 km/s) deviations from the true background values at each Z plane (see Figure 6.2 as the reference). The number of secondary nodes in all three directions is held at 9 (a relative high accuracy in computed travel times, see formula 3.23). In this model configuration, there are in total 5,766 cells and 1,340,151 nodes. The constraint parameters are set at $a = -2 \ km/s$ and $b = -2 \ km/s$, $\mu = 0.01$.

Figure 6.11 shows the filtered image (same filter parameters as before) from travel time tomography with a non-uniform cell size. Again the velocity anomalies are recovered well in both location and size at the planes Z=0 and Z=20 km, but not the actual values (strength), even if more secondary nodes (9) are used in the model representation. A false high velocity anomaly appears in the central area on the Z=40 km plane, partially due to travel time errors introduced with the sudden change in cell size (from 10 km to 20 km in the Z direction). In order to avoid such artifacts, the cell

size should be changed gradually, which in turn results in complexity in the model representation.

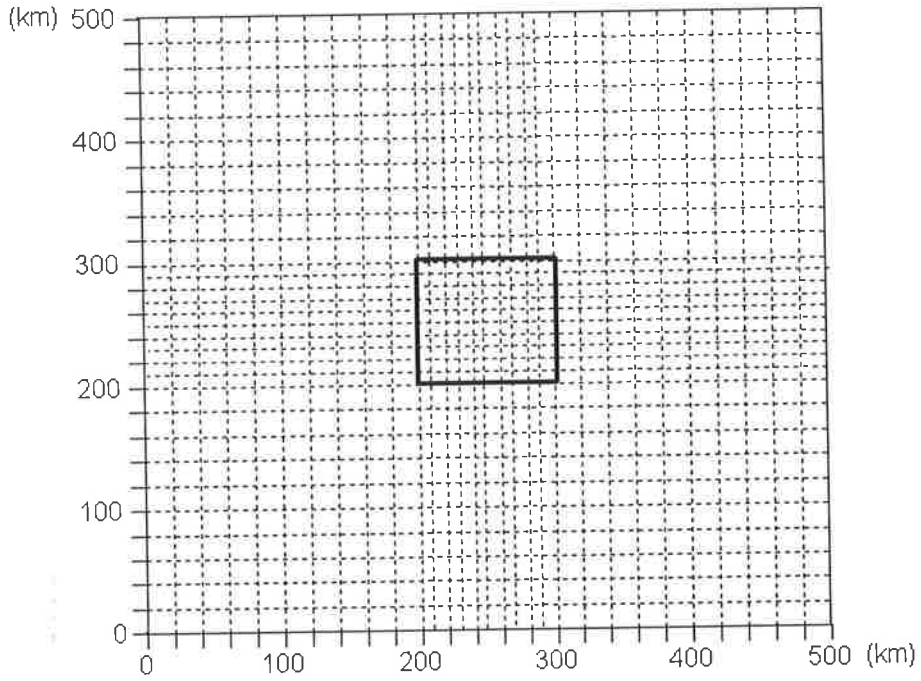

Fig.6.10 The regional velocity model with non-uniform cell size in plan view

It is worth pointing out that an unsuitable non-uniform cell selection will result in serious distortion of the final image. Even worse, no true image may be obtained at all due to large timing errors introduced by the ray geometry. In such cases, one must perform some numerical tests to estimate the error bounds on the calculated travel time so that it can meet the minimum requirement for the accuracy of the travel times. Otherwise, there is no guarantee of obtaining a reasonable solution.

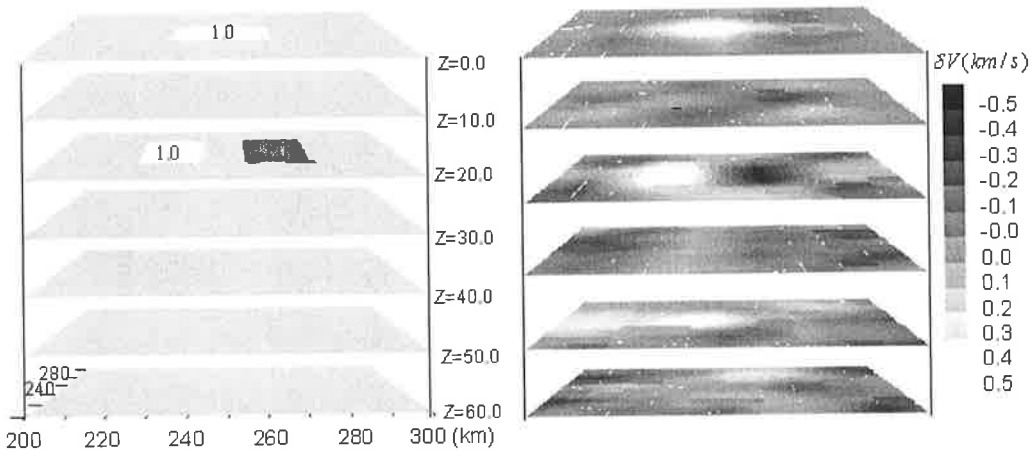

Fig.6.11 The true model perturbation (left panel) and the filtered image (right panel) with a non-uniform cell size model

6.5 Conclusions

With the need to reconstruct the local, deep velocity structure using a combination of regional and local earthquake information, I separated the problem of large-scale tomography into multiple-consecutive steps. The first step is to trace rays on a regional known velocity model, and predict the new source positions where the up-going rays cross the local velocity model volume, and calculate the related travel times up to these points. The second step is to perform travel time tomography on the local velocity model after re-arranging travel time and ray path information according to the original source and receiver pairs. Finally, a 3-D relatively deep velocity structure is obtained from the updated local model. The results of numerical tests indicate that it is a practical and feasible way to proceed. The velocity field is recovered to a reasonable depth using a combination of regional and local ray paths, with only slightly increased effort of data re-arrangement during the process. In the above discussion, one assumes that there is a known velocity distribution on the regional scale, but this velocity distribution is often unknown or poorly estimated in practice. In such circumstances, the two-step tomography procedure may be separated into two real consecutive tomographic processes. One can roughly estimate the regional velocity model with a coarse cell size and use the estimated regional model to predict the new sources and calculate the associated travel times. The rest of the process is the same as discussed previously. This approach will be further tested with real data in Chapter 10.

Chapter 7: 3-D Hypocenter Location with the Irregular Shortest Path Ray Tracing Method

7.1 Introduction

Earthquakes have been located from multi-station arrival time data for more than 50 years (for example, Lee and Stewart, 1981). There are many approaches, but most solve a non-linear inverse problem. In the location process, the most time consuming part is updating the travel time information, which is critical to reducing the location error. So far, there have been some research-style 3-D earthquake location routines developed. For example, the DD method (e.g., Fremont and Malone, 1987; Got et al., 1994; Waldhauser and Ellsworth, 2000), but the most generally used location programs, such as HYPOINVERSE (Klein, 1978, 1988), HYPO71 (Lee and Lahr, 1975) and their revisions thereafter, consider only a 1-D layered velocity model. For dealing with complex velocity structures, what is needed is real 3-D earthquake location software, which requires a 3-D ray-tracing algorithm for an arbitrary velocity medium.

Nelson and Vidale (1990) introduced a 3-D finite-difference travel time algorithm (Vidale, 1988 and 1990) to 3-D earthquake location, where a simple searching method was used to avoid the matrix inversion. Firstly, the travel times to the discretized grid points in the volume that is thought to contain the earthquakes is computed from each receiver location; secondly, for each set of travel times from the particular event, the location that produces the smallest travel time residual is found. This simple searching method is only suitable for the fine re-location of earthquakes or minor adjustment of the hypocentres (where the input source position is close to the real source location). Moser at al (1992) introduced the 'regular' approach of the shortest-path algorithm (Moser, 1991) combined with one of the probability density functions of Tarantola and Valette (1988) to perform 3-D earthquake location, and analyzed the hypocentre uncertainties. This method not only updates the source location, but also shows the

location uncertainties through use of a probability distribution. In that research work, much effort was concentrated on how to incorporate the shortest-ray tracer into the probability density function, but not on the efficiency and accuracy of the shortest-path method itself in the location process.

7.2 Need for Relocating Earthquakes in the Reconstruction of the Rabaul Velocity Structure

The regional earthquake catalogues, with specified error bounds, are determined from worldwide seismic networks subject to the geometric restriction of the seismic station deployment and the averaged earth velocity model used. For regional scale tomography, these location errors (both the source hypocenters and the origin times) are tolerable and meet the minimum requirement for the accuracy of the travel times, but for local scale tomography (for example, the Rabaul volcano study, which is only 100 kilometer square in the horizontal plane and less than 30 km in the depth), these location errors are intolerable and result in large travel time errors. For example, the 0.25° mis-location (roughly equal to 25 km) in latitude and longitude (which is the general distance error in the regional seismic catalogues) will result in an approximate absolute travel time delay or advance of 0.5 second. From this simple explanation, it is clear that it is necessary to re-locate the earthquakes using a more refined 3-D velocity model (at least a refined 1-D model) so as to reduce the travel time errors introduced by the source parameter uncertainty and meet the minimum requirement for the accuracy of the travel times in a local sense. Otherwise, these uncertainties in the travel time data will lead to an unrealistic and erroneous final image in local velocity reconstruction.

One principal objective of this thesis is to combine regional events with local earthquakes (including explosions) to recover local, deep velocity structure for Rabaul volcano. The general tomographic approach for such a problem is to use a non-uniform cell size model. As discussed in chapter 6, artifacts will be introduced into the final image, if an unsuitable non-uniform cell size model is used.

Alternatively, the tomographic problem can be separated into two isolated problems: that is the multi-step tomographic procedure as discussed in chapter 6.

Based on the above discussion, it is necessary to develop a 3-D hypocenter location program to relocate the regional and local earthquakes before starting the final process of local travel time tomography to reconstruct the Rabaul velocity structure. Since there have been no 3-D earthquake location software readily at hand, it was necessary for me to devise a 3-D hypocenter location program with greater accuracy, and the capability to handle high velocity contrast media. A further requirement was the capacity to deal with a large dataset, by which to locate a set of earthquakes simultaneously.

7.3 Methodology

The computed arrival times are in general non-linear functions of the source parameter estimation (hypocenter and origin time), and consequently the location problem is also non-linear. Basically, this non-linear problem is linearized and solved with iterative methods, such as the Gauss-Newton, conjugate gradient and damped least squares methods (Buland, 1976, Lee and Stewart, 1981 and Pavlis, 1986). These methods all have in common the requirement to know (or compute) travel time derivatives near an estimated hypocentre. They are susceptible to instabilities when the problem is ill-conditioned, for instance when the source location is far outside the seismic array (Thurber, 1985; Hirata and Matsu'ura, 1987). In order to develop realistic 3-D hypocenter location software, the ray tracer must be suitable for handling an arbitrary 3-D velocity medium. The inversion algorithm can then tackle the non-linear inverse problem. Based on the above consideration, the 'irregular' shortest-path method (see chapter 3) was used as the ray tracer and DMNLS-1 (see chapter 4) as the inverse solver to form a 3-D hypocenter location program with the required accuracy and large dataset capability. For the inversion part, it is necessary to know the travel time derivatives with respect to the source parameter changes near a hypocenter location as the analytical Jacobian matrix elements (focus co-ordinates

and origin time). In order to simplify the program design and to be able to search more directions, a simple, but robust way to calculate the elements of the analytical Jacobian matrix was found.

7.4 A Simple Way to Calculate the Analytical Jacobian Matrix

Generally, the earthquake location problem using arrival time information can be formulated as the following matrix inverse problem.

$$\delta t_i = \frac{\delta t_i}{\delta x} dx + \frac{\delta t_i}{\delta y} dy + \frac{\delta t_i}{\delta z} dz + \frac{\delta t_i}{\delta t} dt, \quad i = 1,2,.....,n \tag{7.1}$$

where $dx = x_0 - x_i$, $dy = y_0 - y_i$, $dz = z_0 - z_i$, $dt = t_0 - t_i$, and t_{obs}, t_{cal}, t_o are the observed and calculated arrival times, and the origin time, respectively. The quantities (x_0, y_0, z_0, t_0) and (x_i, y_i, z_i, t_i) are the true and updated source parameters, respectively. In matrix notation equation (7.1) takes the following form:

$$\vec{\delta t} = A\vec{dx} \tag{7.2}$$

where $\vec{\delta t} = (\delta t_1, \delta t_2, ..., \delta t_n)$, $\vec{dx} = (dx, dy, dz, dt)^T$ and A is the analytical Jacobian matrix. With an iterative approach it is easy to obtain the earthquake parameters (x_0, y_0, z_0, t_o) by updating the source parameters (x_i, y_i, z_i, t_i).

The key factor in the inversion process is to obtain the elements of analytical Jacobian matrix (the derivatives of time t_i with respect to source parameter changes). Here, I use travel time data (such as in the case of Rabaul volcano, the main purpose is to relocate the regional events), which means that the source parameters (hypocenters and origin time) are roughly estimated with regional seismic network. For simplicity, it is reasonable initially to leave at the origin time uncertainty in the inversion process and only update the source hypocenters to great accuracy. In the final analysis, the time difference between the observed and calculated travel times can be used as the estimate for the origin time uncertainty.

In order to simplify the calculation of time derivatives with respect to source position

changes, there is an alternative (simple, but novel) approach, which involves searching six trial sources around the updated source location. Figure 7.1 gives a diagrammatic explanation of the six trial source positions and the related search directions. In each direction two opposite sources with equal search lengths are inserted around the updated source position (see Figure 7.1 for details). Thus there are six supplementary sources around the updated source. It is possible to have different search lengths in different directions. The elements of the analytical Jacobian matrix are formed in such a way that the travel time derivative along the X direction is the ratio of travel time difference between two trial (opposite) sources to the search length (absolute length) of the X direction, and travel time derivatives along the Y and the Z directions are formed in the same way. Therefore, there are eight search directions in exploring the octant space for different combinations of time derivatives along the three directions. Thus the travel time derivatives are dependent on both the local velocity field and the search length. Theoretically, the search length should not be too large, because it is the approximation to the real time derivative near the updated hypocenter location. In such circumstances, the travel time derivatives can be obtained, regardless of the complexity of the velocity medium and the geometry of the source locations and seismic station deployment. This simplification has a robust physical meaning and also needs less computational effort. The trial sources are formed outside the ray tracing process (because the trial sources and search length are arranged in the input file), and the only thing one should do is to pick out the associated travel times (the travel times from the trial source locations).

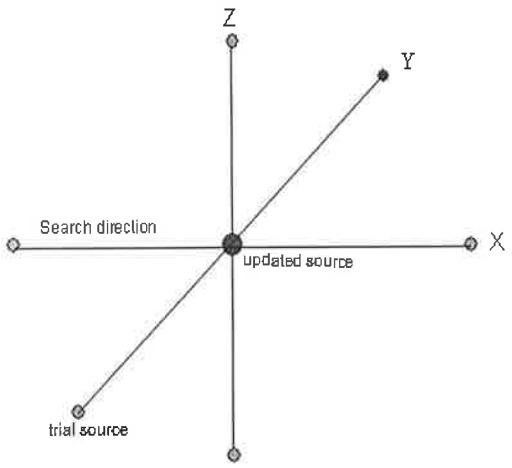

Fig.7.1 The explanation of added trial sources and search lengths

7.5 Error Estimation with Different Search Lengths

To test the efficiency and accuracy of the above approach for hypocenter location, several numerical tests using synthetic examples were undertaken.

7.5.1 Numerical test 1: high velocity gradient model

Most location programs work well in a gradually changing velocity model, but perform relatively poorly with a rapidly changing velocity model. For this purpose, a 1-D velocity model with a high gradient ($V = 2.70 + 0.26 \times Z$ km/s) was first selected.

Figure 7.2 shows the source and receiver locations in plan view. The model parameters are: model dimensions (100 km, 100 km and 30 km in X, Y and Z directions, respectively); cell size (5 km in each direction); the number of secondary nodes (6 in each direction of the cell). I set 16 sources with different depths (from 6 to 30 km) on the model boundary, and 13 receivers on the top central region of the model. I first obtained the theoretical travel times (which will be used as observed travel times later in the location process) according to the model, and then randomly misplaced the input source positions 20 km away from the true source positions in each direction. With such a displacement, there is no need to roughly estimate the source hypocenter before the location procedure starts. The search length is 0.5 km in each direction; the damping factor is 0.01 and the constraint bounds are such that the source must be within the model for the updated hypocenter locations.

Fig.7.2 Source (black) and receiver (grey) distribution for event location of test 1 in plan view

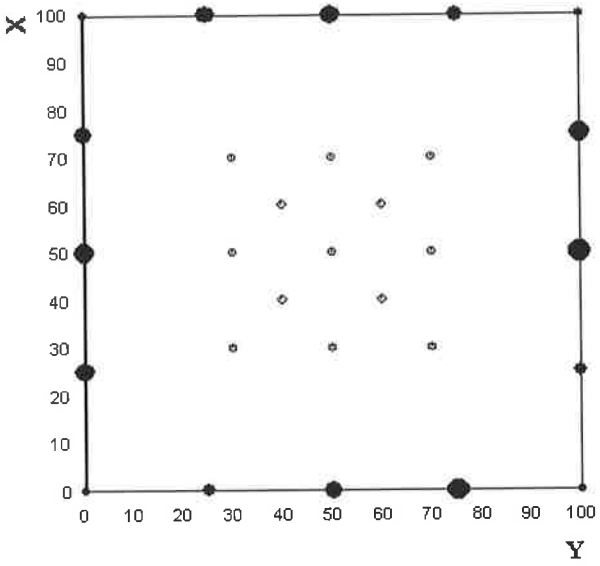

From Table 7.1a, it can be seen that the final located source positions are nearly the same as the true source locations even if the starting source (input source) locations are

more than 32 km away from the true source locations (a large distance error for this sized model). More importantly, there is not much difference in the location error in the horizontal plane and in the vertical direction. Table 7.1b gives the absolute and relative errors of the travel times. The mean absolute and relative travel time errors reach 0.0007 s and 0.01%, respectively, which can be used to estimate the uncertainty of the origin time.

Table 7.1a The true and located source positions and the distances (km) between them

NO	Xo	Yo	Zo	Xe	Ye	Ze	Xeo	Yeo	Zeo	Deo
1	0	0	0	0.0000	0.0000	0.0007	0.0000	0.0000	0.0007	0.0007
2	25	0	10	25.0046	0.0003	9.9961	0.0046	0.0003	0.0039	0.0060
3	50	0	20	50.0008	0.0000	20.0063	0.0008	0.0000	0.0063	0.0064
4	75	0	25	74.9835	0.0000	24.9663	0.0165	0.0000	0.0337	0.0375
5	100	0	2	99.9909	0.0091	1.9949	0.0091	0.0091	0.0051	0.0138
6	100	25	10	99.9996	25.0036	9.9982	0.0004	0.0036	0.0018	0.0040
7	100	50	25	99.9965	49.9935	25.0063	0.0035	0.0065	0.0063	0.0097
8	100	75	25	100.0000	74.9835	24.9663	0.0000	0.0165	0.0337	0.0375
9	100	100	4	99.9946	99.9946	3.9971	0.0054	0.0054	0.0029	0.0082
10	75	100	15	74.9898	100.0000	14.9904	0.0102	0.0000	0.0096	0.0140
11	50	100	25	49.9935	99.9965	25.0063	0.0065	0.0035	0.0063	0.0097
12	25	100	20	24.9957	99.9999	20.0046	0.0043	0.0001	0.0046	0.0063
13	0	100	6	0.0240	99.9760	5.9811	0.0240	0.0240	0.0189	0.0388
14	0	75	20	0.0002	74.9973	20.0029	0.0002	0.0027	0.0029	0.0040
15	0	50	25	0.0036	49.9935	25.0064	0.0036	0.0065	0.0064	0.0098
16	0	25	25	0.0000	25.0020	25.0032	0.0000	0.0020	0.0032	0.0038
Min							0.0000	0.0000	0.0007	0.0007
Mean							0.0056	0.0050	0.0091	0.0131
Max							0.0240	0.0240	0.0337	0.0388

Table 7.1b The absolute (s) and relative (%) origin time uncertainties

SNO	Atmax (s)	Atmean (s)	Rtmax (%)	Rtmean (%)
1	0.0000	0.0000	0.00	0.00
2	0.0000	0.0000	0.00	0.00
3	0.0000	0.0000	0.00	0.00
4	0.0040	0.0034	0.04	0.03
5	0.0006	0.0003	0.01	0.00
6	0.0000	0.0000	0.00	0.00
7	0.0008	0.0005	0.01	0.01
8	0.0040	0.0034	0.04	0.03
9	0.0008	0.0007	0.01	0.01

10	0.0021	0.0021	0.03	0.02
11	0.0008	0.0005	0.01	0.01
12	0.0000	0.0000	0.00	0.00
13	0.0016	0.0005	0.02	0.00
14	0.0000	0.0000	0.00	0.00
15	0.0009	0.0006	0.01	0.01
16	0.0000	0.0000	0.00	0.00
Min. value	0.0000	0.0000	0.00	0.00
Mean value	0.0010	0.0007	0.01	0.01
Max. value	0.0048	0.0034	0.04	0.03

Explanation for Table 7.1:

NO---source number; (Xo, Yo, Zo)---true source coordinates; (Xe, Ye, Ze)---final located (updated) source coordinates; (Xeo, Yeo, Zeo)--the difference between true and final located position in each direction; Deo--the distance between true and final located source position; Atmax and Rtmax----the absolute and relative maximum origin time errors; Atmean and Rtmean --- the absolute and relative mean origin time errors.

To convey visually how the program works on the location process, refer to Figure 7.3, which shows the consecutive search paths with various iterations. The search paths are smooth curves in most cases, and converge to the true source locations.

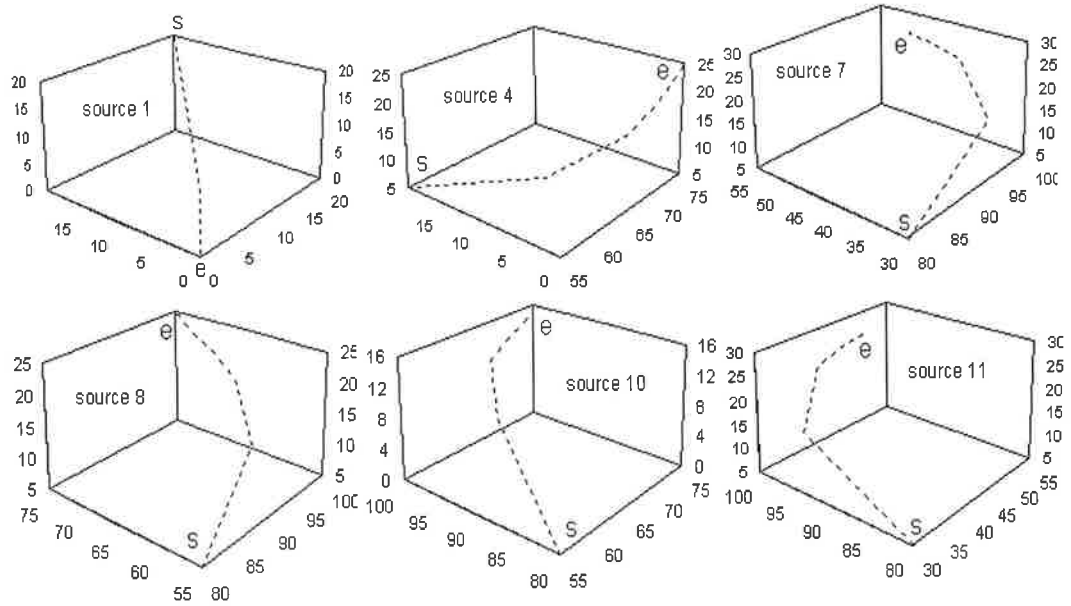

Fig.7.3 Search paths (dashed line) for different sources in the event location process of test 1 (s: starting source positions; e: search end source locations, equal to true source positions)

7.5.2 Numerical test 2: different search lengths

Next the effect of different search lengths was tested on the location error estimation. The same velocity model as for numerical test 1 was selected, but here two sources

were placed beneath the seismic array and the total number of sources is reduced to 10 (see Figure 7.4 for details). The model parameters (such as model length, cell size, number of secondary nodes), velocity distribution, damping factor and constraint bounds remain the same as for numerical test 1. Again the input source (starting source) positions are randomly set 20 km away from the true source locations in each direction.

As mentioned before, the derivatives of time to source position changes are dependent on the search lengths when the local velocity model is unchanged. Thus I selected different search lengths from 0.1 km to 5.0 km (equal to the cell size) and estimate the associated location errors, and hoped to obtain the optimal search length by testing various values. Such results are a useful guide to selecting the proper search length in future work according to certain model parameter specifications. Table 7.2 shows both the distance and origin time errors with different search lengths. The best search length (having the minimum distance and origin time errors) is 1.0 km in all three directions. The search length cannot be too large (comparable to the cell size) nor too small (close to zero). From this experiment, a good search length should be between $\frac{1}{10}$ and $\frac{1}{2}$ of the cell size.

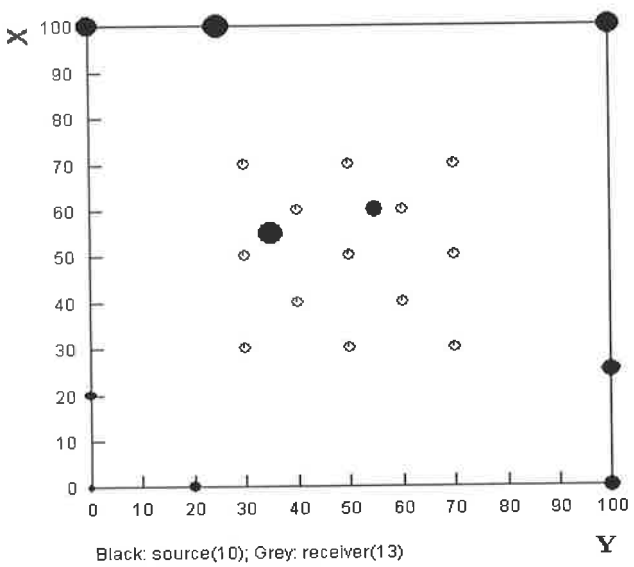

Fig.7.4 Source (black) and receiver (grey) distribution in plan view for event location test 2

Table 7.2a The distance (km) between the true and located sources in three directions with different search lengths

Search-length	Xmax	Ymax	Zmax	Dmax	Xmean	Ymean	Zmean	Dmean	Mk
(0.1, 0.1, 0.10)	1.2977	1.3894	1.1362	2.1585	0.2211	0.3173	0.2489	0.5072	9
(0.5, 0.5, 0.25)	0.1962	0.1962	0.3108	0.4123	0.0464	0.0464	0.0665	0.0948	4
(0.5, 0.5, 0.50)	0.1728	0.1728	0.2762	0.3688	0.0465	0.0480	0.0668	0.0959	3
(1.0, 1.0, 0.50)	0.1962	0.1962	0.3108	0.4123	0.0464	0.0464	0.0665	0.0948	2

(1.5, 1.5, 1.50)	0.1802	0.1802	0.2911	0.3869	0.0482	0.0504	0.0722	0.1015	5
(1.0, 1.0, 1.00)	0.0240	0.0240	0.0337	0.0388	0.0056	0.0050	0.0091	0.0131	1
(2.0, 2.0, 1.00)	0.2164	0.2164	0.3517	0.4662	0.0571	0.0579	0.0792	0.1160	6
(2.5, 2.5, 2.50)	0.2272	0.2272	0.3680	0.4885	0.0638	0.0661	0.0848	0.1276	7
(5.0, 5.0, 5.00)	0.2596	0.2596	0.4222	0.5595	0.0623	0.0651	0.0948	0.1319	8

Table 7.2b. The origin time uncertainties (expressed as percentages) for different search lengths

Search-length (km)	Atmax (s)	Atmean (s)	Rtmax (%)	Rtmean (%)	Mk
(0.1, 0.1, 0.10)	0.0249	0.0084	0.28	0.08	9
(0.5, 0.5, 0.25)	0.0054	0.0032	0.06	0.03	2
(0.5, 0.5, 0.50)	0.0058	0.0031	0.08	0.04	3
(1.0, 1.0, 0.50)	0.0047	0.0027	0.06	0.02	2
(1.5, 1.5, 1.50)	0.0064	0.0035	0.09	0.04	4
(1.0, 1.0, 1.00)	0.0010	0.0007	0.01	0.01	1
(2.0, 2.0, 1.00)	0.0068	0.0037	0.09	0.04	6
(2.5, 2.5, 2.50)	0.0084	0.0048	0.11	0.05	8
(5.0, 5.0, 5.00)	0.0072	0.0038	0.10	0.04	7

Explanation for the Table 7.2:

Xmax, Ymax and Zmax--maximum distance between true and located source in the X, Y and Z direction; Dmax--maximum distance between the true and the located source; Xmean, Ymean, and Zmean--averaged distance between the true and the located source in the X, Y and Z direction; Dmean--averaged distance between the true and the located source; Atmax, Atmean, Rtmax and Rtmean are the same as Table 7.1; Mk-The fitting order for different search lengths.

Theoretically, the search length should be small because of the approximation to the time derivative (the gradient near the hypocenter), but should not be too small for the stability of the ratio $(t^j_{cal} - t^i_{cal})/L_{search}$, where i, j are the two trial sources in opposing directions and L_{search} is the search length (absolute length between two trial sources, see Fig. 7.1) in this direction. Figure 7.5 shows the convergence for both the time residual and the distance error with different search lengths. Except for the search lengths 0.1 km and 5.0 km, there is not much difference in error estimation for both the travel time and the distance. It is possible to have different search lengths in different directions (see Table 7.2) according to a selected model, for example, a relatively small search length is preferred if the vertical length of the model (or cell) is smaller than the horizontal length of the model (or cell).

Figure 7.6a shows the comparison of the distance convergence for the three

co-ordinate directions. In such circumstances, there is no way of telling which direction has the best convergence. That is to say, there is no problem in depth location with this new approach. This is further explained in Figure 7.6b, which shows the RMS errors where the input source positions are allowed to change only in the vertical direction (1-D case), or in all three directions (3-D case). After several iterations both sets of travel time residuals have converged to the same level, which again indicates there are no directional effects in this location process.

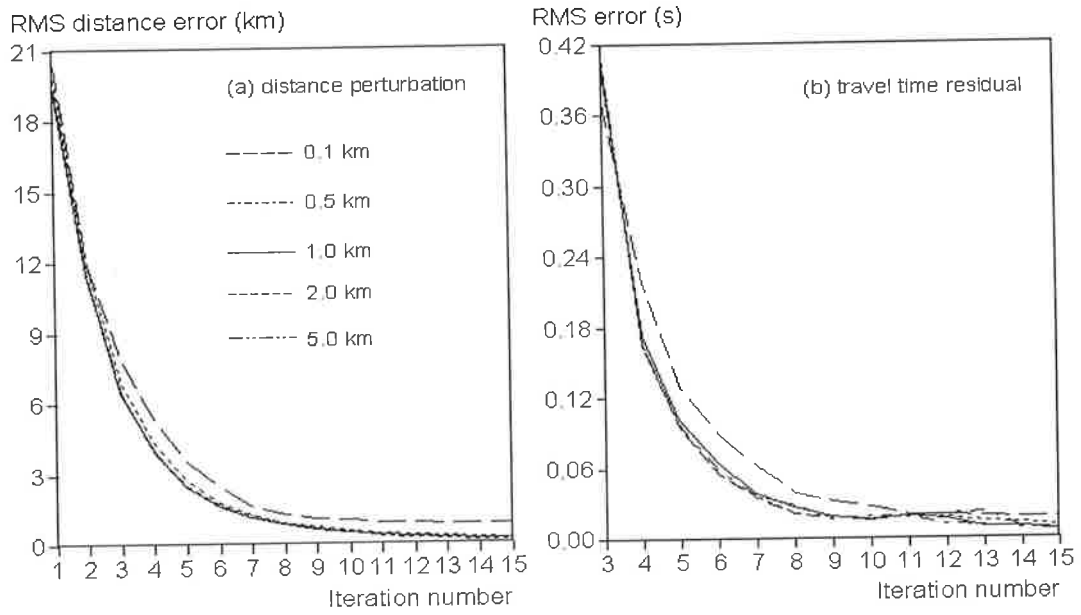

Fig.7.5 The convergence between the travel time residuals and the distance perturbation for different search lengths in test 2 (for comparison, the data begin at iteration 3 in Fig.7.5b)

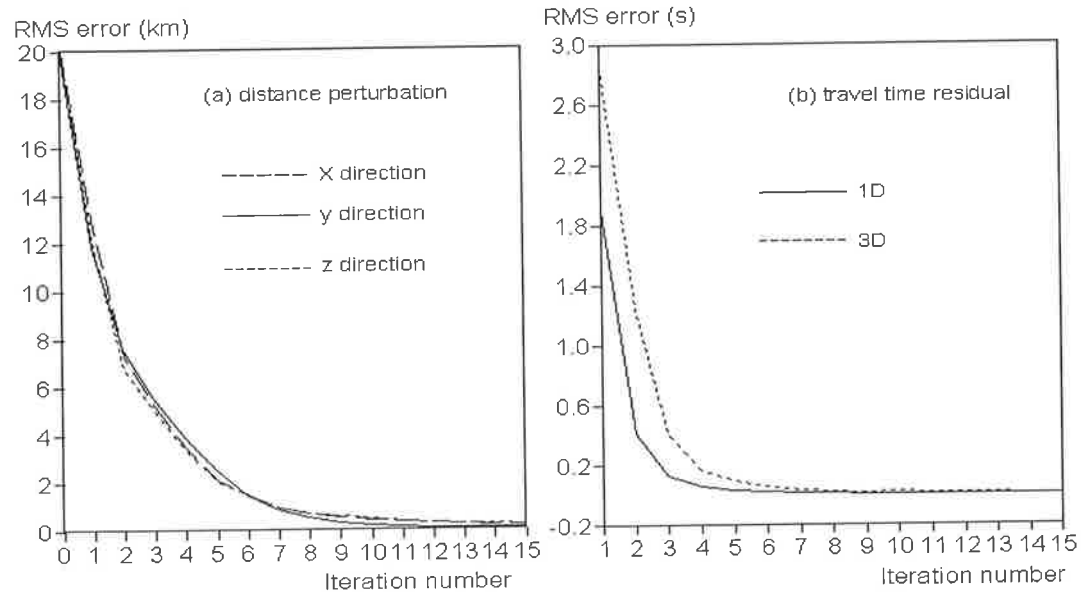

Fig.7.6 The convergence of the distance perturbation in three directions (left panel) and the travel time residuals between the 1-D (only Z direction changed) and 3-D (three directions changed) cases (right panel)

7.5.3 Numerical test 3: true 3-D velocity model

The above two numerical tests are not strictly 3-D cases, because velocity was only allowed to vary in the Z direction. In the next test a true 3-D velocity model was used to further assess the accuracy and efficiency of this approach.

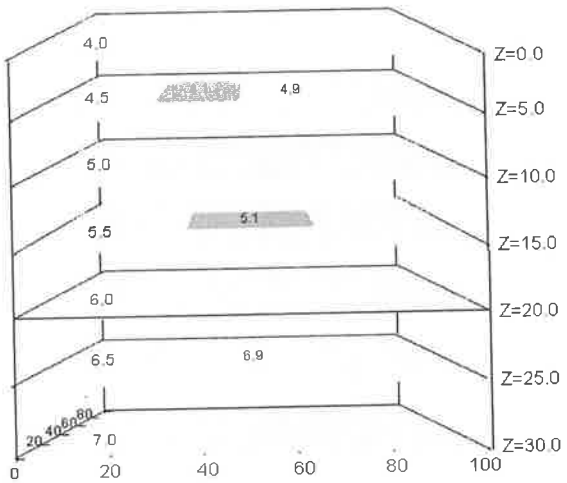

Fig.7.7 3-D model for event location of test 3

Figure 7.7 shows a 3-D velocity model for earthquake location, the model length and cell size are the same as for numerical test 1.

The background velocity distribution is also a 1-D linear function ($V = 4.0 + 0.1 \times Z$ km/s), but at the planes Z=5, 15 and 25 km beneath the seismic array, four velocity anomalies (two low velocity features and two high velocity features) have been introduced. The source and receiver locations are displayed (in plan view) in Figure 7.8. The total number of sources is set at 10, with different depths (from 0 to 24 km), and the number of receivers is set at 13. In this test I took much risk by putting all input source positions (initial guess) at the middle point (geometrical center) of the model, and to see what will happen.

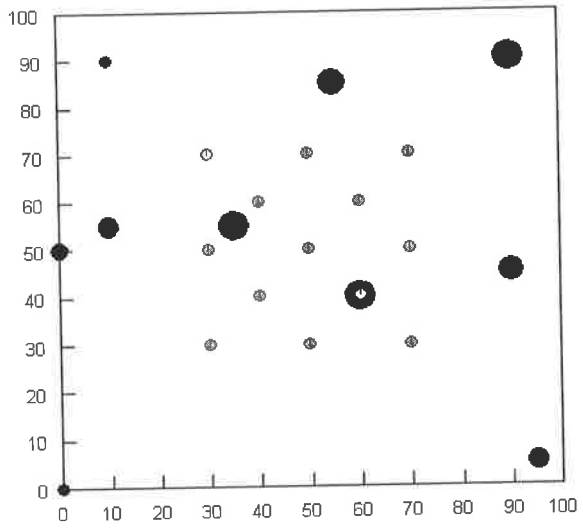

Fig.7.8 Source (black) and receiver (grey) for event location of test 3, in plan view

The location program works very well in the 3-D case, with the mean distance error between the true and the located source being only 0.03 km. The mean location error in

each direction is within 0.02 km (see Table 7.3a). The maximum absolute origin time uncertainty is 0.02s (see Table 7.3b). In a practical sense, this is a very good approach, because one only has the arrival time data at hand and does not know very well the approximate earthquake hypocentre (estimated starting source locations) in most cases. With this approach, there is no need to estimate the starting source location precisely any more; the only information needed is the velocity model.

Table 7.3a Distance (km) between the original and located source positions

No	Xo	Yo	Zo	Xe	Ye	Ze	Xeo	Yeo	Zeo	Deo
1	0	0	0	0.00	0.00	0.00	0.00	0.00	0.00	0.00
2	0	50	10	0.00	50.00	10.00	0.00	0.00	0.00	0.00
3	95	5	15	94.92	5.02	15.02	0.08	0.02	0.02	0.08
4	90	45	20	89.98	45.00	19.97	0.02	0.00	0.03	0.04
5	90	90	30	90.00	90.00	29.99	0.00	0.00	0.01	0.01
6	55	85	25	55.03	84.98	24.99	0.03	0.02	0.01	0.03
7	10	90	0	10.02	90.00	0.00	0.02	0.00	0.00	0.03
8	10	55	15	10.01	55.01	15.00	0.01	0.01	0.00	0.01
9	35	55	30	35.01	54.97	29.98	0.01	0.03	0.02	0.03
10	60	40	30	60.00	40.02	29.99	0.00	0.02	0.01	0.02
Min value							0.00	0.00	0.00	0.00
Mean value							0.02	0.01	0.01	0.03
Max value							0.08	0.03	0.03	0.08

Table7.3b Origin time uncertainties (seconds) for each source-receiver pair

no	st1	st2	st3	st4	st5	st6	st7	st8	st9	st10	st11	st12	st13
1	0	0	0	0	0	0	0	0	0	0	0	0	0
2	0	0	0	0	0	0	0	0	0	0	0	0	0
3	0.015	0.013	0.013	0.015	0.013	0.015	0.013	0.012	0.013	0.011	0.012	0.011	0.009
4	-0.006	-0.006	-0.006	0.004	0.004	0.004	0.004	0.003	0.005	0.004	0.005	0.006	0.003
5	-3E-04	-3E-04	-3E-04	-3E-04	-3E-04	-3E-04	-3E-04	4E-04	-2E-04	2E-04	-2E-04	1E-04	9E-04
6	-0.005	-0.005	-0.005	-0.001	-0.005	-0.002	-0.001	-0.002	0.003	0.004	-0.004	0.004	0.005
7	0.002	0.002	0.004	0.002	0.004	0.003	0.003	0.004	0.003	0.004	0.003	0.003	0.005
8	-0.003	-0.003	0.003	-0.003	0.002	-0.003	0.001	0.002	-0.003	0.002	-0.003	4E-04	0.002
9	0.003	-0.003	-0.005	0.004	-0.004	0.005	0.004	-0.005	0.004	-0.002	0.004	0.003	-0.005
10	-0.003	0.002	0.002	0.002	0.003	-0.003	0.003	0.003	0.002	0.003	-0.003	0.002	0.003

The explanation for Table 7.3c

sti—i-th station. Other quantities defined earlier (Table 7.1)

7.5.4 Numerical test 4: added random noise

Good earthquake location software should be much more dependent on the accuracy of the velocity model, than on the data quality of the travel times. In other words, it should be sensitive to the model perturbation, but not easily influenced by the noise in the data. Another numerical test was performed to analyze the sensitivity of the location procedure to the data error and the perturbation of the velocity model. Following numerical test 2, this time purely random noise is added to the travel time data to simulate picking errors in both P and S arrival times. For P arrival times, the maximum absolute noise is 0.1 s; for S arrival times, the maximum absolute noise is higher at 0.25 s, due to the picking uncertainty following the strong P wave coda. An even higher extreme noise level is added to the travel time (maximum absolute noise equal to 0.5 s). The velocity perturbation is accomplished by randomly modifying the velocities (departure from the true model), with maximum relative noise levels of 2.5% and 5.0%.

Table 7.4 shows the results of error estimation for both travel time and distance with the noisy data. From Table 7.4, two important conclusions can be obtained: (1) the location program is not sensitive to the data quality, and thus it works well with tolerable levels of noise (say with a 0.1 s picking error or even higher); (2) the location program is very sensitive to the model perturbation, or is model-dependent. For example, the location error (both the travel time residual and the distance) with 2.5% relative noise on the model perturbation is comparable to the location error with a 0.25 s absolute picking error in the travel times. Even worse, the location error with a 5.0% relative noise on the model perturbation is comparable to the location error with a 0.5 s absolute picking error in the travel times. Thus, good model estimation is a critical factor at improving the accuracy of earthquake location.

Table 7.4a The distance location errors (km) in each direction with noisy data

NOISE-TYPE	Xmax	Ymax	Zmax	Dmax	Xmean	Ymean	Zmean	Dmean	MK
(T=0.00 s V=0.0%)	0.1802	0.1802	0.2911	0.3869	0.0482	0.0504	0.0722	0.1015	1
(T=0.10 s V=0.0%)	0.2657	0.4233	0.3161	0.5283	0.0824	0.0945	0.0884	0.1903	2
(T=0.00 s V=2.5%)	0.7709	0.5990	0.7856	1.1571	0.1764	0.2025	0.2472	0.4228	3

(T=0.25 s V=0.0%)	0.7919	0.9485	0.6381	1.0741	0.2578	0.2679	0.2368	0.5589	4
(T=0.25 s V=2.5%)	0.6882	1.6509	0.9411	1.9020	0.2215	0.4084	0.3514	0.6726	5
(T=0.00 s V=5.0%)	1.1695	1.1936	1.3426	1.9285	0.2998	0.4483	0.4721	0.8181	6
(T=0.50 s V=0.0%)	2.0884	1.7706	1.2649	2.5226	0.6009	0.5636	0.5236	1.1428	7

Table 7.4b The origin time uncertainties with different levels of noisy data

NOISE-TYPE	Atmax (s)	Atmean (s)	Rtmax (%)	Rtmean (%)	MK
(T=0.00 s, V=0.0%)	0.0064	0.0035	0.09	0.04	1
(T=0.10 s, V=0.0%)	0.0225	0.0139	0.30	0.15	2
(T=0.25 s, V=0.0%)	0.0431	0.0189	0.57	0.24	3
(T=0.00 s, V=2.5%)	0.0564	0.0259	0.62	0.27	4
(T=0.25 s, V=2.5%)	0.0759	0.0307	0.95	0.35	5
(T=0.50 s, V=0.0%)	0.0791	0.0391	1.13	0.46	6
(T=0.00 s, V=5.0%)	0.1039	0.0451	1.15	0.47	7

Explanation for Table 7.4

NOISE TYPE---T: noise is added to travel time;
V: noise is added to velocity model;
TV: noise is added to both travel time and velocity model.

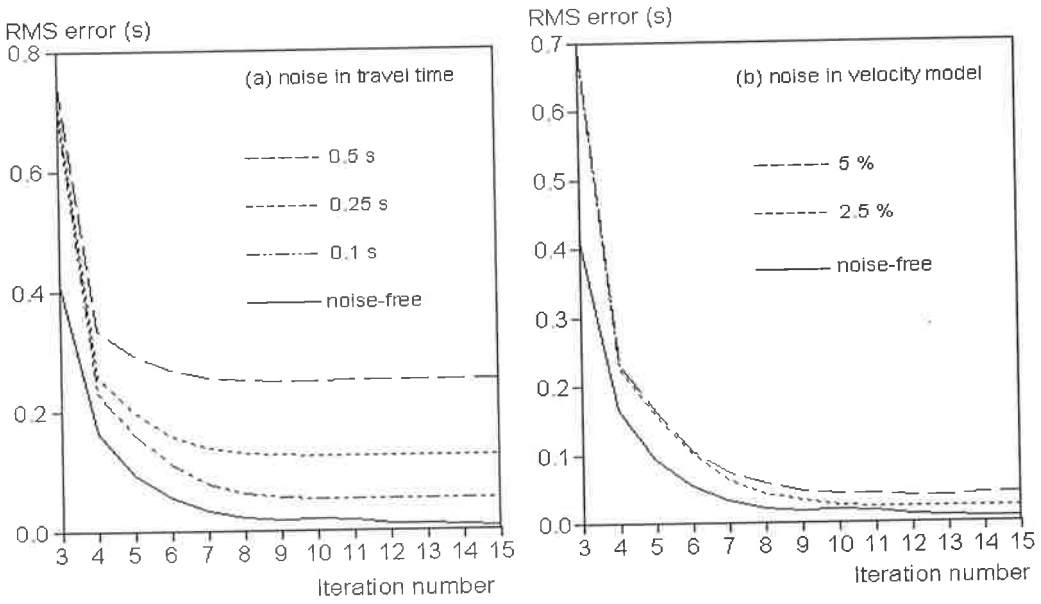

Fig.7.9 The convergence curves in the location sensitivity test when different levels of noise are added to the travel times (left panel) or the velocity model (right panel)

Figure 7.9 shows the convergence curves for the travel time residual with different noise levels. A good estimate of earthquake parameters with a relatively small location error can be obtained (see Table.7.4), provided the picking time error is 0.1 s or less.

7.6 Example of Relocating Rabaul Explosions

The above analysis and discussion were based on numerical tests, where the sources and the receivers can be deployed in the optimal geometrical locations. Furthermore, the velocity field is exactly known (even though errors were purposely introduced). Such conditions are not possible in real cases, because of the uneven distribution of natural earthquakes, the economic and logistical considerations in the seismic array deployment positions, and also because only a rough estimate of the velocity model is available. To further test the effectiveness and accuracy of the location program, I now attempt to locate real events. A good approach is to locate explosions, which have exact timing and known positions.

Figure 7.10 shows the distribution of explosions and receivers in the RELACS dataset (see chapter 1). There are in total 30 explosions and 67 receivers (the data is transformed to Cartesian coordinates according to a certain reference point of spherical coordinates).

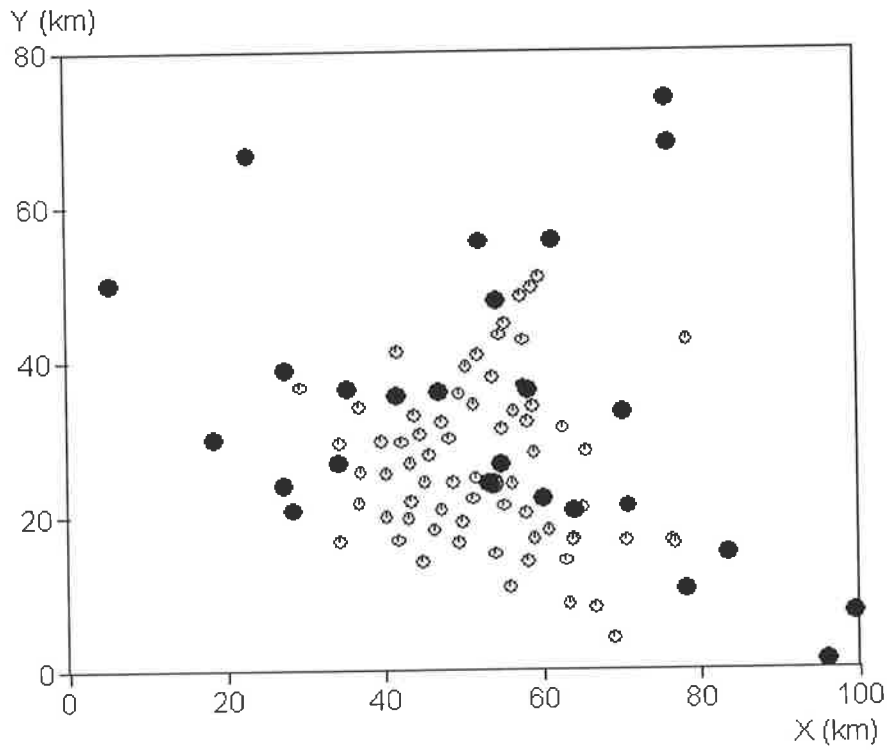

Fig.7.10 The source (black) and receiver (grey) distribution used in explosion location

As discussed above, the main factor that leads to a large location error is the incorrect velocity model. Thus, a suitable velocity model had to be found before locating the explosions. Firstly, I exploited the Wiechert-Herglotz method (Bullen, 1963) to obtain a 1-D background velocity model (which will be discussed in detail in Chapter 10), and took this 1-D velocity model as the input velocity model, and updated it to a 3-D velocity model using the inversion algorithm of Chapter 4. Finally, I relocated the explosions using the smoothed, final updated 3-D velocity model.

Figure 7.11 shows the 1-D velocity model obtained by W-H inversion. The model parameters (such as model length, cell size, number of secondary nodes) will be kept fixed in the later inversion and location process. The input shot positions were randomly displaced from 0.13 to 8.0 km away from the true positions of explosions in the X or Y directions, whereas for the Z coordinates they were set at the top of the model (Z=0 km). Thus the distances (departures) between the true positions and the input shot positions (starting guess hypocenters) range from 2.0 km to 9.5 km.

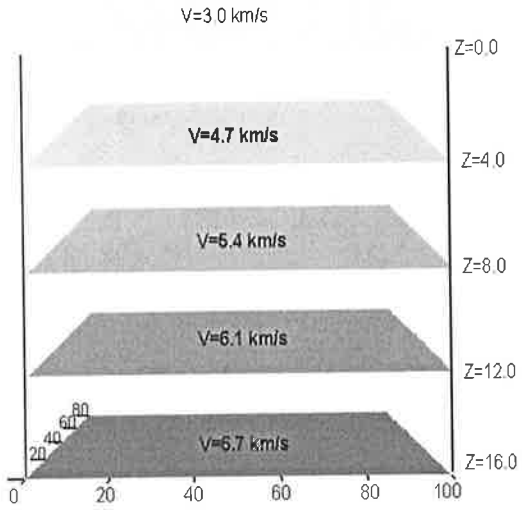

Fig.7.11 The 1-D layered velocity model obtained by H-W inversion

Table 7.5 shows the results of locations after 10 iterations. The mean distance errors in the X, Y and Z directions are 0.45 km, 0.52 km, 0.31 km, respectively, and the mean distance error is 0 .83 km. The hypocentral distances range from 0.26 to 2.53 km before and after relocation (see Figure 7.12 and Table 7.5a). The origin time uncertainty ranges from 0.06 to 0.3 s (see Figure 7.13 and Table 7.5b). Figure 7.12 is a comparison between the true and located shot epicenter positions, while Figure 7.13 shows in diagrammatic form of the origin time uncertainties for each explosion.

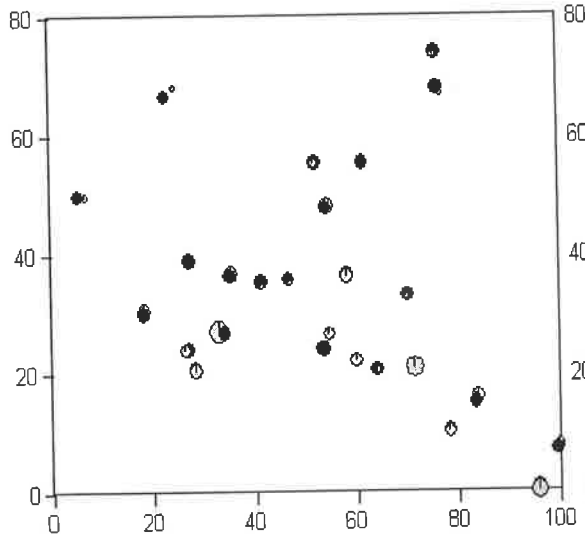

Fig.7.12 The explosion distribution before (black) and after (grey) relocation (The discrepancies, a shift range from 0.26 to 2.53 km)

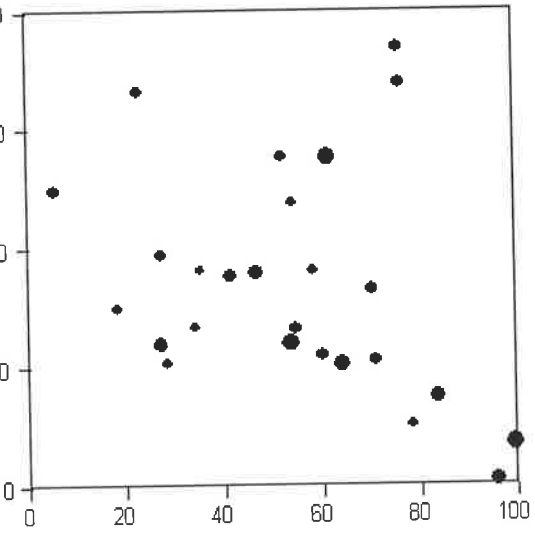

Fig.7.13 The origin time uncertainties in each shot (from 0.062 to 0.2973s)

Table 7.5a. The distance errors (km) between the true and the located explosions

NO	Xo	Xe	Yo	Ye	Zo	Ze	Xeo	Yeo	Zeo	Deo
1	24.24	23.98	53.76	53.85	0.36	0.11	0.26	0.09	0.25	0.38
2	24.12	24.11	53.84	53.99	0.39	0.08	0.01	0.15	0.31	0.35
3	23.97	24.15	53.93	54.03	0.42	0.00	0.18	0.10	0.42	0.47
4	21.13	20.23	70.93	71.91	0.42	1.05	0.89	0.97	0.63	1.46
5	20.58	20.85	64.09	64.29	0.42	0.34	0.27	0.19	0.08	0.34
6	22.09	21.75	60.13	60.11	0.42	0.26	0.35	0.02	0.17	0.39
7	35.36	35.58	41.56	40.91	0.42	0.57	0.22	0.65	0.14	0.70
8	36.39	37.69	35.35	33.79	0.42	1.65	1.29	1.56	1.23	2.37
9	38.80	39.05	27.49	28.05	0.42	0.31	0.25	0.56	0.12	0.62
10	7.22	6.95	99.59	100.00	0.42	0.42	0.27	0.41	0.00	0.49
11	15.04	14.26	83.54	84.12	0.42	0.80	0.78	0.58	0.37	1.05
12	23.96	24.06	53.56	53.33	0.42	0.41	0.10	0.24	0.01	0.26
13	49.88	48.58	5.64	6.96	0.42	0.00	1.30	1.32	0.42	1.90
14	73.76	74.20	76.09	75.88	0.42	0.17	0.45	0.21	0.25	0.56
15	55.38	55.08	61.56	61.64	0.42	0.04	0.30	0.08	0.38	0.49
16	47.72	49.01	54.27	54.59	0.42	0.82	1.28	0.32	0.39	1.38
17	35.86	36.33	46.90	46.13	0.42	0.30	0.47	0.78	0.12	0.91
18	26.79	27.19	34.29	33.67	0.42	0.53	0.40	0.61	0.11	0.74
19	20.67	20.44	28.56	27.98	0.42	0.67	0.23	0.57	0.24	0.66
20	24.18	23.94	53.31	52.89	0.42	0.40	0.25	0.42	0.02	0.49
21	26.55	25.95	54.78	54.97	0.42	0.28	0.61	0.18	0.15	0.65
22	33.15	32.39	70.31	71.16	0.42	0.47	0.75	0.85	0.05	1.13
23	36.22	36.32	58.39	58.62	0.42	0.26	0.10	0.24	0.16	0.30
24	67.82	67.69	76.33	76.82	0.42	0.00	0.13	0.49	0.42	0.66

25	55.35	55.96	52.24	51.65	0.42	0.46	0.61	0.60	0.03	0.85
26	23.97	23.89	27.29	28.01	0.42	0.00	0.09	0.72	0.42	0.84
27	29.98	30.30	18.42	16.30	0.42	1.76	0.32	2.12	1.34	2.53
28	66.49	66.19	23.02	22.46	0.42	0.20	0.30	0.56	0.22	0.68
29	10.35	10.03	78.29	78.26	0.42	0.62	0.32	0.04	0.20	0.38
30	0.95	0.38	95.94	95.90	0.42	0.91	0.57	0.04	0.49	0.75
Min							0.01	0.02	0.00	0.26
Mean							0.45	0.52	0.31	0.83
Max							1.30	2.12	1.34	2.53

Table 7.5b The origin time uncertainties (in seconds) on each explosion

No	Sno	Atmin (s)	Atmax (s)	Atmean (s)	Stn-used
1	536	0.0056	0.3266	0.1131	23
2	538	0.0078	0.2034	0.0967	23
3	539	0.0052	0.2541	0.0944	18
4	543	0.0047	0.2370	0.0861	27
5	545	0.0004	0.2682	0.0960	31
6	546	0.0071	0.2649	0.1186	28
7	553	0.0030	0.2593	0.0620	27
8	554	0.0164	0.2927	0.0964	31
9	555	0.0018	0.3109	0.1074	38
10	566	0.0027	0.2814	0.1383	11
11	567	0.0008	0.2565	0.1109	38
12	573	0.0052	0.3424	0.0861	26
13	577	0.0061	0.3404	0.1238	25
14	584	0.0357	0.3736	0.1635	27
15	585	0.0087	0.3330	0.1097	18
16	588	0.0028	0.3057	0.1176	28
17	596	0.0032	0.1923	0.0682	25
18	598	0.0043	0.2421	0.0985	27
19	603	0.0017	0.2071	0.0776	36
20	654	0.0000	0.4162	0.0969	44
21	655	0.0021	0.2467	0.0793	39
22	657	0.0007	0.2529	0.1065	49
23	658	0.0008	0.2691	0.0925	45
24	661	0.0226	0.3385	0.1297	37
25	662	0.0011	0.2834	0.1055	51
26	670	0.0054	0.3267	0.1035	54
27	671	0.0197	0.3526	0.1088	43
28	675	0.0066	0.3291	0.1081	48
29	679	0.0053	0.2914	0.0983	51
30	682	0.0574	0.5416	0.2973	33
Min		0.0000	0.1923	0.0620	11
Max		0.0574	0.5416	0.2973	54
Mean		0.0082	0.2980	0.1097	33

The explanation of Table 7.5:
No: event number in the RELACS dataset; Stn-used: the total number of stations used to relocate the explosions. Others are the same as Table 7.1.

7.7 Conclusions

I was faced with the need to relocate earthquakes around Rabaul volcano (improving the source hypocenter positions) so as to reduce the travel time errors introduced by the uncertainty of the source parameters and to meet the minimum requirement for reconstructing the local velocity structure using regional seismic data. Consequently, I have developed an earthquake hypocenter location program with the advantages of the 'irregular' approach of the shortest-path algorithm in the ray tracing process, the simple formulation of the analytical Jacobian matrix, and the non-linear inverse problem solver. Several numerical tests show that it works well with a relatively small location error for the source positions. The location error in depth is comparable to that in the horizontal plane, thus there is no problem in focal depth determination. The efficiency of the algorithm is that it is not sensitive to modest levels of picking error (less than, or equal to 0.1 s), but is seriously model-dependent. The capability of the algorithm is that it is suitable for relocating a hundred or more events simultaneously, making it practical for seismic array data and the location of an aftershock sequence. It can easily be incorporated with a 3-D travel time tomography procedure to form a joint seismic tomographic program for updating both the velocity model and the source positions. This forms subject matter of the following chapter.

Chapter 8: 3-D Joint Inversion for the Source Positions and the Velocity Model

8.1 Introduction

It was shown in Chapters 4, 5 and 7 that a 3-D velocity model can be recovered from the observed travel time or arrival time data from a seismic array network and the known source positions, and in turn the source positions can be relocated using the observed travel time data and a velocity distribution known to great accuracy. But in most practical applications, there is only the observed arrival time information available. Both the velocity model and the source positions can only be roughly estimated (or even unknown). In such circumstances, it is possible to invert simultaneously for both the velocity model and the source locations using the travel (or arrival) time data alone, such as in Rabaul volcano study, where the travel time information is available, but with large source parameter uncertainty in regional earthquake data. Thus, the purpose is to use a joint inverse procedure to improve the precision of the source parameters, while update the local velocity model. For this reason, in this Chapter, I incorporate the source hypocenter location algorithm from Chapter 7 into the procedure of 3-D travel time tomography in Chapter 4, to develop a program for joint inversion for determining both the velocity model and the source hypocenters. Some tests are carried out for the effectiveness of this approach, and also some limitations of the algorithm are investigated.

8.2 Methodology

The minimum norm and constrained least squares approach for determining both the hypocenter and the velocity distribution can be rewritten as:

$$\min \frac{1}{2}\left[\left\|\vec{d} - A\vec{m}\right\|_{L_2}^2 + \mu\left\|\vec{m}\right\|_{L_2}^2\right], \qquad \vec{a} \le \vec{m} \le \vec{b} \tag{8.1}$$

Equation (8.1) is in the same form as formula (4.1) in Chapter 4, but the content is somewhat different. Here, the unknown parameters of the model space include not only the velocity unknowns, but also the unknown coordinates of the various source hypocenters ($\vec{m} = [\delta V_1, \delta V_2, ..., \delta V_N; X_1, Y_1, Z_1 ..... X_M, Y_M, Z_M]$). The quantities N and M are the total number of velocity unknowns and the total number of sources, respectively. The analytical Jacobian matrix consists of two parts: one is the derivative of time with respect to velocity changes; the other is the derivative of time with respect to source position changes. The hard constraints are also separated into two parts: one is to constrain the perturbation of the velocity model; the other is to restrict the perturbation length of the source locations. Again I used the DMNLS-1 inversion procedure of section 4.2.

In the program development, due consideration need to be given to the location procedure in which six supplementary sources are added in the search directions. This makes the total number of input sources generally larger than the number of receivers. Thus, it is preferable to loop over receivers, and not sources (based on the principle of reciprocity) to save on computer run time. It is more difficult to adapt the automatic function of the model selection in this approach. Thus the run time for each loop hereafter is comparable to the run time in event hypocentral location.

8.3 Calculation of the Analytical Jacobian Matrix

The variation of travel time is taken to be the result of both velocity changes and source position changes. As in standard source hypocenter location, the origin time uncertainty is ignored and remains unchanged. The travel time errors (from the assigned trial sources to the receivers) can be expressed as:

$$\Delta t_{ij} = \sum_{k=1}^{3} \left(\frac{\delta t_{ij}}{\delta x_{ik}}\right) \Delta x_{ik} + \sum_{k=1}^{n} \left(\frac{\delta t_{ij}}{\delta v_k}\right) \Delta v_k \tag{8.2}$$

where t_{ij} is the travel time at the $j-th$ station which recorded the $i-th$ event, x_{ik} is the source coordinate in the k direction ($k = 1,2,3$) of the $i-th$ event, and v_k is the

$k-th$ velocity value in the model space of length N. Thus the analytical Jacobian matrix contains time derivatives with respect to both velocity changes and source position changes. The derivative of time to velocity changes can be calculated by formulae (4.9), (4.10) and (4.11); and the derivatives of time to source position changes can be simply obtained from section 7.4. Thus, a new analytical Jacobian matrix with length $\{n\times(N+3\times M)\}$ is formed (here n is the total number of raypaths), including the contributions of both the velocity model and the source positions.

8.4 Joint Travel Time Tomography

Theoretically, there is a trade-off between the velocity model estimation and the source position determination in a joint inversion procedure. Therefore, one cannot expect to obtain simultaneously both the velocity image with high quality, and source locations with high accuracy. Three numerical tests were undertaken to test the efficiency of this approach and evaluate both the quality of the image and the location error.

8.4.1 Numerical test 1: joint inversion with true source positions and input model having a large deviation from the true model

The synthetic model displayed in Figure 8.1 was selected to test the velocity field reconstruction capability, and the convergence features of the travel time residual, the perturbation of the velocity model and the disturbance of the source positions. The background velocity of the model is a 1-D layered distribution as shown in the diagram. Four low and two high velocity anomalies are

Fig. 8.1 True model for simultaneous inversion

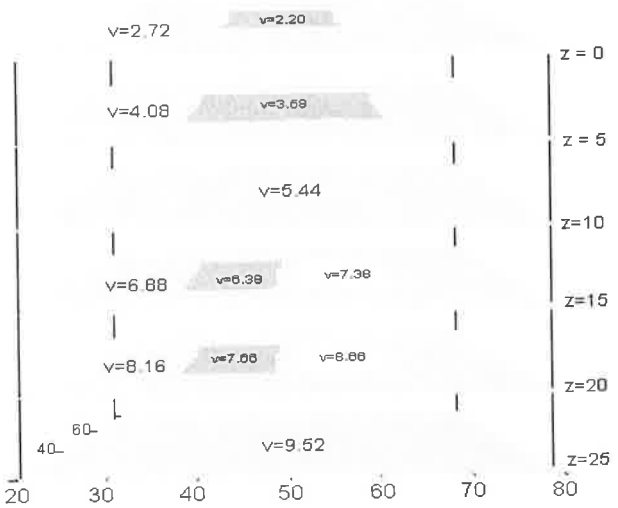

embedded in the model volume. Therefore, it is really a 3-D case for simultaneous inversion. The velocity anomalies have a ± 0.5 km/s deviation from the background velocity of the theoretical (or true) model, and the velocity contrast ranges from 6.0% at the lowest plane Z= 20 km to nearly 20.0 % at the top plane Z=0 km.

The source and receiver locations are shown (in plan view) in Figure 8.2, where there are in total 40 sources with different depths (from 0 to 25 km) arranged along the boundaries of the model, and 41 receivers with a $\sqrt{2} \times 5$ km uniform spacing between neighbouring stations on the top central region of the model. The model parameters are: model length (100 km, 100 km and 25 km in the X, Y, and Z directions); cell size (5 km in all three directions); the number of secondary nodes is 6 (in each direction of the cell); the damping factor is $\mu = 0.01$; the hard constraint for the velocity model is ± 2.5 km/s and the constraint for the source positions are that they are forced to lie within the model volume.

Fig. 8.2 The distribution of sources (black) and receivers (grey) for joint inversion of test 1

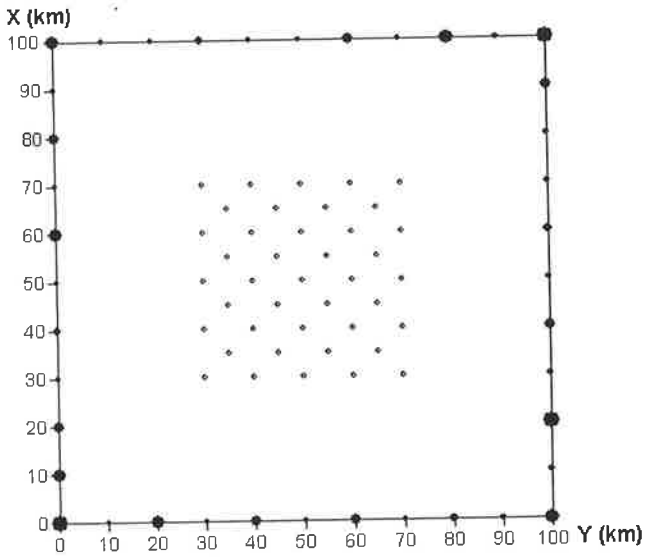

There are in total 1640 ray paths which cross the model and 2646+120=2766 unknown parameters in the inversion process. Following the routines outlined in chapter 7, I first obtained the theoretical travel times according to the true velocity model and the real source locations. These theoretical travel time data will be used as observed travel time data later in the joint inversion process. The starting (input) velocity model is also a 1-D layered velocity model with relatively large deviations from the background velocity of the true model. The deviations are -0.42, -0.58, -0.44, -0.50, -0.50 and -0.50 km/s at the planes Z=0, 5, 10, 15, 20 and 25 km, respectively. This means that the input model has velocities roughly 0.5 km/s lower than that of the

true background values. For the test, the initial source positions are first set at the true hypocentral locations.

If the program works, one can expect that the velocity anomalies within the model should be recovered and the updated source positions should not deviate far from the true hypocentral locations. Figure 8.3 shows the comparison between the true and the recovered velocity model from the joint inversion after 20 iterations. It can be seen that the main features (size and location) of the low and high velocity anomalies are nearly perfectly reconstructed. The two opposing anomalies (one low and the other a high velocity anomaly) at the planes Z=15 and 20 km are nearly the same as the true anomalies.

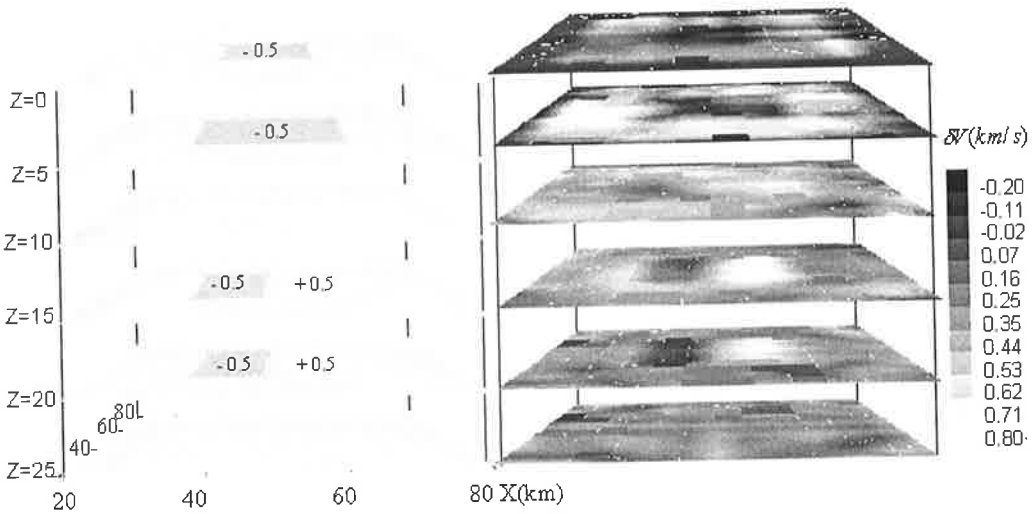

Fig. 8.3 The comparison between the true velocity perturbation (left panel) and the unfiltered image (right panel) from the joint inversion test 1

In order to separate the distance convergence from the model space, two kinds of distances are recognized: one is the distance between the present and previously updated sources, which indicates the convergence status in the joint inversion process; the other is the distance between the present updated sources and the true sources, which represents the absolute location ability in the joint inversion procedure. Figure 8.4 shows the results of these two kinds of distance convergence. Both diagrams 8.4a and 8.4b show the approach has worked. This is especially evident in Figure 8.4b, where the RMS error of the distance between the located and the true source positions

is slightly increased (deviates from the true source positions), but is less than 0.25 km and maintains stability to an acceptable level of accuracy after the 10-th iteration.

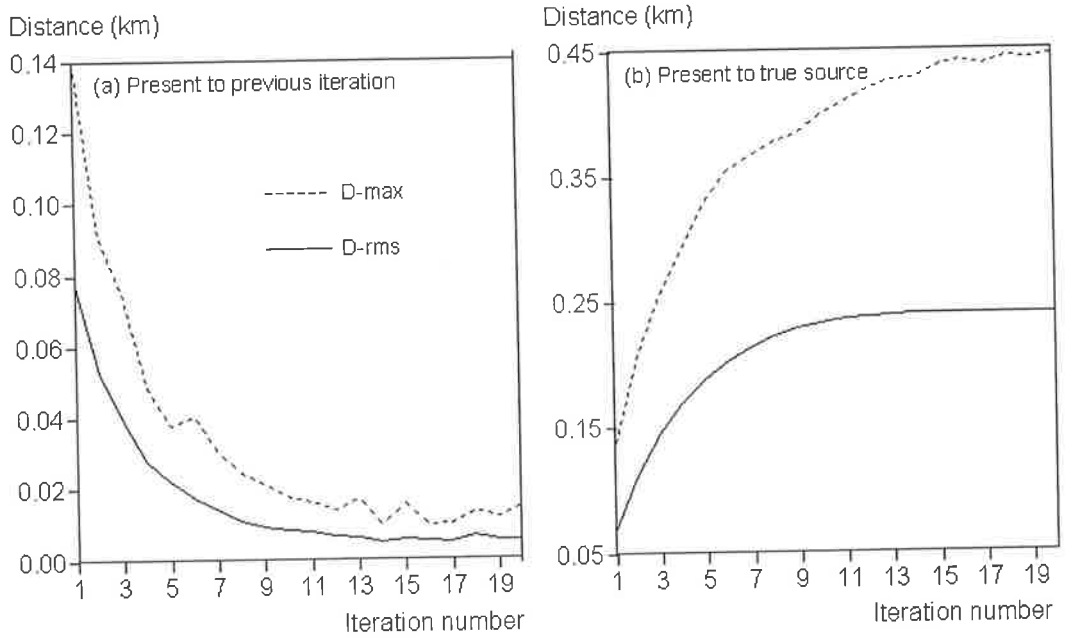

Fig. 8.4 The two kinds of distance convergence for joint travel time inversion of test 1 (In diagram: D-max: maximum distance; D-rms: RMS of distance)

To further analyze the contribution of distance convergence from different directions, I calculated the distance from the updated source to the true source position in all three directions after each iteration. Figure 8.5 shows the statistical results. In the X and Y directions (within the horizontal plane), the distance convergence is nearly the same, but the distance convergence in the vertical direction is comparable to the true distance convergence. This means that the main contributor to the location error is from the vertical direction. This is further evidence to indicate that the algorithm works, because

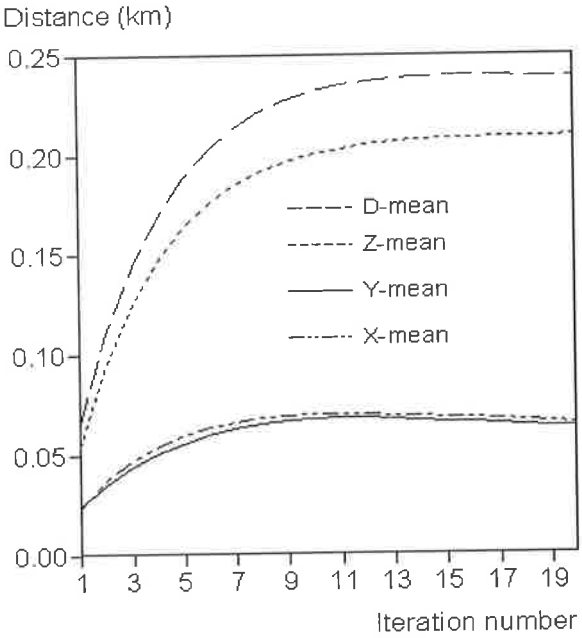

Fig. 8.5 Distance convergence in three directions for the joint inversion of test 1

there is a rapidly changing velocity distribution in the vertical direction as opposed to the other two directions in the horizontal plane. Thus, the favorable direction to reduce the time residual is to adjust the Z coordinate rather than to adjust the co-ordinates in the X or Y directions (horizontal plane).

8.4.2 Numerical test 2: joint inversion with the true source locations and the background velocity field of the true model as the starting model

In this numerical test I will evaluate the effect of the input model on the final results of a joint inversion. For this purpose, I selected exactly the same model as numerical test 1; the model parameters, constraints and input source positions (using real source locations) are the same as in numerical test 1. The only difference is that the actual background velocity of the true model is taken as the starting (input) velocity model in the joint inversion. In such situations, the travel time residuals between the observed and the computed times only arise from the presence of anomalous low and high velocity regions in the true velocity model.

Figure 8.6 is a comparison of the un-filtered images from the two different starting (input) velocity models (one is the result of test 1 and the other is the result of this test). The better image is found for numerical test 2, which involves a close estimation of the starting velocity model and less iterations. In common with numerical test 1, there are two kinds of distance convergence (see Figure 8.7). Note that the distance error (RMS) between the located source after each iteration and the true source is less than 0.035 km. Even the maximum distance error is less than 0.10 km.

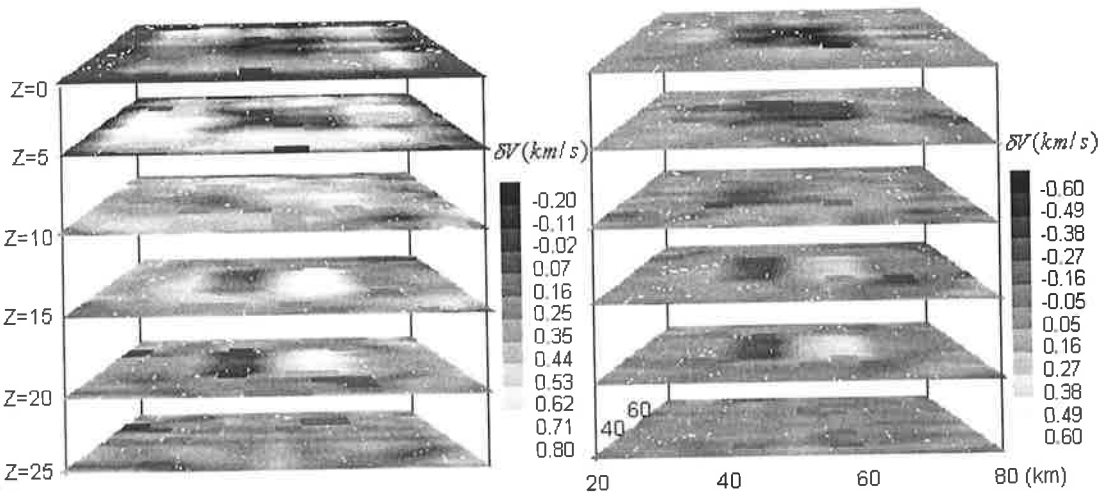

Fig. 8.6 The comparison of the unfiltered images for joint travel time inversion between numerical test 1 (left panel) and test 2 (right panel)

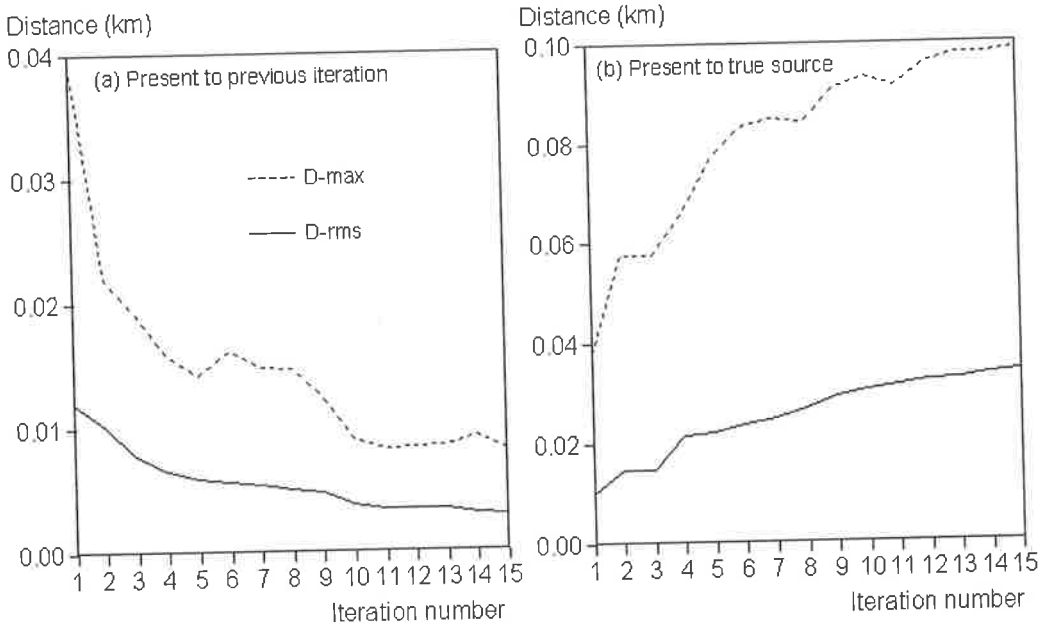

Fig. 8.7 The two kinds of distance convergence for joint travel time inversion of test 2 (In diagram: D-max: maximum distance; D-rms: RMS of distance)

In a mathematical sense, under such conditions of joint hypocenter / velocity model inversion, the source locations are nearly unchanged. This is to be expected, because the residuals between the observed and computed travel times only results from the six velocity anomalies in the true velocity model. Thus the theoretical development of the model is supported by the results of these numerical tests. Figure 8.8 shows the convergence of both the travel time residual and the perturbation of the model (both velocity and source positions). The results of test 2 indicate that the closer the estimated (initial) velocity is to the true model, the better the image.

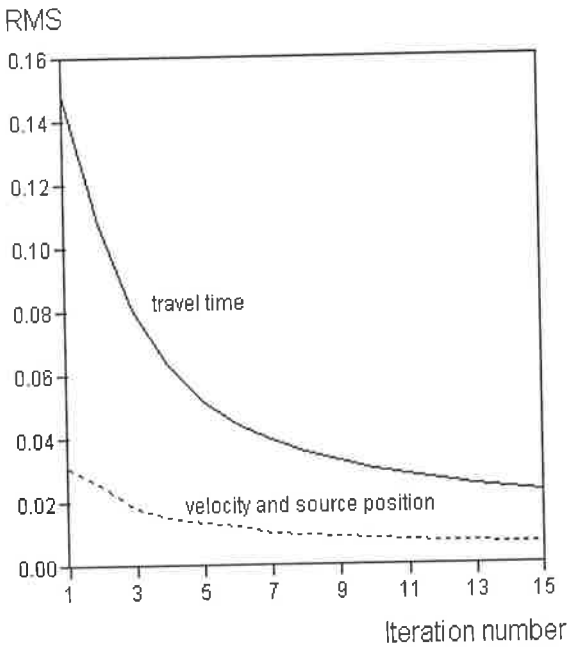

Fig.8.8 The Convergence curves for joint Inversion of test 2

8.4.3 Numerical test 3: Joint inversion with large deviations both in the starting velocity model and in the source positions

To simulate a real problem in joint inversion, the same model as for numerical test 1 was selected, but with a crudely estimated input velocity model and very rough source positions. The input model deviations from the background of the true velocity model are -0.42, -0.58, -0.44, -0.50, -0.50 and -0.50 km/s at the planes Z=0, 5, 10, 15, 20 and 25 km, respectively (see test 1). This means that the first guess model is roughly 0.5 km/s under estimated compared to the true velocity model. I randomly set the input (first guess) hypocenters from 2.8 to 5.0 km away from the true hypocentral locations. This is very challenging test and also a good example to evaluate the effectiveness of the algorithm. The other parameters are the same as for numerical test 1. Figure 8.9 compares the true velocity model and the filtered image from this test (filtering window is 3-point, and a mean value filter is applied in 2-D case). Even for an input model with a relatively large deviation from the true model and for input source locations with a moderate deviation from the true source locations, the main features (size and location) of the velocity anomalies within the model are recovered. This is especially true of the two opposing (positive and negative) anomalies on the planes Z=15 and 20 km, which are nearly identical to the true anomalies.

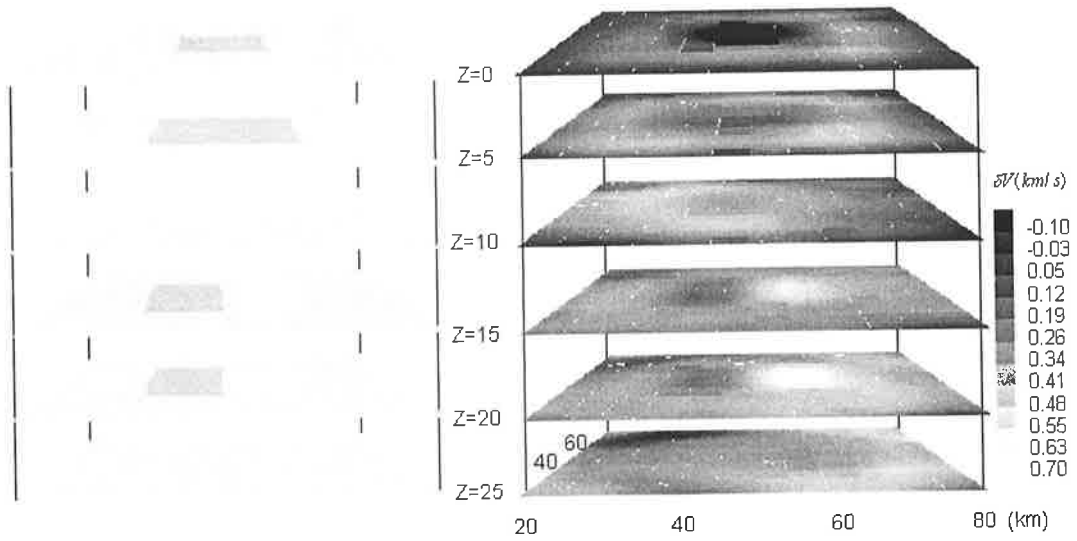

Figure 8.9 The comparison between the true velocity perturbation (left panel) and the filtered image (right panel) from joint inversion test 3

Figure 8.10 illustrates the associated convergence curves for the travel time residual and the model perturbation. Even after 20 iterations there is still a downward error trend for both the time residual and the model perturbation. Compared with the results of numerical test 1, which has the same large deviation of input velocity model from the true velocity model (but with the correct sources as the input sources), the algorithm requires more iterations to converge to the same level of time residual and model perturbation. It also takes more iterations to reach the level of stability achieved in test 1.

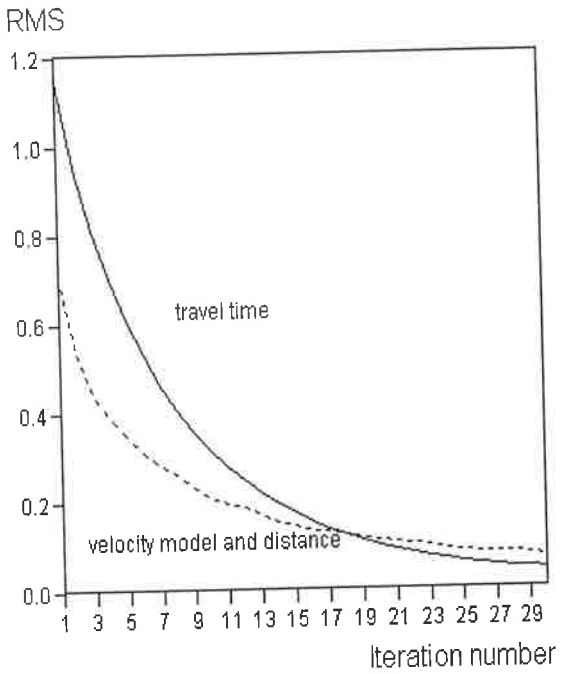

Fig.8.10 Convergence curves for joint inversion of test 3 (In diagram model perturbation is enlarged 10 times for comparison)

The two kinds of distance convergence, as described before, are again calculated (see Figure 8.11). From Figure 8.11b, it can be seen that the located source positions are converging to the true source locations (decreased distance) with increasing iteration number. Because of the effect of trade-off between the perturbation of the velocity model and the disturbance to the source positions, the located source hypocenter positions still have some deviations from the true source locations, but the convergence trends are clear. The maximum distance deviation is reduced by roughly 1.0 km, and the mean distance (or RMS) is also reduced by 1.0 km. This means that the algorithm can improve the accuracy of the location even under such challenging conditions (such as a 3-D case with only a roughly estimated input velocity model and rough input source hypocenters), but only has a relative sense in accuracy. It is worth pointing out that one could not expect to obtain both a good quality image, as in Chapter 4 and 5, and a high accuracy of location result as in Chapter 7, due to the trade-off between the perturbations of the velocity model and disturbing length of the source locations. In practical applications, one must be aware of the limitation (rough

estimation of velocity field and source hypocenters) of a joint inversion.

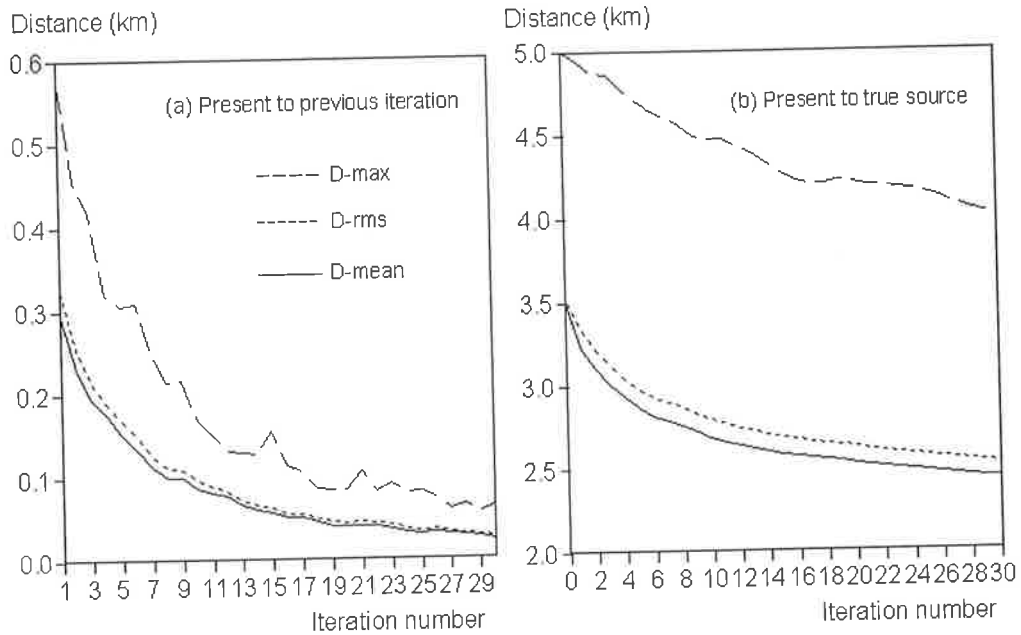

Figure 8.11 The two kinds of distance convergence for joint travel time inversion of test 3 (In diagram: D-max: maximum dist.; D-rms: RMS of dist.; D-mean: mean dist.)

In summary, there is no theoretical problem to simultaneously determine both the velocity distribution and the source hypocenters using travel (or arrival) time information alone, but there are different weights on the time derivative to velocity changes and source position changes in the analytical Jacobian matrix. Thus there is a trade-off between the perturbation of the velocity model and the disturbance of the source locations. In other words, an improvement in image quality may be accompanied by a loss of accuracy in event location, and vice versa. In practical applications, a possible sequence would be as follows: (1) roughly estimate both the velocity model and the source hypocenters; (2) relocate the source hypocenters by using this roughly estimated velocity model; (3) obtain the improved velocity model by using the relocated source hypocenters. It is possible to change the order of steps (2) and (3). It may require more iterations to improve the final results for both the velocity model and the source hypocenters. It is worth pointing out that this separation of steps (2) and (3) is based on the rough guesses for both the velocity model and the source locations of step (1). Theoretically, it is unreasonable to loop through steps (2) and (3)

without having roughly estimated the velocity model and the source locations, because the algorithm for the event location is model-dependent and the method of velocity inversion is source-dependent. If the velocity model has a large deviation from the true velocity distribution, the location algorithm will find the minimum time residual according to this velocity model, and the updated source positions will have a large adjustment that may deviate even further from the true source locations. In turn, the velocity inversion method will find the minimum time residual according to the wrong sources with large distances from the true sources, causing the reconstructed velocity model to deviate further from the true velocity model. That is to say, under such circumstances there is no guarantee of finding a global minimum point in the model space to fit both the velocity distribution and the source locations.

8.5 Discussion

This chapter and the preceding chapters conclude the theoretical developments of travel time tomography. Now it is time to deal with the main driver of the thesis: to reconstruct the Rabaul 3-D velocity structure with full usage of the existing explosion / earthquake dataset. For real data, the basic requirement is to prepare the observed travel time database and re-analyze these data so as to guarantee the data quality. This is an important factor in the final image as discussed earlier. For these purposes, the following chapter will concentrate on the onset time picking and data pre-processing to prepare a relatively good quality dataset for the reconstruction of the Rabaul volcano velocity structure.

Chapter 9: Onset Time Picking and Data Preliminary Analysis

9.1 Introduction

The total number of known events in the RELACS database is 403, including 30 explosions, 187 local earthquakes, 89 regional earthquakes and 97 teleseisms (see chapter 2). The researchers who undertook the RELACS project only picked 145 events, including 30 explosions, 78 local events, 22 regional events and 15 teleseisms. Among the picked phases, more than 90% were P arrivals. The data coverage is not good enough to obtain a reasonable image (see Figure 2.5). Therefore, it is necessary to pick as many additional arrival times as possible, especially S arrival times, so as to improve the data coverage from the near-regional scale and to add more first S arrival times into the database. From Figure 2.5 one can see that to the north of Rabaul there are only a few earthquakes. They are essential for the data coverage. The explosions cover the near-north part of Rabaul and they too are indispensable events. Considering my aim was to combine the near-regional events with local events to image the local, deep velocity structure of the Rabaul region, the additional picking efforts were concentrated within the near-regional scale (see Figure 2.5 for boundary definition). In order to save time, and being aware of the importance of the events referred to above, I decided to determine all arrival times for the above-mentioned events, regardless of whether the events were previously picked by the RELACS project or not.

For the remaining known events in the restricted region, I determined arrival times that had previously been ignored in the RELACS project. The algorithm used was an automatic combined picking function, for detecting both first P and S arrival times with an acceptable error. To fully understand how the picking functions work, I will now briefly introduce and analyze several picking functions that were used in the combined method. This should aid understanding of their physical meaning, and give an estimation of the likely picking error.

9.2 Different Techniques of Onset Time Picking

All current methods of identification and recognition of seismic phases are based on utilizing different characteristics of noise and signal in a variety of domains: e.g amplitude (energy content), frequency (frequency content), waveform (similarity of waveform), angle of arrival (the differences in the wave vectors) and other dynamic features, such as polarization, rectilinearity, and etc. However, there is no single method that can ensure consistent onset time picking for every phase in any situation. The problem is that any single method will fail when the difference between a certain part of the noise and the signal, as far as that characteristic is concerned, is very small (similar characteristics), particularly when the S/N ratio is low. For example, the energy method cannot be used when the noise level is high or the later phases are buried in the strong coda of earlier arrivals. Bandpass filtering will not work when the noise and signal share almost the same frequency content. In order to overcome the drawbacks of any single method, it is necessary to use a combined method (Bai and Kennett, 2000). The combined method includes the energy function, auto-regressive representation, instantaneous frequency, and polarization analysis. Here I introduce the first two methods and then show how to create the combined method.

9.1.1 Energy function

Energy analysis is based on the ratio of the short-term-average (STA) energy to long-term-average (LTA) energy level (STA/LTA) derived from the same seismogram. Several different algorithms have been employed in such energy analysis (for example, Tong and Kennett, 1996; Earle and Shearer, 1994). The differences among them arise from the choice of the energy ratio between different ground motion components and the use of different co-ordinate systems {such as rotated to the P, SH and SV system, or the vertical (Z), radial (R) and transverse (T) system}, and also the length of time window employed when calculating the energy ratio. I followed the expressions of Tong and Kennett (1996) in an unrotated (vertical (Z), north (N) and east (E)) data system:

The total energy $$E_3 = Z^2 + N^2 + E^2$$

Energy in the vertical direction $V_e = Z^2$

Energy in the horizontal plane $H_e = N^2 + E^2$

Here Z, N and E are the amplitudes of the three unrotated (raw) records, respectively.

The recognition and detection scheme is based on the use of a STA/LTA ratio technique in which the local temporal behavior is compared to a longer-term trend.

The energy ratio Z_E can be defined as the ratio of the vertical to the total energy, H_E as the ratio of the horizontal to the total energy, and Z_H as the ratio of the vertical to horizontal energy. Thus six different energy ratios can be generated:

(a) the total energy ratio of short to longer-term trend

$$E_3 = \frac{E_3(STA)}{E_3(LTA)} \tag{9.1}$$

(b) the vertical energy ratio of short to longer-term trend

$$Z_e = \frac{V_E(STA)}{V_E(LTA)} \tag{9.2}$$

(c) the horizontal energy ratio of short to longer-term trend

$$H_e = \frac{H_e(STA)}{H_e(LTA)} \tag{9.3}$$

(d) the energy ratio Z_E of short to longer-term trend

$$Z_E = \frac{Z_E(STA)}{Z_E(LTA)} \tag{9.4}$$

(e) the energy ratio Z_H of short to longer-term trend

$$Z_H = \frac{Z_H(STA)}{Z_H(LTA)} \tag{9.5}$$

(f) the energy ratio H_E of short to longer-term trend

$$H_E = \frac{H_E(STA)}{H_E(LTA)} \tag{9.6}$$

An adaptive time window rather than an explicit one is used, where the STA and LTA

values (S, C) are incremented each time. Thus, taking Z_E as an example,

$$S = C_S(\overline{S} + Z_E), \quad C = C_L(\overline{L} + Z_E) \tag{9.7}$$

Here $\overline{S}$ and $\overline{L}$ are the short-term averaged and long-term averaged value, respectively. The parameters C_S and C_L are chosen to be smaller than unity. These control contributions from the preceding time step, and thus the effective lengths of the STA and LTA windows. If f_0 is the local (short-term) frequency, then C_S and C_L can be chosen as:

$$C_S = 10^{-f_0 \cdot \Delta T}, \quad C_L = 10^{-f_0 \cdot \Delta T/12} \tag{9.8}$$

Here ΔT is the time sampling interval. The LTA time window has been chosen to be 12 times as long as the STA time window in equation 9.8. A recognition or detection trigger is declared when the ratio of STA to LTA measure exceeds a pre-specified threshold value. Figure 9.1 shows an example of arrival time picking using the energy function {formula (9.2)} for a single trace. The main purpose of 'viewsud.c' (a software module written by Arcidiaco Armando of RSES, ANU, one of the staff involved in the RELACS project) was to pick the arrival time on-screen. It is not suitable for my usage. Thus, I modified it and incorporated several picking functions to make it more practical.

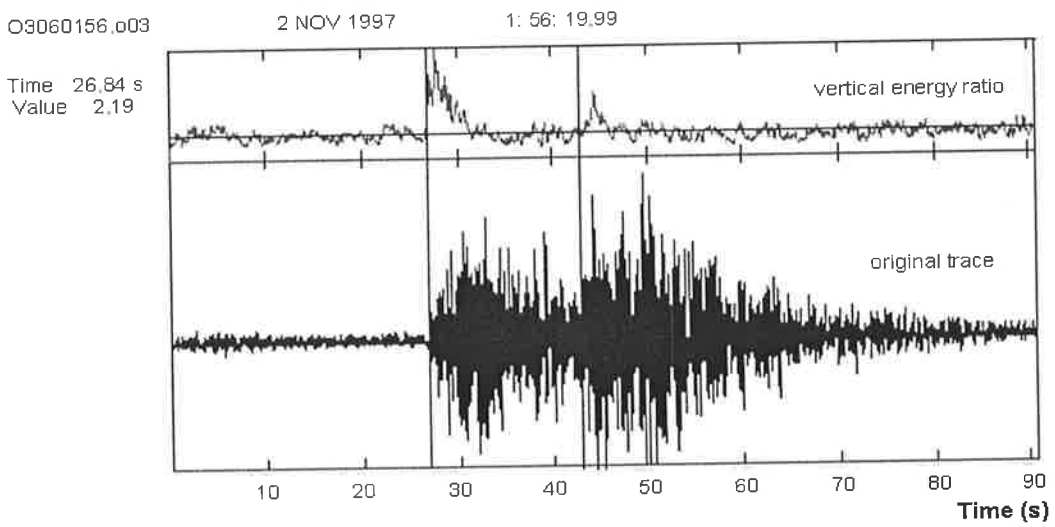

Figure. 9.1 The onset time picking using the energy method (top panel) for a single seismic trace (bottom panel)

Figure 9.2 shows another example of arrival time picking using the energy function for three-component records. In a practical sense, if the epicentral distance of the event is not short (i.e. the S and P arrivals have a detectable separation, or the S arrival does not follow immediately after the strong P wave code), the energy picking function works well for extracting both the first P and S arrivals simultaneously, especially on the three-component records for regional and teleseismic events (Tong and Kennett, 1996).

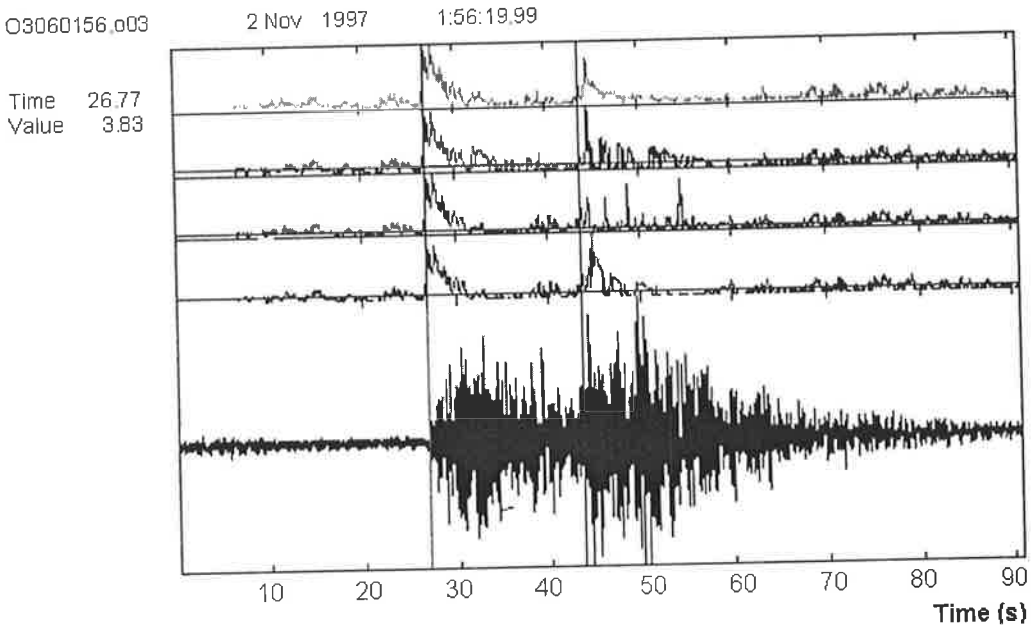

Figure 9.2 The onset time picking using the energy ratio from the different components (from top to bottom are sum of three energy ratio, the total energy ratio, the horizontal energy ratio, the vertical energy ratio, and the original seismic trace)

9.2.2 Auto-regressive coefficient analysis

Seismograms comprise both the desired seismic signals and other unwanted contributions, which are referred to as noise. For the seismic signal, it is assumed that each phase has its own characteristics (energy, frequency, waveform and angle of arrival vector) and will last at least a few seconds. Thus for a particular phase, it is expected that the present value of ground motion will be related to the previous value. Two different styles of noise contributions can be considered: one is white noise that has a stochastic property; the other is microseismic noise such as the ground motion

from distant storms or the unrecognized coda of an earlier event. For random noise the current value is unrelated to the previous value; and for the second style of noise there will be a weak association of the current value with the previous value (which can be alternatively expressed in terms of a lower order correlation than for the seismic signal). The differences in the nature of the signal and noise contributions allow the use of an auto-regressive representation of seismograms for identifying phases and making onset time picks.

If $\vec{u}_t$ is a vector of seismic ground motion and $\vec{v}_t$ is the noise, an m-th order of auto-regressive (AR) model for the 3-component seismic trace can be described as:

$$\vec{u}_t = \sum_{i=1}^{m} A_i \vec{u}_{t-i} + \vec{v}_t \tag{9.9}$$

with

$$A_i = \begin{pmatrix} a_{i11} & a_{i12} & a_{i13} \\ a_{i21} & a_{i22} & a_{i23} \\ a_{i31} & a_{i32} & a_{i33} \end{pmatrix}$$

Here A_i is a tensor AR coefficient. In the representation (9.9) the current seismic motion is predicted by a linear combination of a set of m previous values. In order to simplify the process, I regarded $\vec{V}_t$ as representing only the white noise (the other type of the noise which has a low order correlation will be discussed in a later section). For a random white-noise sequence, the present value will not depend on the prior values. Thus, taking the product of (9.9) with $\vec{u}_s$ and averaging over the stochastic sequence, one obtains:

$$\langle \vec{u}_t \vec{u}_s \rangle = \sum_{i=1}^{m} A_i \langle \vec{u}_{t-i} \vec{u}_s \rangle \qquad s<t \tag{9.10}$$

which can be further rewritten as:

$$r_k = \sum_{i=1}^{m} A_i . r_{k-i} \qquad k = 1,\ldots\ldots,m \tag{9.11}$$

$$r_k = \begin{pmatrix} r_{11} & r_{12} & r_{13} \\ r_{21} & r_{22} & r_{23} \\ r_{31} & r_{32} & r_{33} \end{pmatrix}$$

Here r_k is the tensor auto-correlation, r_{ii} is the auto-correlation, and $r_{ij}(i \neq j)$ is the cross-correlation of component i with component j at a delay of k samples.

There are two ways to use the AR Model for recognition and onset time picking. One approach is to use the Akaike Information Criterion (AIC) (Akaike, 1973) to first determine the order of the AR filter, then apply the AR filter to the seismogram, and finally recognize onset time picks as the point where the style of AR representation changes (Takanami & Mitagawa, 1991; Leonard and Kennett, 1999). Figure 9.3 displays the AIC minimum function (upper panel in diagram a) and related onset time picking using function ($\frac{1}{AIC}$) (upper panel in diagram b). In figure, the long vertical bar indicates where the pick was made.

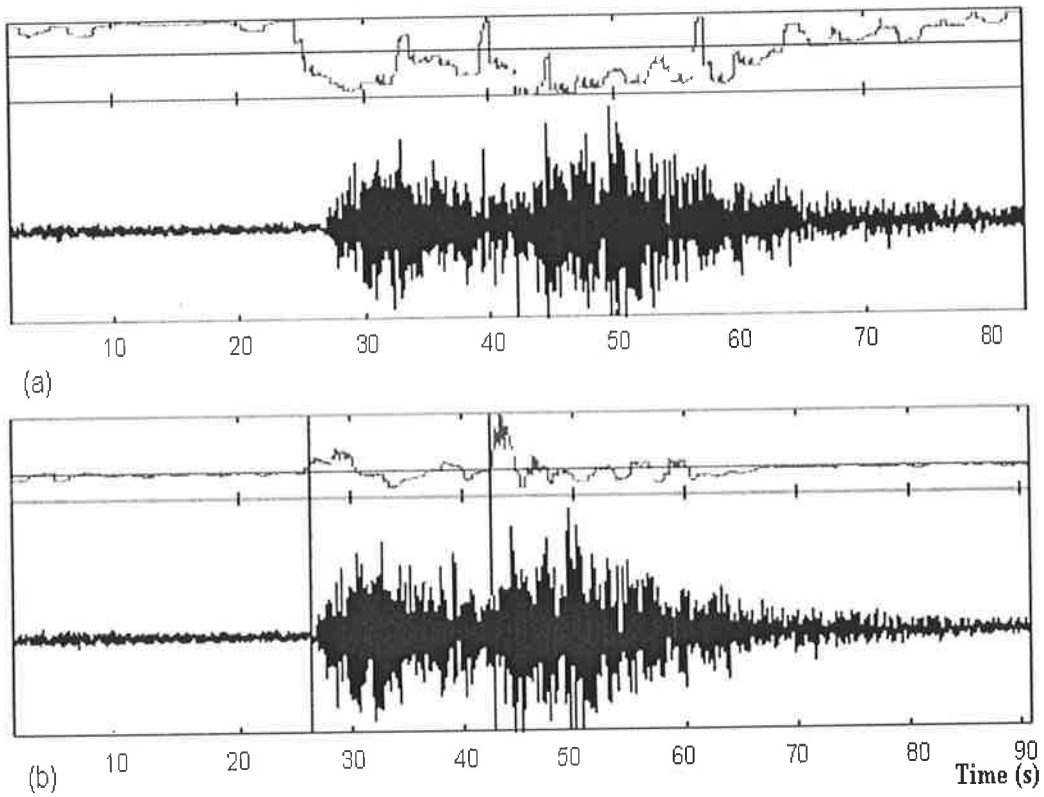

Fig. 9.3 AIC minimum function (diagram a) and the related picking function ($\frac{1}{AIC}$) (diagram b) for a single seismic trace

The other way is to use a predictive AR Model to separate the seismic signal from background noise (Takanami & Mitagawa, 1991, 1993). Figure 9.4 shows an example of a predicted single trace using different adaptive auto-correlative AR models. That is, to use different order (m) of AR model to predict the current ground motion using the previously m values. In Figure 9.4, only the auto-correlation coefficient is used in equation 9.10.

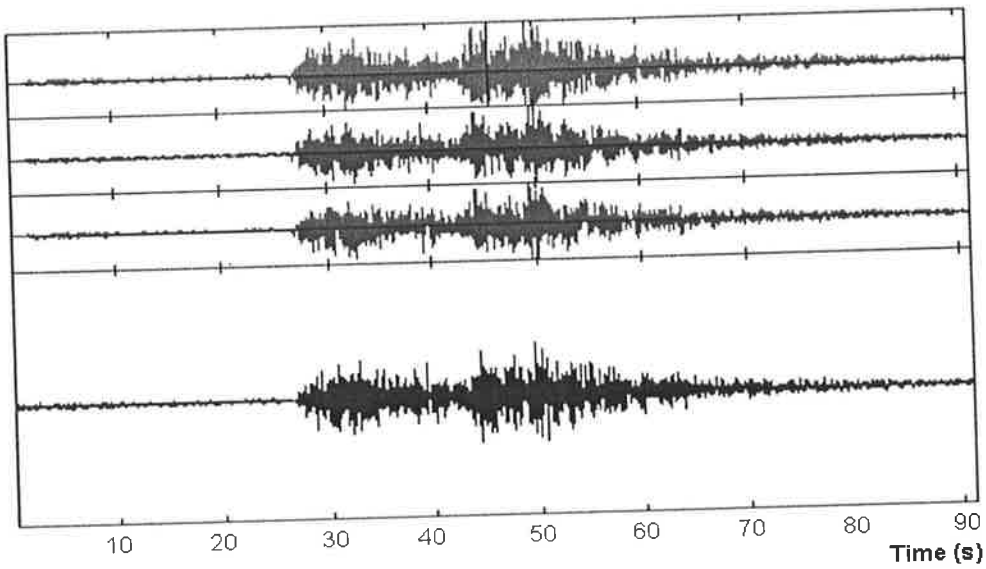

Fig. 9.4 The comparison between the original and predicted traces using different orders of AR model (upper panel: order=12; middle panel: order=9; lower panel: order=6; bottom panel: the original trace)

For display and identification purposes, I use a simpler approach, construct just the tensor coefficients and assume that the values of the auto-regressive coefficient will be enhanced when a seismic phase arrives. Figure 9.5 shows an example of nine attributes of auto- and cross-correlation coefficients.

As mentioned above, the auto-regressive coefficient technique can remove the white noise, but will retain the microseismic noise that has low order correlation (or weak correlation). In order to remove the microseismic noise, the higher order coefficients were extracted. A representation of two joint auto- and cross-correlation coefficients can be used to highlight the seismic signal and suppress the noise. I calculated the difference of the auto- and cross-correlation coefficients in a certain time window using the value obtained by subtracting the first half time window from the second

half time window. Figure 9.6 displays this kind of picking function compared with the auto-correlation function and the energy function. From Figure 9.6, it is clear that the best picking function is the representation of the difference of two joint auto-correlation coefficients. Under such conditions, the signals are normally well separated and further highlighted. As a result, the noise is generally suppressed.

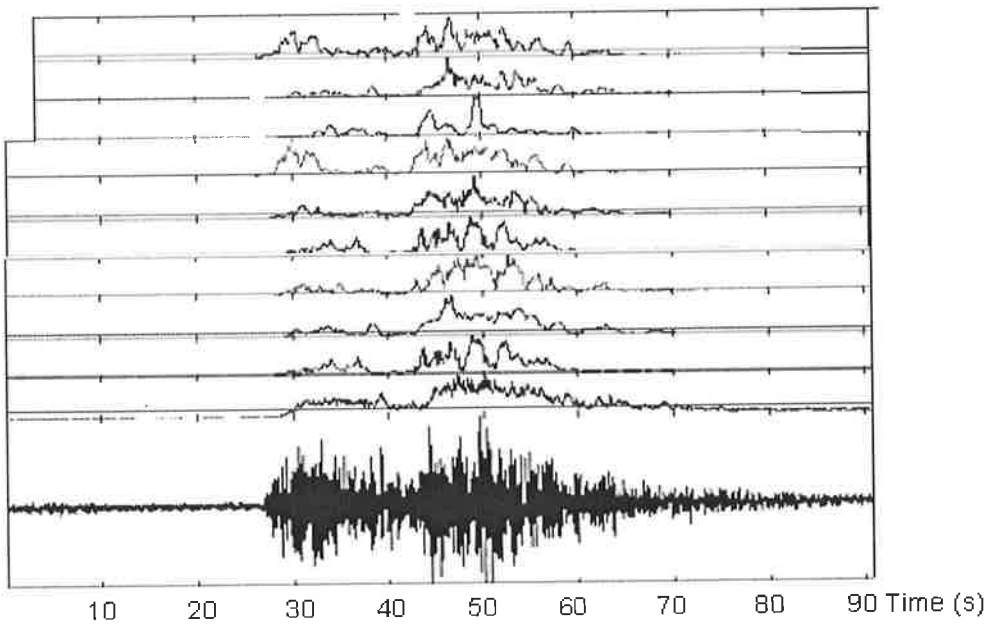

Fig.9.5 The picking function for auto- and cross-correlation coefficient analysis (from top to bottom are ZZ, ZE, ZN; EZ, EE, EN; NZ, NE, NN; energy function and original trace)

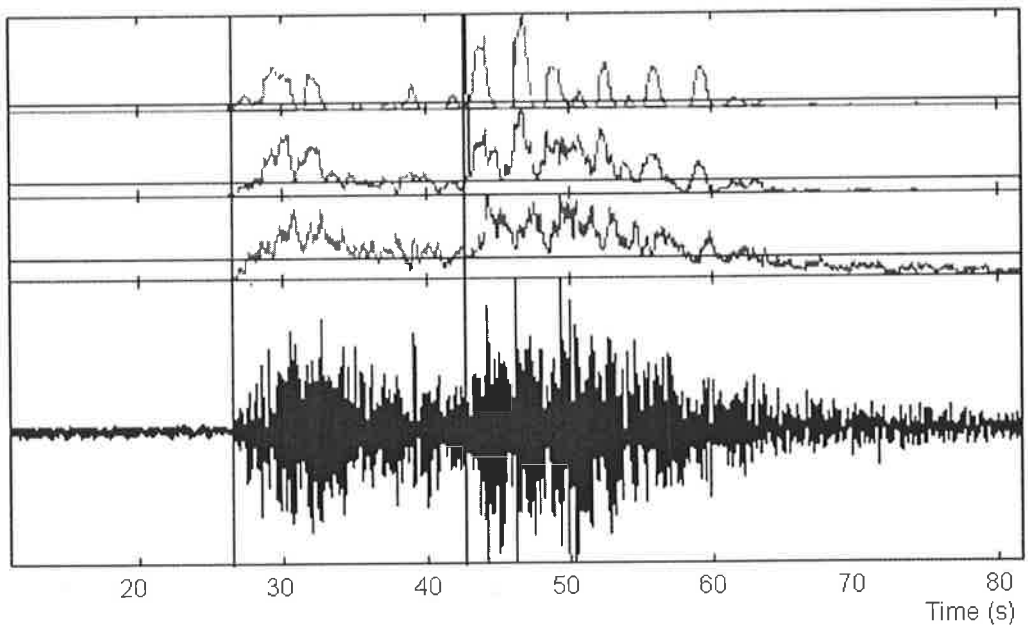

Fig.9.6 The comparison of the three picking functions (upper three panels: the difference of two joint auto-correlation coefficients (top); auto-correlation coefficients (middle); energy (lower) and original seismic trace (bottom panel)

Figure 9.7 shows an example when the nine attributes of two joint auto- and cross-correlation coefficients are used as the picking functions. In practice, the STA/LTA ratio technique is applied to the picking function for the difference of two joint auto- and cross-correlation coefficient representations. Figure 9.8 shows an example of onset time picking when using the difference of two joint auto-correlation coefficients applied to a single trace. Here the two consecutive P arrivals are well separated. Generally, the selected time window is dependent on the sampling rate and also on the local frequency. Such technique problems are not my primary concern in this thesis. For details, see the papers given by Bai and Kennett (2000 and 2001) and Tong and Kennett (1996).

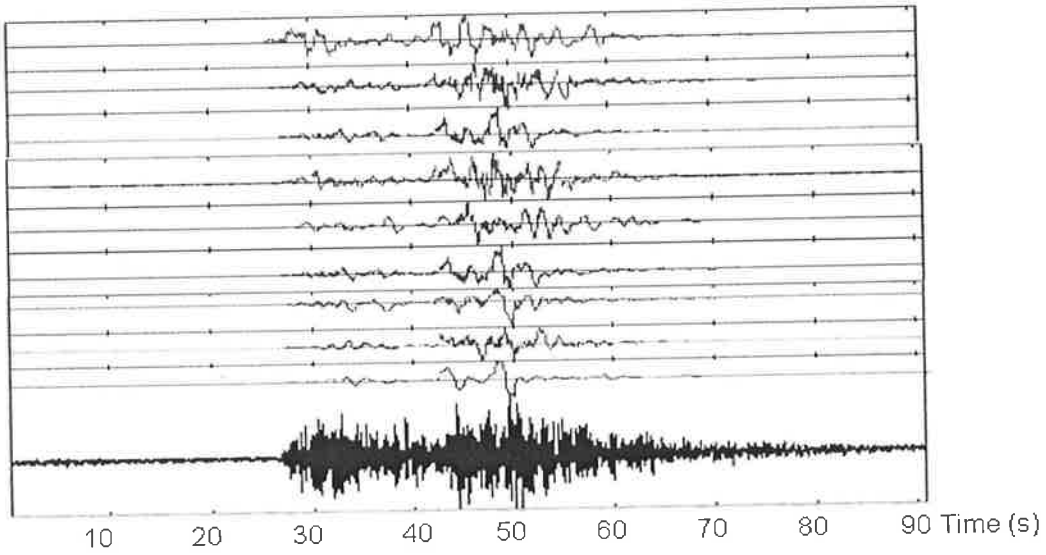

Fig. 9.7 The difference of two joint auto- and cross-correlation coefficients (Upper nine panels are ZZ, ZE, ZN; EZ, EE, EN; NZ, NE, NN) and original trace (Bottom)

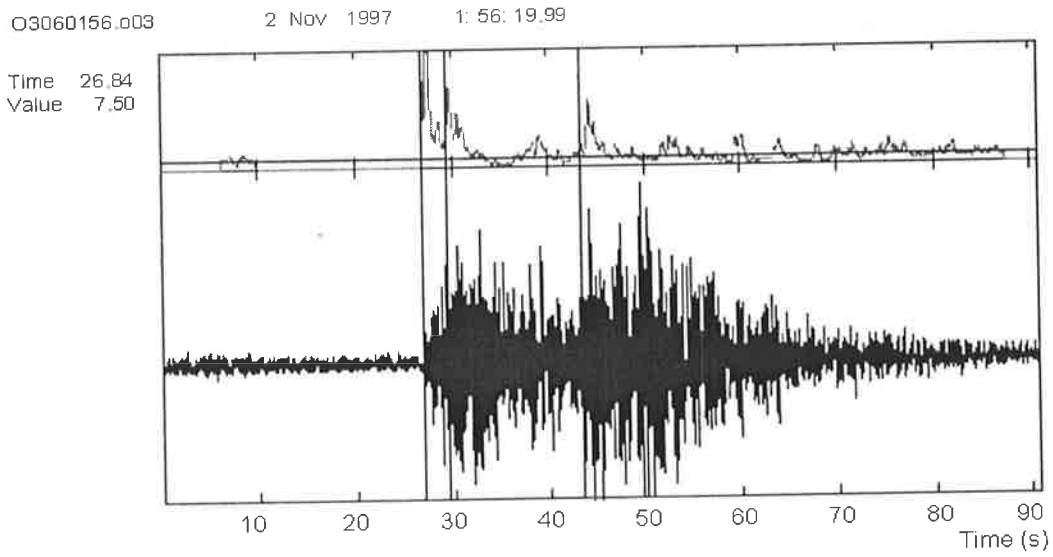

Fig. 9.8 The picking function for the difference of two joint auto-correlation coefficients (top) and original trace(bottom)

9.3 Automatic Onset Time Picking Using A Combined Method

It is possible to combine the different picking techniques that exploit the different seismic characteristics to form a combined picking function (Bai and Kennett, 2000). Such an approach overcomes the drawbacks of a single picking algorithm. With the requirement that the picking function be suitable for both single- and three-component recordings in the RELACS project, here I only exploited the energy technique and the representation of auto- and cross-correlation coefficients to form a combined picking algorithm (Instantaneous frequency and polarization analysis are restricted to three component records and offer additional capability). For single-component records, the combined function includes: the vertical energy ratio (Z_e) of short to long-term trend, and the difference of two joint auto-correlation coefficients. For three-component records, the combined function includes: the six energy ratios (see section 9.2.1) of short to long-term trend, 3 differences of two joint auto-correlation coefficients and 6 differences of two joint cross-correlation coefficients. In total, there are 15 attributes in the combined picking function. Basically, there are three ways to form the combined picking function according to these 15 attributes: (1) simple summation over these 15 quantities; (2) summation over these 15 quantities with a certain weighting factor applied to each quantity; (3) simple multiplication of these 15 quantities. Generally, the latter approach (3) can highlight the signal well, but totally loses the signal when one of these quantities has a zero value. Approach (1) is the simplest one, but does not weight the different attributes. Thus I preferred approach (2). Therefore, in the combined picking function, an equal weight is set on the energy technique and auto-regressive representation. That is, for each quantity in energy analysis of three-component records, the weight is $\frac{1}{2}\times\frac{1}{6}$; for each quantity in auto-regressive representation of three-component records, the weight is $\frac{1}{2}\times\frac{1}{9}$. For single-component records, the weight is $\frac{1}{2}$ for both the energy and auto-regressive analysis. An arrival is declared when the value of the combined function exceeds a specified trigger level. In order to select a fixed trigger level, I normalized the value of the combined picking function in

the data processing. Due to the different sampling rates among the different recorders, the time window is selected according to the time, and not according to the sample points.

9.4 Onset Time Picking for Real Data

The above automatic picking function works well both for first P and S arrivals, but lacks the information to separate P arrivals from S arrivals. For three-component records, where available, I used the approach of Bai and Kennett (2000) to separate P arrivals from S arrivals according to the polarization attributes. But for single-component records, there are no efficient techniques to separate P arrivals from S arrivals. In such circumstances, in order to avoid mis-picking the first S arrival, I first ran the automatic picking routine, and then double checked the first P and especially the first S arrival with the on-screen computer aid (revised 'viewsud.c' program). Finally, the picked arrival times were written to the file (vpicka.xxx).

I compared my picking results with the results of the RELACS project on 30 explosion records. There is generally not much difference between the two sets of picks for the first P arrivals (the picking uncertainties are within ± 0.03 second). The RELACS project seldom had S arrivals picked. Thus, for the first S arrivals, my picking uncertainties are within ± 0.06 second. Finally, I picked a total of 161 events, including 30 explosions (re-picked for obtaining the first S arrival time), 109 regional events and 22 teleseismic events. Figure 9.9 is a comparison of the picked events (within the near-regional scale) for first P and S arrivals between the RELACS project and this study. In Figure 9.9a, the total number of events is 157. Of these, 89 are original picked events from the RELACS project; the rest (98, including 30 explosions) are picked in this study. It is clear that the picked events in this study are mostly to the south of Rabaul volcano. By supplementing with the additional picked events in this study, the data coverage around Rabaul volcano is much improved. For the events shown in Figure 9.9b, there are in total 94 events, which have the first S-arrival times. The RELACS project picked only 31 of these events, the rest (63) were picked in this study.

Of the 31 RELACS-picked S arrivals, most were re-picked. This group of events was restricted to the near south of Rabaul volcano (Figure 9.9b). With the supplementation of picked S events in this study, the data coverage is improved considerably and is comparable to the data coverage for the picked first P-arrival events.

Figure 9.10 shows the total number of picked P and S arrivals at each station during 3 stages of deployment over a five-month period. Basically, the station coverage for P arrivals {see Figure 9.10(a)} is better than the station coverage for S arrivals {see Figure 9.10(b)}. But for both, the number of picked events on stations to the east of Rabaul volcano is less than for those in other directions.

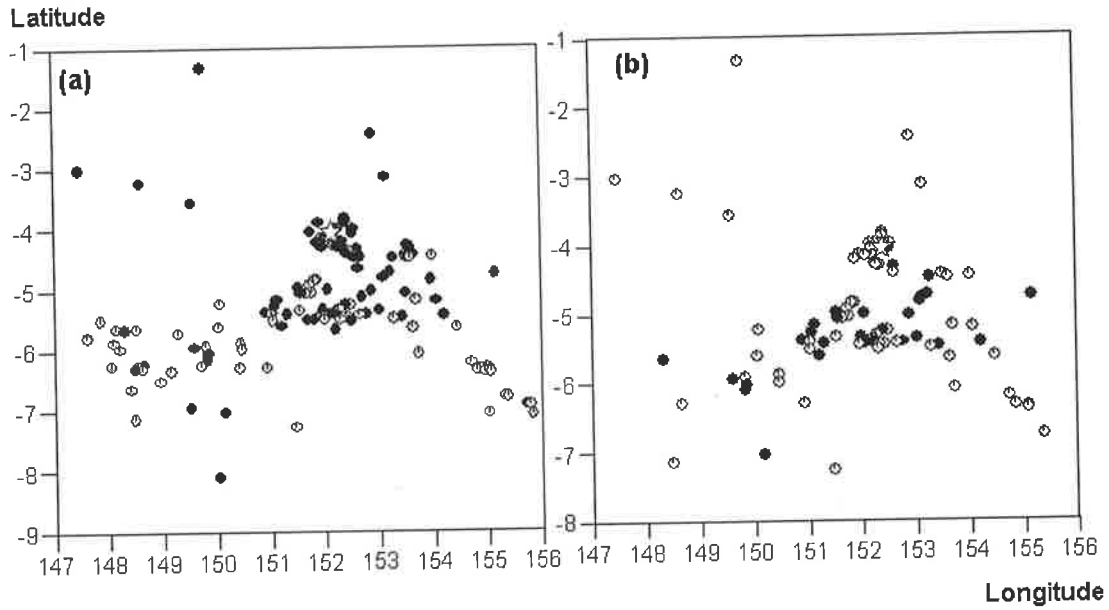

Fig. 9.9 The comparison of the picked events with first P arrival (diagram a) and first S arrival (diagram b) between the RELACS project and this study (Star: Rabaul; Black: RELACS picked events; Grey: picked events in this study)

9.5 Primary Analysis of Data Consistency

For each known event, I checked the NEIC or USGS websites and obtained the origin times for each event in the RELACS database. The P or S arrival time from file 'vpick.xxx' or 'vpicka.xxx' subtracts the origin time to form the travel time information, which is saved as 'p-time.xxx' or 's-time.xxx'. Here 'xxx' is the event number. A few records had incorrect timing. It was therefore necessary to analyze the record consistency so as to adjust or to remove some suspect records for certain events.

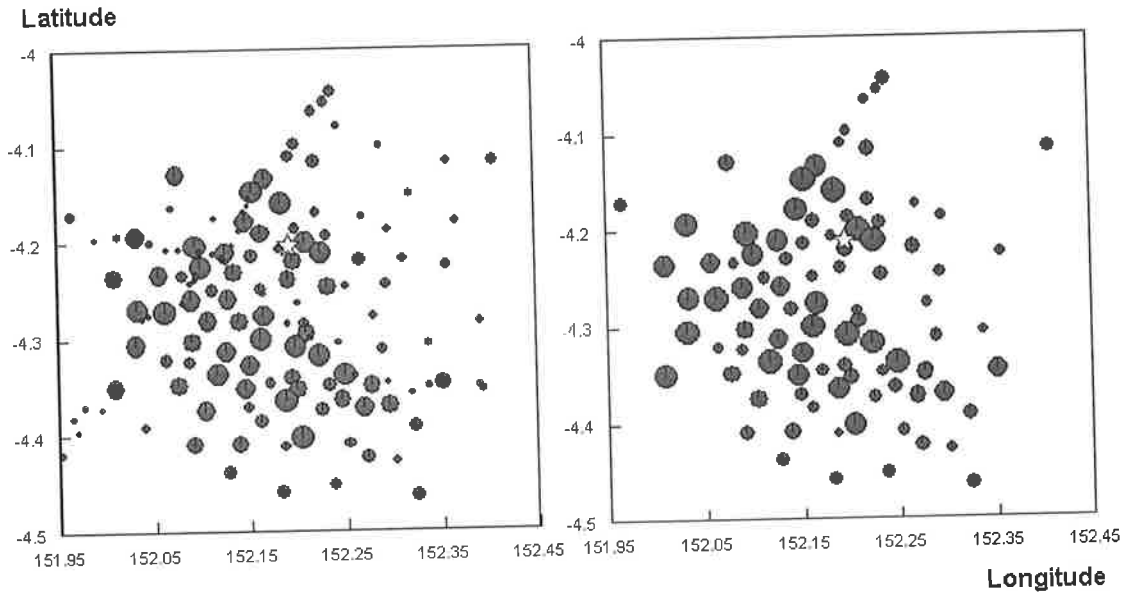

Fig. 9.10 The comparison between the total numbers (indicates by the circular size) of events picked with first P-arrival (diagram a, maximum=157) and first S-arrival (diagram b, maximum=64) by each station; white star: Rabaul

The basic method exploited here is use the T-D curve (travel time vs distance). For simplicity, for each picked event, I first plotted the T-D curves and set a soft error bar, and then deleted the records that lay outside the error bar. It is necessary to delete these corrupt records, because there is no information on timing corrections to apply to such records. Generally, there were only a few such corrupt records for a certain event, with suspect timing, and not much loss in data coverage by deleting them. From the T-D curves and associated averaged velocities (D/T), it is easy to find any suspect records and remove them from the travel time database. For some events, there exists a systematic travel time error due to the large source parameter uncertainty (see Fig. 10.3 later). For such event records, the travel time data is consistent over the entire distance range (all stations), and only needs a DC time shift to adjust them to the correct travel time data. As discussed in Chapter 5, in such circumstances, relative arrival time tomography can be exploited. Thus, such records in the travel time database were retained so as to obtain as wider a data coverage around Rabaul volcano as possible.

9.6 Conclusions

I have devised a combined on-screen picking technique to automatically determine both the first P and S arrival times simultaneously. A benefit of the combined picking method is that it yields a wide data coverage of picked events for both first P and first S arrivals in the near-regional scale. Using the T-D curves, it is possible to identify and remove a few corrupt records, and retain those events that have systematic (consistent) timing errors in the arrival time database.

Chapter 10: 3-D Velocity Structure of Rabaul Volcano

10.1 Introduction

The RELACS project obtained a 3-D velocity model of P-wavespeed for Rabaul volcano, but only to 10 km depth, due to the restriction of using just local earthquakes and explosions (Gudmundsson at al, 1999; Finlayson at al, 2003). This is similar to results (less than 15 km depth) obtained for other volcanic regions of the world (for example, Thurber, 1984; Dawson et al., 1999; Laigle and Hirn, 1999; Haslinger et al., 2001), and is a general limitation when only local sources are used. To obtain information on the deep local velocity structure, regional earthquake data needs to be incorporated. To do so, it is necessary to create a large 3-D velocity model to include the regional sources with a dense cell size, comparable to the local station density (say, less than a few kilometers). With such a model, it is difficult or impossible to invert for 3-D velocity field due to the computational demands. Alternatively, increasing the cell size or using a non-uniform cell size will make the problem tractable, but with a loss of the resolution or at the expense of introducing large travel time errors (as discussed in chapter 3 and 6).

To overcome the above problems and to fully use all available earthquake information (for example, regional event information), I proposed in chapter 6 a novel approach—3-D multi-step travel time (or relative arrival time) tomography, which separates the whole seismic tomography process into two (or more, if required) steps to realize the final goal by combining regional events with local earthquake information. The results of the numerical tests in chapter 6 demonstrate that this approach works well for obtaining a relatively deep velocity image of the local structure. Thus, this new approach will be exploited to deal with the RELACS data and to finally obtain the 3-D deep velocity model for Rabaul volcano.

To obtain a reasonable velocity image, it is first necessary to relocate the regional events to minimize the travel time residuals. They have a relatively large error in source hypocentral coordinate and origin time determinations, in a local sense. The relocation procedure requires a fine scale 1-D velocity model around Rabaul volcano. Meanwhile, this 1-D velocity model will be the input velocity model in the final inversion process. Thus, in this chapter, I first obtained a 1-D velocity model for both the P- and S-wavespeeds using the Weichert-Herglotz inversion method (see for example, Bullen, 1963), and then relocated the regional events taking this 1-D velocity model as a reference model. Finally, I started the process of multi-step travel time tomography with these refined source locations, as well as local earthquakes (including explosions).

10.2 1-D Velocity Model for both P-and S-Wavespeed

To make comparisons and to refine the shallow velocity structure, I recovered two kinds of 1-D velocity model: the first is the shallow velocity model obtained by using only explosion data; the second is the deep velocity model obtained from a combination of local earthquakes (includes explosions) and regional events.

10.2.1 1-D shallow velocity model from explosion data

Thirty explosions were used in the RELACS project. On average, there were more than 50 seismic recordings for each shot, but for most of them, the epicentral distance was less than 60 km. At such short source-receiver distances, it is very difficult to pick the first S-arrivals due to the strong coda of the early P-wave phases (see chapter 9 for details). Only 13 explosions with a relatively large epicentral distance could be picked. Among them, around 10 recordings per shot were picked. Figure 10.1 shows the travel time vs distance curves for both P-waves and S-waves using the explosion data.

Figure 10.2 is the 1-D shallow, smoothed velocity model for both P- and S-wavespeed derived from the (best fit) data plotted in Figure 10.1 using the W-H inversion method (Greenhalgh et al, 1980). For the shallow P-wavespeed, velocity increases rapidly down to a depth of 4 km, below that depth it changes slowly, reaching a value at 5.8 km/s at 10 km depth. For the shallow S-wavespeed, velocity is generally very low in the

upper 10 km of the crust. The P-wave velocity model obtained from the explosion data extends to 20 km depth, but for comparison, it has been truncated to 10 km depth. Between 10 and 20 km, the velocity changes slowly with the depth, and reaches a value of 6.7 km/s at 20 km depth.

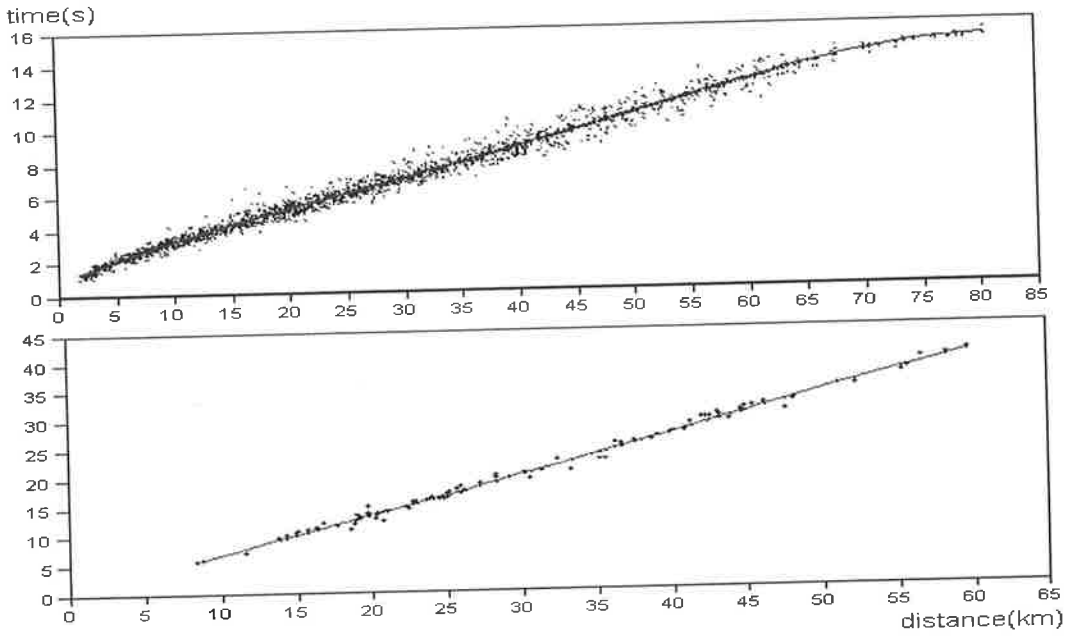

Fig.10.1 The travel time-distance curve of both P- (upper) and S-wavespeed (bottom) for only explosion data

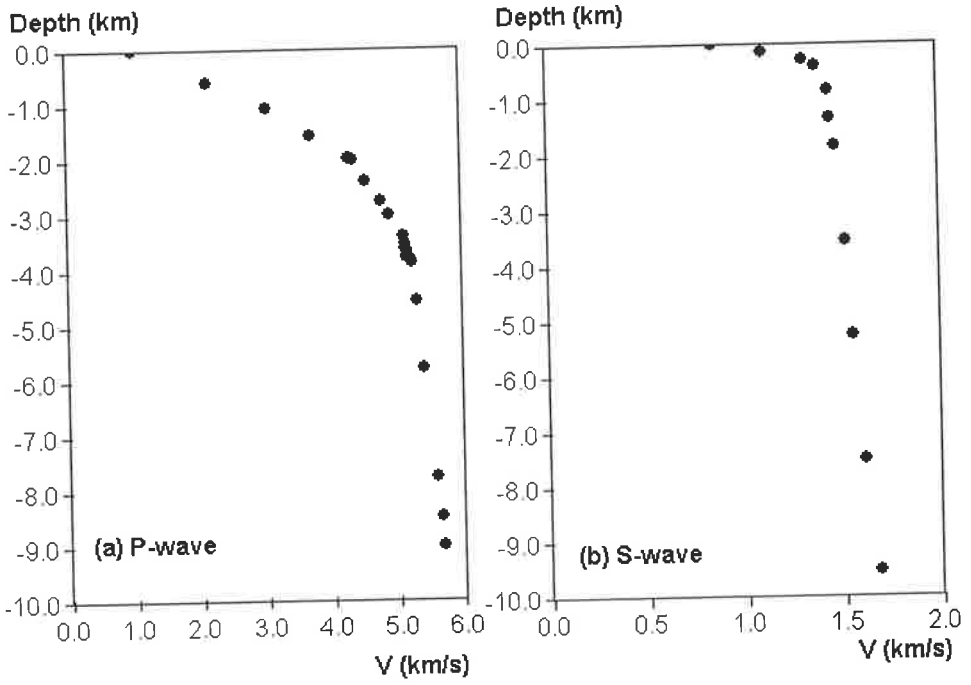

Fig.10.2 The 1-D velocity model of both P- (diagram a) and S-wavespeed (diagram b) for only explosion data

10.2.2 1-D deep velocity model

In using the W-H inversion method to obtain a 1-D deep velocity model, it is first necessary to apply a source depth correction, to restore observations to a datum plane (for example, sea level). This includes a distance correction ($\delta\Delta$) and a travel time correction (δt):

$$\delta\Delta = -\frac{(h-H)\times\frac{V}{111.195}\times\frac{\delta t}{\delta\Delta}}{\sqrt{1-(\frac{V}{111.95}\times\frac{\delta t}{\delta\Delta})^2}} \tag{10.1}$$

$$\delta t = -\frac{h-H}{V\times\sqrt{1-(\frac{V}{111.95}\times\frac{\delta t}{\delta\Delta})^2}} \tag{10.2}$$

where h and H are the source depth and the depth of the datum plane, V is the average P-wave velocity between the datum plane and the source depth, and $\frac{\delta t}{\delta\Delta}$ is the slope of the travel time curve (Zhu, 1988). For the near-oceanic region, I set $V = 8.0$ km/s. Here the sea level was selected as the datum plane, giving H=0.0 km.

Figure 10.3 shows the travel time-distance curves for both P-and S-waves for the combination of the local earthquakes, explosions and regional events after depth correction. From Figure 10.3, the data fit for P-waves is better than for S-waves, except there are some systematic time shifts (up and down), which indicates the location errors both in the hypocentral co-ordinates and the origin times. This was discussed in chapter 5. Such data can easily be adjusted to the correct times according to the fitting function, or can be used directly in relative arrival time tomography (see chapter 5 for details).

Figure 10.4 shows the 1-D deep, smoothed velocity model for both P- and S-waves derived from the T-D data plotted in Figure 10.3 by W-H inversion. The P-wave velocity features are consistent with the early results of crustal velocity structure (down to the depth of 40 km) around the Rabaul region obtained from the 1967-1969 seismic refraction surveys. This was discussed in chapter 2 (Finlayson et al., 2001). These velocity interpretations currently form the basis for crustal models used in regional event relocation and final inversion in this study.

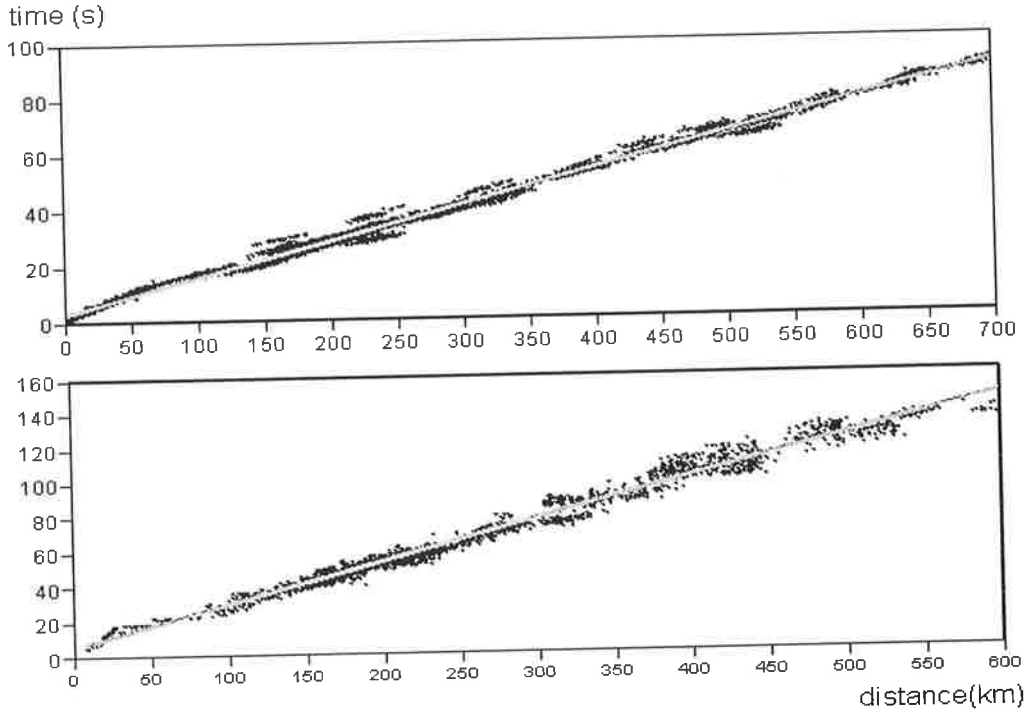

Fig.10.3 The travel time-distance curves of both P- (top panel) and S-waves (bottom panel) for the combined data (local + regional)

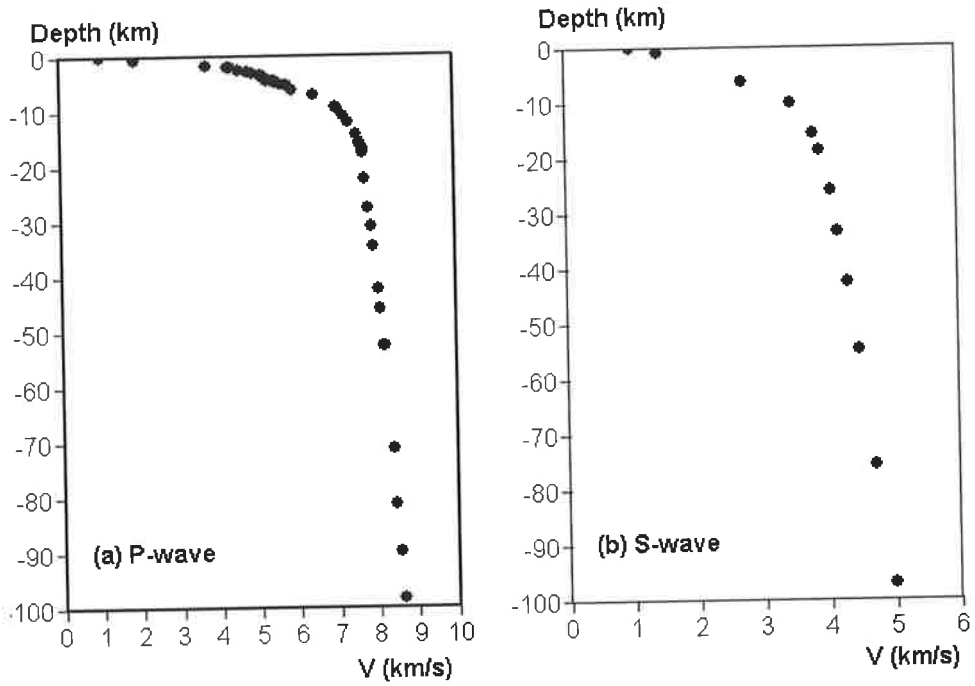

Fig.10.4 The 1-D deep velocity model of both P- (diagram a) and S-wavespeed (diagram b) for the combined data (local + regional)

10.3 Relocation of the Regional Events

For recovering fine scale, local velocity structure, the location errors associated with regional events are intolerable. For example, travel time errors of up to 0.5 s will be introduced if the hypocenter location error is as large as 20.0 km. Therefore, such travel time errors will destroy any attempt to image velocity variations on a local scale, especially when the target has a relatively small velocity contrast. Traditionally, this kind of travel time error in regional events can be partially reduced by using a simultaneous inversion technique (for example, Pavlis and Booker, 1980; Thurber, 1983). This involves updating both the velocity model and the source parameters at the same time. There is a coupling effect between the event hypocenters and the velocity model (Thurber, 1992). Also as concluded in chapter 8, there is a trade-off between the velocity model and the source parameters when applying joint travel time inversion. In other words, in a joint inversion procedure, it is only possible to relocate the source parameters and update the velocity model in a relative sense, not in an absolute sense. In order to overcome the above drawbacks in joint inversion, Zhao and Thurber (2003) attempted to use a double-difference (DD) method to achieve event location in an absolute sense. With this in mind, I preferred to relocate the regional events before local tomographic imaging was undertaken.

10.3.1 Event selection

The explosions have exact locations so it is not necessary to relocate them. Thus I only concentrated on relocation of the regional events. The total number of regional events selected for final analysis (the ray coverage and source-receiver distance were both considered here) was 65, with the source depth ranging from 0 to 100 km. Their distribution is shown in Figure 10.5.

10.3.2 Regional event relocation

To relocate the regional events with greater accuracy, it is helpful to divide the whole region (see Figure 10.5) into four sub-regions (Figure 10.6: cases a, b, c and d) to get a small cell size. The cell size selected is 20 km in the horizontal plane and 10 km in depth. The number of the secondary nodes added in each direction is kept at 9 to obtain

a relatively high accuracy in the computed travel times. The search length is the same in all three directions (2.0 km). The event location procedure was described in chapter 7. The velocity model is the 1-D velocity model that was obtained from W-H inversion (see Fig.10.4).

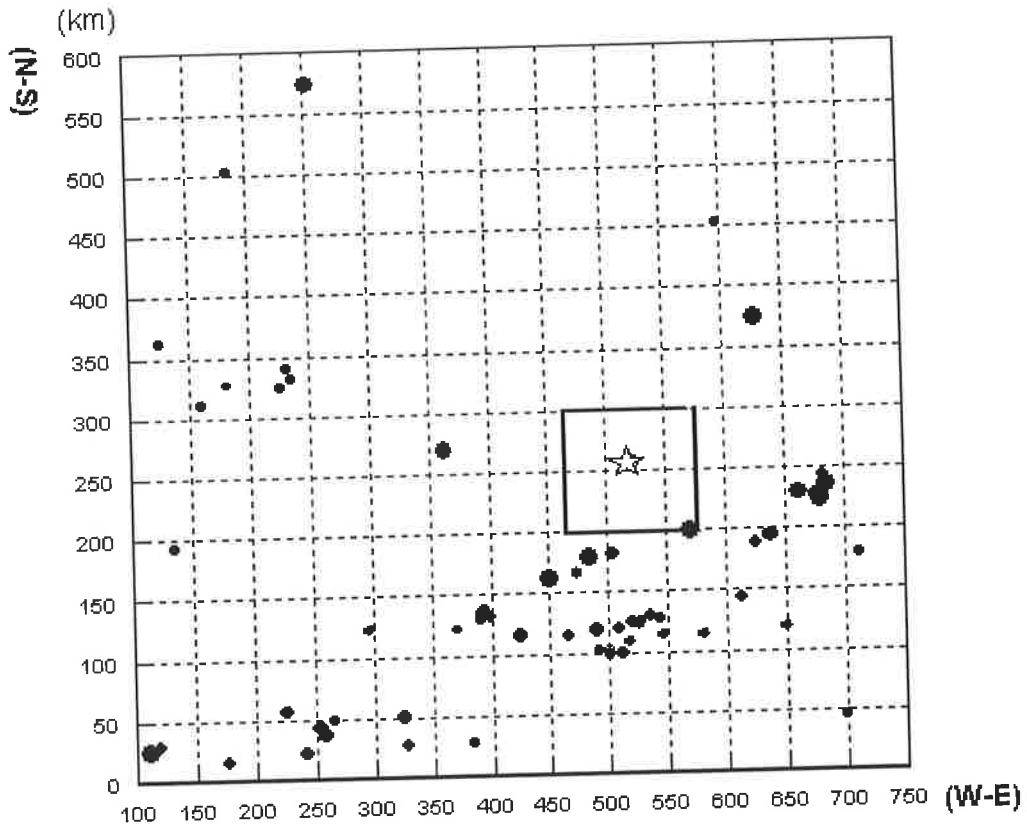

Figure 10.5 The final selected regional events for relocation in plan view (Black: Events; Star: Rabaul; Inner square: local model scale)

For relocating events in sub-region a, there are 29 stations and 10 events; in sub-region b, there are 32 stations and 4 events; in sub-region c, there are 32 stations and 28 events; and in sub-region d, there are 22 stations and 23 events. After 10 iterations, the RMS of the travel time residuals drops from 0.6575 s to 0.1970 s in case (a); from 1.3629 s to 0.2220 s in case (b); from 1.1430 s to 0.2172 s in case (c) and from 1.0740 s to 0.19920 s in case (d). From Figure 10.6, the station distribution is restricted to a small region near the sub-model boundary and the events are far from the seismic network. Even in such challenging situations, I still obtained reasonable location results as indicated by the small RMS errors in all cases.

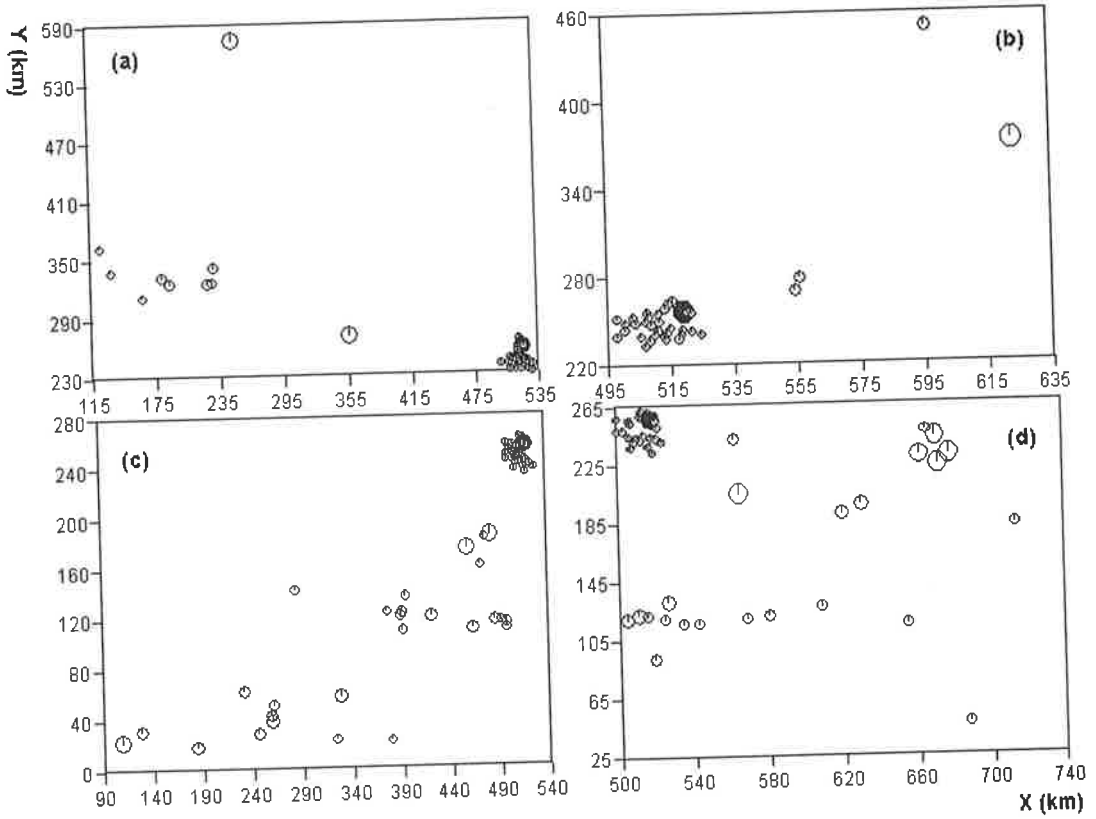

Fig.10.6 The source and receiver distribution in the separate sub-region relocation process (diagram a-d: sub-regions; Circle: denotes events with size indicating the different depths; Grey dot: denotes receivers)

10.3.3 Location error analysis

Figure 10.7 displays the epicentral distribution before and after relocation. On average, there is less than a 15 km distance discrepancy (see figure, the circular size denotes the focal depth) before and after event relocation. To further analyze the relocation results, I calculated the differences in distance for every event in each co-ordinate direction before and after event relocation. Figure 10.8 shows the distance residuals in the horizontal plane, where the size of the circle denotes the magnitude of the discrepancy.

Fig. 10.7 The comparison of event distribution before (black) and after (open circle) relocation (In figure Star: Rabaul; different sizes of circle denote the different depths of events, from 0 to 100 km)

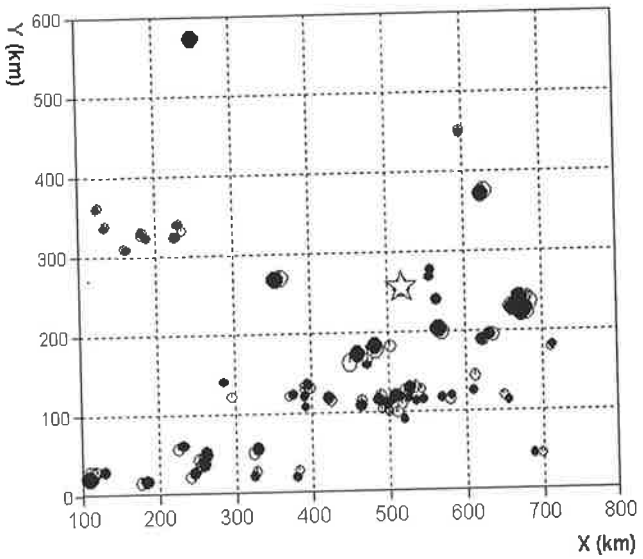

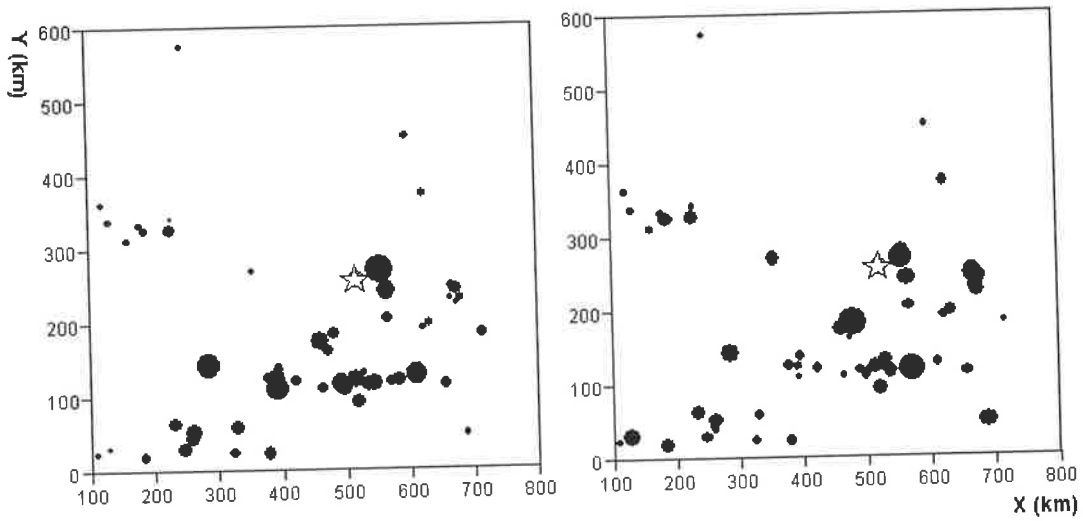

Fig.10.8 The distance residual in the horizontal plane before and after event relocation left panel: X-direction, magnitude from 0.13 to 26.37 km; right panel: Y-direction, magnitude from 0.11 to 27.11 km; Star: Rabaul location

The maximum distance discrepancy is less than 30 km in the horizontal plane. There is no systematic distance trend in Figure 10.8, which means that the 1-D reference model is the best fitting model for relocation. The distance discrepancy in the Z-direction before and after relocation is comparable to the values obtained for the horizontal plane. The maximum shift in distance with event relocation was 37 km. From the results of regional event relocation, the uncertainty of travel time errors is reduced to a satisfactory level (on average, from 1.0 s to less than 0.23 s), which is comparable to the picking errors (0.1 s) in regional events. Theoretically, the information that pertains to the velocity structures on a regional scale is removed, and only information on local velocity anomalies remains after relocation.

10.4 Station Selection

There are 98 events available in total, including 65 relocated regional events, 3 local earthquakes and 30 explosions. I hope to exploit the maximum data coverage with these sources and have an even distribution of recorders. The RELACS project involved seismic recorder deployment over 5 months in three stages. The total number of recorders in operation was changed between the different stages (see chapter 2 for details). Figure 10.9a shows the 98 stations that recorded 10 or more events among

these 98 selected events. The station coverage is poor in the east and northeast area, especially offshore. Using 4 or more events recorded on each station as the criteria, a more evenly distributed seismic network was obtained (Figure 10.9b), involving 146 seismic stations in total. Thus the final tomographic inversion was based on these 146 stations and 98 events. With such a configuration of source-receiver pairs, there were in total 3369 ray paths.

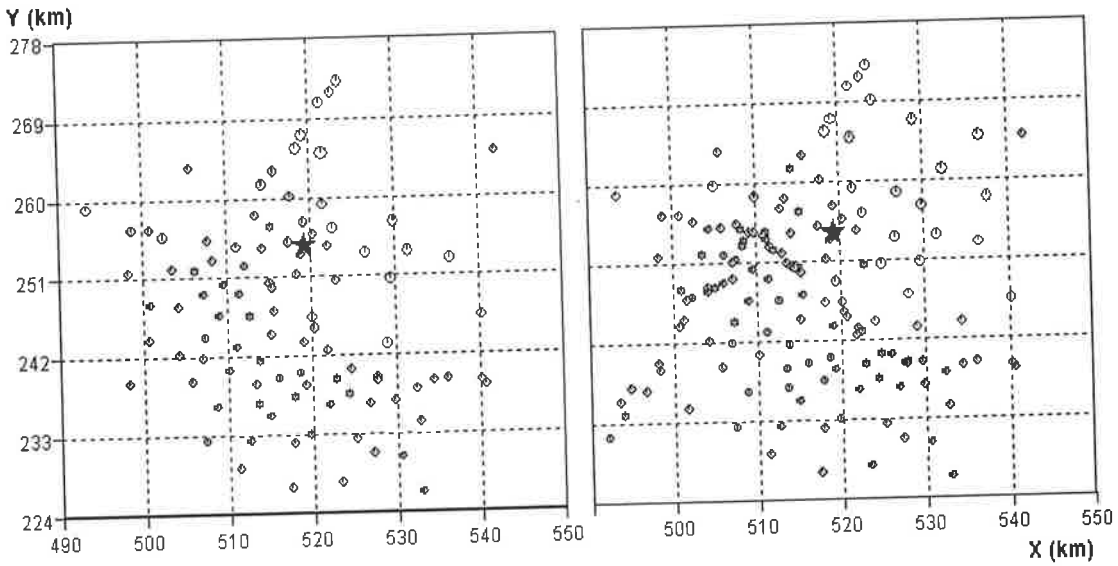

Figure10.9 The station distribution of the recorded first P-arrival in travel time tomography (Left: Stations recording 10 or more events; Right: Stations recording 4 or more events) (In figure: Grey dot: Onshore stations; Open circle: Ocean bottom stations; Star: Rabaul)

10.5 The New Predicted Source Positions and Travel Times

In similar fashion to the relocation process described above, this time I used a much finer cell size (10 km), and 9 secondary nodes added in each direction of the cell so as to obtain more precise determinations of the "new source" locations (where rays intersect local model volume) and related travel times (see chapter 6 for details). Figure 10.10a displays the final source positions and stations used in the local tomographic inversion. From Figure 10.10a, the data coverage is improved considerably with the new sources from the regional events. Note that there is an actual distribution of new source positions for each regional event across the local model volume (corresponding to each recording station), but for clarity, I averaged such a distribution into a single point, i.e,

each new source in Figure 10.10a represents a certain distribution of new sources from a specific regional event. Therefore, the original observed travel times minus these predicted travel times constitute the new observed travel times for these new sources in the local tomographic inversion procedure.

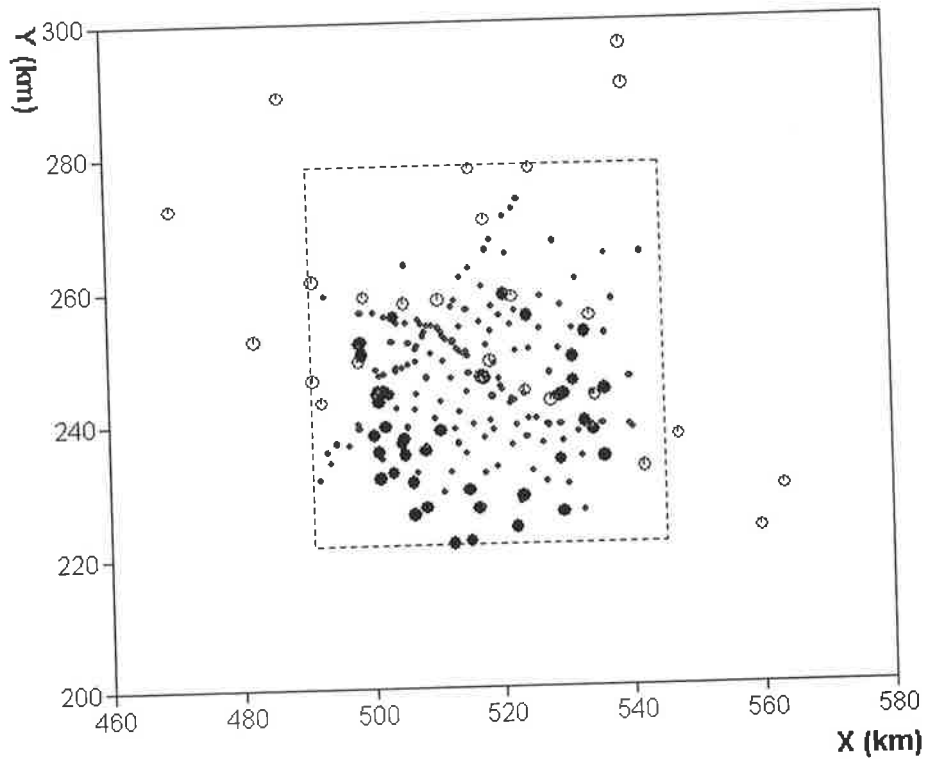

Fig.10.10a The station and event distribution (in plan view) for final local tomography (In figure: Open circle: Explosions; Big black dot: New sources; Small black dot: Receivers; Inside dashed square is the display region)

10.6 The Velocity Structure of Rabaul Volcano

The multi-step travel time tomography procedure of chapter 6 was applied to reconstruct the velocity structure of the Rabaul region. Basically, the horizontal scale of the computed model, as shown in Figure 10.10b, is 120 km in the X direction (W-E) and 100 km in the Y direction (S-N). The station deployment was restricted to the central part of the model, from 225 to 275 km in the Y direction and from 490 to 545 km in the X direction (see Figure 10.9). In the final velocity representation I used a much smaller region (see inner square in figure 10.10a, and resolution test later). Being

aware of the rapid changes in velocity with depth for the upper 16 km of the crust (see Figure 10.4), it is important to concentrate on reconstructing the velocity field down to 20 km depth. Below 20 km depth, the velocity field is much more uniform.

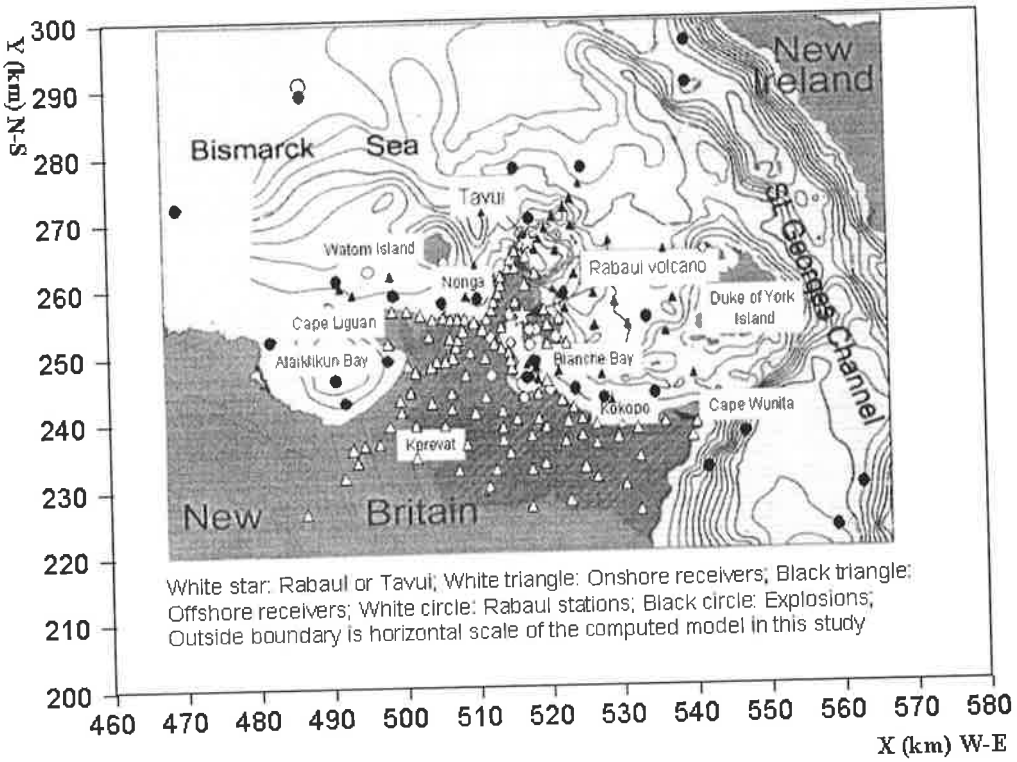

Fig.10.10b The Rabaul volcano and its surrounding area (middle) and the boundary of computed model shown in plan view, as used in this study

10.6.1 The checkerboard resolution test

Humphreys and Layton (1988) presented the Impulse Test method (ITM) to assess resolution. It uses synthetic travel time data to obtain the column vector of the resolution matrix, so as to test the distortion effect of ill-conditioning upon the image resolution. However, this method can only obtain resolution at a single sampled velocity node. Inoue et al. (1990) overcame this problem using the Checkerboard test, which extends the ITM to the whole model space. The basic procedure of the checkerboard test is that the real travel time data is replaced by synthetic travel time data calculated from a special velocity model that has regular velocity perturbations (positive and negative in sequence) within the input model. Then the synthetic travel time data is inverted with exactly the same source-receiver layout as used in the real

data. The solution reliability is assessed by directly comparing the inversion results to the 'checkerboard' input velocity perturbation.

Taking a 4 km cell size model as an example, a synthetic travel time dataset was computed (predicted) using a ± 0.3 km/s velocity perturbation (positive and negative sequence) within the planes Z=4 (± 6 % perturbation), 8 (± 5.2 % perturbation) and 16 km (± 4.7 % perturbation). The inverted velocity images are shown in Figure 10.11.

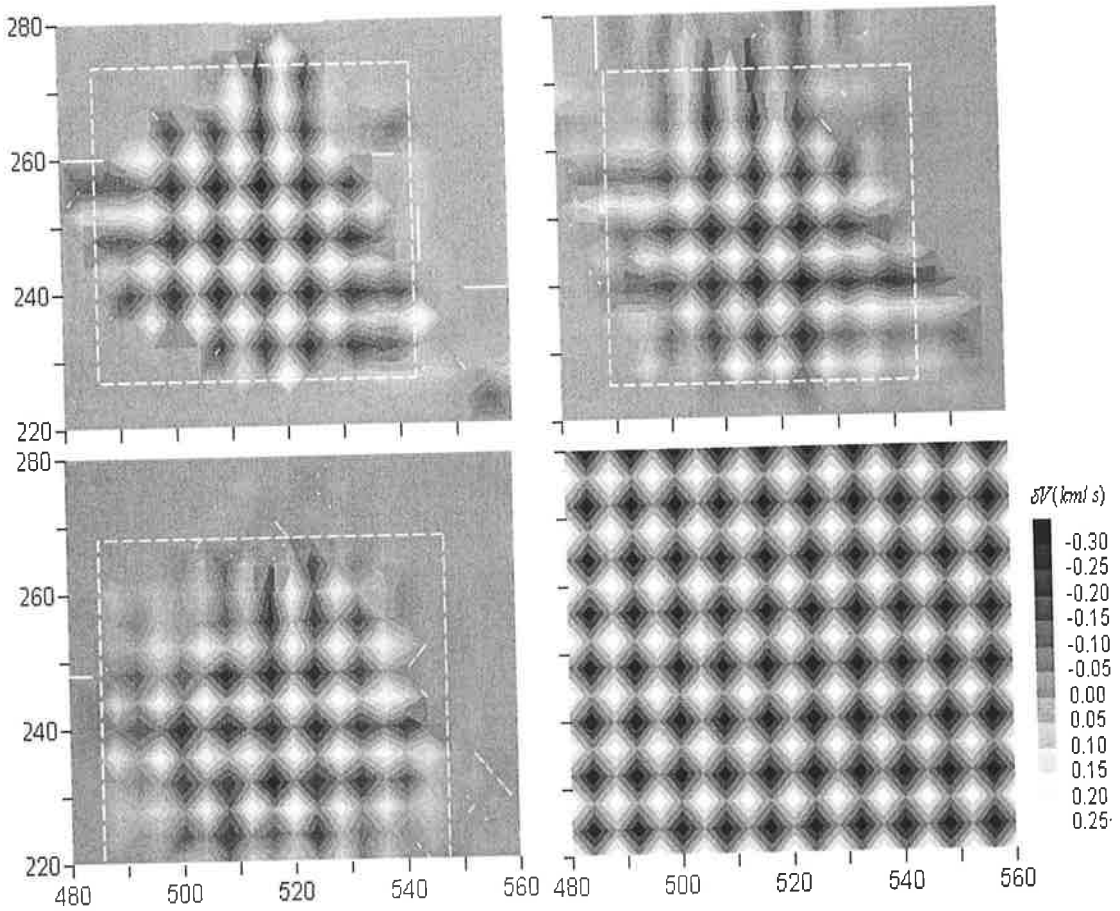

Fig.10.11 The checkerboard test at the planes Z=4 (top left), 8 (top right), 16 km (bottom left) and synthetic velocity perturbations at the same planes (bottom right) Inner square shows the best resolution area

From Figure 10.11, it is clear that the solution is reliable under the seismic network. This is a square region increasing its size slightly with depth. The minimum square region is from 490 to 540 km in the X direction, and from 224 to 270 km in the Y direction. Outside this region and even in the corners of the above region, the images should be treated with caution due to partial distortion of the solution, or even worse no changes in the model (i.e., no ray path passes through, thus no velocity is updated in

such regions). The resolution of the various depth slices from checkerboard tests with different cell size models (3, 4 and 5 km cell size, as discussed later) shows similar patterns. Thus there is no need to further discuss this issue. From these checkerboard tests, it is reasonable to expect satisfactory velocity images within the above square region down to 20 km depth with the specified source-receiver geometry. With the 3 km cell size model, the resolution is 3 km both in the horizontal plane and in depth, at least for the above square region. With the aid of 4 km and 5 km cell size models, on average, the resolution in depth is 2 km. The available depth slices are Z=0, 3, 4, 5, 6, 8, 9, 10, 12, 15, 16, 18, 20 and 21 km.

10.6.2 The three different computed velocity models

Theoretically, the smaller the cell size, the better the velocity representation. Three different cubic cell sizes were selected to grid the velocity model. In all three cases, the number of secondary nodes was set at 6 for considerations of both accuracy (generally 6 secondary nodes is suitable to obtain satisfactory accuracy in ray tracing-see chapter 3 for details) and program run time.

Model-1: 5 km cubic cell size

In this computed model, a relatively large cell size was selected (5 km cubic cell) to divide the velocity field, and the lower depth boundary of the velocity model is at 30 km. There are in total 2,880 cells, 3,675 velocity unknowns and 402,567 nodes.

Model-2: 4 km cubic cell size

In this model, a moderate cell size was used (4 km cubic cell) to grid the velocity field, and the depth boundary of the velocity model was set at 20 km. There are in total 3,750 cells, 4,836 velocity unknowns and 526,896 nodes.

Model-3: 3 km cubic cell size

In this model representation, a relatively small cell size was exploited (3 km cubic cell, comparable to station density) to grid the velocity model, and the lower depth boundary of the velocity model was placed at 21 km. There are in total 9,520 cells, 11,480 velocity unknowns and 1,301,630 nodes.

Several different starting velocity models (around the reference model, see Fig. 10.4) with different damping factors were tested. The final selected starting model is the

model with a small initial RMS error in travel time residual (that is, the best fitting velocity model), and also rapid convergence trend for both the travel time residual and the velocity model perturbation in the first few iterations. Finally, a soft damping factor (0.1) and the physical constraint for model-updating were selected in three cell size models. That is, the velocity was not allowed to be negative, or larger than a specified value (in this case, I set the specified value as 10 km/s).

In the inversion using the 5 km cell size model, the RMS error of the travel time residual starts at 0.3610 s, and is reduced to 0.1964 s after 15 iterations; in the inversion with the 4 km cell size model, the RMS of the travel time residual is reduced from 0.3987 s to 0.1914 s after 15 iterations; while inversion of the 3 km cell size model shows a drop in the RMS travel time residual from 0.3450 s to 0.1875 s after 15 iterations.

10.6.3 Velocity field reconstruction-comparison of depth slices

Basically, the main features of the reconstructed velocity field are preserved among the three different cell size models, especially between the 3 km and 4 km cell size models. But more details on the velocity field are extracted with the finer grid size model. To make the following discussion more compact, when I refer to 'previous results' of the RELACS experiment. I mean the papers of Gudmundsson at al (1999) and Finlayson at al (2003). They have been the only published results to date.

The comparison between models with cell sizes of 4 and 5 km

Figure 10.12 displays the reconstructed velocity fields at two depth slices for the 4 and 5 km cell size models. From Figure 10.12, the main features of the reconstructed velocity fields are the same, such as a dominant high velocity region in the west, and a low velocity zone near the southeastern model boundary (Kokopo southeast), and two low velocity zones (which can be associated with the volcano magma chamber-see later) within the high velocity region around 4-5 km depth (Fig.10.12a). This is especially true for the 4 km depth slice (right panel in Fig.10.12a). In addition, there are two dominant opposing velocity zones separating the velocity field into a western low velocity zone (between Cape Liguan and Kerevat) and a central high velocity zone (beneath southern Rabaul volcano) at 20 km depth (Figure 10.12b). Meanwhile, from

the velocity image at 5 km depth, it is possible to roughly determine the depth extent for the magma chamber as no more than 5 km (low velocity zones are barely visible in this depth, see left panel in Fig.10.12a). This is much shallower when compared with the 6 km depth for the volcano magma chamber beneath southeastern Rabaul (Rabaul caldera complex) from previous studies. Also two low velocity zones are imaged at this depth range, one is located beneath southeastern Rabaul (Rabaul caldera complex); the other is under Tavui caldera, which is a new discovery in this study.

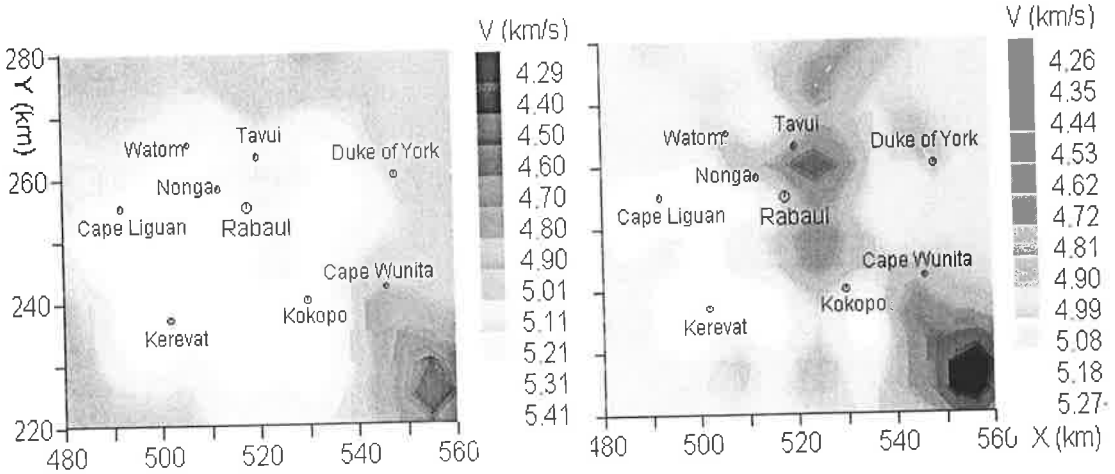

Fig.10.12a The comparison of images with different cell size models at comparable depths {Left: 5 km depth slice with 5 km cell model; Right: 4 km depth slice with 4 km cell model; note that the location of low velocity zone at southeastern corner of the model is out of the region for best resolution (see Fig.10.11a). It represents an artifact image}

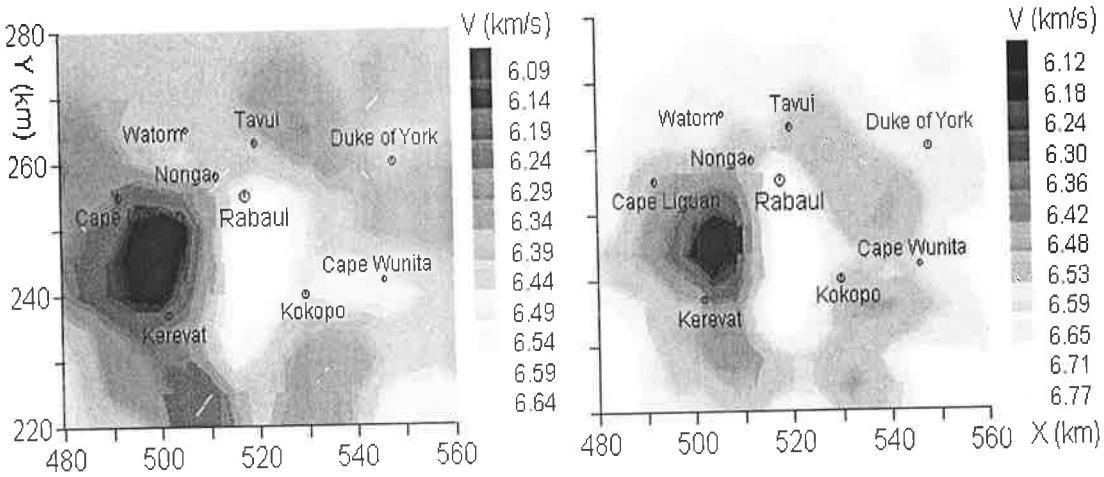

Fig.10.12b The comparison of velocity images with different cell size models at 20 km depth (Left: with 5 km cell size model; Right: with 4 km cell size model)

The comparison of velocity models with cell sizes of 3 and 4 km

Figure 10.13 is a comparison of the recovered velocity images at two other depth slices obtained from 3 km and 4 km cell size models. Again, the smaller the cell size, the better the resolution. For example, the central near-surface low velocity zone (Left panel in Fig.10.13a) is resolved into two adjacent low velocity zones with the 3 km cell size model (Right panel in Fig.10.13a); while the large dominant low velocity region (Left panel in Fig.10.13b) is restricted to the western region (between Cape Liguan and Kerevat) at 12 km depth with the 3 km cell size model (Right panel in Fig. 10.13b).

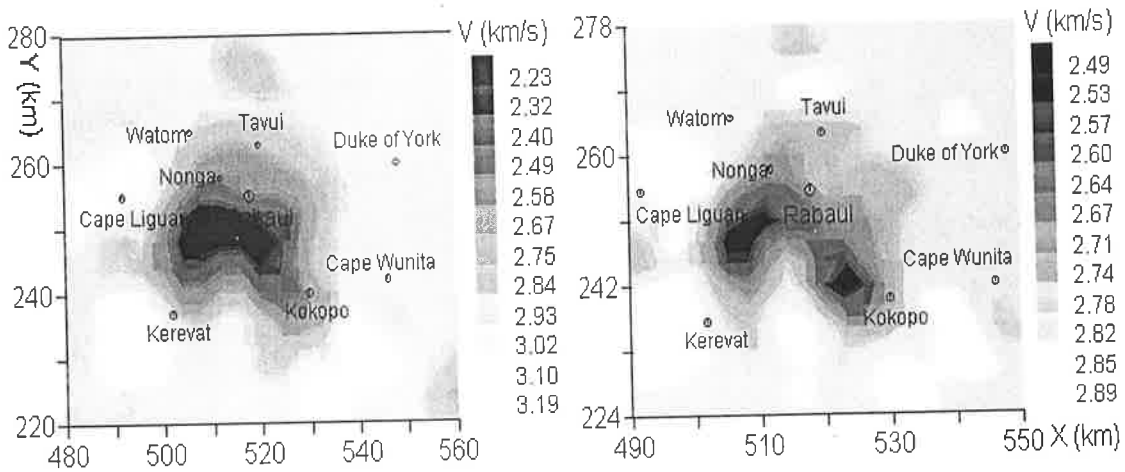

Fig.10.13a The comparison of images with different cell size models at Z=0 km depth (Left panel: with 4 km cell size model; Right panel: with 3 km cell size model)

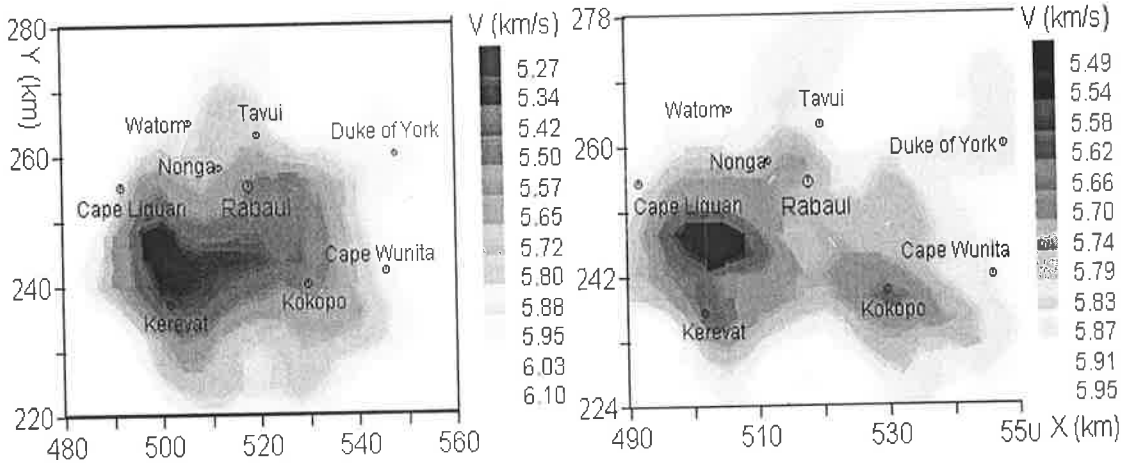

Fig. 10.13b The comparison of images with different cell size models at Z=12 km depth (Left panel: with 4 km cell size model; Right panel: with 3 km cell size model)

From inspection of depth slices over the range 0 to 21 km for the different cell size models, the main velocity features can be summarizes as follows:
(a) there are two low velocity zones (high temperature zones) between 3-4 km depth, one is under Rabaul caldera complex (southeastern Rabaul), which is referred to as the volcano magma reservoir in the previous results, the other is under Tavui caldera, which is a new discovery in this study, to be discussed later; (b) at shallow depth (upper 6 km depth), there is a pronounced high velocity region in the western Rabaul area, which coincides with earlier results; (c) between 6 km and 10 km depth, there is a pronounced high velocity region under Rabaul volcano; (d) below 10 km depth, there is a dominant low velocity zone on the southwestern side of Rabaul volcano. It splits into two opposing velocity zones that separate the velocity field into a western low velocity zone (between Cape Liguan and Kerevat) and a central high velocity zone (beneath southern Rabaul volcano) at depth.

10.6.4 Velocity cross sections near Rabaul volcano

Figure 10.10b shows Rabaul volcano and Tavui caldera to be centered on co-ordinates X=518 km and Y=255 km, and X=522 km and Y=263 km, respectively. To analyze the main velocity structures and interpret the velocity anomalies, it is helpful to show the velocity images (in the sense of velocity perturbations from the reference or 1-D starting model) as cross-sections from different profiles in the X (W-E) and the Y (S-N) directions. The results depicted here are for the 3 km cell size model to emphasize the fine features.

Velocity perturbation along X-direction (W-E) profiles

Figure 14 displays the velocity perturbations (the difference between the inverted velocity and the input velocity model) in four X-direction profiles. From south to north they are: (1) the southern section profile of Rabaul volcano (along Kerevat profile, Fig. 10.14a); (2) the Rabaul volcano section (along the Cape Liguan to Rabaul volcano via Nonga, Fig.10.14b); (3) the Tavui caldera section (along Tavui caldera to Duke of York Island, Figure 10.14c); and (4) the northern section of Tavui caldera (along Watom Island profile, Fig.10.14d). From Figure 10.14 and other (not displayed) X-direction

profiles, three main velocity structures on these consecutive cross-sections can be recognized:

(1) Volcano magma chamber

A low velocity anomaly is clearly visible at 3 km depth. It is roughly 8 km wide in the X (W-E) direction profiles (between X=521 and 529 km). This low velocity anomaly appears when the cross-section approaches Rabaul volcano from the south, beginning with the Y=245 km cross-section having a width of < 8 km. It later widens up to 8 km extent in the X direction when the profiles cross Rabaul volcano (Fig.10.14b). Thereafter it reduces in size when the profiles cross Tavui caldera (Fig.10.14c), and finally vanishes when the profiles departs from Tavui caldera northward (Fig.10.14d). This low velocity zone at 3 km depth, centered on eastern Rabaul, can be associated with the Rabaul volcanic magma chamber found in the previous studies. Note that there is a low velocity anomaly at 3 km depth both under Rabaul volcano and Tavui caldera, but it is indistinguishable, due to a relatively small separation distance (4 km) in the X direction between Rabaul volcano and Tavui caldera, but they will be distinguished later in the Y-direction profiles due to nearly doubling of separation distance (7 km).

(2) High velocity layer

Around 6 km depth, there is a notable high velocity layer present on the X-direction cross sections. From south to north, it begins fairly flat on the Y=239 km cross-section, and then thickens in the eastern part beneath Rabaul volcano for the Y=245 and 248 km cross-sections. For the Y=251 and 254 km cross-sections, it thickens to the west beneath Rabaul volcano, and finally it splits as western and central high velocity zones beneath the shallow low velocity zone (volcano chamber) when the profile crosses Rabaul volcano (Fig.10.14b). These two isolated high velocity zones can be clearly seen when the profile crosses Tavui caldera (Fig.10.14c).

(3) Low velocity zones below 6 km depth

Below 6 km depth, there are two dominant low velocity anomalous zones on the Y=230 km cross-section (Fig.10.14a); one is on the western part (beneath Kerevat); the other is on the eastern part. Moving northward, the western low velocity zone is still

present on the Y=245, 248, 251 and 254 km cross-sections, but the other low velocity zone (under the eastern part of the profile) vanishes (Fig.10.14b). Finally, the western low velocity zone migrates to the central region, and lies beneath the two isolated high velocity zones (Fig.10.14b), and links to the shallow low velocity zone by a pipe-like low velocity funnel (Fig.10.14c).

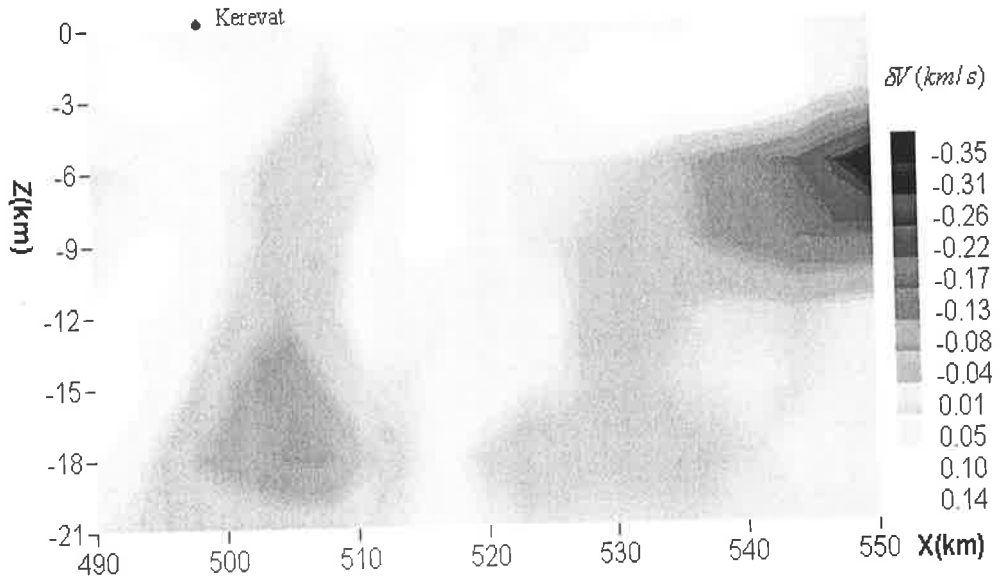

Figure 10.14a Velocity perturbations along the Y=230 km cross-section

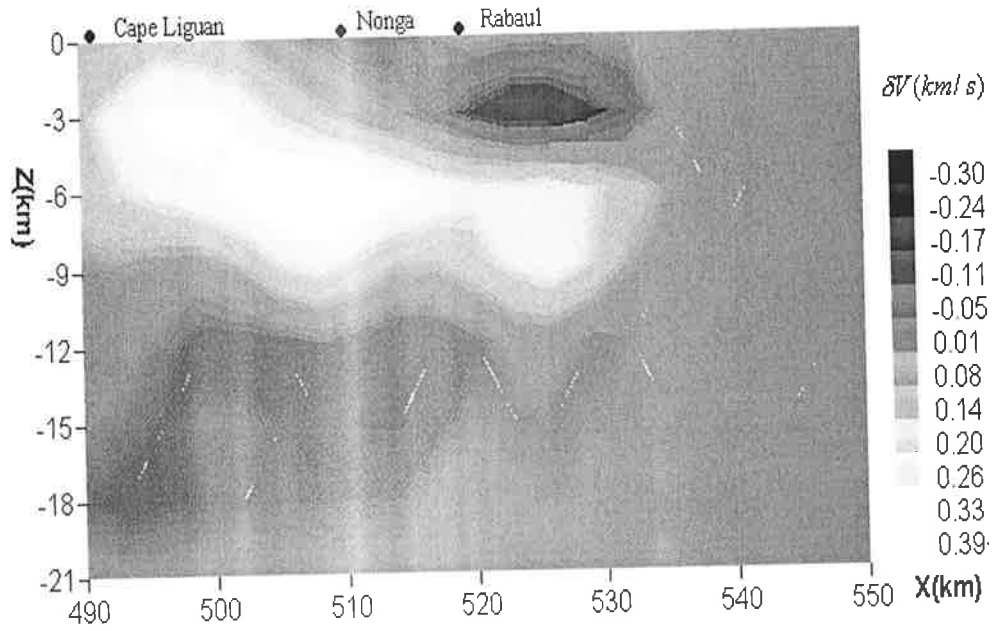

Figure10.14b Velocity perturbations along the Y=257 km cross-section

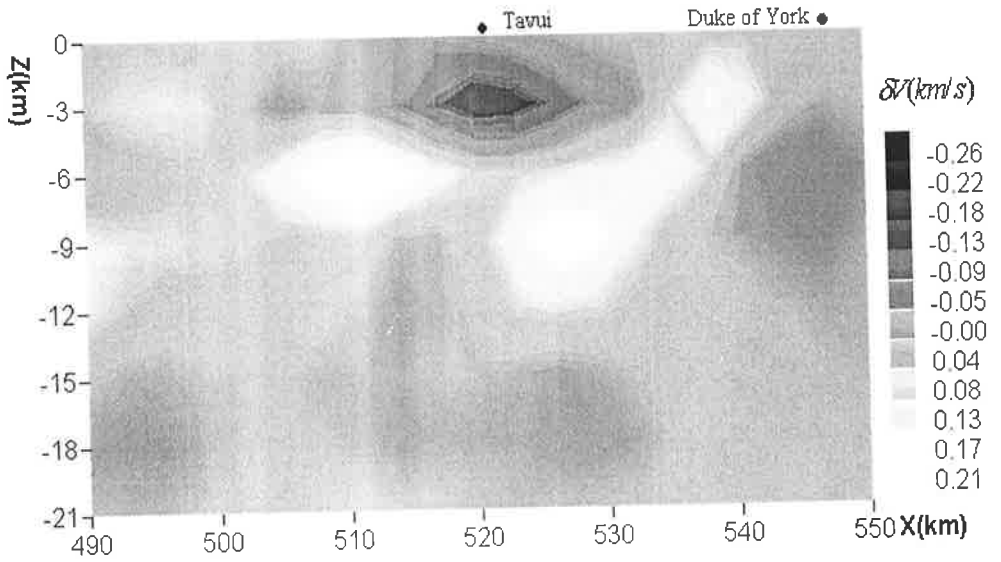

Figure 10.14c Velocity perturbations along the Y=263 km cross-section

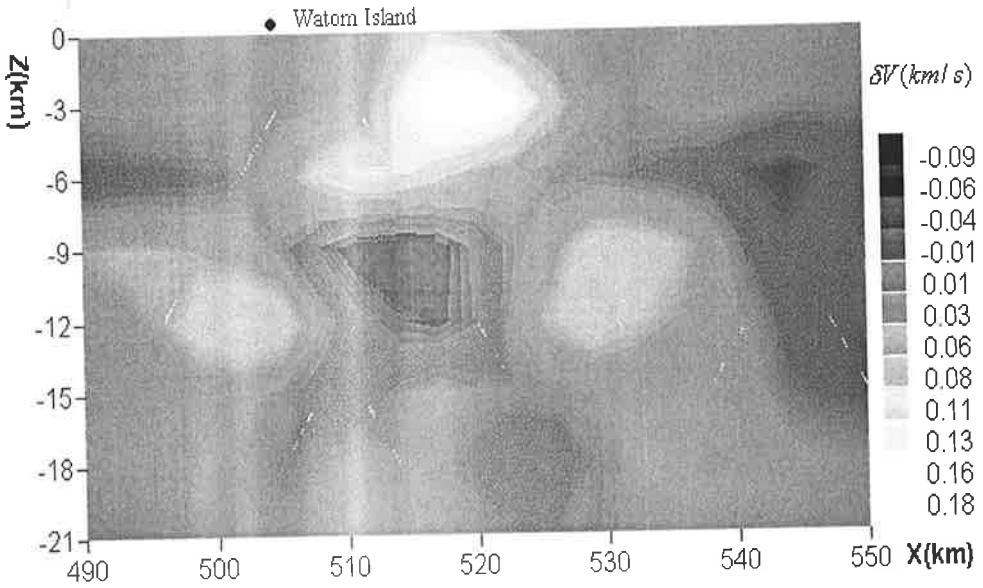

Figure 10.14d Velocity perturbations along the Y=269 km cross-section

The three main velocity structures described above were also found on the corresponding X-direction cross-sections using a larger cell size model of 4 km. The actual velocity contrast against the background velocity in the low velocity zone under Rabaul caldera complex is more than 10 % (see Figure 10.14b), and under Tavui caldera is up to 8 % (see Figure 10.14c). The velocity contrast in the central deep low velocity zone (which reaches as deep as 18 km) beneath the upper two-isolated high

velocity zones is up to 10 % (see Figure 10.14b). A deep magma body (down to 9 km depth maximum) was suggested for Kilauea volcano, in Hawaii (Haslinger et al, 2001). This is new evidence, because there have been no such deep features reported in the literature on volcano images before, due to the restriction of sources (generally only local earthquakes and explosions are used in the imaging).

Velocity perturbation along Y-direction (S-N) profiles

Figure 10.15 shows velocity perturbations along four Y-direction profiles. From west to east they are: (1) the western section of Rabaul volcano (along Kerevat to Watom Island section, Fig. 10.15a); (2) the Rabaul volcano profile (Fig.10.15b); (3) the Tavui caldera profile (Fig.10.15c); and (4) the eastern section of Rabaul volcano (Fig.10.15d). Three principal velocity features can be identified in these parallel S-N profiles.

(1) Two consecutive low velocity magma chambers

The 3 km depth low velocity anomaly, described in the X-direction cross-sections, is still present in the Y-direction profiles, but now the low velocity zones can be distinguished as two isolated anomalies (simply called southern and northern low velocity zones). The southern zone (6 km wide in Y direction, with ~10 % velocity contrast) appears in the X=508, 511 and 514 km cross-sections (Figure 10.15b); the northern zone (4 km wide in Y direction, with ~8 % velocity contrast) is present in the X=517, 520 and 523 km sections (Figure 10.15b and 10.15c). The two consecutive low velocity zones are obviously tectonically related to Rabaul volcano and Tavui caldera. The southern zone identified in these profiles is centered on Y=250 km (Rabaul is located at Y=255 km); the northern zone is centered on Y=262 km (Tavui caldera is located at Y=263 km). These two distinct low velocity zones were not recognised in the previous studies.

(2) High velocity zone

As with the X-direction profiles, the high velocity layer around 6 km depth is still a dominant feature in these Y-direction profiles, but with slightly different patterns. The high velocity zone appears in the central region on the X=502, 505,507 and 511 km cross-sections (Figure 10.15a), and then becomes a flat layer on the X=514, 517 and 520 km cross-sections in the vicinity of the Rabaul volcano (Figure 10.15b). It finally

splits into two isolated high-speed zones on the X=523, 526 and 529 km cross-sections where the profiles depart from Tavui caldera (Figure 10.15d).

(3) Low velocity zone beneath 6 km depth

Beneath 6 km depth, there is also a pronounced low velocity zone, which can be clearly seen on the X=502 and 505 km cross-sections (under Kerevat, Figure 10.15a), and is still present on the X=508 and 511 km cross-sections. This low velocity zone becomes faint on the X=517, 520 and 523 km cross-sections (Figure 10.15b and 10.15c). It develops into two isolated low velocity zones, one located to the south, the other in the central region beneath the 3 km low velocity zone on the X=526 and 529 km cross-sections.

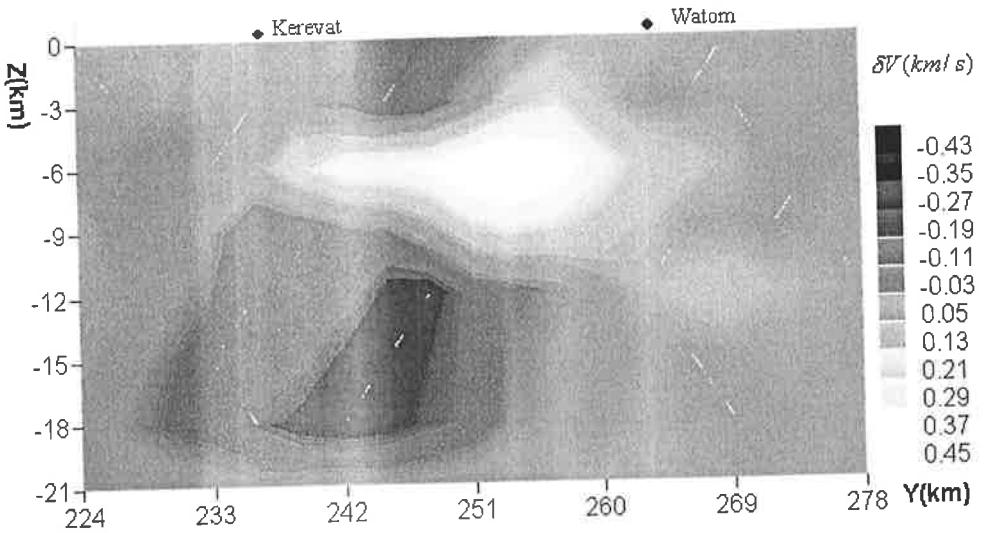

Figure 10.15a The velocity perturbations along the X=505 km cross-section

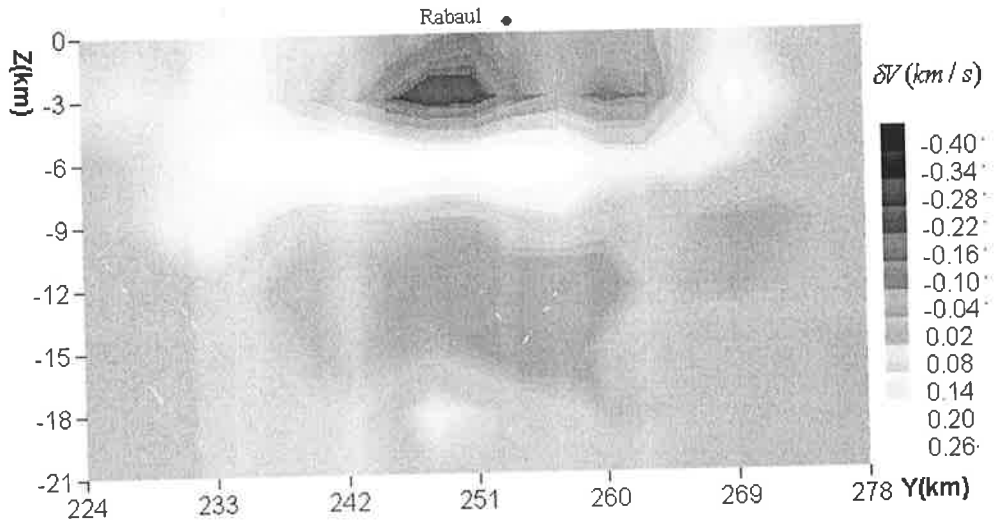

Figure10.15b The velocity perturbations along the X=517 km cross-section

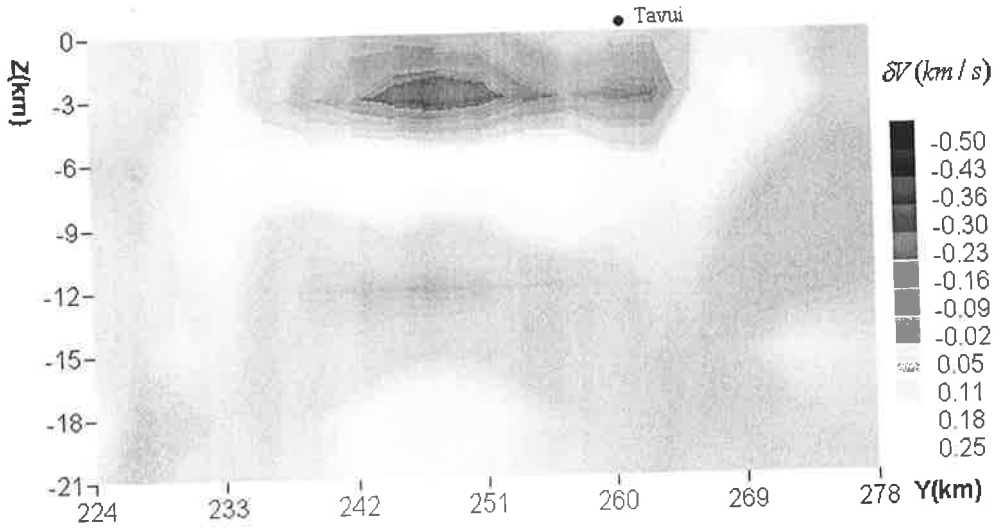

Figure10.15c The velocity perturbations along the X= 523 km cross-section

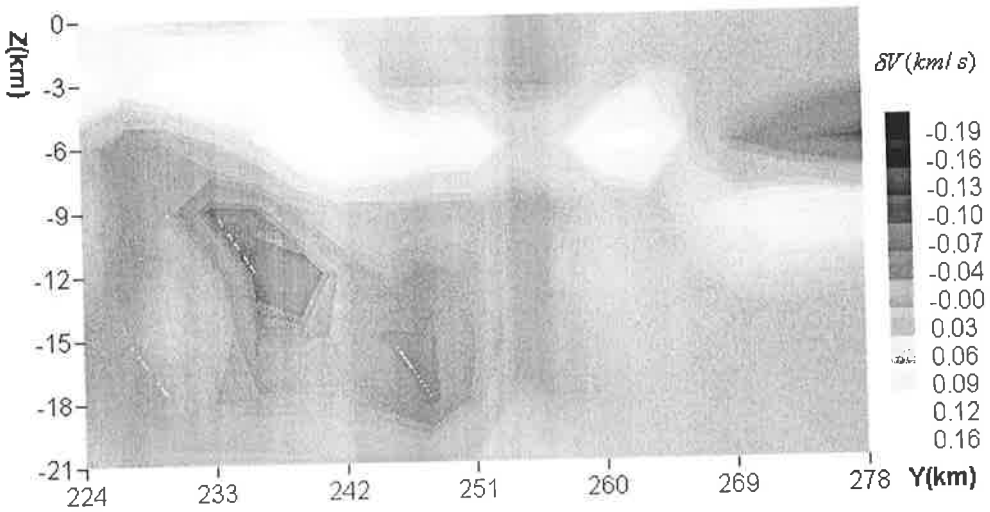

Figure10.15d The velocity perturbations along the X=535 km cross-section

The size of the low velocity zone (north) beneath Tavui caldera is smaller than the low velocity zone (south) beneath Rabaul caldera complex (see Figure 15b-c). Comparing the velocity images between different direction profiles and different cell size models, the extent of the southern low velocity zone under the Rabaul caldera complex is restricted to a rectangular region (X= 8 km, Y=6 km) in the horizontal plane. The lateral extent of the northern low velocity zones under Tavui caldera is about 4 km. Combining the results from three different cell size models, it is possible to restrict the vertical extent for both low velocity zones to 3-4 km depth range, because these two low velocity zones are barely visible on the 5 km depth slice (see Fig.10.12a).

10.6.5 2-D slices through 3-D velocity model along various X- and Y-direction profiles

To analyze the main velocity structure in the upper 20 km crust, it is useful to discuss the results of the 4 km cell size model. In order to show the fine scale velocity variations in the upper shallow crust, I add a value of 1.5 km/s to the top surface of the inverted velocity field. This is to better visualize the large velocity difference between the Z=0 and Z=4 km planes (the starting velocity model for the 4 km cell size model is 3.0, 5.0, 5.7, 6.1, 6.4 and 6.7 km/s at Z=0, 4, 8, 12, 16 and 20 km, respectively). Therefore, in Figures 10.16-10.19, the starting minimum velocity value in the legend is the real velocity value plus 1.5 km/s. Actually, the velocity value is very low within or around the volcano crater near Earth's surface (about 2.0 km/s, see Fig.10.13a), which is very close to the values of 1.5-2.0 km/s obtained in the previous studies.

X-direction cross-section profiles (W-E)

Figure 10.16 displays a number of 2-D cross-sections with an 8 km distance interval along the X direction. From south to north these are: (1) the southern section (crossing Kerevat, upper panel in Fig.16a); (2) the Kokopo-Cape Wunita cross-section (bottom panel in Fig.10.16a); (3) near-south section of Rabaul volcano (upper panel in Fig.10.16b); (4) the Rabaul volcano cross-section (bottom panel in Fig.10.16b); (5) the Tavui caldera cross-section (upper panel in Fig.10.16c); and (6) the northern section of Tavui caldera (bottom panel in Fig.10.16c). From these and other (not displayed) cross-sections along the X direction, several main features are found in the 2-D velocity field:

(a) In the top zone beneath Rabaul volcano (bottom panel in Fig.10.16b) and Tavui caldera (upper panel in 10.16c), there is a low velocity zone down to 4 km depth. Another dominant low velocity zone to the east of the model boundary (Fig.10.16a) is present in the Y=232 km cross-section, but this low velocity feature is located outside the best resolution region (see Fig.10.11) and thus it should be interpreted with caution.

(b) At medium depth (around 8 km depth), the velocity field is more complex than the velocity model obtained previously. There is a high velocity layer (between Y=240km and Y=252 km) that overlies the low velocity zone (bottom panel in Fig. 10.16a and

Fig.10.16b). It disappears in the vicinity of Rabaul volcano and Tavui caldera (Fig.10.16c). This overturned velocity structure may be associated with the regional plate movement and can be clearly seen in the Y=240 km cross-section (bottom panel in Fig.10.16a). The high velocity zone is uplifted from east to west and the low velocity zone dips from west to east.

(c) In the deep part of the cross-sections (below 10 km depth), there is a V-shaped low velocity zone under Kerevat (upper panel in Fig.10.16a), which then dips to the east as the high velocity zone shallows to the west where the profile approaches Rabaul volcano. The velocity structure is overturned where the profile crosses Rabaul volcano (bottom panel in Fig.10.16b). This feature is replaced by a V-shaped low velocity zone where the profile crosses Tavui caldera (Figure 10.16c). Basically, the velocity values increase gradually from west to east at the same depth.

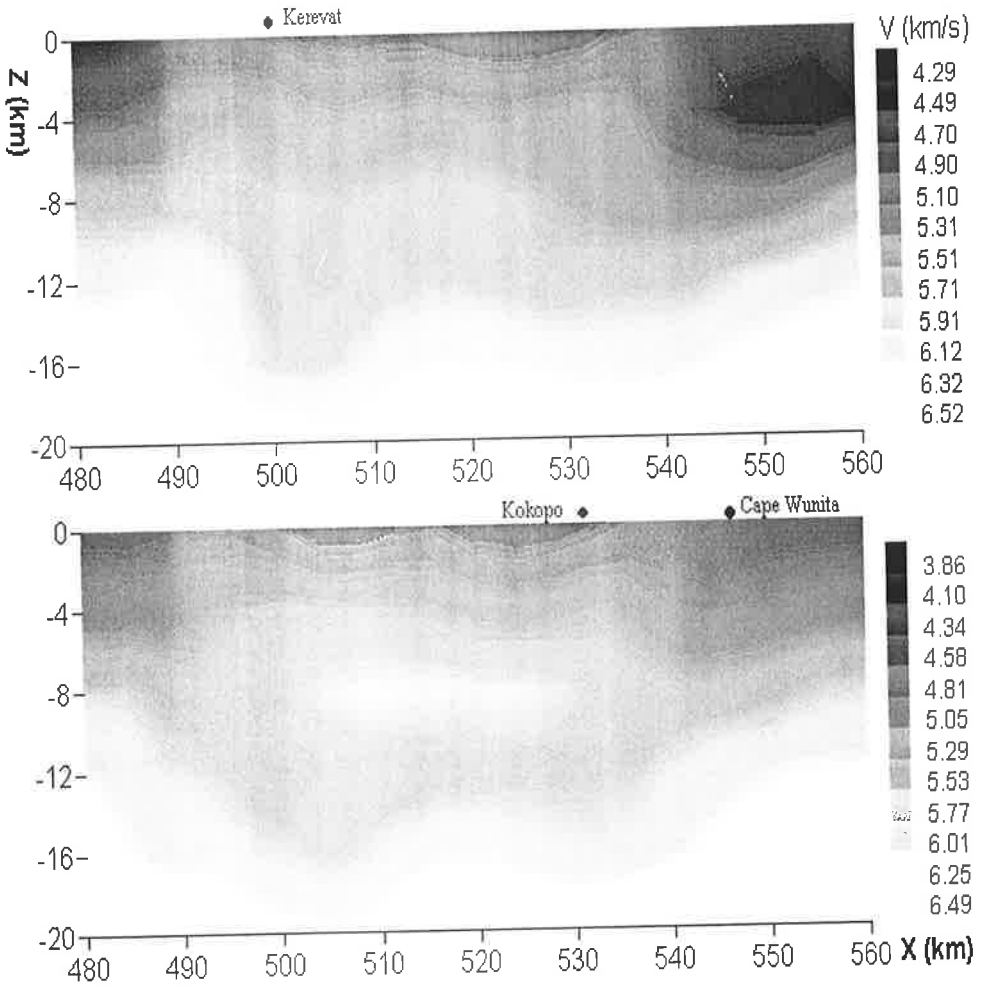

Fig.10.16a Velocity images along the cross-sections Y=232 (top) and 240 km (bottom)

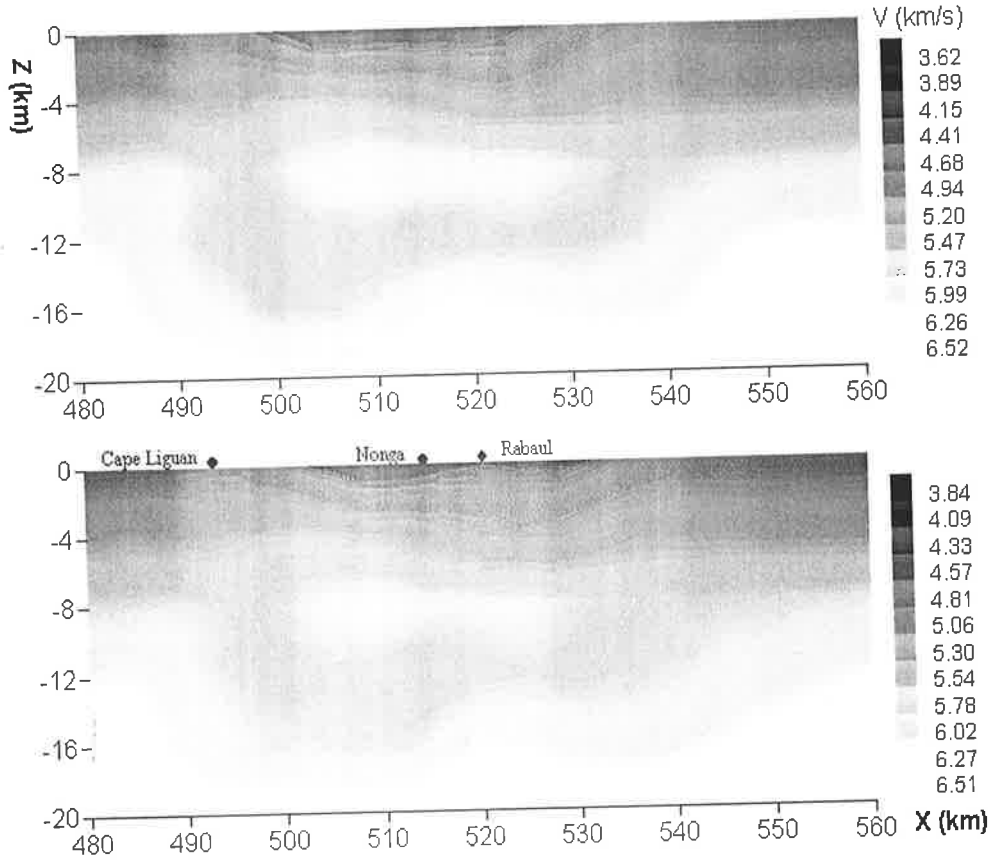

Fig.10.16b Velocity images along the cross sections Y=248 (top) and 256 km (bottom)

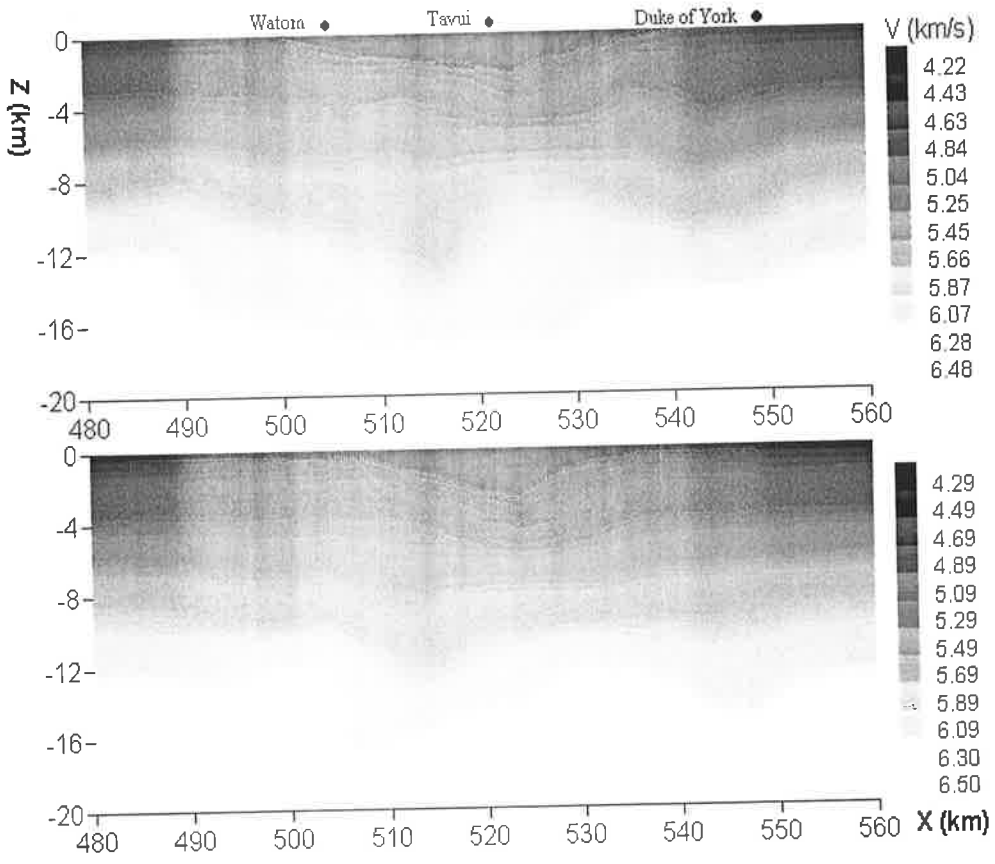

Fig.10.16c Velocity images along the cross-sections Y=264 (top) and 272 km (bottom)

Y-direction cross-section profiles (S-N)

The velocity field for the Y-direction profiles exhibit somewhat different features than the X-direction profiles. Figure 10.17 displays several cross-sections, again with an 8 km distance interval in the Y direction. From west to east they are: (1) the west cross-section of Rabaul (upper panel in Fig.10.17a); (2) the Watom Island cross-section (bottom panel in Fig.10.17a); (3) the Rabaul cross-section (upper panel in Fig.10.17b); (4) the Tavui caldera cross-section (bottom panel in Fig.10.17b); (5) the Kokopo cross-section (upper panel in Fig.10.17c); and (6) the eastern cross section of the Rabaul volcano (bottom panel in Fig.10.17c). The main velocity features observed along the Y-direction profiles are:

(a) In the top zone, beneath Rabaul volcano and Tavui caldera, a low velocity zone is present which extends to 4 km depth (Figure 10.17b);

(b) At medium depths (around 8 km depth), there exists a high velocity layer (between Y=240 km and Y=255 km). It shallows to the south and overlies the southern low velocity zone that dips to the north (bottom panel in Fig. 10.17a), and becomes an overturned velocity structure (with a high velocity zone above a low velocity zone) when the profile approaches Rabaul volcano. This feature is well depicted in the X=508 km cross-section (bottom panel in Fig.10.17a). Comparing with results obtained from the X-direction profiles (for example, Y=240 km cross-section, bottom panel in Fig.10.17a), the high velocity zone actually uplifts from northeast to southwest, and in turn, the low velocity zone dips from the southwest to the northeast. Such features indicate that something has occurred (possibly, massive hot material has migrated from deep to shallow crust) in this depth range, and as a result an overturned velocity structure has formed.

(c) Below 10 km depth, there is a low velocity zone located beneath Kerevat, extending to 18 km depth. It may be a deep volcanic source as was found for Kilauea volcano, in Hawaii (Haslinger et al., 2001). This low velocity zone dips to the north when the profile approaches Rabaul volcano (bottom panel in Fig.10.17a), and becomes a flat-lying low velocity zone beneath the top high velocity zone as the profile crosses Rabaul volcano (upper panel in Fig.10.17b) and Tavui caldera (bottom panel in

Fig.10.17b). It finally pinches out as the profile departs from Tavui caldera (Fig.10.17c).

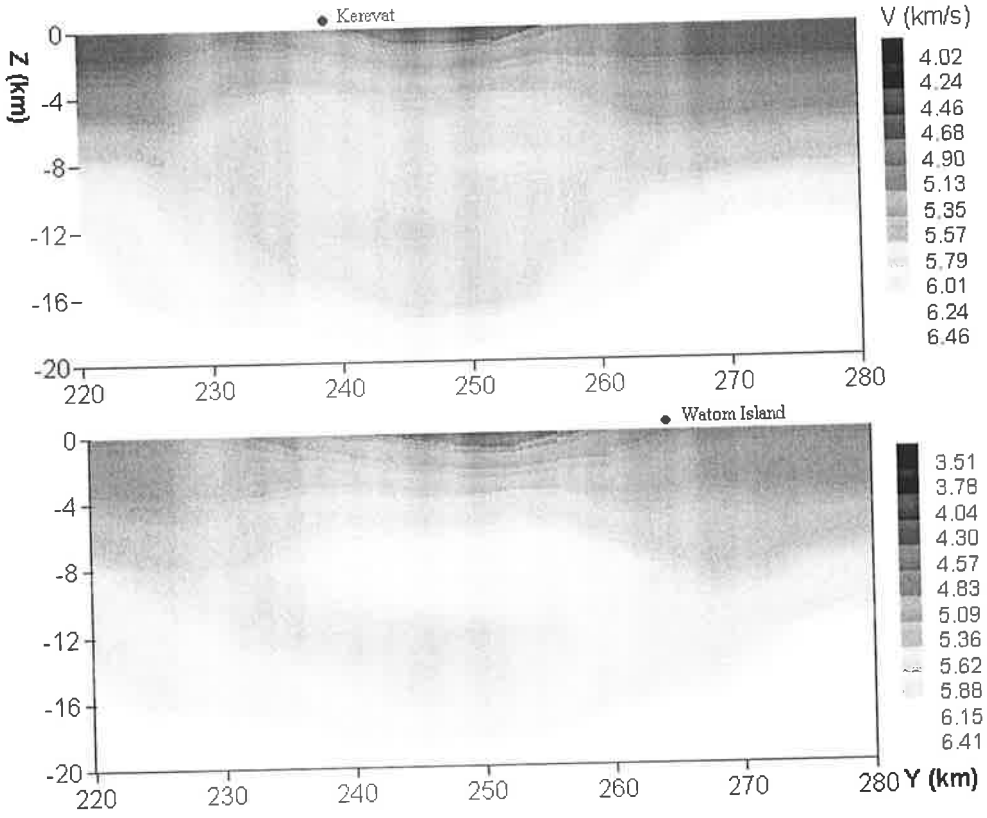

Fig.10.17a Velocity images along the cross-sections X=500 (top) and 508 km (bottom)

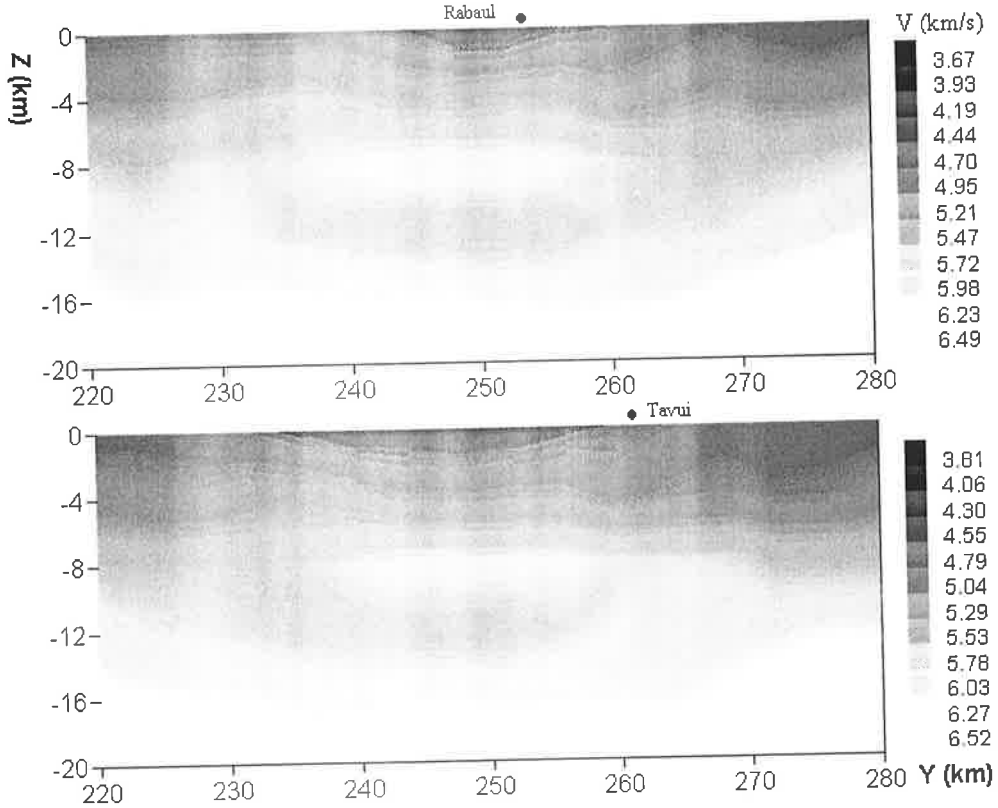

Fig.10.17b Velocity images along the cross-sections X=516 (top) and 524 km (bottom)

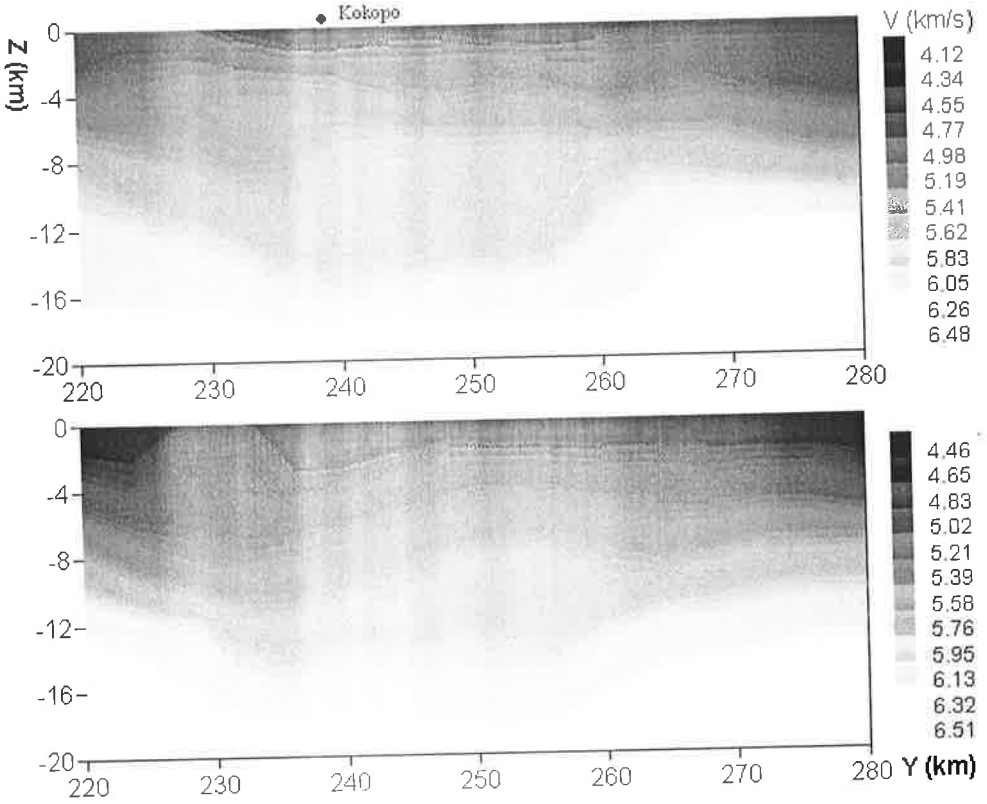

Fig.10.17c Velocity images along the cross-sections X=532 (top) and 540 km (bottom)

10.7 Comparison with the Previous Results

Combining the regional earthquake sources with local events (mostly explosions), it was possible to recover the 3-D local, deep structure for P-wavespeed (down to 20 km depth) around the Rabaul region. It is not easy to compare the present results with the previous results, due to different datasets being used, but some similar features on the recovered velocity fields are observed in both studies.

10.7.1 Shallow velocity structure around Rabaul volcano

The southern low velocity zone was previously recovered by the RELACS project (see Finlayson et al., 2003). Figure 10.18 shows the recovered velocity perturbation (measured against the input velocity model) at the 3 and 4 km depth slices from the present study. The main features in the velocity fields at these two depth slices are similar to those obtained previously. For example, the low velocity anomalous zone under southeastern Rabaul, and the high velocity region beneath the western, or

southwestern Rabaul are the same for both cases (see 3 and 4 km depth slices in Fig. 11 of Finlayson et al., 2003).

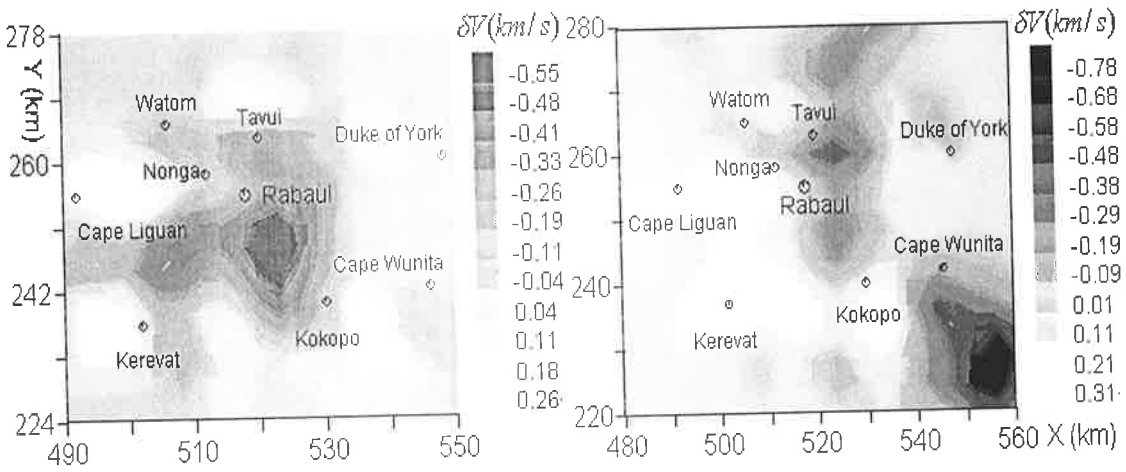

Fig.10.18 Velocity perturbations at the two different depth slices (left panel: 3 km depth with 3 km cell size model; right panel: 4 km depth with 4 km cell size model)

I was more interested in the northern low velocity zone, which is located under Tavui-another volcano caldera, near the Rabaul volcano. Note that the scale of horizontal plane in Fig. 11 of Finlayson et al (2003) is smaller than that of Figure 10.18 in this study, and does not include Tavui caldera. They suggested that Tavui might be inactive, due to the lack of similar feature as they found for Rabaul (i.e., the lack of a low velocity anomalous zone beneath the cross-section). The northern low velocity zone is well recovered from my study, which can be further viewed from the cross-section along the Rabaul-Tavui tectonic line (Fig. 10.20).

Compared with the previous RELACS results, there are several new findings in the shallow structure of Rabaul volcano from this study. They are: (1) Instead of one low velocity zone under the Rabaul caldera complex, I found an additional low velocity zone under the Tavui caldera; (2) the vertical extent of the southern low velocity zone in this study (3-4 km) is much shallower than that of previous results (3-6 km); (3) the scale of the northern low velocity zone under Tavui caldera (around 4 km^2 in horizontal plane) is smaller than that of the southern low velocity zone under Rabaul caldera complex (up to 6×8 km^2 in horizontal plane), but the location of the northern zone is slightly deeper than that of the southern zone (Fig. 10.20).

10.7.2 Medium deep velocity structure beneath Rabaul volcano

Figure 10.19 shows one W-E cross-section profile obtained with the 3 km cell model. This is a cross-section (Y=260 km) between Rabaul volcano and Tavui caldera. The upper panel is the recovered velocity field, and the bottom panel is the velocity perturbation against the input (starting) velocity model. The main captured velocity feature in this depth range is the V-shaped low velocity anomaly, which can reach as deep as 12 km. This feature is very similar to the previous results obtained from wide-angle profiling data. The only difference is that this V-shaped low velocity zone in the previous results (see, Fig. 9 of Finlayson et al., 2003) only reaches 9 km depth, due to the restriction of only explosion data being used.

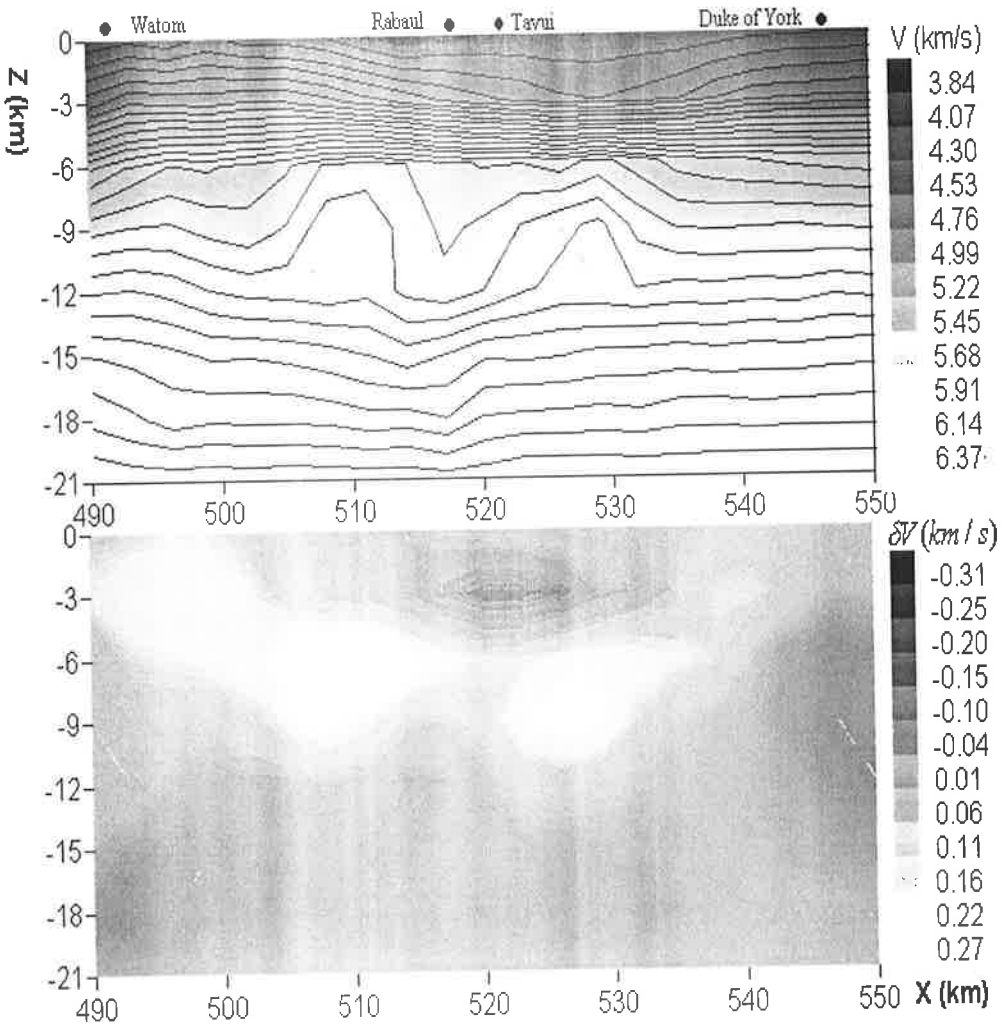

Fig.10.19 Velocity images of W-E profile (Y=260 km) crossing between Rabaul and Tavui
(Top panel: Inverted velocity, with a 0.15 km/s velocity contour superimposed)
(Bottom panel: Velocity perturbation against the input velocity model)

Interestingly, both studies obtained the same velocity features, even though different data was used in each case. Knowing that the cross-section is not exactly the same in both cases, there are some fine velocity differences between the present results (Fig.10.19) and the previous results (Fig. 9 of Finlayson et al., 2003).

10.7.3 Deep velocity structure under Rabaul volcano

Previous investigations failed to recover information on crustal structure below 10 km depth. Figure 10.20 displays one of our cross-sections along Rabaul volcano and the Tavui caldera tectonic line (It corresponds roughly to the profile given as Fig. 10 of Finlayson et al (2003). As mentioned when discussing the shallow velocity structure, the northern and southern low velocity zones are well isolated in this cross-section profile. In the previous studies (see Fig.10 of Finlayson et al, 2003), there is insufficient (small scale) point of low velocity zone around 2 km depth under Tavui caldera, but I found it to be a dominant feature. The similarity between both studies is the high velocity zone at the southern part of cross-section, which dips to the northeast.

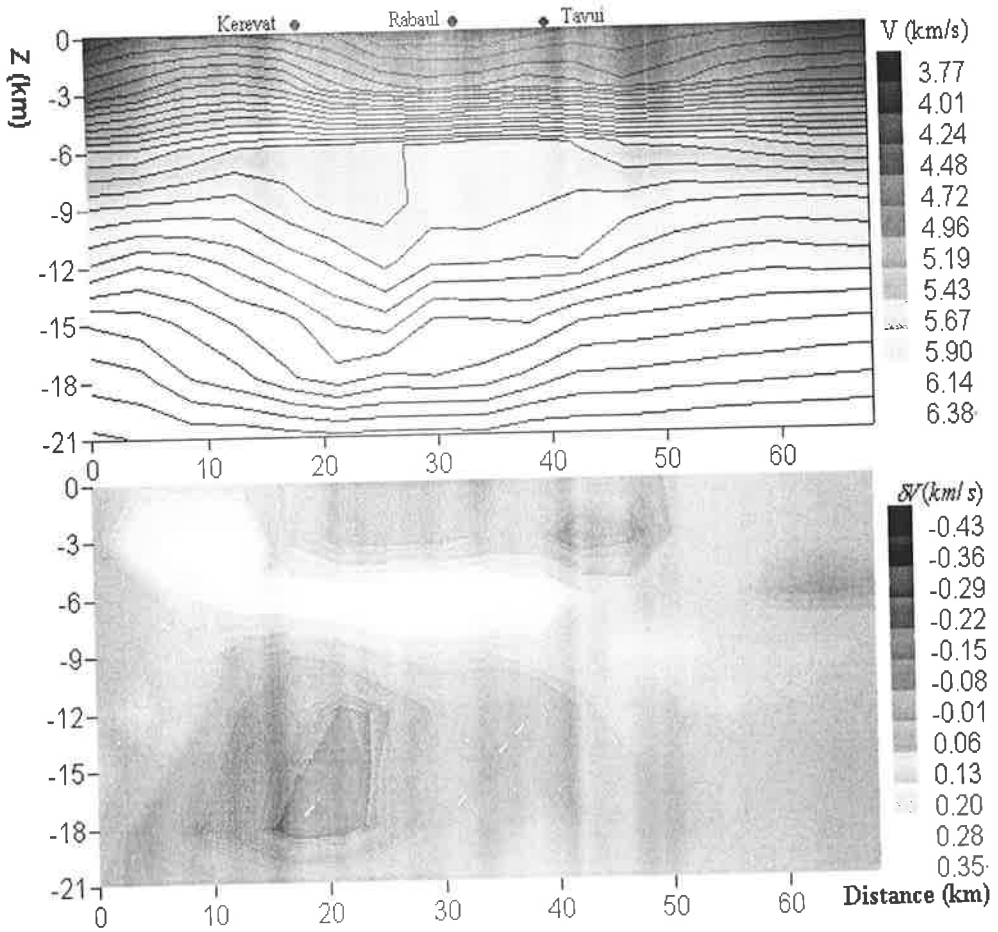

Fig.10.20 Velocity images along the cross-section of Rabaul-Tavui tectonic line
(Top panel: Inverted velocity, with a 0.15 km/s velocity contour superimposed)
(Bottom panel: Velocity perturbation against the input velocity model)

Below 10 km depth, there is a prominent cylindrical-shaped low velocity zone (between 12 and 18 km depth range) under Rabaul volcano. It exhibits a velocity contrast of more than 10% against its surroundings. This deep, low velocity zone is tectonically linked to the shallow volcano chamber by a pipe-like low velocity feature, as seen on the W-E cross-section between Rabaul volcano and Tavui caldera (Fig.10.19).

10.8 Discussion and Conclusions

The high velocity zone around the magma chamber at 3-4 km depth is interpreted as the cooled magma remnant, as suggested for other volcanic structures (i.e., Okubo et al., 1997; Haslinger et al., 2001). The outlier of the magma chamber is hardened, preventing the hot magma from spreading outside. The theoretical calculations for seismic-wave velocities of different melt geometries (Mavko, 1980) and constitutive relations of solid-liquid composites (Takei, 1998) suggest that an approximately 1 % perturbation in P-wave velocity is equivalent to a 1 % volume fraction of mafic melt. If these low velocity zones with ~10 % velocity contrast represent partial molten material, then the ~10% velocity contrast may indicate ~10 % partial melt (Lyer and Dawson, 1993). Alternatively, if these low velocity zones are simply the regions of increased temperature as other authors have suggested (Haslinger et al., 2001), then the temperature contrast against the surrounding materials, may be as high as 500° C. These are the results for ophiolitic rocks from Papua New Guinea (Kroenke et al, 1976). The Vp/Vs structure would help discriminate between these possibilities.

Despite the different data used, the main velocity features obtained from this study are quite similar in the shallow depth range to the previous results obtained from wide-angle profiling seismic explosion data, and tomographic images with only local earthquake data being used. This includes the shallow low velocity zone under Rabaul caldera complex, the V-shaped low velocity in the medium depth range from the nearly W-E cross-section, and the high velocity zone in the southwestern part which dips to the

northeast, along the Rabaul and Tavui tectonic line. But I obtained additional information about the deeper velocity structure around Rabaul volcano. In summary, the present studies have revealed the following new discoveries:

- The top volcanic magma chamber (with ~10 % velocity contrast, $6\times8\times2\ km^3$ anomalous volume) was found to lie at 3-4 km depth under the Rabaul caldera complex;
- Another low velocity zone (with ~8 % velocity contrast, $4\times4\times2\ km^3$ anomalous volume) is present under Tavui caldera down to 4 km depth, with a relatively small scale and deeper location when compared with the low velocity zone under Rabaul caldera complex;
- The velocity field is consistent with the geology around Rabaul volcano. That is, generally the velocity field increases from southwest of Rabaul volcano (continental crust) to northeast of Rabaul volcano (ocean crust) at comparable depth;
- The V-shaped low velocity zone under Rabaul volcano reaches as deep as 12 km depth;
- An overturned velocity structure exists in the medium depth region (around 8 km depth), with a high velocity zone overlying a low velocity structure beneath Rabaul volcano. This suggests some processes have occurred (for example, hot magma transportation) in this depth range as a result of SW-NE compression, with the principal stress direction dipping to the northeast;
- The deep low velocity zone (with ~10 % velocity contrast, possibly with ~10% partially melt status) extends to 18 km depth, and is linked to the top shallow magma reservoir by a pipe-like low velocity channel. This is the deepest low velocity zone under a volcano structure to have been found worldwide so far. It infers the possibility of deep magma storage.

Chapter 11: Summary and Directions of Future Study

11.1 Conclusions and Achievements

The Rabaul region of PNG is an area of major volcanic and seismological interest. The last major eruption of Rabaul volcano was in 1994. Two main active seismic investigations have so far been conducted in the Rabaul region. (1) 1967 and 1969 seismic refraction surveys; (2) the RELACS project (the project of Rabaul Earthquake Location and Caldera Structure, conducted from 1997 to 1998). From the above studies, three basic velocity models have been determined for the Rabaul region:

(1) a 1-D velocity model for P-wavespeed down to a depth of 40 km deduced by W-H inversion of the seismic explosion data from the 1967 and 1969 experiments;

(2) two 2-D roughly layered velocity models for P-wavespeed down to a depth 40 km determined by time-term analysis of the 1967 and 1969 seismic refraction data;

(3) a 3-D velocity model for P-wavespeed down to 10 km depth around Rabaul volcano using only local earthquake and explosion data of the RELACS project.

The 1967 and 1969 refraction profiles mainly concentrated on delineating the tectonic boundaries and determining the Moho topography on a large scale, while the RELACS project was concerned with only a relatively small region around Rabaul volcano. The latter was designed to map the velocity structure in detail, but its original purpose has up until now not been fulfilled. There are several outstanding questions. They include:

(a) What is the deep 3-D velocity structure under the Rabaul region, which is important to explain the volcanism (say to at least 20 km depth)?

(b) What is the S-wave velocity model (1-D, 2-D and 3-D) around the Rabaul region, which is more critical to explain the shear modulus or Poisson ratio?

(c) How can the volcanic earthquakes be located more precisely, which needs a deep 3-D velocity model for mid-depth events around the Rabaul region (these mid-depth earthquakes may be much more associated with generation and development of volcanic structure)?

In order to answer these questions, my doctoral research was undertaken. It comprised eight parts and the main results are summarized as follows:

11.1.1 Data collection and onset time picking

I revised an automatic onset time picking algorithm (Bai and Kennett, 2000) to determine at least two arrival times (say first P and first S arrival) simultaneously for both single- and three-component records of local, and especially regional events from the RELACS database. This adds both P and (especially) S arrival time picks to the database of the RELACS project, ready for P and S-wave travel time tomography. In chapter 9, I incorporated several picking functions (such as energy function, polarization filtering, auto-regressive technique) into the analysis routine, and compared several picking algorithms. Finally I used a combined picking technique to simultaneously deduce both first P and S-arrival times as far as possible for local events (including explosions), and especially near-regional earthquakes.

As a result, there were 161 events with first P-arrivals and 93 events with first S-arrivals that were picked in the present study, adding roughly more than 20,000 arrival times to the RELACS database.

11.1.2 Ray tracing in 3-D arbitrary media

I developed a new 3-D ray-tracing program for arbitrary media, with less memory storage and relatively fast execution speed to calculate the travel times of first arrival and associated ray paths with great accuracy. This is dealt with in the chapter 3, where I devised a 3-D ray-tracing program based on the 'irregular' approach of graph theory, but with modified cell node definition and a tri-linear velocity function linked to secondary nodes. The maximum relative error bound of the computed travel times was estimated within a homogeneous media, which may be used as an upper error bound for the whole model in real problems. The emphasis was directed at a comparison between the 'regular' and the 'irregular' approach for the shortest-path method, in the sense of both computational efficiency and the accuracy of the computed travel times.

To reduce the computer memory requirement and speed up the program run time, I incorporated an automatic function into the ray tracing process to select a variable (small) model according to each source to seismic network deployment. This results in a nearly 50% reduction in the memory requirement and a corresponding decrease in the run time, and thus has more practical usage in 3-D seismic forward modeling.

The results show that the new ray tracer is an effective method with fewer cells (velocity unknowns) than the 'regular' approach of the shortest path method, and is suitable for incorporation with any inversion procedure. It yields great accuracy in travel time and ray path predictions if enough secondary nodes are used, and has the capability to deal with a large 3-D model.

11.1.3 Non-linear travel time inversion

The purpose of chapter 4 was to find an efficient and accurate procedure for non-linear travel time inversion so as to incorporate it with the forward modeling to form a fast and reliable algorithm for 3-D nonlinear tomography. I have favored a damped, minimum norm, least squares and constrained solution (DMNLS). Instead of taking segments of ray paths as the elements of the Jacobian matrix, I calculated the time derivatives to changes in velocity as elements of analytical Jacobian matrix according to velocity and the travel-time equations. To estimate the efficiency and accuracy of inversion, I defined five quantities of convergence to assess the inversion process.

The results for efficiency, accuracy and sensitivity indicate that the program works well in high contrast velocity media (say, more than 20% velocity contrast), and also is relatively insensitive to tolerable levels of noise (say, less than 10% relative error both in travel time and model perturbation), which has a practical usage in real problems.

11.1.4 Hypocenter location in 3-D arbitrary media

A new source hypocenter location program was developed in chapter 7 for 3-D arbitrary media to relocate the near-regional events around the Rabaul volcano before starting the final RELACS data inversion. This procedure is robust and accurate. It used a modified 'irregular' shortest-path algorithm as the ray tracer and DMNLS-1 as the inversion solver. To avoid the instability of elements of the Jacobian matrix, a simple, but robust method of analytic Jacobian matrix calculation was created to obtain the time derivatives to the source position changes in three directions, which has six search directions in exploring the octant space for different combinations of time derivatives along the three directions.

Several numerical tests show that it works extremely well with a relatively small location error for both the travel times and the source positions, especially in real 3-D cases. The focal depth determination has a comparable high accuracy to the location in the horizontal plane (epicentral co-ordinate). A feature of the algorithm is that it is

not sensitive to the tolerable picking error, but is model-dependent. The algorithm is capable of locating a hundred events simultaneously, which has a practical use for seismic array data and the location of an aftershock sequence.

11.1.5 Relative arrival time tomography

To find another way to obtain a reasonable velocity image in the presence of systematic travel time errors, such as source parameter uncertainty on some recorders, and also to maximally increase the data coverage and eliminate artefacts introduced by timing errors, it was necessary to try an alternative approach other than absolute travel time tomography or simultaneous inversion with arrival times. In chapter 5, I developed 3-D relative arrival time tomographic procedure, referred either to the minimum or to the mean arrival time as an auxiliary method to overcome the above drawbacks.

Several numerical tests on synthetic models confirm that relative arrival time tomography can yield a reasonable and comparable image to travel time tomography. With the different formulation of the Jacobian matrix over the previous one (travel time tomography), relative arrival time tomography can do a comparable job to travel time inversion. It is the best way to proceed when the source parameters have a large uncertainty or the travel times have been contaminated with systematic timing errors in the data gathering and processing.

11.1.6 Joint seismic tomography

In chapter 8, I developed a program of 3-D joint travel time (or arrival time) inversion for updating both the velocity model and the source positions. It is an application and extension of the 3-D earthquake hypocenter location and the 3-D travel-time tomographic procedure, mentioned above. Three numerical tests were carried out to test the accuracy and efficiency of the procedure.

The results show that satisfactory velocity images and improved source locations can be obtained only if there is a rough initial estimate of the velocity model and the hypocenter. Otherwise, there is no reason to proceed. As expected, there is a trade-off between the quality of the velocity model and the accuracy of the source hypocenters.

11.1.7 Multi-step travel time tomography

With the need to reconstruct local, deep 3-D velocity structure using regional seismic data (maximize the data coverage and illuminate deeper parts of the structure) and to make 3-D seismic tomography feasible, practical, as well as realizable on a personal computer, I proposed in chapter 6 an alternative approach—multi-step travel

time tomography. The local velocity model (small model) is embedded into a regional velocity model (large scale model) and the seismic tomographic imaging is separated into two (or more) steps.

The results indicate that it is a possible and also a feasible way to transform the large-scale problem to a small-scale problem to save on computational requirements without loss the accuracy of the algorithm itself in general.

11.1.8 Application to reconstruction of the Rabaul volcano structure

The newly developed techniques have been applied to real data analysis in chapter 10 to recover the 3-D velocity structure of Rabaul volcano. I first obtained the 1-D velocity model both for P- and S-wavespeed around the Rabaul region by the Weichert-Herglotz inversion method, and then used this 1-D velocity model to relocate regional earthquakes so as to reduce the location errors associated with the large-aperture (global) seismic array. This was undertaken before the final 3-D travel time tomographic imaging. I recovered the 3-D velocity model under Rabaul region down to a depth of 20 km. This is more complex and detailed than that has been obtained from the previous studies. Despite the different data used, the main velocity features obtained from this study are quite similar in the shallow depth range to the previous results obtained from wide-angle profiling seismic explosion data, and tomographic images with only local earthquake data being used. The results have revealed the following new discoveries:

- *The top volcanic magma chamber is found to lie at 3-4 km depth under the Rabaul caldera complex;*
- *Another low velocity zone is present under the Tavui caldera down to 4 km depth;*
- *The velocity field is consistent with the geology around Rabaul volcano;*
- *A medium deep range V-shaped low velocity zone was imaged under Rabaul volcano, it reaches as deep as 12 km;*
- *An overturned velocity structure exists in the medium depth region, with a high velocity zone overlying a low velocity structure beneath Rabaul volcano;*
- *A deep low velocity zone (possible magma source) was delineated to 18 km depth, and is linked to the top shallow magma reservoir by a pipe-like low velocity channel.*

11.2 Directions of Future Research

The research work restated here can be extended in several ways, along with some other interesting ideas for further study, as summarised below.

3-D ray tracing for later arrivals

So far, the developed 3-D ray tracing software can only deal with travel times and ray paths of first breaks. It would be useful to extend it to calculate travel times and ray paths of later arrivals, such as reflected and refracted phases, depending on the input velocity model.

3-D travel time (or arrival time) inversion with multi-parameters

In order to overcome the limitations of travel time (kinematics) inversion (high frequency assumption) and further constrain the model space, it would be worthwhile incorporating amplitudes (energy) and waveforms using a dynamic inversion to map discontinuities and other velocity features.

3-D event location with arrival times, not travel times

The location software could be made more applicable to real world cases, by reformulating the hypocentral determination problem in terms of arrival time, and not the travel time.

3-D joint inversion with relative arrival time

In similar fashion to the widely used double-difference method (DD), it would be advantageous to exploit relative arrival time inversion referred to the mean arrival time (or the minimum arrival time) to simultaneously update the velocity model and the source parameters.

3-D velocity model of S-wavespeed for Rabaul volcano

The first arrival S wave dataset is ready for inversion, but I ran out of time to do it. It would be worth building up the 3-D model for S velocity beneath Rabaul volcano as a supplement to further analyze and understand the tectonic structure of the Rabaul volcano. This would permit assessment of Poisson's ratio (or the V_P/V_S structure), which should relate to fluid content.

Bibliography

Aki, K. and Lee, W.H.K., 1976, Determination of three-dimensional velocity anomalies under a seismic array using first P arrival times from local earthquakes: 1. A homogeneous initial model, *J. Geophys. Res.*, 81, 4381-4399.

Aki, K., Christoffersson, A. and Husebye, E.S., 1977, Determination of the three-dimensional seismic structure of the lithosphere, *J. Geophys. Res.*, 82(2), 277-296.

Bai, C.-Y. and Kennett, B.L.N., 2000, Automatic phase-detection and identification by full use of a single three-component broadband seismogram, *Bull. Seism. Soc. Am.*, 90, 187-198.

Bai, C.-Y. and Kennett, B.L.N., 2001, Phase identification and attribute analysis of broadband seismograms at far-regional distances, *J. Seismology*, Vol.15, No.2, 217-231.

Bai, C-Y., Greenhalgh, S.A. and Zhou, B., 2004, 3-D ray tracing by an irregular shortest path method, *Geophys. J. Int.*, (in press).

Bai, C-Y. and Greenhalgh, S.A., 2004, 3-D non-linear travel time tomography: Imaging high contrast velocity anomalies, *Pure & Applied Geophysics,* (in press).

Bai, C-Y. and Greenhalgh, S.A., 2004, 3-D multi-step travel time tomography: Imaging the local, deep velocity structure of Rabaul volcano, Papua New Guinea, *Phys. Earth Planet. Inter.* (in review).

Bai, C.-Y., and Greenhalgh, S.A., 2004, 3-D local earthquake hypocenter determination with an 'irregular' shortest-path method, *Bull. Seism. Soc. Am.* (in review).

Bijiwaard, H., Spakman, W. and Engdahl, E.R., 1998, Closing the gap between regional and global travel time tomography, J. Geophys. Res., 103(B12), 30055-30078.

Bohm, G. and Vesnaver, A.L., 1999, In quest of the grid, *Geophysics*, 64, 1116-1125.

Bregman, N.D., Bailey, R.C. and Chapman, C.H., 1989, Determination of the three dimensional seismic structure of the lithosphere, *J. Geophys. Res.*, 82, 277-296.

Buland, R., 1976, The mechanics of locating earthquakes, *Bull. Seim. Soc. Am.*, 66, 173-187.

Bulau, J.R., 1991, Acoustic tomography for reservoir surveillance: the integration of geology, geophysics, petrophysics, and petroleum engineering in reservoir delineation, description and management, *Proc. Of first Archie Conf., AAPG*, 159-170.

Bullen, K.E., 1963, An introduction to the theory of seismology, Cambridge University Press.

Bunks, K.P., Saleck, F.M., Zaleski, S. & Chavent, G. 1995, Multiscale seismic waveform inversion. *Geophysics*, 60, 1457-1473.

Cao, S., and Greenhalgh, S.A., 1993, Calculation of the seismic first-break time field and its ray path distribution using a minimum traveltime tree algorithm, *Geophys. J. Int.*, 114, 593-600.

Cao, S. & Greenhalgh, S.A. 1994 Finite-difference solution of the eikonal equation using an efficient first-arrival wavefront tracking scheme: Geophysics 59, 632-643.

Cao, S., and Greenhalgh, S.A., 1995, High-resolution seismic tomographic delineation of ore deposits, preview-conference Handbook, *ASEG 11th Geophysical Conference and Exhibition*, 57, P. 119.

Cao, S. & Greenhalgh, S.A. 1995, Crosswell seismic tomographic delineation of mineralisation in a hard rock environment. *Geophys. Prosp.*, 45, 449-460.

Carrion, P.M., 1989, Generalized non-linear elastic inversion with constraints in model and data space, *Geophys. J.*, 96, 151-162.

Carrion, P.M., 1991, Dual tomography for imaging complex structures, *Geophysics*, 56, 1395-1404.

Červený, V., Klimeš, L. & Pšenčík, I., 1988, Complete seismic-ray tracing in three-dimensional structures, in Seismological Algorithms, pp. 89-168. ed. Doornbos, D. J., Academic Press, New York.

Chiu, S.K.L. & Stewart, R.R. 1987, Tomographic determination of three-dimensional seismic velocity structure using well logs, vertical seismic profiles and surface seismic data. *Geophysics,* 52, 1085-1098.

Chunduru, R.K., Sen, M.K. & Stoffa, P.L. 1997. Hybrid optimization methods for geophysical inversion, *Geophysics,* 62, 1196-1207.

Colombo, D., Cimini, G.B., and de Franco, R., 1997, Three-dimensional velocity structure of the upper mantle beneath Costa Rica from a teleseismic tomography, *Geophys. J. Int.,* 131, 189-208.

Coultrip, R.L., 1993, High-accuracy wavefront tracing traveltime calculation, *Geophysics*, 58, 284-292.

Dawson, P. B., Chouet, B. A., Okubo, P. G., Villasenor, A. and Benz, H. M., 1999, Three-dimensional velocity structure of the Kilauea caldera, Hawaii, *Geophys. Res. Letter*, 26, 2805-2808.

Den, N. & Pang, C., 1984, Shortest-path algorithms: taxonomy and annotation, *Networks*, 14, 275-323.

Dijkstra, E.W., 1959. A note on two problems in connexion with graph, *Numer. Math.*, 1, 269-271.

Dobroka, 1992, Tomographic inversion of normalized data: Double-trace tomography algorithm, *Geophysical Prospecting*, 40, 1-14.

Dorren, H.J.S. & Snieder, R.K. 1997. Error propagation in non-linear delay time, *Geophys. J. Int.*, 128, 632-638.

Earle, P.S. and P.M. Shearer, 1994, Characterization of global seismograms using an automatic-picking algorithm, *Bull. Seism. Soc. Am.*, 84, 366-376.

Eberhart-Phillips, D., 1990, Three-dimensional P and S velocity structure in the Coalinga region, California, *J. Geophys. Res.,* 95(B10), 15343-15363.

Engdahl, E.R. and Lee, W.H.K., 1976, Relocation of local earthquake by seismic ray tracing, *J. Geophys. Res.*, 81, 4400-4406.

Faria, E.L. & Stoffa, P.L., 1994. Traveltime computation in transversely isotropic media, *Geophysics*, 59, 272-281.

Finlayson, D.M, Gudmunsson, O., Itikarai, L., Nishimura, S.and Shimamura, H., 2003, Rabaul volcano, Papua New Guinea: Seismic tomographic imaging of an active caldera, *J. Volc. & Geotherm. Res.*, 124, 153-171.

Finlayson, D.M, Gudmunsson, O., Itikarai, L., Nishimura, S., Shimamura, H., and Johnson, R.W., 1999, Wide-angle seismic profiling across the Rabaul volcano: A framework for tomographic imaging of caldera architecture, *IUGG 99, Birmingham.*

Finlayson, D.M. and Cull, J.P., 1973, Structural profiles in the New Britain / New Ireland region, *J. Geo. Soc. Am.*, 20, 37-48.

Finlayson, D.M., Cull, J.P., Wiebenga, W.A., Furumoto, A.S. and Webb, J.P., 1972, New Britain—New Ireland crustal seismic refraction investigation 1967 and 1969, *Geophys. J. R. astr. Soc.*, 29, 245-253.

Finlayson, D.M. and Cull, J.P., 1973, time-term analysis of New Britain—New Ireland Island Arc structures, *Geophys. J. R. astr. Soc.*, 33, 265-280.

Finlayson, D.M., Gudmundsson, O., Itikarai, I., Saunders, S., Powell, L., Thurber, C.H., Shimamura, H., and Nishimura, Y., 2001, The Rabaul earthquake location and caldera structure (RELACS) program: *Operations Report, AGSO Record 2001/01.*

Fischer, R. & Lees, J.M., 1994. Shortest path ray tracing with sparse graphs, *Geophysics*, 58, 987-996.

Frazer, L.N., Xinhua Sun and Wilkens, R.H., 1997, Inversion of sonic waveform with unknown source and receiver functions, *Geophys. J. Int.*, 129, 579-586.

Frazer, L.N. and Xin-hua Sun, 1998, New objective function for waveform inversion, *Geophysics,* 63, 213-222.

Fremont, M.-J., and S.D. Malone, 1987, High precision relative locations of earthquakes at Mount St. Helens, Washington, *J. Geophys. Res.*, 92, 10223-10236.

Gallo, G. & Pallottino, S., 1986, Shortest path methods: a unifying approach, *Mathematical Programming Study*, 26, 38-64.

Gan, H., Levin, P.L., and Ludwig., R., 1993, Finite element formulation of acoustic scattering phenomena with absorbing boundary conditions in the frequency domain, *J. Acoust. Soc. Am.*, 94, 1651-1661.

Gan, H., Ludwig., R., and Levin, P.L., 1994, Non-linear diffraction inverse scattering for multiple scatters in inhomogeneous acoustic background media, *J. Acoust. Soc. Am.*, 97, 764-776.

Gelius. L.J., 1995a, Generalized acoustic diffraction tomography, *Geophysical Prospecting*, 43, 3-29.

Gelius. L.J., 1995b, A sample of controlled experiments in diffraction tomography, *Geophysical Prospecting*, 43, 31-50.

Gelius. L.J., 1995c, Limited-view diffraction tomography in a non-uniform background, *Geophysics*, 60, 580-588.

Geoltrain, S. and Brac, J., 1993, Can we image complex structures with first-arrival traveltime?, *Geophysics*, 58, 564-575.

Gersztenkorn, A. and Scales, J.A., 1988, Smoothing seismic tomograms with alpha-trimmed means, *Geophys. J.*, 92, 67-72.

Giovanni, B. Cimini and Pasquale De Gori, 2001, Nonlinear P-wave tomography of subducted lithosphere beneath central-southern Apennines (Italy), *Geophys. Res. Lett.*, 28, 4387-4390.

Gochioco, L.M., 2000, High-resolution 3-D seismic survey over a coal mine reserve area in the U.S.—A case study, *Geophysics*, 65, 712-718.

Graeber, F., Houseman, G & Greenhalgh, S.A. 2002, Teleseismic tomography of the western Lachlan Orogen and the Newer Volcanic Province, southeast Australia, *Geophys. J. Int.*, 149, 249-266.

Gresilaud, A. & Cara, M., 1996, Anisotropy and P-wave tomography: a new approach for inverting teleseismic data from a dense array of stations. *Geophys. J. Int.*, 126, 77-91.

Grechka, V.Y. and MeMechan, G.A., 1997, Analysis of reflection traveltimes in 3-D transversely isotropic heterogeneous media, *Geophysics*, 62, 1884-1895.

Gruber, T., 1998, Crosshole seismic tomography incorporating later arrivals, *Ph.D. thesis*, The University of Adelaide.

Gruber, T. and S.A. Greenhalgh, 1998, Short note: Precision analysis of first-break times in grid models, *Geophysics*, 63, 1062-1065.

Gualtiero Bohm and Vesnaver, A.L., 1999, In quest of the grid, *Geophysics*, 64, 1116-1125.

Gudmunsson, O., and Miller, H., 1997-1999, RELACS---Imaging the Rabual volcano, *Annual Report*, *RSES*, The Australian National University.

Gudmunsson, O., Finlayson, D.M., Itikarai, L., Nishimura, S., Shimamura, H., and Johnson, R.W., 1999, velocity tomography of shallow structure beneath Rabaul Caldera based on local earthquake and explosion data, *IUGG 99, Birmingham*.

Guiziou, J.L., Mallet, H.L. & Madariaga, R., 1996, 3-D seismic reflection tomography on top of GOCAD depth modeler, *Geophysics*, 61, 1499-1510.

Guiziou, J.L., Mallet, H.L. & Madariaga, R. 1996, 3-D seismic reflection tomography on top of GOCAD depth modeler, *Geophysics,* 61, 1499-1510.

Haslinger, F., Thuber, C., Mandernach, M. and Okubo, P., 2001. Tomographic Image of P-velocity structure beneath Kilauea's East Rift Zone and South Flank: seismic evidence for a deep magma body, *Geophys. Res. Letter*, 28, 375-378.

Hirata, N. and Matsu'ura, M., 1987, Maximum-likelihood estimation of hypocenter with origin time eliminated using nonlinear inversion technique, *Phys. Earth Planet. Inter.*, 47, 50-61.

Humphreys, E. and R.W. Clayton, 1988, Adaptation of back projection tomography to seismic travel time problems, *J. Geophy. Res.*, 93, 1073-1085.

Inoue, H., Fukao, Y., Tanabe, K. and Y. Ogata, 1990, Whole mantle P-wave travel time tomography, *Phys. Earth Planet. Inter.*, 59, 294-328.

Julian, B.R. and Gibbins, D., 1977, Three dimensional seismic ray tracing, *J. Geophys.*, 43, 95-119.

Johnson, D.B., 1977, Efficient algorithms for shortest paths in sparse networks, *Journal of ACM*, 24, 1-13.

Johnson, R.W., 1979, Geotectonics and volcanism in Papua New Guinea: A review of the late Cainozoic, *BMR Journal of Australian Geology and Geophysics*, 4, 181-207.

Justice, J.H., Mathisen, M.E., Vassilion, A.A., Singh, S., Cunningham, P.S., and Van der Hilst, R.D., Widiyantoro, S., and Engdahl, E.R., 1997, Evidence for deep mantle circulation from global tomography, *Nature*, Vol. 386, April 10.

Justice, J.H., Mathisen, M.E., Vassilion, A.A., Singh, S., Cunningham, P.S., and Van Trier, J., and Symes, W.W., 1991, Upwind finite-difference calculation of traveltimes, Geophysics, 56, 812-821.

Kennett, B.L.N., Sambridge, M.S. and Williamson, P.R., 1988, Subspace methods for large inverse problems with multiple parameter classes, *Geophys. J. Int.*, 94, 237-247.

Kennett, B.L.N., Widiyantoro, S., and van der Hilst, R.D., 1998, Joint seismic tomography for bulk sound and shear wave speed in the Earth's mantle, *J. Geophys. Res.*, 103, 12469-12493.

Klein, F.W. 1978. Hypocenter location program—HYPOINVERSE: user's guide to version 1, 2, 3 and 4, *U.S.Geol.Surv. Open-File Rept.*78-694, 1-113.

Klein, F.W. 1988. User's guide to HYPOINVERSE, a program for VAX computers to solve for earthquake location, *U.S. Geol.Surv. Open-File Rept.*, 88.

Klimeš, L. & Kvasnička, M., 1994, 3-D network ray tracing, *Geophys. J. Int.*, 116, 726-738.

Koch, M., 1986, Non-linear inversion of local seismic travel times for the simultaneous determination of 3D –velocity structure and hypocenters—application to the seismic zone Vrancea, *J. Geophys.*, 56, 160-173.

Kornig, M.1995, Cell ray tracing for smooth isotropic media: a new concept based on a generalized analytic solution, *Geophys. J. Int.*, 123, 391-408.

Kroenke, L.w., M.H. Manghnani, C.S. Rai, P. Fryer, and R. Ramananantoandro, 1976, Elastic properties of selected ophiolitic rocks from Papua New Guinea: nature and composition of oceanic lower crust and upper mantle, in The Geophysics of the Pacific Ocean Basin and its Margin, Am. Geophys. Un. Monograph 19, 407-421.

Laigle, M. and Hirm, A., 1999, Explosion-seismic tomography of a magmatic body beneath Etna: volatile discharge and tectonic control of volcanism, *Geophys. Res. Letter*, 26, 2665-2668.

Lambare, G., Lucio, P.S. & Hanyga, A., 1996, Two-dimensional multivalued traveltime and amplitude maps by uniform sampling of a ray field, *Geophys. J. Int.*, 125, 584-598.

Lee, W.H.K. and Lahr, J.C., 1975, HYPO71 (revised): a computer program for determining hypocenter, magnitude, and first-motion pattern of local earthquakes, *U.S. Geol.Surv. Open-File Rept.*75-311, 1-116.

Lee,W.H.K. and Stewart, S., 1981, Principles of Microearthquake networks, *Academic Press, New York.*

Lenonard, M. and Kennett, B.L.N., 1999, Multi-component auto-regressive techniques for the analysis of seismograms, *Phys. Earth Planet. Inter.*, 113, 247-263.

Li, Zhiming, 1991, Compensating finite-difference errors in 3-D migration and modelling, *Geophysics*, 56, 1650-1660.

Lin, C.-H., and Roecker, S.W., 1997, Three-dimensional P-wave velocity structure of the Bear Valley region of central California, *PAGEOPH*, 149(4), 667-688.

Luo, Y. and Schuster, G.T., 1991, Wave-equation traveltime inversion, *Geophysics*, 56, 645-653.

Lyer, H.M., and P.B. Dawson, 1993, Imaging volcanoes using teleseismic tomography, in: Lyer, H.M. and Hiahara, K. (eds), Seismic tomography: Theory and Practice, Chapman & Hall, Landon, 466-492.

Madriad, J.A. and Traslosheros, J.C.V., 1993, Joint determination of velocity structure and depth of discontinuities, *Geophys. J. Int.*, 112, 74-80.

Mao, W. & Stuart, G.W., 1997, Transmission-reflection tomography: application to reverse VSP data, *Geophysics,* 62, 884-894.

Matsuoka, T. and Ezaka, T., 1992, Ray tracing using reciprocity, *Geophysics*, 57, 326-333.

Mavko, G.M., 1980, Velocity and attenuation in partially molten rocks, *J. Geophys. Res.*, 85, 5173-5189.

Menke, W. (1984), Geophysical data analysis: discrete inverse theory, Academic Press Inc., New York.

McGaughey, M. & Singh, S.C., 1997, Simultaneous velocity and interface topography of normal-incidence and wide-aperture seismic traveltime data, *Geophys. J. Int.*, 131, 87-99.

Mcmechan, G.A., Harris, J.M. and Anderson, L.M., 1987, Cross-hole tomography for strongly variable media with application to Scale model data, *Bull. Seism. Soc. Am.*, 77, 1945-1960.

Mcqueen, H.W.S. and Lambeck, K., 1996, Determination of crustal structure in central Australia by inversion of traveltime residuals, *Geophys. J. Int.*, 126, 645-662

Michelini, A., 1995, An adaptive-grid formalism for traveltime tomography, *Geophys. J. Int.*, 121, 489-510.

Michelena, R.J. & Harris, J. M., 1991, Tomographic traveltime inversion using natural pixels, *Geophysics*, 56, 635-644.

Moser, T. J., 1989, Efficient seismic ray tracing using graph theory, in Expended Astracts, 59th Annual Int. SEG Meeting, pp.1106-1108, Soc. Explor. Geophys., Tulsa, Oklahoma.

Moser, T. J., 1991, Shortest path calculation of seismic rays, *Geophysics*, 56, 59-67.

Moser, T.J., T. Van Eck and G. Nolet, 1992. Hypocenter Determination in strongly heterogeneous earth models using the shortest path method. *J. Geophys. Res.*, 97, 6563-6572.

Moser, T.J., 1994, Migration using the shortest-path method, *Geophysics*, 59, 1110-1120.

Mufti, I.R., 1990, Large-scale three-dimensional seismic models and their interpretive significance, *Geophysics*, 55, 1166-1182.

Nakanishi, I. and Yamaguchi, K., 1986. A numerical experiment on nonlinear image reconstruction from first-arrival times for two-dimensional island arc structure, *J. Phys. Earth*, 34,195-201.

Neele, F., VanDecar, J.C. & Snieder, R., 1993, A formalism for including amplitude data into tomographic inversions, *Geophys. J. Int.*, 115, 482-496.

Nemeth, T., Normark, E. & Qin, F., 1997, Dynamic smoothing in crosswell traveltime tomography, *Geophysics*, 62, 168-176.

Okuba, P.G., H.M. Benz, and B.A. Chouet, 1997, Imaging the crustal magma sources beneath Mauna Loa and Kilauea volcanoes, Hawaii, *Geology*, 25, 867-870.

Pavlis, G.L., 1986, Appraising earthquake hypocenter location errors: a complete, practical approach for single-event location, *Bull. Seism. Soc. Am.*, 76, 1699-1717.

Pavlis, G. L. and Booker, J, R., 1980, The mixed discrete continuous inverse problem: application to simultaneous determination of earthquake hypocenter and velocity structure, *J. Geophys. Res.*, 85, 4801-4810.

Phillips, W.S. and Fehler, M.C., 1991, Traveltime tomography: A comparison of popular methods, *Geophysics*, 56, 1639-1649.

Podvin, P. and Lecomte, I., 1991, Finite difference computation of traveltimes in very contrasted velocity models: a massively parallel approach and its associated tools, *Geophys. J. Int.*, 105, 271-284.

Pratt, R.G. and Goulty, N.R., 1991, Combining wave-equation imaging with traveltime tomography to form high-resolution images from crosshole data, *Geophysics*, 56, 208-224.

Pratt, R.G., McGaughey, W.J. & Chapman, C.H., 1993, Anisotropic velocity tomography: a case study in a near-surface rock mass, *Geophysics,* 58, 1748-1763.

Pratt, R.G., 1999, seismic waveform inversion in the frequency domain, part 1: theory and verification in a physical scale model, *Geophysics*, 64, 888-901.

Qin, F.-H., and Luo, Y., 1992, Finite-difference solution of the eikonal equation along expanding wavefronts, *Geophysics*, 57, 478-487.

Qin, F., and Schuster, G. T., 1993, First-arrival traveltime calculation for anisotropic media, *Geophysics*, 58, 1349-1358

Quan, Y.-L. and Harris, J.M., 1997, Seismic attenuation tomography using the frequency shift method, *Geophysics*, 62, 895-905.

Reiter, D.T. & Rodi, W., 1996, Nonlinear waveform tomography applied to crosshole seismic data, *Geophysics*, 61, 902-913.

Roecker, S.W., 1982, Velocity structure of the pamir-Hindu Kush region; possible evidence of subducted crust, *J. Geophys. Res.*, 87(B2), 945-959.

Rowe, C.A., R.C. Aster, W.S. Phillips, R.H. Jones, B. Borchers and M.C. Fehler, 2002, Using automated, high-precision repicking to improve delineation of microseismic structures at the Scoultz geothermal reservoir, Pure Appl. Geophys., 159, 563-596.

Saito, H., 1989, Traveltimes and raypaths of first arrival seismic waves: computation method based on Huygens' principle, in Expended Astracts, 59th Annual Int. SEG Meeting, pp.244-247, Soc. Explor. Geophys., Tulsa, Oklahoma.

Saito, H., 1990, 3D ray-tracing method based on Huygens' principle, in Expended Astracts, 60th Annual Int. SEG Meeting, pp.1024-1027, Soc. Explor. Geophys., Tulsa, Oklahoma.

Sambridge, M.S., 1990, Non-linear arrival time inversion: constraining velocity anomalies by seeking smooth models in 3-D, *Geophys. J. Int.*, 102, 653-677.

Sambridge, M.S. and Kennett, B.L.N., 1990, Boundary value ray tracing in heterogeneous media: a simple and variable algorithm, *Geophys. J. Int.*, 101, 157-168.

Sambridge, M.S., Tarantola, A. and Kennett, B.L.N., 1991, An alternative strategy for non-linear inversion of seismic waveforms, *Geophys. Prospec.*, 39, 723-736.

Sambridge, M., Braun, J. and McQueen, H., 1995, Geophysical parameterization and interpolation of irregular data using natural neighbours, *Geophys. J. Int.*, 122, 837-857.

Sambridge, M.S. and Gudmundsson, O., 1998, Tomographic systems of equation with irregular cells, *J. Geophys. Res.*, 103(B1), 773-781.

Schneider, W.A. Jr., Ranzinger, K.A., Balch, A.H. & Kruse, C., 1992, A dynamic programming approach to first arrival traveltime computation in media with arbitrary distributed velocities, *Geophysics*, 57, 39-50.

Sehudandi, Ch. & Toint, P.L., 1994, Non-linear optimization for seismic traveltime tomography, *Geophys. J. Int.*, 105, 929-940.

Shearer, P.M., 1997, Improving local earthquake locations using the L1 norm and waveform cross correlation: Application to Whittier Narrows, California, aftershock sequences, *J. Geophys. Res.*, 102, 8269-8283.

Snieder, R. and Sambridge, M. S., 1992, Ray perturbation theory for traveltimes and ray paths in 3-D heterogeneous media, *Geophys. J. Int.*, 109, 294-322.

Song, Z.M., and Williamson, P.R., 1995, Frequency-domain acoustic wave modeling and inversion of crosshole data: Part 1-2.5 D modeling, *Geophysics*, 60,784-795.

Spencer, C. and Gubbins, D., 1980, Traveltime inversion for simultaneous earthquake location and velocity determination on laterally varying media, *Geophys. J. R. astr. Soc.*, 63, 95-116.

Squires, L.J., Blakeslee, S., and Stoffa, P.L., 1992, The effect of statics on tomographic velocity reconstructions, *Geophysics*, 57, 353-362.

Squires, L.J., Stoffa, P.L. & Cambois, G., 1994, Borehole transmission tomography for velocity plus statics, *Geophysics*, 59, 1028-1036.

Su, W.-J., and Dziewonski, A.M.,1997, Simultaneous inversion for 3D variations in shear and bulk velocity in the mantle, *Phy. Earth Planet. Inter.*, 100, 135-156.

Sun, Y., 1993, Ray tracing in 3-D media by parameterized shooting, *Geophys. J. Int.*, 114, 145-155.

Takanami, T. and Kitagawa, G., 1988, Anew efficient procedure for the estimation of onset times of seismic waves, *J. Phys. Earth.*, 36, 267-290.

Takanami, T. and Kitagawa, G., 1993, Multivariate time-series models to estimate the arrival times of S waves, *Computers and Geosciences*, 19, 295-301.

Takei,Y., 1998, Constitutive mechanical relations of solid-liquid composites in terms of grain-boundary contiguity, *J. Geophys. Res.*, 103, 18183-18203.

Tarantola, A. and Valette, B., 1982, Inverse problem =quest for information. *J.Geophys.*, 50, 159-170.

Tarantola, A and Valette, B., 1982, Generalized non-linear inverse problems solved using the least-squares criterion, *Rev. Geophys. Space. Phys.*, 20,219-232.

Tarantola, A., 1984, Inversion of seismic reflection data in the acoustic approximation, *Geophysics*, 49, 1259-1266.

Thomson, C.T., 1999, The gap between seismic ray theory and a full wavefield extrapolation, *Geophys .J. Int.*, 137, 364-380.

Tinti, S. & Ugolini, S., 1990, Pre-selection of seismic rays as a possible method to improve the inversion problem solution, *Geophys. J. Int.*, 102, 45-61.

Thurber, C.H., 1983, Earthquake locaions and three-dimensional crustal structure in the Coyote Lake Area, Central California, *J. Geophys. Res.*, 88, 8226-8236.

Thurber, C.H. and Ellsworth, W.L., 1980, Rapid solution of ray tracing problems in heterogeneous media, *Bull. Seism. Soc. Am.*, 70, 1137-1148.

Thurber, C.H., 1985, Non-linear earthquake location: theory and examples, *Bull. Seism. Soc. Am.*, 78, 2062-2076.

Thurber, C.H., 1987, Seismic structure and tectonics of Kilauea volcano, Hawaii. In: Decker, R.W., Wright, T.L. and Stauffer, P.H. (Eds.), Volcanism in Hawaii, US Geological Survey, pp. 919-934.

Thurber, C.H., 1992, Hypocenter-velocity structure coupling in local earthquake tomography, *Phys. Earth Planet. Inter.*, 75, 55-62

Thurber., C. and Eberhart-Phillips D., 1999, Local earthquake tomography with flexible gridding, *Comput. Geosci.*, 25, 809-818.

Tong, C. and B.L.N. Kennett, 1996, Automatic seismic event recognition and later phase identification for broadband seismograms, *Bull. Seism. Soc. Am.*, 86, 1896-1909.

Um, J. and Thurber, C., 1987, A fast algorithm for two-point seismic ray tracing, *Bull. Seism. Soc. Am.*, 77, 972-986.

Vasco, D.W., 1997, Groups, algebras, and the non-linearity of geophysical inverse problems, *Geophys. J. Int.*, 131, 9-23.

Vasco, D.W., Peter Jr., J.E., and Majer, E.L., 1996, A simultaneous inversion of seismic traveltimes and amplitude for velocity and attenuation, *Geophysics*, 61, 1738-1757.

Vesnaver, A.L., 1996, Irregular grids in seismic tomography and minimum-time ray tracing, *Geophys. J. Int.*, 126, 147-165.

Vidale, J.E.,1986, Complex polarization analysis of particle motion, *Bull. Seism. Soc. Am.*, 76, 1393-1405.

Vidale, J.E., 1988, Finite-difference calculation of travel times, *Bull. Seism. Soc. Am.*, 78, 2062-2076.

Vidale, J.E., 1990, Finite-difference calculation of traveltimes in three dimensions, *Geophysics*, 55, 521-526.

Vinje, V., Iversen, E. & Gjoystdal, H., 1993, Traveltime and amplitude estimation using wavefront construction, *Geophysics*, 58, 1157-1166.

Virieux, J. and Farra, V., 1991, Ray tracing in 3-D complex isotropic media: An analysis of the problem, *Geophysics*, 56, 2057-2069.

Vladimir, Y. G. and George, A.M, 1997, analysis of reflection traveltimes in 3-D transversely isotropic heterogeneous media, *Geophysics,* 62, 1884-1895.

Wagner, G. and Owens, T., 1996, Signal detection using multi-channel seismic data, *Bull. Seism. Soc. Am.*, 86, 221-231.

Waldhouser, F., and W.L. Ellsworth, 2000, Double-difference earthquake location algorithm: method and application to the northern Hayward fault, California, *Bull. Seism. Soc. Am.*, 90, 1353-1368.

Wang, B., and Braile, L.W., 1996, Simultaneous inversion of reflection and refraction seismic data and application to field data from Northern Rio Grande rift, *Geophys. J. Int.*, 125, 443-458.

Wang, Y. & Houseman, G.A., 1994, Inversion of reflection seismic amplitude data for velocity variation, *Geophys. J. Int.*, 117, 92-100.

Wang, Y. & Pratt, R.G., 1997, Sensitivities of seismic traveltimes and amplitudes in reflection tomography, *Geophys. J. Int.,* 123, 355-372.

Wielandt, E., 1987, On the validity of the ray approximation for interpreting delay times, in G. Nolet (Ed), Seismci tomography, D. Reidel Publishing Co., 85-98.

William A. Schneider, Jr., 1995, Robust and efficient upwind finite-difference traveltime calculations in three dimensions, *Geophysics*, 60, 1108-1117

Williamson, P.R., 1991, A guide to the limits of resolution imposed by scattering in ray tomography, *Geophysics*, 56, 202-207.

Withers, M., Aster, R., Young, C., Beiriger, J., Harris, M., Moore.S. and Trujillo, J., 1998, A comparison of select trigger algorithms for automated global seismic phase and event location, *Bull. Seism. Soc. Am.*, 88, 96-106.

Witten, A., Gillette, D.D., Sypniewski, J., and King, W.C., 1992, Geophysical diffraction tomography at a dinosaur site, *Geophysics*, 57, 187-195.

Wright, J., Harrell, H.C., Wang, J., and Gibbs, D., 1988, Cross-hole seismic tomography for engineering evaluation at Theodore Roosevelt Dam, Arizona, *58th Annual Internat. Mtg., Soc. Expl. Geophys., Expanded Abstracts, Session ENG 2.5.*

Xu, T., McMechan, G.A. & Sun, R., 1995, 3-D pre-stack wavefield inversion, *Geophysics*, 60, 1805-1818.

Zelt, C.A., 1994, 3-D velocity structure from simultaneous traveltime inversion of in-line seismic data along intersecting profiles, *Geophys. J. Int.,* 108, 795-801.

Zhao, D.-P., Hasegawa, A. and Horicuchi, S., 1992, Tomographic imaging of P and S wave velocity structure beneath northeastern Japan, *J. Geophys. Res.*, 97, 19909-19928.

Zhao, D.-P., Xu, Y.-B., Douglas, A.W., Dorman, L., Hildebrand, J. and Webb, S., 1997, Depth extent of the Lau Back-Arc spreading center and its relation to subduction processes, *Science*, 278, 254-257.

Zhao, H.-J., and Thurber, C.H., 2003, Double-difference tomography: The method and its application to the Hayward fault, California, *Bull. Seism. Soc. Am.*, 93, 1875-1889.

Zhou, Hau-wei, 1993, Traveltime tomography with a spatial-coherency filter, *Geophysics*, 58, 720-726.

Zhou B., C. Sinadinovski and S.A. Greenhalgh, 1992, Non-linear inversion travel-time tomography: imaging high-contrast inhomogeneities, *Exploration Geophysics*, 23, 459-464.

Zhou B., Greenhalgh, S.A. and Sinadinovski, C., 1992a. Iterative algorithm for the damped minimum norm, least-squares and constrained problem in seismic tomography. *Exploration Geophysics*, 23, 497-505.

Zhou, B., Greenhalgh, S.A. and Sinadinovski, C., 1992b, Iterative inverse techniques for DMNLS in seismic tomography: in *Geotomography – Vol II, Society of Exploration Geophysicists, Japan*, 111-128.

Zhou, B., Greenhalgh, S.A.& Zhe, J. 1993. Numerical seismogram computations for inhomogeneous media using a short, variable length convolutional differentiator: Geophysical Prospecting 41, 751-765.

Zhou, B. and Greenhalgh, S.A., 1998, Composite boundary-valued solution of 2.5-D Green's function for arbitrary acoustic media, *Geophysics*, 63, 1813-1823.

Zhou, C.X., Cai, W.Y., Luo, Y. & Schuster, G., 1993, High resolution crosswell imaging by seismic traveltime + waveform inversion, *The Leading Edge*, 12, No. 10, 988-991.

Zhou, C.X., Cai, W.Y., Luo, Y. & Schuster, G., 1995, Acoustic wave equation traveltime and waveform inversion of crosshole seismic data, *Geophysics*, 60, 765-773.

Zhu, J-S, 1988, The computational algorithms in seismology, Seismological Press, Beijing, China (in Chinese)